The Shoelace Antenna: A Device to Induce Short-Wavelength Fluctuations in the Edge Plasma of the Alcator C-Mod Tokamak

by

Theodore Golfinopoulos

Submitted to the Department of Electrical Engineering and Computer Science

in partial fulfillment of the requirements for the degree of

Doctor of Science

at the

MASSACHUSETTS INSTITUTE OF TECHNOLOGY

June 2014

Author .....

Department of Electrical Engineering and Computer Science

May 21, 2014

Certified by .....

Ronald R. Parker

Professor

Thesis Supervisor

Certified by .....

Brian LaBombard

Senior Research Scientist

Thesis Supervisor

Certified by .....

Luca Daniel

Associate Professor

Thesis Supervisor

Accepted by .....

Leslie Kolodziejski

Chairman, Department Committee on Graduate Theses

The Shoelace Antenna: A Device to Induce Short-Wavelength Fluctuations in the Edge Plasma of the Alcator C-Mod Tokamak

by

Theodore Golfinopoulos

Submitted to the Department of Electrical Engineering and Computer Science
on May 21, 2014, in partial fulfillment of the
requirements for the degree of
Doctor of Science

Abstract

The "Shoelace" antenna is a unique device built to induce short-wavelength fluctuations in the edge plasma of the Alcator C-Mod tokamak, at a wave number and in the frequency range associated with the Quasi-Coherent Mode (QCM). The QCM is a continuous, drift-mode-like fluctuation, restricted to the low-field side of the tokamak in a 3 mm region around the last closed flux surface, and spanning both open and closed field lines. The study presented here is motivated by the fact that the QCM plays a crucial role in regulating particle transport across the plasma boundary in the Enhanced D_α (EDA) H-mode. It is this transport channel which sustains the EDA H-mode, flushing impurities from the plasma without the appearance of bursting Edge Localized Modes (ELMs). Because of the damage they cause to first-wall components, large-amplitude ELMs do not extrapolate to a full-size, steady state fusion reactor, and so it is of critical importance for the worldwide fusion research endeavor to identify, understand, and exploit ELM-free mechanisms of impurity flushing. It is in this context that the antenna's mission is defined.

The Shoelace antenna is wound with field-aligned rungs spaced to produce a perpendicular wave number, $k_\perp = 1.5 \pm 0.1$ cm^{-1}, that precisely matches the QCM spatial structure, while the power system, with custom matching network, provides up to 2 kW of radio-frequency source power at any frequency in the band, $45 < f <$ 300 kHz. Initial experiments show that when the antenna is energized into L-mode plasmas, it produces a steady response in poloidal magnetic field, only. However, after transition to H-mode, the antenna drives both field and electron density fluctuations that are aligned with, and guided by, the background equilibrium field, propagate in the electron diamagnetic drift direction in the laboratory frame, have amplitude comparable to that of the intrinsic QCM, and display a weakly-damped resonance ($\gamma/\omega \sim 5 - 10\%$). In EDA H-mode, the resonance is centered on the QCM frequency, but in ELM-free H-mode, it persists in the same frequency range, even in the absence of a QCM. This result is significant, offering the possibility that externally-driven

modes might be used to enhance particle transport. However, additional measurements are required before a definitive statement can be made regarding transport resulting from the antenna-driven mode, as well as the driven mode's relationship with the QCM. This work has been scheduled for the 2014 Alcator C-Mod experimental campaign as part of a broader exploration of the plasma response to the Shoelace antenna.

Thesis Supervisor: Ronald R. Parker
Title: Professor

Thesis Supervisor: Brian LaBombard
Title: Senior Research Scientist

Thesis Supervisor: Luca Daniel
Title: Associate Professor

Acknowledgments

It is impossible to thank adequately all of the people who deserve thanking, but it is wrong not to try.

To my advisors, Professor Ronald R. Parker and Dr. Brian LaBombard, I express my sincere gratitude. It is because of Professor Parker that I was able to find a home in plasma physics. And Dr. LaBombard's infectious enthusiasm and energy made working on this project exciting and enjoyable. Before I started as a graduate student at MIT, members of my family commented on my good fortune of going to a place where I would be surrounded by, and would learn from, the world's greatest minds. Eight years later, having learned so much from my advisers, I can say unequivocally that my family was right.

Thanks, also, to my committee member, Professor Luca Daniel. Professor Daniel was one of my first teachers at MIT, and I am very grateful to have had the chance to continue working with him through my years as a graduate student. (I'll record here one of Professor Daniel's rules of thumb: when it comes to solving linear systems numerically, never invert a matrix! You can always do better.)

I want to acknowledge the memory of Professor David Staelin – a brilliant scientist, a patient educator, and a wise mentor, and a former member of my thesis committee – and the memory of Professor Jin Au Kong, who made electromagnetics a joy.

Thanks to Dr. Jason Sears, my first guide and friend at the PSFC, and a pioneer of the Active MHD research program at C-Mod.

I sincerely thank Dr.'s Stephen Wolfe and Robert Granetz, scientists of the first rank, mentors, and friends. I have learned under Bob inside the cramped classroom of the Alcator C-Mod tokamak, or in the clean (enough) room, or anywhere where hand and mind work together to make science. And I don't think I would have been able to make any sense of the terabytes of 1's and 0's pouring forth from our experiment without Steve's patient, and occasionally animated, guidance.

And I sincerely thank the many members of the Shoelace mechanical and electrical engineering teams, who have also been my trusted mentors. Firstly, thanks to Mr.

William “Willy” Burke. When I entered the Plasma Science and Fusion Center, I had already two degrees in Electrical Engineering. Ironic that I should quickly discover I knew almost nothing about how to be an electrical engineer. In terms of the practical aspects of the art, the education I received that mattered most was that from Willy.

Thanks, also, to Bill Parkin for expert layout of a number of our circuit boards, and for being an ever-patient and ever-pleasant member of the engineering team; to Rick Leccacorvi for brilliant CAD and design work on the Shoelace antenna; to Rui Vieira for sharing his invaluable experience in all things C-Mod; to Jeff Doody for analysis to make sure our antenna design was safe and sound; to Jim Zaks for a steady hand in navigating the complicated tasks of procurement.

Thanks to Dr.'s Martin Greenwald and Steven Wukitch, Jerry Hughes, and Jim Irby, who were involved in the early discussions of the Shoelace antenna, even before that name was coined, and who offered advice and encouragement throughout the project. And to Dr.'s Amanda Hubbard and Catherine Fiore, not only mentors and advisors for I-modes, EDA H-modes, science, and safety, but also my neighbors in the Control Room.

I also want to acknowledge helpful discussions with Dr. Joseph Snipes, currently working with the ITER organization. While not directly involved in the Shoelace antenna project, Dr. Snipes spearheaded much of the early work on fluctuations in EDA H-mode, as well as the Active MHD program.

I would like to thank Joshua Stillerman and Thomas Fredian for myriad rescues when the data collection and storage system threatened disaster, and interesting discussions – part technical and part philosophical – on software design and big data.

Thanks to my friends and colleagues in the electronics shop, Maria Silveira and Dave Bellofatto and Bruce Wood – the most experienced and fun team of circuit stuffers that has ever been assembled. And in the machine shop – Charlie Cauley and Bill Forbes and Mark Iverson and Eric Anderson – much of the hardware we used was realized by their able hands.

Thanks to Ed Fitzgerald and Andy Pfeiffer and Rick Murray for all of the times they provided a critical component or piece of wisdom when I got stuck, and the

pleasant hallway conversations in between.

Thanks to Sam Pierson, our resident C-Mod in-vessel ninja, one of the most talented and positive individuals I have ever met.

Thanks to Paul "Mr. Magnet" Thomas for encouraging me and being the best example of why teaching and sharing science is both worthwhile and fun.

Thanks to the Phase Contrast Imaging team, past, present, and future – and especially Evan Davis, Paul Ennever, and their adviser, Miklos Porkolab – for their diligent attention in keeping this excellent diagnostic available. PCI provided data crucial to the diagnosis of the Shoelace-antenna-driven fluctuations. Moreover, there are a remarkably small number of people in this world with whom you can excitedly compare notes on the latest wiggle someone has found in the plasma. Those of us plasma fluctuation enthusiasts who do so – maybe "spectrum gazers" might be a good term for us – are indeed kindred spirits.

As of the preparation of this thesis, Evan also studies the QCM from a numerical perspective using the `BOUT++` tool; many enjoyable conversations on this and other topics have benefited my graduate work. I also thank the members of the `BOUT++` team – Dr.'s Ben Dudson, Maxim Umansky, Xueqiao Xu, and Ilon Joseph – for helpful conversations and advice.

A great thank you and good luck to my other contemporaries among the graduate student denizens of the C-Mod Control Room and surrounding environs, many of whom have already graduated, but I knew them when.... At the risk of leaving someone out, I'll mention a few names: Aaron Bader, Seung Gyou Baek, Harold "$\hbar$" Barnard, Dan Brunner, Mark Chilenski, Michael Churchill, Arturo Dominguez, Eric Edlund, Ian Faust, Chi Gao, Mike Garrett, Christian Haakonsen, Zach Hartwig, Nathan Howard, Cornwall Lau, Ari Le, Yunxing Ma, Orso Meneghini, Dan Miller, Bob Mumgaard, Roman Ochoukov, Obioma Ohia, Geoff Olynyk, Jude Safo, Jen Sierchio, Brandon Sorbom, Choongki Sung, Naoto Tsujii, Arturs Vrublevskis, John Walk, Greg Wallace, Kevin Woller, and Peng Xu.

And in case I left anyone out: thanks to the whole Alcator C-Mod and Plasma Science and Fusion Center communities!

I thank Professor Terrence Orlando for being a constant, trusted, and, above all, trustworthy guide throughout my graduate career.

I thank my academic adviser, Cardinal Warde, for the encouragement and the smiles.

To my masters thesis supervisor, Professor Yang Shao Horn, and undergraduate research supervisors, Professor Hanchen Huang and Dr. Richard Gee, and colleagues, Dr. Jian Wang and Dr. Longguang Zhou and Dr. Hyun Woo Shim, I owe my gratitude. It is from this group of excellent scientists that I first learned what it was to be a researcher.

I would like to thank Dr. Christophoros Vassiliou for many discussions on the topics of science, engineering, politics, and life, as well as for the replacement capacitors he gave me after the ones on our first capacitive voltage divider iterations exploded. Likewise, thanks to Christian Theiler for the same (minus the capacitors, but plus the in/on-vessel safety-monitoring, or "babysitting," as the C-Mod lingo goes), and to Dr. Syun'ichi Shiraiwa (plus the `python` conversations).

I am extremely lucky to have been involved in a wonderful program – Middle East Education through Technology (MEET) – during these past eight years at MIT. The Jerusalem-based program brings together excelling Palestinian and Israeli teenagers, and delivers to them a challenging curriculum rooted in computer science and entrepreneurship. The professional skills I have developed in the program have served me well in my scientific career, but I think the more important reward has been the chance to interact with so many outstanding future leaders. Their enthusiasm and smiling faces have been an inspiration for me, and have recharged my soul time and again. I thank all of MEET, and especially the students. (To any former or current students who might be reading this, know that you have my respect and my love.)

Thank you to my friends. You have lightened my heart when it was heavy, and have illuminated the long road of graduate school. An incomplete list: Wishtasb, Billy, Andrew, Eric, Geoff, David, Çağatay, Rokhsanna, Seung Woo, Christiana, Nabil, Zeynep, Sertaç, Yetkin, Rosa, Jessica, Ilke, Danial, Nikos, Sheila, Donny, Tamer, DJQ, Youssef, Rahul, Magda, Ben, Kayahan, Sefa, Halil, Senseis Riccardo

and Patrick and Nico and Filip and Vittorio Recupero, Michael, Enrico, Gyorgy, Camille, Henrique, Clarice, Evangelos, Yola, Kimon, Manolis, Ivanova, Colin, Chiara, Adam, Max, Jon, Kim, Aaron, Alex, Wissam, Mustafa, Abeer, Talya, Will, Sotirios, Smaro, Ioannis, Eleni, Aalap, Sean, Uchupol, and Shanti.

Thank you to all of my teachers and coaches. Thank you, thank you, thank you.

And special thanks to my family, with special mention of my brother-in-law, Jasmin, my eight wonderful cousins – in descending age order: Rebecca, Niki$_1$, Samantha, Anna, Litsa, Niki$_2$, Antonis, and Theodoros – my aunts and uncles – Harlan, Shelly, Antonis, Eleni, Vaso, Andreas$_1$, Athanasia, and Andreas$_2$ – and my grandparents, Martin, Eunice, Ioannoula, and Theodoros. They are spread across the planet, but are near to my heart. Along those lines, I dedicate this work to my parents

Sara and Elias Golfinopoulos

and my sister

Elisa Golfinopoulos.

You are the stars in my universe: you give me warmth and point the way home. My gratitude and love for you know no bounds.

Lastly, I had wanted to devote some pages of this thesis to the case for fusion power, based on a technical assessment of the needs of our civilization as our human family grows, while our world continues to get smaller. But there was not time to perform the analysis, which has, anyway, already been skillfully carried out elsewhere, for example, in [1]. However, I think the two poems below capture the spirit of the idea just as well, and they have served as inspiration for me throughout my years as a graduate student at MIT.

Excerpt from *THE AXION ESTI from THE GENESIS* by Odysseus Elytis
Translated by Edmund Keeley and George Savidis [2, pp. 374-377], reproduced with permission of Cosmos Publishing

"Each word a swallow
to bring you spring in the midst of summer," he said
"And ample the olive trees

to sift the light through their fingers
that it may spread gently over your sleep
and ample the cicadas
which you will feel no more
than you feel the pulse inside your wrist
but scarce the water
so that you hold it a god and understand the meaning of its voice
and the tree alone
no flock beneath it
so that you take it for a friend
and know its precious name
sparse the earth beneath your feet
so that you have no room to spread your roots
and keep reaching down in depth
and broad the sky above
so that you read the infinite on your own"

THIS WORLD
this small world the great!

On Living by Nazim Hikmet
translated by Randy Blasing and Mutlu Konuk

I.
Living is no laughing matter:
you must live with great seriousness
like a squirrel, for example–
I mean without looking for something beyond and above living,
I mean living must be your whole occupation.
Living is no laughing matter:
you must take it seriously,
so much so and to such a degree
that, for example, your hands tied behind your back,
your back to the wall,
or else in a laboratory
in your white coat and safety glasses,
you can die for people–
even for people whose faces you've never seen,
even though you know living
is the most real, most beautiful thing.
I mean, you must take living so seriously
that even at seventy, for example, you'll plant olive trees–
and not for your children, either,
but because although you fear death you don't believe it,
because living, I mean, weighs heavier.

II.
Let's say we're seriously ill, need surgery–
which is to say we might not get up
from the white table.
Even though it's impossible not to feel sad
about going a little too soon,
we'll still laugh at the jokes being told,
we'll look out the window to see if it's raining,
or still wait anxiously
for the latest newscast...
Let's say we're at the front–
for something worth fighting for, say,
There, in the first offensive, on that very day,
we might fall on our face, dead.
We'll know this with a curious anger,
but we'll still worry ourselves to death

about the outcome of the war, which could last years.
Let's say we're in prison
and close to fifty,
and we have eighteen more years, say,
before the iron doors will open.
We'll still live with the outside,
with its people and animals, struggle and wind–
I mean with the outside beyond the walls.
I mean, however and wherever we are,
we must live as if we will never die.

III.
This earth will grow cold,
a star among stars
and one of the smallest,
a gilded mote on blue velvet–
I mean *this*, our great earth.
This earth will grow cold one day,
not like a block of ice
or a dead cloud even
but like an empty walnut it will roll along
in pitch-black space...

You must grieve for this right now
–you have to feel the sorrow now–
for the world must be loved this much
if you're going to say "I've lived"...

Contents

List of Figures

List of Tables

Chapter 1

Introduction

> ...while the alternatives in achieving sustainability are technological, the social directions served by their use and the criteria for what is acceptable will always remain social. Thus, sustainable energy must be concerned not only with energy and environmental technologies, but also with the economic, social, and political factors that impact human lifestyles.

–J. Tester *et al.*, *Sustainable Energy* [1, p. 5-6]

At its most basic level, a tokamak is a fireplace (Fig. 1-1). Fuel goes in and is "burned," releasing energy. The energy must be safely and efficiently conducted toward a useful purpose, while the containing structure must be sufficiently robust so as not to be degraded by the harsh conditions created by this process.

Within the fireplace, we track the flow of both thermal and material exhaust. We desire the escape of heat to be small - this helps keep the "fire" sufficiently hot to continue burning. But the material exhaust - the particles exiting the fire - must be sufficiently high such that impurities do not build up within the fire. Since the processes that transport heat are typically coupled to those that transport particles, it is a challenge to regulate the two flows independently, keeping one sufficiently low and the other sufficiently high.

Clearly, the analogy of a domestic wood-burning fireplace to a tokamak fusion reactor is limited, as the specifics of the processes of energy transformation and material

Figure 1-1: Fusion: the greatest invention since fire. Reproduced with permission from the author, Z. Weinersmith [4].

and thermal transport are quite different (chemical versus fusion reaction, ~ 1000°C versus $\sim$100 000 000°C temperatures, a brick enclosure versus magnetic confinement, etc.). Nonetheless, the image helps to motivate the discussion that follows.

And the motivating question for this discussion is this: can we mimic the naturally-occurring process that regulates material flow such that we may control it independently of the thermal flow? In answering this question, there are intermediate issues that need also be addressed: which naturally-occurring processes should we try to mimic (there are several)? What is the nature of these processes? (How) can we mimic them? Are there other useful (or deleterious) results that come from this process?

With regard to "how," the nature of the fusion plasma restricts which engineering solutions may be attempted. Within the fusion context, edge (outer plasma) temperatures are measured in electronvolts (1 eV$= k_B/e \approx$10 000°C), while core (inner plasma) temperatures are quoted in thousands of eV (keV). Material structures that will survive in a steady state must therefore be placed outside the plasma.

In this work, I describe the construction of a unique antenna - the "Shoelace"

antenna - which sits just outside of the plasma, and induces filamentary surface electric currents in the plasma matching, as closely as possible, those associated with the transport-regulating fluctuation - the Quasi-Coherent Mode (QCM) - associated with a favorable, steady-state operational regime called the Enhanced D_α H-mode. This study represents the first-ever attempt to couple to this fluctuation directly using an inductive structure.

In the remainder of this chapter, this study's contribution is placed within the wider context of regulating transport in high-performance, steady-state tokamak operational scenarios (Section 1.1). The design goals of the antenna built to investigate active transport control are then described (Section 1.2). And finally, the outline of the thesis is presented (Section 1.3). The goal of this chapter is to provide a high-level discussion of these topics. A detailed and thorough account of the material follows in the subsequent chapters.

1.1 A Zoo of Modes: Confinement Regimes in Tokamaks and their Associated Fluctuations

A plethora of "modes" exist in the terminology of tokamak physics. This situation is exacerbated by the fact that the word serves a dual purpose, referring both to *operational* modes and *eigen*modes (particular varieties of fluctuations). As a result, we speak of, for example, EDA H-modes with a Quasi-Coherent Mode as being quite distinct from (Edge-Localized Mode)y H-mode. This section points out which modes are important for the present study. The reader may find the key to abbreviations included in Appendix A (Table A.2) helpful to keep track of the overlapping nomenclature. Moreover, a capital M is sometimes used to refer to the names of particular modes in the context of fluctuations, while a lower-case m is always used when referring to confinement regimes.

Painting a simplified picture, we can think of tokamaks as having access to different confinement regimes. These may be classified according their thermal conductivity,

Table 1.1: Confinement Regimes: A Simplified Picture

	High χ (low τ_E)	Low χ (high τ_E)
High D (low τ_n)	L-mode	I-mode
Low D (high τ_n)	(undesirable)	H-mode

χ, and particle diffusivity, D; higher energy confinement corresponds to smaller χ, and higher particle confinement to smaller D. We will also speak of particle confinement time, τ_n, and energy confinement time, τ_E; these are the equilibration e-folding times for density and stored energy. The names associated with the different relative combinations of these quantities are shown in Table 1.1. Higher energy confinement is "good" - it means that heat is retained such that the fusion reaction can be sustained[1]. But higher particle confinement results in a build-up of impurities (typically heavy ions coming from wall components). These impurities radiate energy more efficiently than the lighter, typically hydrogenic main ion species, producing greater line and continuum emission. The plasma is then rapidly cooled, resulting in a thermal instability that leads, in the best case, to transition to a lower confinement regime, and in the worst case, to a sudden collapse of the plasma. As such, high particle confinement is not sustainable without some additional impurity-flushing mechanism.

The Improved Energy Confinement Regime, or I-mode [5, 6], offers an example of the desired combination of confinement properties. This operation scenario has high energy confinement, but low particle confinement. Chronologically, I-mode is the most recently-discovered regime, but it is a helpful example against which to compare the other confinement regimes discussed below.

A state characterized by both low thermal and particle confinement is often associated with the L-mode regime (though a careful definition narrows the set of circumstances under which the label applies). Transport in L-mode is dominated by turbulent fluctuations covering many spatial and temporal scales[2]. This offers stable

[1] It is also important for the heat exhaust to be distributed over a wide surface area to avoid damaging plasma-facing components (PFCs) from excessive loading.

[2] More specifically, the turbulence results from nonlinear coupling between individual unstable eigenmodes, collectively conspiring to cascade energy from larger-scale disturbances, which access the free energy in gradients of equilibrium quantities, to smaller-scale disturbances, in which the energy is dissipated.

tokamak operation, but the lower energy confinement means that a commercial reactor must be very large (and therefore expensive) – only then will it have enough heat capacity ("thermal mass") to hold on to the heat needed to sustain the fusion burn[3].

Historically, the "low" confinement of L-mode was defined relative to ohmic confinement. "Ohmic," in turn, refers to the operating scenario in which (non-fusion) heating power to the plasma is supplied primarily by Joule heating resulting from the current driven in the plasma. Since plasma collisionality, and hence resistivity, decreases with increasing temperature, ohmic heating must be supplemented with auxiliary heating power (typically via radio frequency (RF) waves or energetic neutral beam injection (NBI)). Initial experiments showed that the use of auxiliary heating tended to degrade confinement times from ohmic levels. This is a frustrating situation: it means that the more you add heat, the faster you lose it.

However, in 1982, members of the ASDEX team found that, above a sufficient threshold heating power, the higher confinement times associated with ohmic operation could be recovered thanks to the appearance of a transport barrier [9] producing a region of sharply increasing density and temperature (the density and temperature "pedestals") at the edge. This mode of operation was termed H-mode, for higher confinement time relative to L-mode (by roughly a factor of two).

But energy and particle transport are typically correlated. This means that the higher confinement associated with H-mode cannot be sustained, due to the build-up of impurities and subsequent thermal collapse discussed above.

The build-up of particles, and the attendant evolution of sharp pressure gradients, can also lead to periodic, bursting instabilities. These are localized to the edge, motivating the name, Edge Localized Modes (ELMs). ELMs play the role of a pressure relief valve, relaxing the strong pressure gradients and expelling particles. This flushes impurities from the plasma while still retaining relatively high energy confinement, allowing for continuous operation of small, pulsed experimental tokamaks.

[3]This requirement is expressed via a threshold value of the product of total pressure and energy confinement time, $p\tau_E \approx 8$ atm·s [7], in order to achieve power balance (ignition), under which condition the heat produced by the fusion reaction, itself, is sufficient to sustain the reaction. The earliest treatment of the issue of power balance in a fusion reaction is due to Lawson [8], who specified a constraint on the product, $n\tau_E$.

Figure 1-2: Tantalus, forced to endure an eternal punishment. [10].

Unfortunately, large, violent ("Type I") ELMs, which are associated with the most readily-accessible operating scenario on most of the world's large tokamaks[4], do not scale to a steady-state, reactor-sized experiment, since the small fraction of total plasma energy expelled by each ELM event is nonetheless large enough to destroy material surfaces inside the tokamak in a fairly short amount of time.

The many difficulties encountered in the quest for improved tokamak performance are demoralizing, and conjure images of an ever-receding finish line, with the objective always just out of reach (see Figure 1-2).

Fortunately, a variety of steady-state operating scenarios have been discovered which provide a gentler mechanism of impurity exhaust. Finding such scenarios typically requires careful adjustment of plasma control parameters to produce the impurity-flushing mechanism. The motivation of the present work derives from a desire to be able *to reproduce such a mechanism via an external actuator*, thereby providing the capability *to control particle transport independently of energy transport*, and allowing plasma control parameters to be optimized for other ends. But a related and intermediate goal is to improve the understanding of this flushing mechanism.

[4]Alcator C-Mod is an exception to this trend - Type I elements do not readily appear on this high-field device.

1.2 Mimicking Nature: Building an Antenna to Reproduce and Exploit Favorable Edge Modes

A unifying observation across virtually all steady-state, high-confinement fusion plasma regimes is the critical role played by edge fluctuations in regulating transport across the plasma boundary (see, *e.g.*, [11, Sec. 6],[12, Sec. 2.4.7]). This may not be surprising given that fluctuations[5] of one variety or another are known to dominate transport in every tokamak regime of operation (see, *e.g.*, [13, Chap. 2, Table 1]). It is significant that the fluctuations are typically localized to the edge of the plasma, near the boundary between open and closed field lines[6] – the last closed flux surface (LCFS). It is also significant that, in steady-state regimes, many of the relevant edge fluctuations are coherent, narrow-band structures. This is distinct from the kinds of turbulent, broadband instabilities which dominate transport in L-mode.

It was a desire to exploit this state of affairs that inspired the present work. If the same coherent fluctuation responsible for flushing impurities from the plasma could driven externally, it was conjectured, then perhaps particle transport could be actively controlled through this channel.

To proceed along this line of inquiry, we need some concept of the nature of these fluctuations. Many such fluctuations are field-aligned, propagating roughly perpendicular to, and often with current filaments traveling along, the helical magnetic field lines immersed in the plasma. Dramatic images of this are provided by the filamentary structures found in ELMs[7], as illustrated by Figure 1-3, which shows an image of such a structure on the MAST spherical tokamak.

In designing an antenna to produce the desired effect on particle transport, we imitated the naturally-occurring pattern of current filaments of a specific plasma instability – the Quasi Coherent Mode (QCM), associated with the Enhanced D_α (EDA) H-mode – by creating a field-aligned array of wires, producing image currents

[5] Here, the term, "fluctuation," is meant in a broad sense as any oscillation in the plasma.

[6] "Closed field lines" refer to magnetic field lines which never intersect a material surface, as compared with "open field lines," which do.

[7] It should be noted that the target mode in this study - the Quasi Coherent Mode - is not the same as the Edge Localized Mode.

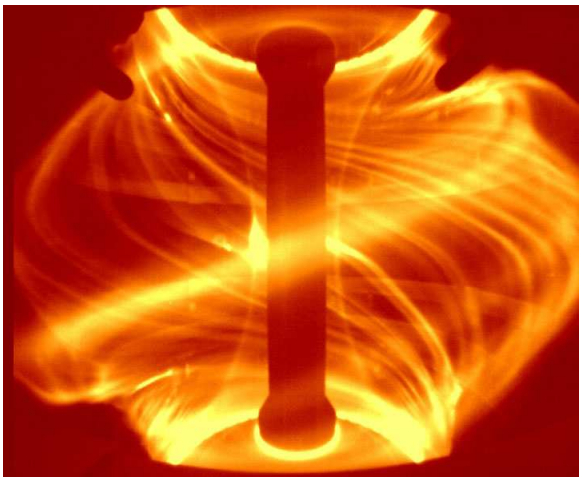

Figure 1-3: An ELM crash on the Mega Amp Spherical Tokamak in Culham, UK. Used with permission from, and photo credit to, Culham Centre for Fusion Energy, http://www.ccfe.ac.uk/, [14].

with the same spatial pattern and frequency as the intrinsic modes. The result – the "Shoelace" antenna – is shown in Figure 1-4.

The idea of triggering confinement transitions by an external actuator is not new. For example, feedback stabilization of broadband turbulence via electrostatic probes was attempted on the TEXT and KT-5C tokamaks [15, 16, 17]. The CCT and TEXTOR teams achieved an "electric H-mode" by polarizing the edge plasma with electrostatic probes [18, 19]. Other related examples will be discussed in the next chapter.

Moreover, while the specific design of the Shoelace antenna is unique, RF antennas which match wave number and frequency to a plasma mode to maximize coupling are also common in plasma physics.

The approach followed in the present work departs from other investigations in several respects. Firstly, to the author's knowledge, there have been no previous attempts to couple directly[8] and inductively to the edge modes that determine the confinement regime[9].

[8] i.e. at the same wave number and frequency

[9] The closest relevant work on a tokamak uses coils with constant currents to produce a "Resonant Magnetic Perturbation" (RMP) to stochasticize (i.e. make field lines volume-filling instead of surface-filling) the edge background field in order to suppress unacceptably-large Edge Localized Modes [20]. This approach uses an inductive actuator with a much different configuration, and couples indirectly to a different kind of edge fluctuation.

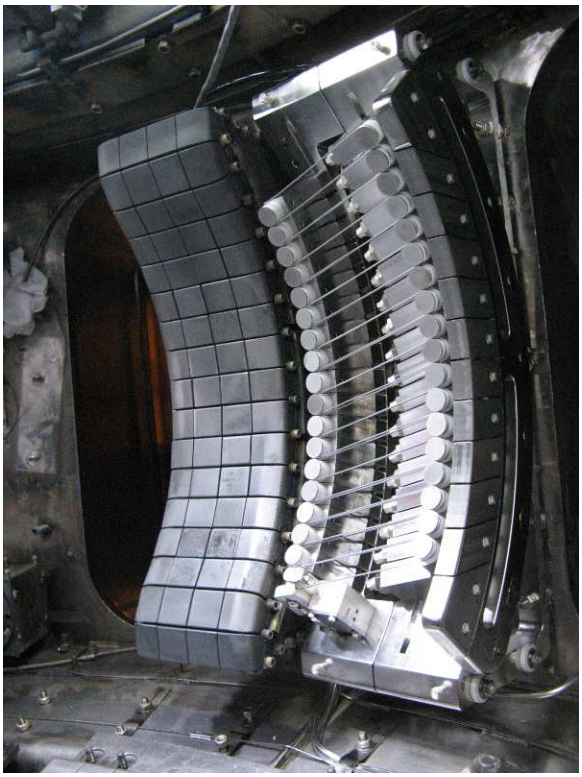

Figure 1-4: The Shoelace antenna inside the Alcator C-Mod tokamak vacuum vessel.

Secondly, previous work in the community concerned with coupling to transport-driving edge modes has focused on suppressing or otherwise controlling extant fluctuations, usually with the goal of reducing energy transport in the pursuit of ever-higher tokamak performance. The goal of the present work is rather to *increase particle transport*, so as to flush impurities, and thereby make sustainable, a regime with otherwise good energy confinement.

Lastly, the Shoelace antenna faces special challenges in coupling inductively to short-wavelength modes, which tend to produce a magnetic field perturbation that falls off rapidly through the quasi-vacuum outside the main plasma, requiring the exciting structure to be extremely close to the plasma. The solutions employed by the Shoelace antenna for achieving this coupling while surviving the high heat flux exiting the plasma, as well as for maximizing power throughput at arbitrary frequency and phase into the low-resistance, inductive load presented by the antenna, are novel, at least in the category of Active MHD antennas under which the Shoelace antenna might be classified, and may prove useful tools for future investigations.

The initial round of Shoelace antenna experiments showed that the antenna successfully drives a field-aligned fluctuation at the QCM wave number and propagation direction, with a weakly-damped ($\gamma/\omega \sim 5 - 10\%$) resonance at the QCM frequency, and with amplitude comparable to the intrinsic fluctuation. These results are promising, but as yet, it is unknown whether the antenna is able to directly drive particle transport. It is hoped that the answer to this question will be obtained from experiments that are being planned concurrently with the writing of this thesis.

1.3 Outline of this Thesis

The remainder of this thesis is organized as follows: in Chapter 2, a more topical and detailed context for the creation and operation of the Shoelace antenna is given, identifying the niche filled by the antenna within the fusion research community. Chapter 3 provides a simplified theoretical description of some of the linear instabilities that give rise to the (typically non-linear) fluctuations associated with various confinement regimes, with special attention payed to drift waves due to their relation to the Quasi Coherent Mode. Chapter 4 discusses the design and construction of the Shoelace antenna and its power system, while Chapter 5 describes the results obtained from the initial campaign of experiments with the antenna, as well as their interpretation. Finally, the work is summarized in Chapter 6, with the direction of future work indicated. Detailed information regarding mathematical derivations, the experimental setup, and other topics, together with a glossary of abbreviations, symbols, and terms, are provided in the appendix.

Chapter 2

Background

> Dr. Peter Venkman: So what, I guess they just don't make them like they used too, huh?
> Dr. Ray Stantz: No! Nobody ever made them like this! I mean, the architect had to be a certified genius or an authentic wacko.
> Dr. Peter Venkman: Ray, for a moment, pretend like I don't know anything about metallurgy, engineering, or physics and just tell me what the hell is going on.
> Dr. Ray Stantz: You never studied.

–From the film, *Ghostbusters*, written by Harold Ramis and Dan Aykroyd, © Columbia Pictures Industries, Inc. (1984)

The purpose of this chapter is to provide the context for the present work, describing how this study fits into developments recorded in the existing literature. It introduces the Alcator C-Mod tokamak, summarizing the research program on this device. It then surveys steady-state, high-performance tokamak confinement regimes, emphasizing the edge fluctuations which define them, and focusing in particular on the Enhanced D_α (EDA) H-mode and the associated Quasi-Coherent Mode (QCM). A discussion of experimental and theoretical inquiry into the behavior and origin of the QCM follows. Finally, a review is given of other relevant experiments, performed both at C-Mod and elsewhere, which have attempted to couple actively to low frequency modes.

2.1 The Alcator C-Mod Tokamak

Alcator C-Mod is a compact, all-metal-wall device which, at a maximum of better than 8 T on-axis, boasts the highest magnetic field of any current tokamak in the world[21, 22]. Its operating parameters are summarized in Table 2.1. Figure 2-1 shows photographs of the interior of the vacuum vessel, as well as a CAD model of the device and its superstructure.

The Alcator C-Mod research program has made significant contributions in the fields of plasma-material interaction, RF heating and current drive, divertor design, and edge physics, and its uniquely high field and density improve the robustness of extrapolations from empirical scaling models based on cross-machine studies. C-Mod has also discovered steady-state, ELM-free confinement regimes, EDA H-mode (discussed in detail below) and I-mode (which may extrapolate favorably to a reactor-scale device). A February, 2012, proposal had scheduled to terminate the Alcator C-Mod program, and experiments ceased in October of that year. However, funding to the project was restored in January, 2014, after a successful campaign to save the device, and experiments recommenced shortly thereafter. Major upgrades planned for the machine include an advanced heated outer divertor; a second field-aligned, four-strap ICRF antenna; and a second lower-hybrid antenna. Pending funding decisions, several or all of these new systems may be built and installed in 2015.

Additional information on the diagnostic systems available on Alcator C-Mod will be provided in Chapter 4 in the discussion of the experimental design.

2.2 Coherent Edge Fluctuations in the Context of Tokamak Performance

High performance tokamak confinement regimes are typically accompanied, and perhaps defined, by an associated edge fluctuation which regulates transport through the plasma boundary. These instabilities are often coherent. This is distinct from low-confinement regimes, which are characterized by broadband turbulent edge fluc-

Table 2.1: Alcator C-Mod by the Numbers

In operation since	1991
Magnetic Field (on-axis), B_T	2-8.19 T
Plasma Current, I_p	0.24-2 MA
Pulse Flattop	1 s (typical)
Major Radius, R_0	0.68 m (typical)
Minor Radius, a	0.22 m (typical)
Max. Electron Temp, T_e	$\sim$9 keV ($\sim$ 100000000°C)
Max. Ion Temp, T_i	$\sim$6 keV
Avg. Pressure, p_0	$<$ 1.8 atm
Plasma Density	$0.2 - 8 \times 10^{20}$ m^{-3}
Aux. Heating Power	$\lesssim$ 6 MW (ICRF H minority, $\sim$ 80 MHz)
Cur. Drive Power	$\lesssim$ 1 MW (LH, 4.6 GHz)
Energy confinement time, τ_E	20-50 ms
Plasma Volume	$\sim$1 m^3
Wall material	molybdenum (PFCs)
Magnet material	copper (cryo. cooled)
Divertor Config.	Vertical target on bottom; flat target on top

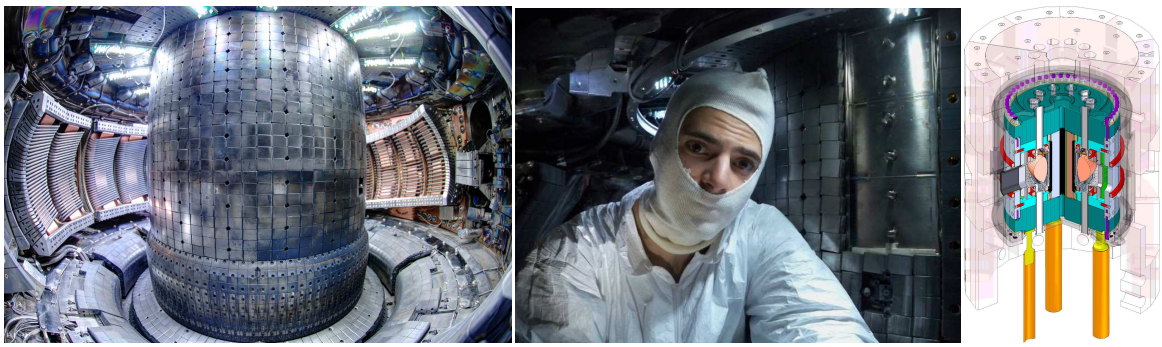

(a) (b) (c)

(d)

Figure 2-1: (a) Alcator C-Mod vacuum vessel. (b) A person (the author) in a clean-room suit, sitting in the C-Mod vacuum vessel (to demonstrate scale). (c) CAD model of Alcator C-Mod; plasma shape is orange torus filling interior space. (d) Unwrapped view of the tokamak. (Credit: 2-1a, 2-1d Robert Mumgaard 2013; 2-1b Theodore Golfinopoulos 2012.)

tuations, predominantly drift-wave-like in character for a low- to moderate-β edge plasma[1], and interchange/ballooning-like for a moderate- to high-β edge [23, 24].

On the Alcator C-Mod tokamak, two instances of high-performance regimes sustained by steady, coherent edge fluctuations are offered by the Enhanced D_α (EDA) H-mode [25, 26] - which features a Quasi-Coherent Mode (QCM, $f = 50 - 150$ kHz, $k_\perp = 1.5$ cm^{-1}) - and the Improved Energy Confinement Regime (I-Mode) [5, 6] - associated with the Weakly Coherent Mode (WCM, $f = 100 - 500$ kHz, $k_\perp = 1.5$ cm^{-1}). Examples from other devices include an improved L-mode on ASDEX-Upgrade [27], as well as the Quiescent H-mode first observed on the DIII-D tokamak [28], the High Recycling Steady (HRS) H-mode seen on the JFT-2M tokamak [29, 30], and the High-Density H-mode (HDH) found on the W7-AS stellarator [31], the latter two sharing some characteristics with C-Mod's EDA H-mode. The Quiescent H-mode features the Edge Harmonic Oscillation, while the HRS H-mode displays Low- and High-Frequency quasi-coherent modes, and the HDH is accompanied by its own quasi-coherent mode.

Table 2.2 compiles a number of properties associated with each of these fluctuations, as well as of the Type II ELMs. (See also Table 1 in Oyama *et al.* [11, Sec. 6], which describes a subset of these modes.)

In the next section, experimental and theoretical investigations of the EDA H-mode and QCM are described in greater detail, since the QCM was chosen as the primary target fluctuation to which the Shoelace antenna was designed to couple. The design parameters of the Shoelace antenna also overlap with the WCM of the I-mode; interaction between the antenna and this mode is not the subject of this thesis, but will be explored during the 2014 C-Mod campaign.

[1] where $\beta \equiv 2\mu_0 p/B^2$ is the ratio of plasma to field pressure

Table 2.2: Steady State Regimes and Associated Edge Fluctuations

Regime	**Edge Fluct.**	**Freq. [kHz]**	**Mode/Wave Number**	**Meas. Fluct. Quantities**	**Phase Vel. Dir. (Lab Frame)**	**Experiment [ref.]**
Enhanced D_α (EDA)	Quasi-Coherent Mode (QCM)	50-150	$k_\perp \sim 1.5$ cm^{-1} ($k_\perp \gg k_\parallel$)	$\tilde{B}_\theta$, $\tilde{n}_e$, $\tilde{T}_e$, $\tilde{\Phi}$	EDD	C-Mod [32, 26, 33, 34, 35, 36, 37, 38, 39]
Improved Energy Confinement Regime (I-mode)	Weakly Coherent Mode (WCM)	100-500	$k_\perp \sim 1.5 - 2.1$ cm^{-1} ($k_\perp \gg k_\parallel$)	$\tilde{B}_\theta$, $\tilde{n}_e$, $\tilde{T}_e$	EDD	C-Mod [5, 6, 40, 41]; possibly ASDEX-Upgrade [27], EAST [42]
High Recycling Steady (HRS) H-mode	Low freq. (LF); High freq. (HF)	LF: 10-100; HF: 200-450	LF: $n = 1$, $m \sim 4 \pm 1$; HF: $n \sim 7 \pm 1$	$\tilde{B}_\theta$, $\tilde{I}_{sat}$ (*e.g.* $\tilde{n}_e$, $\tilde{T}_e$)		JFT-2M [29, 30, 43]
Type II ELMy H-mode	Small, broadband ELMs	30-50	$n = 3 - 4$ (AUG), $n = 8$ (JET), $k_\theta \approx 0.4$ cm^{-1} (AUG)	$\tilde{B}_\theta$, $\tilde{n}_e$, $\tilde{T}_e$	IDD [44] or EDD [45]	AUG, JET, DIII-D, C-Mod, MAST, NSTX, etc. [46, 44, 11, 45]
Quiescent H-mode (QH)	Edge Harmonic Oscillation (EHO)	5-15 (fundamental)	multiharmonic, $n = 1 - 11$, with $n = 2, 3$ dominant on DIII-D; DIII-D: $m = 5$, AUG: $m = 6$; FA	$\tilde{B}_\theta$, $\tilde{n}_e$, $\tilde{T}_e$	co-NBI	DIII-D, AUG, JET, JT-60U [28, 47, 48, 49, 50]
High-Density H-mode (HDH)	Quasi-Coherent Mode (QCM)	50-150	rapid fall-off of $\tilde{B}_\theta \Rightarrow$ high-$k_\perp$)	$\tilde{B}_\theta$		W7-AS (stellarator) [31]

2.3 The Enhanced D_α Regime and the Quasi Coherent Mode

The Enhanced D_α (EDA) H-mode [25, 51, 52, 26, 33, 35, 38, 32] is a steady-state, high-confinement regime without ELMs that is readily produced on the Alcator C-Mod tokamak[21] (R=0.68 m, $B_t \leq 8$ T, $\bar{n}_e \lesssim 4 \times 10^{20}$ m^{-3}). It features a continuous edge fluctuation, the Quasi-Coherent Mode (QCM), which is responsible for exhausting particles through the plasma boundary, regulating the pedestal. The reduction in particle confinement relative to ELM-free H-mode is accompanied by an increase in D_α emission, motivating the name of the regime. However, the energy confinement time is only slightly reduced, and is comparable to the level achieved in ELMy H-mode.

Figure 2-2 shows representative spectrograms from the phase contrast imaging (PCI) diagnostic sensitive to line-averaged electron density fluctuations, $\tilde{\bar{n}}_e$, as well as a Mirnov coil measuring $\tilde{B}_\theta$, from a discharge with an EDA H-mode. Several parameter traces are also shown. Early in the discharge, the confinement transitions from L-mode to ELM-free H-mode, but the reduction in particle transport is accompanied by a build-up of impurities, indicated by a strongly-increasing radiated power signal. This leads to a back-transition to L-Mode. Shortly afterward, the plasma again transitions to H-mode, but now, a continuous fluctuation develops - the QCM - visible in the PCI spectrogram as the narrow feature sweeping down in frequency before modulating around a stable average value. The rise of both radiated power and density is arrested, while the D_α light increases, indicating an increase in particle transport that provides a defining characteristic of the EDA regime.

Several experimental characterizations of the QCM [33, 34, 53, 35, 37, 38, 54, 32], including the most recent, have described a narrow edge mode having a stable frequency $50 \lesssim f \lesssim 150$ kHz (after a 30-60 ms transient phase with frequency sweeping down from an onset between $150 < f_0 < 250$ kHz) and $k_\perp \sim 1.5$ cm^{-1} at the midplane, with lab-frame propagation in the electron diamagnetic drift direction, approximately field-aligned with $k_\perp \gg k_\parallel$, absent from the high-field side, and with large amplitude

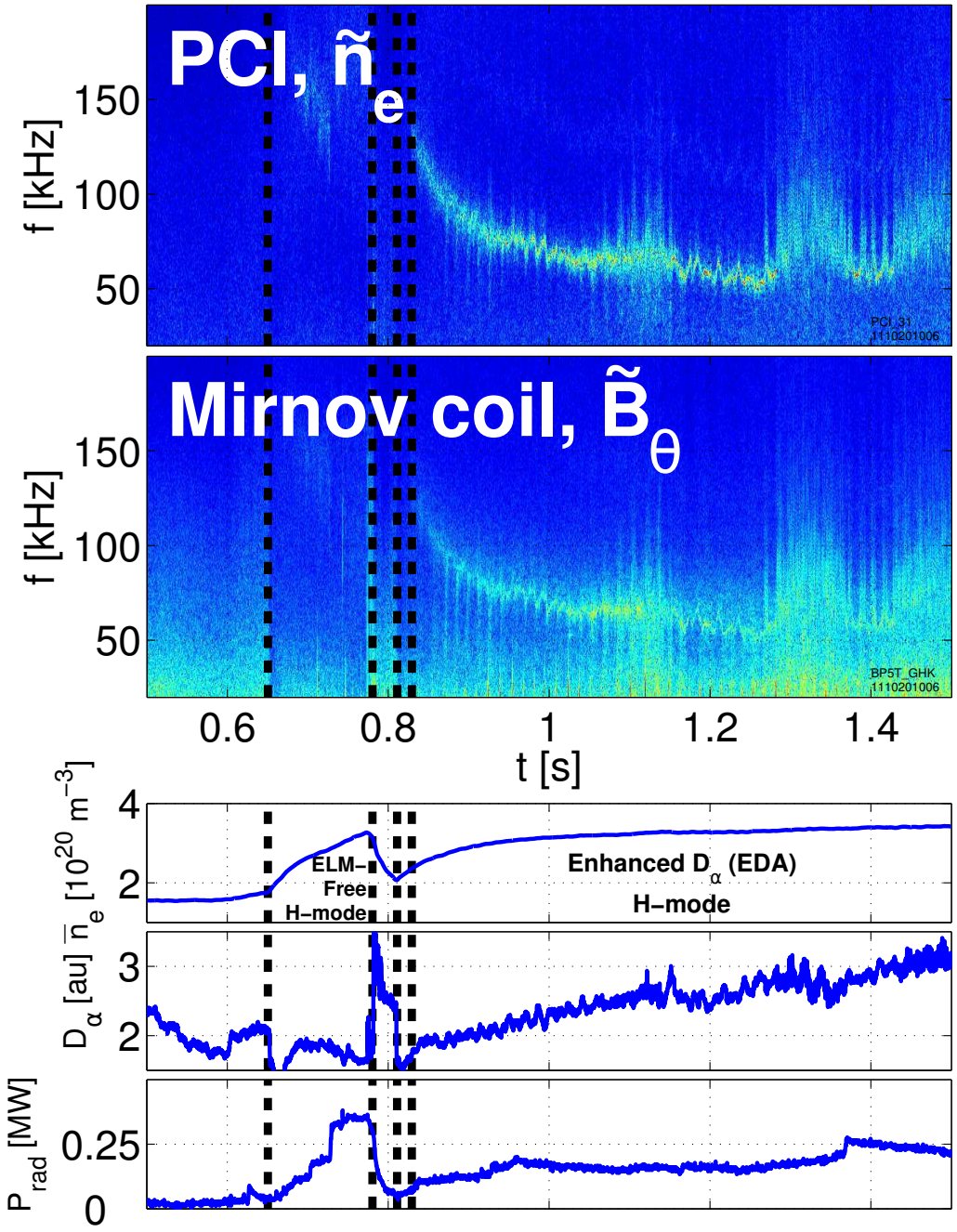

Figure 2-2: Spectrograms of phase contrast imaging (PCI, $\tilde{\bar{n}}_e$) and Mirnov coil ($\tilde{B}_\theta$) fluctuation signals, together with line-averaged density ($\bar{n}_e$), D_α, and radiated power (P_{rad}) traces, from a discharge exhibiting both ELM-free and EDA H-modes. The reduced particle confinement of the EDA H-mode relative to the prior ELM-free H-mode is indicated both by the slower density rise and increased D_α light.

Table 2.3: Comparison of QCM Characterizations

k_θ (midplane)	$r - r_{LCFS}$	Δr (FWHM)	$\Delta u/u$ (peak-to-peak)	Phase Vel. Dir. (Plasma Frame)	Diagnostic [ref.]
1.5 [cm^{-1}]	0 ± 1 [mm]	3 [mm]	$\frac{\Delta n_e}{\bar{n}_e}$ ~30%, $\frac{\Delta T_e}{T_e} \sim 40\%$, $\frac{e\Delta\Phi}{T_e} \sim 40\%$, $\tilde{B}_r/B_\theta \sim 0.1\%$	EDD	MLP [32]
1.8 [cm^{-1}]	-7 to -10 [mm]	7.5 [mm]	$\frac{\Delta n_e}{\bar{n}_e} = 35\%$	IDD	GPI [54, App. A]
	1 ± 0.5 [mm]	1 ± 0.4 [mm]	$\frac{\Delta n_e}{\bar{n}_e} = 60\%$		Reflectometry [34, P. 93, Sec. 5.3.2]
1 to 2 [cm^{-1}]	-1 to -2 [mm]	< 9 [mm]	$\frac{\Delta n_e}{\bar{n}_e} > 15\%$		BES [37, p.102-6, Sec. 5.2.2-3]
~1.5-2 [cm^{-1}] $\sim 0.04/\rho_s$					PCI [53, p. 95, p.97,100]
1.5 [cm^{-1}]			$\frac{\Delta n_e}{\bar{n}_e} = 30\%$		Scanning Langmuir probe & Mirnov coil, PCI [33]
1.0 [cm^{-1}]	2 peaks, 1 ± 2 mm and -9 ± 2 mm	5 mm			GPI [38]

fluctuations. Table 2.3 compares the varying characterizations of the QCM from different diagnostics. The mode frequency is omitted from the comparison since it is essentially identical between diagnostics. In comparing the parameters in the table, it should be noted that measurements from a particular diagnostic are often reported for a small set of discharges which are typically designed to optimize the quality of data from that diagnostic. As such, some of the spread in values is accounted for by the variability of the QCM, itself, across these different plasma conditions.

The most important discrepancies between the different characterizations of the QCM are the location of the mode layer, as well as its width. The spread in radial locations is about 1 cm, about 5% of the plasma major radius. However, due to the high degree of spatial inhomogeneity in the edge plasma, the inferred propagation direction of the mode in the plasma frame[2] can be inverted between differing char-

[2]that which is rotating at the $\mathbf{E} \times \mathbf{B}$ velocity

acterizations of the mode. Since the propagation direction is a major discriminant in determining the physical origins of the mode (in particular, drift wave (EDD) versus ballooning mode (stationary), this uncertainty has led to widely varying physical interpretations of the mode.

The most recent and detailed measurements of the mode [32], performed with a reciprocating Mirror Langmuir Probe (MLP) that scans through the mode layer, have revealed the overall character of the QCM to be primarily that of an electron drift wave that further displays both interchange and electromagnetic physics, spans the last closed flux surface in a narrow (∼3 mm) layer, and shows strong fluctuation amplitudes, with $\Delta n_e/\bar{n}_e$ ∼30% and $\Delta T_e/\bar{T}_e \sim e\Delta\tilde{\Phi}/T_e \sim 40\%$, and (extrapolating to the mode layer from scanning Mirnov coil data) $\tilde{B}_r/B_\theta \sim 0.1\%$. Here, $\Delta u/\bar{u}$ refers to the peak-to-peak amplitude of the fluctuating quantity normalized by the time-average of the quantity. Moreover, measurements of the particle flux driven by the QCM corroborate earlier investigations that ascribe to the QCM the role of exhausting particles from the plasma in the EDA regime. The importance of drift waves and drift-Alfvénic turbulence[55, 56, 57, 58, 59, 60, 61, 62, 63, 64, 65, 66, 23, 24] in controlling the C-Mod edge plasma state had already been revealed [67], but their association with the QCM is only recently established.

The MLP technique is the most robust of the methods used to characterize the QCM for the crucial reason that it provides a simultaneous, co-located measurement of both the background profile and the fluctuation. This is critical because it decouples the characterization of the mode from uncertainties in the magnetic reconstruction of the plasma. Characterization with Mirnov coils, reflectometry, gas puff imaging (GPI), beam emission spectroscopy (BES), and phase contrast imaging (PCI) rely on flux-surface mapping to dedicated diagnostics measuring background profiles and flows (*e.g.* charge exchange recombination spectroscopy (CXRS), Thomson scattering, etc.) in order to locate the mode and understand the plasma conditions in its local environment. Biased uncertainties in these reconstructions of ∼ 5 mm – which are typical – combined with the coarse radial resolution of the diagnostics just listed, are sufficient to explain the differences in the location of the mode layer between the

varying characterizations of the QCM. As such, in the present work, the data and interpretation afforded by the MLP results are taken to be the most accurate.

Nonetheless, the MLP technique is limited by the depth to which the scanning probe can be plunged into the plasma before melt damage becomes unacceptable and/or too perturbative to the plasma. It is possible that there are additional important dynamics further up the pedestal (see [38], which suggests the possibility of two peaks in the fluctuation measurement, separated radially by ~ 1 cm). Synchronizing the measurements between these differing diagnostic methods is an active research activity.

Experiments in 2012 showed that the lower hybrid antenna can have a profound effect on the QCM and the edge, tending to reduce the QCM frequency and spectral width [68]. This is likely through an effect on the radial electric field – this will be explored experimentally during the 2014 C-Mod experimental campaign.

2.3.1 Toward Finding a Theory for the QCM

There have been several attempts at modeling the QCM, but as yet, none have satisfactorily captured the experimentally observed behavior of the mode. The starting point for these approaches is to use a fluid closure appropriate for a collisional plasma, named for Braginskiĭ after his authoritative exposition on the subject [69]. This approach is justified when the electron-ion collisional mean free path along a field-line, λ_{mfp}, is shorter than the parallel wavelength (typically on the order of twice the connection length, $L_c \approx \pi q R$), and the collision frequency is faster than the mode dynamics in question. For the edge parameters in the C-Mod discharges belonging to this study, near the last-closed flux surface (LCFS), $T_e \sim 50 - 100$ eV$\Rightarrow v_{th,e} = 4 - 6 \times 10^6$ m/s, and the electron-ion collision time is $\tau_{ei} = 75 - 210 \times 10^{-9}$ s. Then the electron parallel mean free path is $\lambda_{mfp} \approx v_{th,e}\tau_{ei} \approx 0.3 - 1.3$ m, while the connection length is $L_c \approx 6 - 11$ m, and the frequency of the QCM is on the order of 100 kHz, with $(\omega\tau_{ei})^{-1} \approx 20$. As such, the dynamics around the LCFS on the QCM time and length scales can be considered collisional.

The free energy sources for the instabilities in such models are the inhomogeneities

in the plasma pressure and the magnetic field. Instabilities driven primarily by the former source include ideal drift waves; for the latter case, interchange modes, which become "ballooning" modes in a toroidal geometry. By contrast, shear in background (especially $\mathbf{E} \times \mathbf{B}$) flows and in the magnetic field tends to stabilize the modes, and the usual notions of "good" and "bad" curvature apply[3]. Broadband turbulence observed in the edge of magnetically-confined, toroidal plasmas is usually dominated by fluctuations of one or both of the drift and interchange varieties, with $\mathbf{E} \times \mathbf{B}$ advection giving rise to the nonlinear coupling in saturated turbulent states [65, 23, 24]. Additional complications arise from the treatment of high magnetic shear (especially near X-points) [72, 73], strong $\mathbf{E} \times \mathbf{B}$ shear and diamagnetic flows [74] [65, Chap. 9-11], heavy ion impurities [75], electromagnetic effects at higher β [23, Sec. 5.IX], effects of electron and ion temperature [65, Chap. 12-13] [76, Chap. 14], etc. The edge plasmas that give rise to the QCM tend to suffer from all of these complexities.

The theory behind drift waves, ballooning modes, and other instabilities will be summarized in the next chapter. The following outlines the results from the literature pertinent to the QCM.

Initial work by Mazurenko *et al.* and Myra and D'Ippolito using the original `BOUT` simulation package suggested that the resistive X-point mode is unstable in EDA H-mode plasmas[35, 73]. The modeled instability matched the wave number of the QCM and some aspects of access to the EDA regime, but could not recover the QCM plasma-frame phase velocity, which was measured to be oriented in the electron diamagnetic drift direction[32]. Unfortunately, the same is true of the description offered by Coppi and Zhou [75], which sought to develop a unified analytical theory for the fluctuations behind high-performance, steady-state tokamak confinement regimes. More recent

[3] "Good" curvature corresponds to a topology where the field bends away from the plasma (i.e. the radius of curvature, which points toward the center of the arc's circle, points away from the plasma), such that a prominence in the plasma pushes against an increasingly strong field, which tends to restore the initial state. "Bad" curvature refers to the opposite situation. In a tokamak, the inner half (in major radius; also, called the "high field side") tends to have good curvature, and the outer half (low field side), bad curvature (see Figure 3-3). For an authoritative description of these terms, the reader is directed to a text on ideal magnetohydrodynamics (ideal MHD), *e.g.* [70] or [71].

work using the flexible BOUT++ fluid simulation framework did isolate a mode traveling in the electron diamagnetic drift direction in the lab frame, but the calculated phase relationship between density and potential ($\sim 90^\circ$) [77] was ballooning-mode-like, as opposed to the smaller, drift-mode like difference measured in experiment ($\sim 10^\circ$) [32].

Having identified the stabilizing effects on ideal ballooning modes of ion diamagnetic drift and the strong radial localization of the pedestal, Rogers and Drake [74] explored "surface" waves, which depend only on the pressure drop across the pedestal. These arise when $\mathbf{E} \times \mathbf{B}$ and ion diamagnetic flows balance, and when the normalized ion diamagnetic flow exceeds the ballooning growth rate; under these conditions, ideal ballooning modes are stabilized. While the QCM was not explicitly examined by those authors, subsequent reports used the results of this study to explain QCM phenomenology [34, Sec. 5.2.2], [35]. Under the plasma conditions relevant to the present thesis, the surface wave has a poloidal wave number, $k_\theta \sim 1/\delta_R = (\rho_s^2 R)^{-1/3} \approx 1.7 - 1.9$ cm^{-1}, and a frequency, $\omega \sim c_s/\sqrt{\delta_R R} = c_s/(\rho_s R^2)^{1/3} \ll \omega_{*i} = k_\perp \rho_i^2 \Omega_{ci}/L_{pi} = \rho_i^2 \Omega_{ci}/L_{pi}/(\rho_s^2 R)^{1/3} = 2\pi(100-130)$ kHz, matching closely the QCM wave number and (lab-frame) frequency. However, the derivation of this mode relies on the $\mathbf{E}\times\mathbf{B}$ and ion diamagnetic drifts precisely counterbalancing, where the directions of these two drifts align at the location of the mode.

In addition to their effect on resistive ballooning modes, Myra *et al.* also examined the effect of X-point geometry on electromagnetic drift waves [72], finding that the X-point geometry tends to destabilize the electromagnetic drift wave. In numerical work, they found an interesting coherent feature reminiscent of the QCM (see Fig. 3 of [72] and corresponding discussion), and explain the observed selectivity in the toroidal mode number, n, by a competition between the destabilizing skin effect[4] and the stabilizing polarization drift. However, in obtaining this result, the authors neglected curvature-driven modes in order to focus on the drift wave physics, where it would be preferable to understand how coherent modes develop when the drift wave and interchange physics are combined, especially since measurements indicate that

[4] deriving from the electron inertia term in Ohm's law - see Eq. 5.73, [65, Sec. 5.IX]

both are important [32]. Indeed, as of the preparation of this thesis, this is the task of current studies using the `BOUT++` framework [77].

In short, despite over a decade of literature on the subject, modeling the QCM remains an active area of research. All that is certain is that an adequate theoretical description of the QCM demands a fairly complex model that incorporates the physics of ballooning and drift waves under realistic geometries and profiles, and with realistic $\mathbf{E} \times \mathbf{B}$ and diamagnetic flows.

2.4 External Coupling to Low-Frequency ($\omega \ll \Omega_i$) Plasma Oscillations

The field of RF wave interactions with plasmas is rich and well-developed, spanning far beyond the domain of magnetically-confined fusion plasma research[76]. Within the fusion context, wave-launching structures have been developed to excite waves across the full range of frequencies, from much less than the ion cyclotron frequency, $\omega \ll \Omega_i \sim 40$ MHz on the magnetic axis of Alcator C-Mod (for the main ion species), to much greater than the electron cyclotron frequency, $\omega \gg \Omega_e \sim 150$ GHz on C-Mod. The goals of such structures include heating, diagnosing, and driving current in the plasma.

The interest in the present context is in coupling to low-frequency plasma oscillations, with $\omega \ll \Omega_i$. Perhaps the most fundamental plasma wave in this frequency range is the shear Alfvén wave, and an extensive body of literature exists recording attempts to interact with this mode. However, other low frequency modes have also been explored from a wave coupling perspective. This section gives a brief overview of the literature on this subject.

The approaches of the different coupling experiments are distinguished by the type of excitation structure (typically an inductive coil or an electrostatic probe), whether the modes are excited directly (*i.e.* the exciter is driven at the target mode frequency) or parametrically (one or more exciters are driven at different, typically higher fre-

quencies than the target mode, relying on nonlinear coupling), whether the target modes are stable (common for "Active MHD" experiments) or unstable (common in control experiments) in the background plasma, whether the excitation structure (for example, a single, small dipole loop) couples to a broad set of wave numbers or is very selective. Experiments may also be classified by their goals: whether the intention is to perturb or gently diagnose the background plasma, whether the target mode is to be promoted or suppressed. In the literature reported below, nearly all of these permutations are explored.

The importance of edge fluctuations in controlling edge transport has prompted a number of experiments attempting to interact with these modes. Uckan *et al.* employed electrostatic launching probes on the Texas Experimental Tokamak (TEXT), together with a feedback system, and found that they were able to suppress or promote broadband edge turbulence depending on the phase delay in the feedback circuit [15]. Similar results were found by Zhai *et al.* on the KT-5C tokamak after reproducing the experimental setup from TEXT, with the additional observation that, for a particular phase delay, a quasi-coherent mode accompanied the suppression of broadband turbulence[16, 17]. Work on linear devices by Schröder *et al.* [78] and Brandt *et al.* [79, 80] employed a set of eight probes arranged azimuthally around the plasma column. They demonstrated open loop control resulting in both suppression of broadband drift wave turbulence, with decreased turbulence-driven transport, and nonlinear interaction with coherent drift waves. They also found that a mode- and frequency-selective (spatiotemporal) excitation structure was essential to coupling to drift waves, as was driving parallel currents with the same spatial structure as the intrinsic mode. Interestingly, these works also showed that promoting a coherent fluctuation with an external actuator could reduce the overall fluctuation energy of both the background turbulent and driven modes.

In addition to probes, inductive structures have also been used to stimulate edge activity, as in the study by Borg *et al.* on the TORTUS tokamak [81]. There, a single-winding dipole antenna was employed with the goal of driving shear Alfvén modes in the plasma edge. The antenna winding could be rotated arbitrarily with

respect to the equilibrium magnetic field; it was found that the maximum response was achieved when the winding was exactly aligned with the background field, and also that the driven mode was strongly guided by the field lines. Brandt *et al.* also complemented their electrostatic probe exciter with an inductive setup using eight saddle coils, arranged azimuthally around, and external to, the plasma [80]. The saddle coils reproduced the same open-loop control of drift waves as the electrostatic probes.

There have also been many attempts to excite specific, stable plasma modes - typically Alfvénic - in order to diagnose the background plasma in which they appear. Such work falls under the category of Active MHD (AMHD) spectroscopy. Early work in this area was performed on the TCA and PETULA tokamaks by Collins *et al.* [82, 83]. The TCA team employed an unshielded "bar" antenna meant to drive low-power discrete Alfvén waves (DAWs). This was driven with between 1 and 5 A of current at variable frequency between 2.5 and 11 MHz (where $\Omega_i/(2\pi) = 21$ MHz on-axis) with the help of a broadband, low-Q matching network. Frequency was either scanned in a sawtooth ramp across the DAW band, mapping out the spectrum, or pinned to a particular DAW using a phase-locked loop (PLL) in order to closely track how varying plasma parameters affected the mode's frequency.

The methodology of this approach was placed on firmer theoretical ground by Goedbloed *et al.*, who coined the term, Active MHD. Subsequently, extensive work in this area was carried out at the Joint European Torus (JET) [84, 85, 86, 87, 88]. These experiments sought to couple to toroidal Alfvén eigenmodes (TAEs) both by direct inductive and nonlinear parametric means. In the former case, multiple saddle coils were arranged to selectively excite stable TAEs of low- and intermediate-range toroidal mode numbers. These were energized at frequencies in the TAE band, with the frequency scanned to reveal the poles in the spectrum. In the latter case, the frequency of two ICRF heating antennas was modulated so that their beat frequency scanned across the TAE band. The nonlinear coupling between the ICRF antennas, driven at 10's of MHz with megawatts of power, is ultimately limited by the Manley-Rowe relations, which restrict the power that may be coupled to the driven mode by

the ratio of frequencies between it and the pump wave [89].

Similar AMHD experiments were performed on Alcator C-Mod[90, 91, 92, 93], finding broadly comparable results. The bulk of these experiments utilized a pair of dedicated coils, placed in the same toroidal plane and mirrored about the midplane. However, parametric drive was also explored via *amplitude* modulating a single ICRF antenna at the TAE frequency, achieving the same effect as the beat experiment on JET – a unique approach, to the author's knowledge. This work was not published, but the experimental design may be reviewed from the relevant proposals [94, 95], and results reviewed from the Alcator C-Mod Logbook [96].

Bootstrapping on this work, experiments on Alcator C-Mod in 2011 attempted to use the ICRF amplitude modulation technique to couple to the QCM parametrically. The proposal for this work is publicly available [97]. However, only five discharges discharges on C-Mod were run under this experiment in 2011, and the project was abandoned after a lack of positive results. Nonetheless, this was the first attempt to actively couple to the QCM.

A different approach toward controlling edge fluctuations, and in particular, ELMs, is to setup a static, resonant magnetic perturbation field in the edge of the plasma. This results in field lines near the plasma edge being randomly scattered across a volumetric region, rather than lying on a surface. This "stochasticization" of the edge plasma has been shown to suppress large ELMs without significantly degrading H-mode confinement [20]. In this way, the target fluctuation is affected by changing the magnetic topology of the background plasma in which the mode appears, rather than by directly or parametrically coupling to the mode.

For comparison, Figure 2-3 shows several of the excitation structures employed in these experiments, alongside the new Shoelace antenna.

2.5 The Shoelace Antenna: Mission and Context

The Shoelace antenna project is a union of two areas of interest and expertise at Alcator C-Mod: studying coherent, transport-inducing edge modes, as well as Active

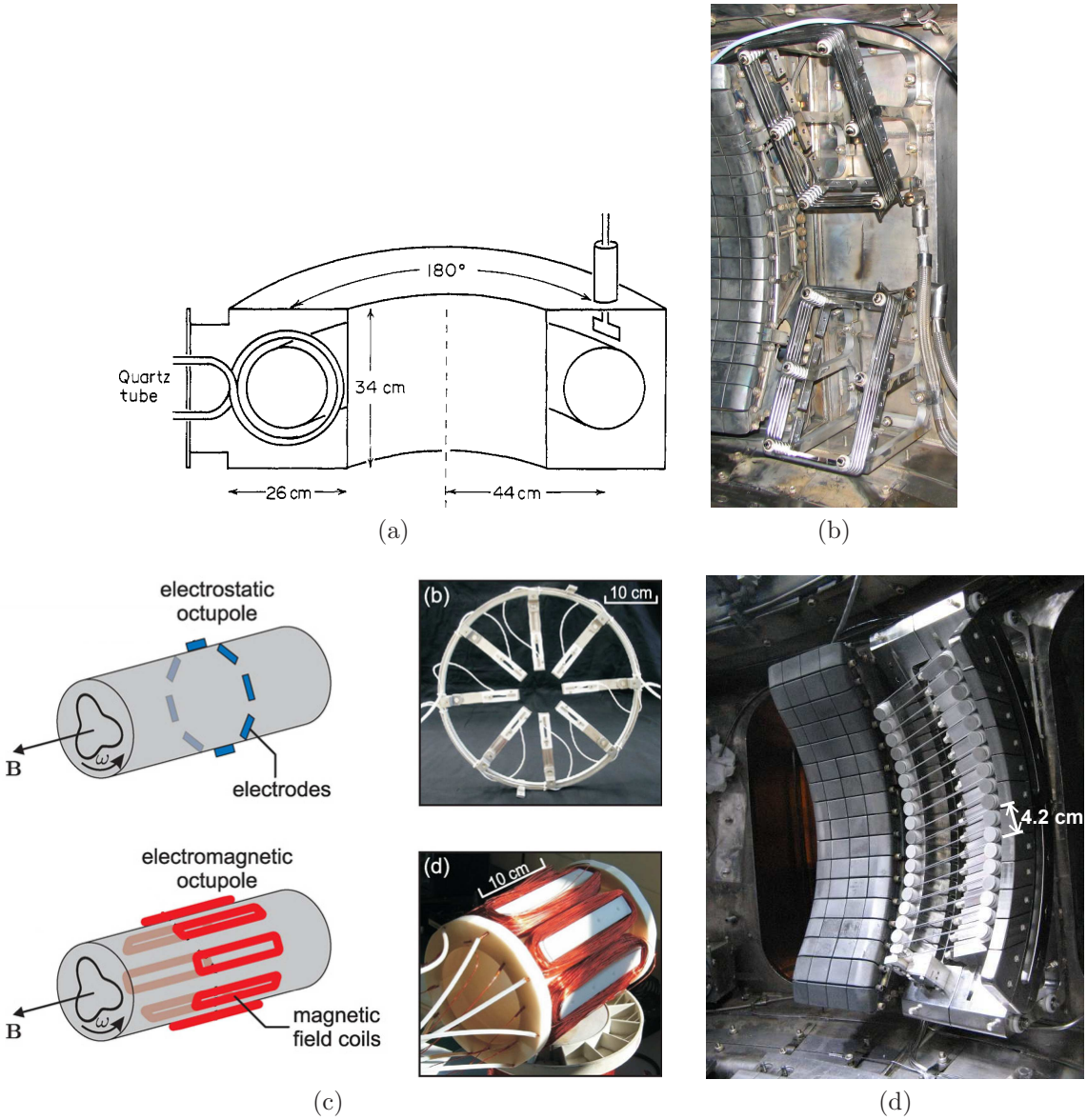

Figure 2-3: (a) Experimental setup of experiments by Borg *et al.* - reproduced from Figure 5 from [81], doi:10.1088/0741-3335/29/6/001; (b) Antenna from Active MHD experiment by Sears – reproduced from Figure 3.5.c of [92], photo credit to Jason Sears. (c) Experimental setup of experiments by Brandt *et al.* - reproduced from Figure 3 of [80], doi:10.1088/0741-3335/52/5/055009. (d) Photograph of Shoelace antenna mounted in vessel. Photo credit B. LaBombard. Permission granted for all figures by the authors. (a) and (c):

MHD spectroscopy. The technical experience in the latter helped in the design and construction of the Shoelace antenna, particularly in developing its new power system. The former provided the motivation for the experiment: to better understand how continuous, coherent edge fluctuations regulate transport across the edge plasma, and to determine whether these fluctuations might be excited actively to achieve the same control via an external actuator.

Alcator C-Mod provides two such edge fluctuations, the QCM and the WCM, which happen to have similar wave numbers. The QCM was selected as a primary target, partly because its narrower frequency spectrum appeared easier to mimic, and partly because the "recipe" for low-power, ohmic EDA H-mode discharges – necessary to reduce the gap between the plasma and antenna as much as possible (maximizing coupling) without damaging the antenna – had already been developed. But the antenna and power system were designed to couple to either fluctuation.

Since the formal inception of the Shoelace project[5], new insights into the QCM have been obtained thanks to the Mirror Langmuir Probe [32], which revealed the mode's drift-wave-like nature. This created a new and exciting link between the Shoelace study and the work on linear devices by Schröder and Brandt [78, 79, 80], which showed that it is possible to couple to drift waves inductively provided frequency and selective wave number matching are respected, and that this coupling can affect transport. However, the Shoelace antenna marks the first-ever attempt to interact directly with a drift-like mode in a high-performance tokamak plasma, which displays a richer set of physics, and which presents a more restrictive set of technical challenges. Moreover, the goal of the project was to promote particle transport by a coherent mode, rather than to reduce transport by broadband turbulence, reflecting the need to obtain steady-state, high-performance tokamak confinement regimes without ELMs in order to prepare the way for future, reactor-scale devices.

[5] on 11 June 2010

Chapter 3

Theory

> The analysis is based on simple assumptions; it is designed to illustrate the essential features of the problem, and is neither rigorous nor complete. The assumptions made are in all cases optimistic, so that the criteria established are certainly necessary, though by no means sufficient, for the successful operation of a thermonuclear reactor.

–J.D. Lawson, in the paper introducing what would become known as the "Lawson criterion" [8]

3.1 Introduction

This chapter gives a brief introduction to the basic theory underlying drift waves, interchange/ballooning modes, shear Alfvén waves, and electrostatic modes of homogeneous plasmas. The goal is to provide a sufficient level of detail to help the reader interpret the experimental results obtained from operating the Shoelace antenna, which is the subject of Chapter 5.

The models developed below suffer from a number of handicaps, including the facts that they (a) are linearized versions of the equations, ignoring nonlinearities which change the character and stability of the fluctuations, (b) apply to simplified geometries, where it is well-known that X-points and other aspects of real tokamak magnetic topologies may have a profound effect on instabilities [72, 73], (c) examine different kinds of dynamics in isolation (*e.g.* exploring the effects of either resistivity or

curvature, but not both), where the real plasma does not selectively neglect a term and thereby "turn off" the associated physics, and (d) ignore kinetic effects outside of the fluid scope. The models' simplicity is useful for developing a conceptual understanding of the underlying plasma dynamics. But we should not become too distracted by the pursuit of applying a linearized label to a complex, nonlinear phenomenon, nor should we expect any such label to completely capture the physics of an instability appearing in a real tokamak edge. Realistic models of such instabilities are extremely complex, requiring delicate numerical treatment [65, 98, 77].

Example calculations performed throughout the chapter use the parameters, $T_e = 50$ eV, $B = 2.27$ T, $\bar{n}_e = 10^{20}$ m^{-3}, and $L_p = |(\nabla p_e)/p_e| = 3.6$ mm, roughly corresponding to conditions at the last-closed flux surface for the low-field, deuterium plasma discharges typical of the Shoelace antenna experiments.

3.2 Drift Waves

3.2.1 An Overview

Drift waves can appear in magnetized plasmas wherever there are density or temperature gradients, and, in their nonlinear turbulent steady-state, serve as a relaxation mechanism of those gradients. They are destabilized by parallel currents arising from collisional resistivity, or from collisionless mechanisms fulfilling the same role, while magnetic and flow shear provide stabilization, as do ion-ion collisions. Since gradients are always present in real plasmas, and since drift waves are readily destabilized, drift waves are omnipresent. They are sometimes called the "universal instability" ([56, 58],[62, p. 182]) owing to the fact that their linear growth rate is always positive in certain idealized circumstances.

There is an extensive literature on drift waves. The earliest theoretical treatment, to the author's knowledge, dates to 1957, when Tserkovnikov [99] examined waves with a pure-flute character, $k_\parallel = 0$, with phase velocities near the drift velocity. Rosenbluth and Simon [59] applied powerful variational methods to the $k_\parallel$=0 case,

extending the understanding of mode stability in this limit. Moiseev and Sagdeev offered a link between the Bohm diffusion coefficient and the collisionally-unstable drift wave in 1963 [57]; this may be the first suggestion that drift waves provide a mechanism for "anomalous" (*i.e.* greater than neoclassical) transport in plasma confinement devices. Roberts and Taylor gave an early treatment of the gyroviscous cancellation in 1962 [55], vital to the theoretical foundation of the drift wave model; this was extended in a thorough treatment by Hinton and Horton in 1971 [63]. Though the slab model with collisions indicated a drift wave which was always unstable [56, 58], in 1966 and 1967, Coppi *et al.* [60] and Kitao [61] demonstrated that magnetic shear provides stabilization. After several other contributions, Krall provided an excellent review in 1968 [62]; another review by Cap in 1976 also compiled many early results on drift waves [100].

Subsequent theoretical investigations have probed nonlinear effects, showing that a self-sustained, nonlinear, drift wave turbulent steady state can arise even in the presence of damping from magnetic shear [101, 64]. The effects of local magnetic shear [66] and X-points [73] have also been studied. A contemporary area of inquiry involves modeling the transition between closed field lines in the "edge" region just inside the last closed flux surface (LCFS) and open field lines[1] outside the "scrape-off layer" (SOL) region. To correctly model this problem, it is necessary to capture the interplay between drift-wave turbulence (expected in the "edge" region) and interchange-like resistive ballooning mode (RBM) turbulence (expected in the SOL) in setting cross-field transport and profiles at the plasma boundary [65, 102, 103].

Recent textbooks by Bellan [104], Hazeltine and Meiss [105], and Stix [76] provide descriptions of drift waves, while a very thorough and cogent treatise on drift waves, and indeed the broad range of physics accessed by the two-fluid[2] model under drift ordering[3], was prepared by Scott in 2001 [65].

[1] Open field lines are those which terminate on a material surface, typically a limiter or divertor tile.

[2] ions and electrons

[3] which assumes $k_\perp \gg k_\parallel$, $\rho_s/L_\perp \sim v_*/c_s \ll 1$, and $\beta_e = \mu_0 p_e/B^2 = c_s^2/v_A^2 \ll 1$ [65, p. 3.2]; all of these inequalities are satisfied by an order of magnitude or more in the edge plasmas used during the Shoelace antenna experiments.

Experimental studies have also demonstrated the importance of electromagnetic drift turbulence in setting transport at the boundary [67].

Drift waves can be viewed as a branch of the acoustic wave system which develops in the presence of gradients [65, p. 5.10-11]. Despite this, drift waves exist outside of the magnetohydrodynamic (MHD) treatment. This is because an essential ingredient to the drift wave description is the difference in physical response between electrons – in particular, their Boltzmann-like response – and the much more massive ions. Because the MHD model does not account for this two-fluid effect, it excludes drift waves.

While drift waves arise in an electrostatic treatment, electromagnetic effects can be important. A basic criterion for the importance of these effects is $\beta = 2\mu_0 p/B^2 > \mu \equiv m/M \approx 2.7 \times 10^{-4}$ [62, p. 155], though this neglects other relevant factors, including collisionality [65, Chap. 5]. In these experiments, the edge plasma displays $\beta \sim \mu$. Moreover, waves in uniform plasmas (MHD waves) are modified in the presence of gradients. This suggests the importance of kinetic shear Alfvén effects, from which we might expect that $\omega \sim k_\parallel v_A$, where v_A is the Alfvén velocity ([62, p. 155], [65, p. 3.2]).

3.2.2 Fluid Model

At the most basic level, drift waves correspond to the perturbed $\mathbf{E} \times \mathbf{B}$ advection of the density gradient. A near-Boltzmann electron response locks together $\tilde{\Phi}$ and $\tilde{n}_e$ perturbations, causing the potential perturbation to follow the density perturbation, creating a wave-like motion within the flux surface.

A cartoon description of the drift wave is offered by Figure 3-1. In the presence of a potential perturbation, a perturbed $\mathbf{E} \times \mathbf{B}$ drift develops, with vortices surrounding the peaks and troughs of $\tilde{\Phi}$ (Figure 3-1a). When this is superimposed on the background density profile, it results in radial advection and a density perturbation, $\tilde{n}_e$ (Figure 3-1b) – the surfaces of constant pressure are pushed or pulled depending on the direction of the perturbed $\mathbf{E} \times \mathbf{B}$ flow, as low-density plasma is carried inward and high-density plasma, outward. This, in turn, produces a pressure perturbation,

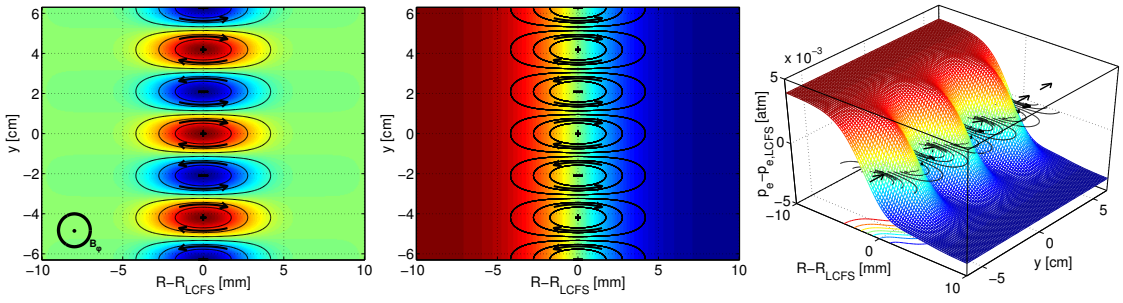

(a) (b) (c)

Figure 3-1: Cartoon summarizing the physics of a drift wave, with wave and profile parameters roughly matching those of the QCM. (a) Plot of perturbation, $\tilde{\Phi} \propto e^{-x^2/\Delta x^2} \cos(k_\perp y)$, $\Delta x = 3$ mm, $k_\perp = 1.5$ cm^{-1}, $x = R - R_{LCFS}$, with direction of background field (out of the page) and $\mathbf{E} \times \mathbf{B}$ drift indicated. (b) $\mathbf{E} \times \mathbf{B}$ drift superimposed on background density, $n_e \propto \tanh(-x/L_p)$ with $L_p = 3.6$ mm, and/or pressure profile (taking T_e to be a uniform constant). (c) Electron pressure profile with perturbation superimposed, and $\mathbf{E} \times \mathbf{B}$ drift also reprised in the xy plane.

$\tilde{p}_e$ – in the present case, $\tilde{p}_e = \tilde{n}_e T_e$, with T_e assumed a uniform constant for simplicity.

Now, the near-Boltzmann-like response of the electrons enforces that $e\tilde{\Phi}/T_e \approx \tilde{p}_e/p_e = \tilde{n}_e/n_e$. If the perturbations in $\tilde{\Phi}$ and $\tilde{p}_e$ align in phase, then the tendency of the $\mathbf{E} \times \mathbf{B}$ flow is to push up the density just ahead of a peak in $\tilde{p}_e$, and to depress it behind. But this would tend to misalign $\tilde{p}_e$ with respect to $\tilde{\Phi}$. The only solution which locks these two perturbations together is a traveling one which moves at the speed and in the direction of the electron diamagnetic drift velocity, $\mathbf{v}_*$ (Figure 3-1c) – the wave is constantly "falling forward," like a child tipping forward and walking in the same direction in order to maintain balance. The fact that the perturbation of moves at $\mathbf{v}_*$ is potentially confusing - it suggests that diamagnetic physics provide the key to the drift wave. But we have seen that no diamagnetic behavior need be invoked to arrive at a drift wave response, a point cleverly noted by Stix in his derivation of the drift wave dispersion relation with the zero perpendicular temperature, $T_\perp = 0$, effectively turning off plasma diamagnetism [76, Sec. 3.8].

Before discussing a model that leads to drift waves, it will be useful to catalog several of the fluid drifts, which are readily retrieved by applying the drift operator [65, p. 3.3], $\frac{\mathbf{B}}{B}\times$, to the momentum equations, balancing the terms at equilibrium

with an appropriate drift, $\mathbf{u}$, through the Lorentz force, $\propto \mathbf{u} \times \mathbf{B}$. The momentum equations are

$$m_e n_e \frac{\mathrm{d}_e \mathbf{v}_e}{\mathrm{d}t} = -n_e e \left(\mathbf{E} + \mathbf{v}_e \times \mathbf{B}\right) - \nabla p_e - \nabla \cdot \bar{\bar{\Pi}}_e + m_e n_e \bar{\bar{\nu}}_e \cdot \left(\mathbf{u}_i - \mathbf{v}_e\right) \tag{3.1}$$

for the electrons, and

$$M_i n_i \frac{\mathrm{d}_i \mathbf{u}_i}{\mathrm{d}t} = Z n_i e \left(\mathbf{E} + \mathbf{u}_i \times \mathbf{B}\right) - \nabla p_i - \nabla \cdot \bar{\bar{\Pi}}_i - m_e n_e \bar{\bar{\nu}}_e \left(\mathbf{u}_i - \mathbf{v}_e\right), \tag{3.2}$$

for the ions, where $\frac{\mathrm{d}_e \mathbf{v}_e}{\mathrm{d}t} = \frac{\partial \mathbf{v}_e}{\partial t} + \mathbf{v}_e \cdot \nabla \mathbf{v}_e$ is the total derivative[4] of the electron velocity field, and likewise for $\frac{\mathrm{d}_i \mathbf{u}_e}{\mathrm{d}t}$. $\bar{\bar{\nu}}$ is an effective collisionality tensor (which will later be assumed diagonal, with differing parallel and perpendicular frequencies), such that $\mathbf{R}_{ei} = -\mathbf{R}_{ie} = m_e n_e \bar{\bar{\nu}}_e \cdot \left(\mathbf{u}_i - \mathbf{v}_e\right)$ is the resistive friction force. The quantities, $\bar{\bar{\Pi}}_i$ and $\bar{\bar{\Pi}}_e$, are the anisotropic parts of the ion and electron pressure tensors (or "momentum flux"), $\bar{\bar{\Pi}}_\sigma \equiv n_\sigma m_\sigma \langle \mathbf{w}_\sigma \mathbf{w}_\sigma \rangle_\sigma - p_\sigma \bar{\bar{I}}$, for each species, σ, where p_σ is the isotropic pressure, $\mathbf{w}_\sigma \equiv \mathbf{u} - \langle \mathbf{u} \rangle_\sigma$ is the velocity relative to the bulk, mean flow, and $\langle Q \rangle_\sigma$ represents the ensemble average of a quantity, Q, over the distribution function of species, σ [70, p. 14]. The divergences of these quantities fold in dissipation due to viscosity; they also lead to the cancellation of flux advected by the diamagnetic drift velocity[5]. Strictly speaking, at least the diamagnetic component, $\bar{\bar{\Pi}}_*$, of the momentum flux should be included to make this cancellation; it will be tacitly assumed that this has been done, and terms involving $\bar{\bar{\Pi}}$ will suppressed in the analysis that follows, which has the limited goal of presenting a basic description of drift waves. Retaining these terms is important for more detailed analyses of the drift-ordered system, particularly where sound waves are excited.

Let $\frac{\mathrm{d}}{\mathrm{d}t} \to 0$; this corresponds to the equilibrium case, $\frac{\partial}{\partial t} \to 0$, where the back-

[4]This quantity is known by several other labels, including the material or convective derivatives; it accounts for time variation in, for example, a volume fluid element which is advected (or convected in the case of a vector quantity) along with the background flow of the fluid.

[5]the famous "diamagnetic cancellation" [65, p. 2.37 and p. 3.4]

ground flow is negligible, as are nonlinear combinations of perturbed quantities. The $\mathbf{E} \times \mathbf{B}$ drift is

$$\mathbf{v}_E = \mathbf{u}_E \equiv \frac{\mathbf{E} \times \mathbf{B}}{B^2}. \tag{3.3}$$

The diamagnetic drift comes about from the pressure gradient term. It is

$$\mathbf{v}_* = \frac{\nabla p_e \times \mathbf{B}}{n_e e B^2} \tag{3.4}$$

for the electrons and

$$\mathbf{u}_* = \frac{\mathbf{B} \times \nabla p_i}{Z n_i e B^2} \tag{3.5}$$

for the ions.

The polarization drift is the first-order correction to the zeroth-order approximation, in the parameter, ω/Ω_s, of neglecting the inertial contribution (the left-hand side) of the momentum equations. It is

$$\mathbf{u}_p = \frac{\mathbf{B}}{B} \times \frac{M_i}{ZeB} \frac{\mathrm{d}_E}{\mathrm{d}t} \left(\frac{\mathbf{E} \times \mathbf{B}}{B^2} + \frac{\mathbf{B} \times \nabla p_i}{n_i Z e B^2} \right) = \frac{1}{\Omega_i} \frac{\mathrm{d}_E}{\mathrm{d}t} \left(\frac{\mathbf{E}_\perp}{B} - \frac{\nabla_\perp p_i}{n_i Z e B} \right) \tag{3.6}$$

for the ions and

$$\mathbf{v}_p = -\frac{\mathbf{B}}{B} \times \frac{m_e}{eB} \frac{\mathrm{d}_E}{\mathrm{d}t} \left(\frac{\mathbf{E} \times \mathbf{B}}{B^2} - \frac{\mathbf{B} \times \nabla p_e}{n_e e B^2} \right) = -\frac{1}{\Omega_e} \frac{\mathrm{d}_E}{\mathrm{d}t} \left(\frac{\mathbf{E}_\perp}{B} + \frac{\nabla_\perp p_e}{n_e e B} \right) \tag{3.7}$$

for the electrons, with $\frac{|\mathbf{u}_p|}{|\mathbf{v}_p|} \sim \frac{M_i}{m_e} = \mu^{-1} \approx 3646$ for the main ion species in these experiments, deuterium.

Henceforth, we will take $Z = 1$, which also applies to deuterium.

The *parallel* Ohm's law is formed by subtracting the parallel component of Eq. 3.1 from μ times the parallel component of Eq. 3.2 and dividing through by $n_e e$:

$$\boxed{\frac{1}{\epsilon_0 \omega_{pe}^2} \frac{\partial J_\parallel}{\partial t} = E_\parallel + \frac{1}{n_e e} \nabla_\parallel p_e - \eta_\parallel J_\parallel} \tag{3.8}$$

where $\nabla_\parallel \equiv \hat{\mathbf{b}} \cdot \nabla$

The electron or ion continuity equations will also prove useful. They are,

$$\frac{\partial n_e}{\partial t} + \nabla \cdot (n_e \mathbf{v}_e) = 0 \tag{3.9}$$

and

$$\frac{\partial n_i}{\partial t} + \nabla \cdot (n_i \mathbf{u}_i) = 0. \tag{3.10}$$

We also approximate the plasma as isothermal[6], with[7]

$$p_e = n_e T_e, \tag{3.11}$$

and moreover, temperature is assumed constant[8]. The continuity equation, together with the zeroth-order drifts ($\mathbf{v}_E$ and $\mathbf{v}_*$), is used to eliminate the fluctuating part of n_e from the parallel Ohm's law. Within the electron continuity equation, the advection of the density gradient by the perturbed $\mathbf{E} \times \mathbf{B}$ velocity, $\tilde{\mathbf{v}}_E \cdot \nabla n_e$, deserves special attention. Using the identity, $\mathbf{A} \times \mathbf{B} \cdot \mathbf{C} = \mathbf{B} \cdot \mathbf{C} \times \mathbf{A}$, and assuming an isothermal plasma with uniform temperature and electrostatic perpendicular field, we have

$$\tilde{\mathbf{v}}_E \cdot \nabla n_e = -\frac{n_e e}{T_e} \mathbf{E} \cdot \mathbf{v}_* = -i \frac{n_e e}{T_e} v_* k_\perp \tilde{\phi} = -i n_e \omega_* \frac{e\tilde{\phi}}{T_e}. \tag{3.12}$$

where $\omega_* \equiv k_\perp v_*$, and v_* is the component of $\mathbf{v}_*$ that is perpendicular to the background field, but inside the equilibrium flux surface[9].

The simplest drift wave dispersion relation follows immediately from the continuity equation when only advection by the perturbed $\mathbf{E} \times \mathbf{B}$ flow is included. In this case, making use of Eq. 3.12,

[6] This is appropriate when $\omega/(k_\parallel v_{th,e}) \ll 1$ [76, pp. 58-59, 62]. In the present circumstances, $\omega/(k_\parallel v_{th,e}) \approx 2 f L_c \sqrt{\mu}/c_s \approx 0.6$, which only marginally satisfies the inequality, and suggests Landau damping need be included.

[7] It is common in the plasma physics literature to quote temperatures in units of energy, absorbing the Boltzmann constant, k_B, into T. This is done here.

[8] It should be noted that the temperature is not constant for the QCM, with $\Delta T_e/T_e \approx 45\%$ (peak-to-peak). Accounting for a fluctuating temperature within a more complete drift-ordered model is treated in [65, Chap. 13].

[9] Mathematically, we can write this as the $\frac{\nabla n_e}{|\nabla n_e|} \times \hat{\mathbf{b}} = \hat{\mathbf{y}}$-component.

$$\frac{\partial \tilde{n}_e}{\partial t} = -\tilde{\mathbf{v}}_E \cdot \nabla n_e = \frac{n_e e}{T_e} \mathbf{E} \cdot \mathbf{v}_*, \tag{3.13}$$

which, after Fourier decomposition and slight rearranging, is

$$\omega \frac{\tilde{n}_e}{n_e} = \omega_* \frac{e\tilde{\phi}}{T_e}. \tag{3.14}$$

Finally, taking $\tilde{n}_e/n_e = \tilde{p}_e/p_e$ when T_e is constant, and applying the Boltzmann response,

$$\boxed{\omega = \omega_* = \mathbf{k}_\perp \cdot \mathbf{v}_*}. \tag{3.15}$$

As discussed previously, this dispersion relation gives precisely the perpendicular phase velocity, $\omega/k_\perp = v_*$, which satisfies the two constraints that the potential perturbation (1) always overlays in phase with the density perturbation, while (2) still advecting the background density profile, thereby producing the correct density perturbation at the next instant of time.

Note also that the dispersion relation is not quadratic; the wave propagates unidirectionally.

Alternatively, the dispersion relation may be determined by treating the plasma as a refractive medium, finding the $\hat{\mathbf{b}}\hat{\mathbf{b}}\cdot$ component of the susceptibility, $\bar{\bar{\chi}}$, and setting it to zero.

In this isothermal case, and with T_e constant, the electron diamagnetic drift velocity may also be expressed as

$$v_* = c_s \frac{\rho_s}{L_p} \tag{3.16}$$

where $c_s = \sqrt{T_e/M_i} \approx 50$ km/s is the sound speed, and $L_p = \left|\frac{1}{p_e}\nabla p_e\right|^{-1} \approx 3.6$ mm is the pressure gradient length scale, using typical parameters at the LCFS in these experiments. $\rho_s \equiv \frac{c_s}{\Omega_i} \approx 0.4$ mm is the drift wave dispersion length scale [65, p. 5.7], which plays a similar role as the ion Larmor radius, but replaces the ion with the electron temperature. Using these same typical parameter values, $v_* \approx 6$ km/s. With the nominal QCM wave number, $k_\perp \approx 150$ m^{-1}, this gives $\omega_*/(2\pi) \approx 150$ kHz, which

is near the observed plasma-frame frequency of the mode.

The dispersion relation in Eq. 3.15 neglects both ion and electron inertia. Accounting for ion inertia to the next order requires including the polarization current, discussed previously, which is generally proportional to $\omega/\Omega_i \approx 6 \times 10^{-3}$ (the electron polarization current is proportional to $\omega/\Omega_e \approx 2 \times 10^{-6}$, and may still be neglected).

The polarization current is important because it satisfies the *quasineutrality condition*, encapsulated by

$$\nabla \cdot \mathbf{J} = \mu_0 \frac{\partial \rho_c}{\partial t} \approx 0, \tag{3.17}$$

where $\rho_c \equiv Zen_i - en_e$ is the charge density, and the middle equality follows from the divergence of Ampère's law (including Maxwell's displacement current contribution). This is a differential expression of Kirchoff's current law, and states that charges cannot accumulate over time in any location.

The parallel component of the current is carried almost entirely by electrons, which move rapidly in response to the parallel electric field. But consider the case when there is a parallel gradient in the electric field ($k_\parallel \neq 0$). This is the fundamental pathway by which drift waves become unstable, as described below. Electron forcing then becomes uneven along a field line, and a cross-field current is required to prevent the accumulation of charge. The ion polarization drift is the most accessible mechanism for this perpendicular current, due to the relatively large ion mass, and it discharges any built-up charge.

Including the polarization current in the fluid model results in a correction to the drift wave dispersion relation[10],

$$\omega = \frac{k_\perp v_*}{1 + k_\perp^2 \rho_s^2}. \tag{3.18}$$

The dispersion hinted at in the name of ρ_s is now apparent.

In the present case, $k_\perp^2 \rho_s^2 \approx 5 \times 10^{-3} \ll 1$, and so the correction to the simple drift wave dispersion relation is slight.

[10] *cf.* Eq. 5.16 in [65]

Unfortunately, the basic dispersion relation, alone, is not sufficient to discern one mode from another, particularly when comparing interchange (ballooning) modes and drift waves. This is so because the time scales for different instabilities may overlap, because $k_\parallel$ is difficult to measure, and because it is difficult to explore a wide enough parameter range so that unambiguous trends between $\mathbf{k}$ and ω can be identified. As such, other "diagnostics" are needed to illuminate the differences between the modes [65, Chap. 11].

One such diagnostic is the phase difference between the density and potential [65, Fig. 11.3, p. 259]. The parallel Ohm's law illustrates this with slight modification,

$$\eta_\parallel J_\parallel = ik_\parallel \frac{T_e}{e}\left(-\frac{e\tilde{\Phi}}{T_e} + \frac{\tilde{n}_e}{n_e}\right). \tag{3.19}$$

When the resistive term on the left-hand-side is small, as is often assumed in idealized models, the phases of the fluctuating electrostatic potential, $\tilde{\Phi}$, and the fluctuating density, $\tilde{n}_e$, are locked to be close to one another, resulting in a near-Boltzmann response. This is quite distinct from the case for interchange modes; we will see below that the phase difference between $\tilde{\Phi}$ and $\tilde{n}_e$ for these modes is near $\frac{\pi}{2}$ radians. For the QCM, $\tilde{\Phi}$ was measured as lagging $\tilde{n}_e$ by $\sim 16^\circ$ [32]. This indication, as well as the fact that the mode travels in the electron diamagnetic drift direction in the plasma (co-rotating) frame, robustly identifies the dynamics of the QCM as predominantly drift-wave-like.

The linear growth rate of the drift wave in this model is (see Eq. D.49 of Section D.2 in the appendix)

$$\gamma = \epsilon_0 \eta_s \frac{c_s^2}{L_p^2}\frac{k_\perp^2}{k_\parallel^2}\frac{k_\perp^2 c_s^2 \omega_{pi}^2}{\Omega_i^4} = \eta_s \omega_{pi}^2 \epsilon_0 \frac{k_\perp^2}{k_\parallel^2}\frac{\omega_*^2}{\Omega_i^2}\left(\frac{1}{1-\frac{\omega_*^2}{\omega_A^2}}\right) \tag{3.20}$$

where $\eta_s = \eta_\parallel = 0.51\frac{m_e}{n_e e^2 \tau_{ei}} \approx 2\times 10^{-6}\ \Omega\cdot\mathrm{m}$ is the Spitzer resistivity, which is the same as the Braginskiĭ parallel resistivity.

Using parameters from experiment applying to the QCM and Shoelace antenna, $\gamma/\omega \approx 6\%$. However, it is not the numerical value of the linear growth rate that is of

interest, since we have excluded damping mechanisms – particularly flow shear and magnetic shear – from the analysis, as well as the destabilizing contributions entering from the nonlinear treatment of the problem[11], which give rise to self-sustaining turbulence. Rather, it is the qualitative information that is of value here.

The linear growth rate conveniently summarizes two important points. Firstly, electron-ion collisions, through resistivity, destabilize the drift wave, with the growth rate increasing linearly as the Spitzer (or parallel) resistivity. Secondly, while the growth rate is stronger for smaller $k_\parallel$, it is not defined for $k_\parallel \to 0$; when $k_\parallel \to 0$, the mode is metastable, neither growing nor dissipating. This is generally true for the simple drift wave model, although there are situations where purely fluted ($k_\parallel \to 0$) drift wave instabilities exist [59, 100].

The physical origin for this behavior is seen in the parallel Ohm's law, Eq. 3.19. When $\eta_\parallel > 0$, a nonzero phase difference must exist between $e\tilde{\Phi}/T_e$ and $\tilde{p}_e/p_e$ in order to balance the resistive potential drop resulting from the parallel current. The result is that the potential and density wavefronts are not aligned. This makes it possible for outward $\mathbf{E}\times\mathbf{B}$ advection to be weighted to the location where density is increased, while inward $\mathbf{E}\times\mathbf{B}$ advection is weighted to positions where the pressure perturbation depletes the local density, as shown in Figure 3-2. The result is a net outward radial transport of particles. Not only does this begin to describe a mechanism by which fluctuations may drive the particle flux which sustains high-performance H-modes, but it also demonstrates how the drift wave can access the free energy manifest in the strong density gradient at the plasma edge. Coupling to this free energy source ultimately leads to destabilization of the mode.

Collisionless processes, including Landau damping, can also fulfill the role of resistivity in producing a non-zero phase difference between $e\tilde{\Phi}/T_e$ and $\tilde{p}_e/p_e$ [76, 104].

[11] the most important of which being the nonlinear $\mathbf{E}\times\mathbf{B}$ advection of the vorticity, $\mathbf{v}_E \cdot \nabla\left(\nabla_\perp e\tilde{\Phi}/T_e\right)$ [65, Sec. 8.V]

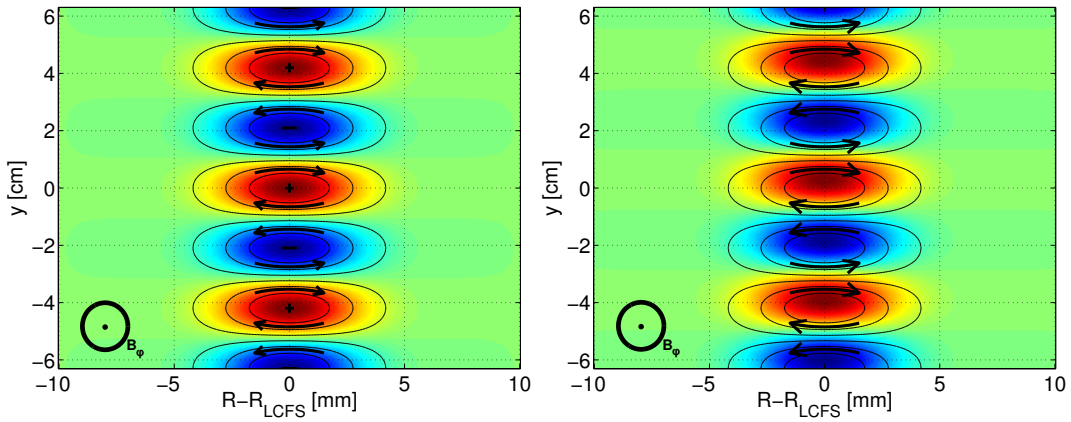

Figure 3-2: Conceptual illustration of (a) potential, $\tilde{\Phi}$, and (b) density, $\tilde{n}_e$, perturbations. The contours in both plots correspond to level sets of $\tilde{\Phi}$. When a phase difference develops such that $\tilde{n}_e$ leads $\tilde{\Phi}$ slightly, the outward radial $\mathbf{E} \times \mathbf{B}$ advection is weighted on the positive $\tilde{n}_e$ disturbance, and the inward on the negative, resulting in net outward flow, down the density gradient.

3.3 Ballooning Modes

Ballooning modes are the toroidal version of the interchange mode. Their name derives from their shape; they are localized to the "bad-curvature" (low-field) side of the plasma, making them appear to "balloon" outward.

Interchange modes are understood conceptually from the linear z-pinch picture [70, pp. 267-269]. In this configuration, the mode is also known as the "sausage" instability. The cylindrical plasma column has purely axial current, and the magnetic field circulates azimuthally around the axis of the column. Impose a perturbation on the plasma of the form, $\cos(k_\perp z)$, where $k_\perp = 2\pi n/L$ is the wave number perpendicular to the purely azimuthal ($\hat{\theta}$-oriented) field. In this case, two bundles of field-lines (flux tubes) change places. One links vacuum. The other, adjacent tube links plasma. The plasma flux tube shifts to form the volume where the column bulges. The vacuum flux tube comprises the void left by the shifted plasma flux tube. The field strength follows $|B_\theta| \propto 1/r$. Where the plasma column is constricted, the field increases, and the magnetic pressure increases as the square of the field. Meanwhile, the plasma has now been displaced axially to a region of expanded radius; there, the magnetic

pressure is reduced. The tension in the field lines offers some restoring force against the bulge in the plasma, but also promotes the constriction in the necked region. The overall competition is between unfavorable curvature and compression of the plasma, with a relatively shallow threshold to instability.

The toroidal geometry of the tokamak modifies this situation. The most unstable modes are still approximately field-aligned (fluted along magnetic field lines, like an architectural column), with $k_\perp \gg k_\parallel$. However, curvature changes from being "good" to "bad" along a field line due to its helical trajectory (*i.e.* due to the rotational transform). In a tokamak, the field lines are bent around the axis of symmetry, with $B_\phi \gg B_\theta$, such that the radius of curvature points primarily outward with the major radial coordinate, R. By contrast, the plasma pressure points outward along the minor radial coordinate, r. On the inside (high-field) half of the plasma, $\hat{\mathbf{R}}$ and $\hat{\mathbf{r}}$ are opposite one another - this is the "good-curvature" side of the plasma. On the outer half of the cross-section (the "low-field" side), $\hat{\mathbf{R}}$ and $\hat{\mathbf{r}}$ align. This is the "bad-curvature" side of the plasma.

One way to to elucidate "good" from "bad" curvature is to realize that $|\mathbf{B}|$ falls primarily as $1/R$ in the tokamak case. This is seen by enforcing Ampère's law in cylindrical geometry with axisymmetry, noting that the vertical component of $\mathbf{J}$ will be small. On the inside half of the plasma, the plasma pressure pushes in the direction of increasing field strength, so that a bulge outward faces increasing magnetic pressure, tending to restore equilibrium. However, on the outside half, the plasma pressure pushes in the direction of weakening field strength, such that a bulge will encounter a decreasing restoring force, tending toward instability. The rotational transform means that the same field line will wrap through both good and bad curvature regions. The flux-surface-averaged curvature tends to be good, with field-line-bending also having a stabilizing effect, as well as shear in the magnetic field (the case when field lines on adjacent surfaces follow trajectories that are not parallel).

The net effect of the toroidal geometry on the interchange mode is to restrict the instability to the "bad" curvature side. The instability then "balloons" out on the outer half of the plasma. In order to localize the mode in this way, high perpendicular

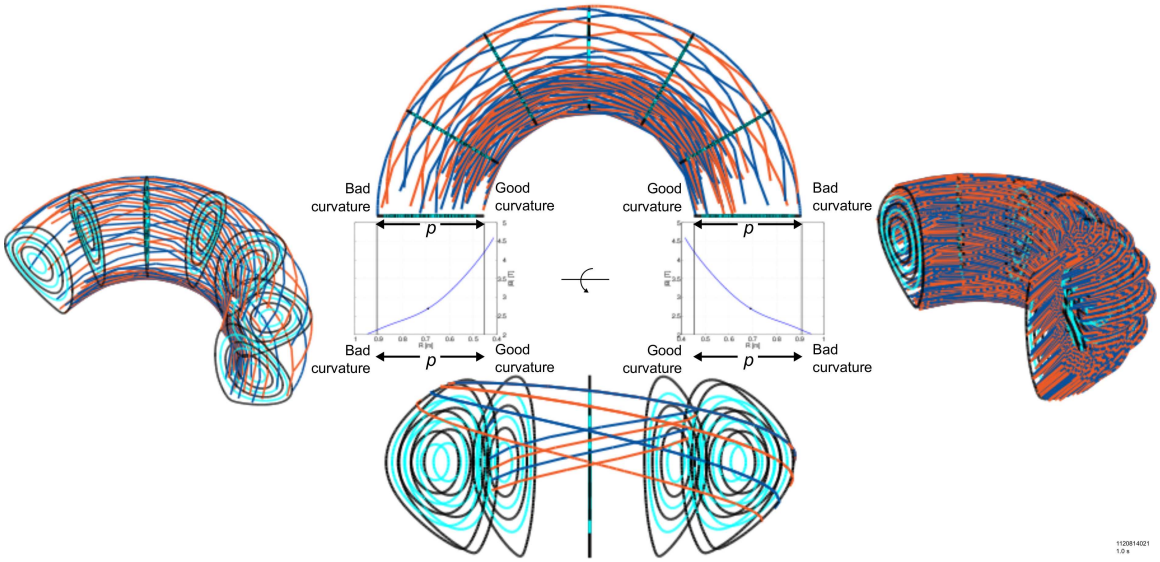

Figure 3-3: Cartoon of ballooning instability, using magnetic geometry from an EFIT reconstruction of one of the C-Mod plasma discharges used in these experiments. The left-most figure shows field-lines on the 99.5% flux surface, as well as several interior flux surfaces. The perturbation on the bad-curvature side meets decreasing magnetic pressure as it bows outward, while expansion on the high-field side encounters higher magnetic pressure, tending to restore equilibrium. Perturbations become localized to the bad-curvature side, a requirement which selects for higher mode numbers, as shown in the right-most panel.

wave numbers are favored. The limit of infinite wave number leads to the Mercier stability criterion, which, in the large-aspect-ratio limit with $\beta_\theta \sim 1$, is approximated by

$$\left(\frac{rq'}{q}\right) + 4r\beta'(1-q^2) > 0, \tag{3.21}$$

with $\beta = \frac{2\mu_0 p}{B^2}$ the normalized pressure and q the safety factor[12]. Shear in the magnetic field leads to greater stability (through $q' = \mathrm{d}q/\mathrm{d}r$), as does a higher safety factor and a gentler pressure profile. The Mercier criterion cannot capture the full picture of the diverted tokamak plasma far beyond these qualitative statements, however, and we must resort to more involved, typically numerical analyses to make progress.

It is well-known that the QCM has a ballooning shape [38], and the high perpendicular wave number, $k_\perp \gg \left(k_\parallel, 2\pi/a\right)$, is also consistent with the ballooning picture. However, in analyses using the `ELITE` MHD code applied to carefully-measured edge profiles, Mossessian *et al.* and Hughes *et al.* found that the C-Mod edge plasma in EDA H-mode is stable to peeling-ballooning modes [36, 39]. Nonetheless, important corrections to this picture arise from the inclusion of X-points in the magnetic topology, as indicated in works examining the resistive X-point mode in the EDA context [73, 35]. Again, a more precise fingerprint is needed to identify the prevailing physics of the QCM, and it is provided by the phase difference between $\tilde{n}_e$ and $\tilde{\Phi}$.

To arrive at a basic model for interchange modes, we start with the quasineutrality (also called "vorticity") and the electron continuity equations in the electrostatic limit, with the quasineutral result, $\tilde{n}_i = \tilde{n}_e$, and also taking $n_i = n_e$. These are

$$0 = \nabla \cdot \mathbf{J} = e\nabla \cdot \left(n_i \mathbf{u}_i - n_e \mathbf{v}_e\right) \tag{3.22}$$

and

$$\frac{\partial n_e}{\partial t} + \nabla \cdot n_e \mathbf{v}_e = 0 \tag{3.23}$$

which, zeroing the ion temperature but taking $n_i = n_e$, can be rewritten as (see

[12] In the "straight" tokamak, where the torus is unwrapped into a cylindrical column, $q = \frac{rB_\phi}{RB_\theta}$.

Section C.7 in the Appendix)

$$\boxed{-\nabla\cdot\left[\epsilon_0\frac{\omega_{pi}^2}{\Omega_i^2}\frac{\mathrm{d}_E}{\mathrm{d}t}\left(\nabla_\perp\tilde{\Phi}\right)\right]=B\nabla_\parallel\left(\frac{\tilde{J}_\parallel}{B}\right)+\mathcal{K}\left(\tilde{p}_e\right)} \tag{3.24}$$

and (Section C.8)

$$\boxed{\frac{\mathrm{d}_E\tilde{n}_e}{\mathrm{d}t}=n_e\mathcal{K}\left(\tilde{\Phi}\right)-\frac{1}{e}\mathcal{K}\left(\tilde{p}_e\right)-\tilde{\mathbf{v}}_E\cdot\nabla n_e+\frac{B}{e}\nabla_\parallel\left(\frac{\tilde{J}_\parallel}{B}\right)-B\nabla_\parallel\left(\frac{n_e\tilde{u}_\parallel}{B}\right)} \tag{3.25}$$

where the diamagnetic divergence operator, $\mathcal{K}(u)\equiv-\nabla\cdot\left(\frac{\mathbf{B}}{B^2}\times\nabla u\right)=-\left(\nabla\times\frac{\mathbf{B}}{B^2}\right)\cdot\nabla u$, is as described in Section C.6 of the appendix. These equations include the contributions from the ion polarization drift.

The terms that lead to the interchange modes are those relating to inhomogeneity in $\mathbf{B}$. $\mathbf{B}$ can change both along and perpendicular to field lines; the former case implies shear and is stabilizing. We focus on the the latter case, which corresponds, for example, to the $1/R$ variation in $|\mathbf{B}|$ in a tokamak. Assume a model field of the form [65, *cf.* Eq. 10.4],

$$\mathbf{B}=B_0\left(1-\frac{x}{L_B}\right)\hat{\mathbf{z}}. \tag{3.26}$$

If x is the distance outside the LCFS, then the corresponding toroidal field is

$$B_\phi\approx B_L\frac{R_c}{R}\approx B_L\left(1-\frac{x}{R_c}\right) \tag{3.27}$$

where $B_L\gtrsim 2$ T is the typical toroidal field, and $R_c\approx 0.9$ m the major radius, of the LCFS at the outer midplane in the Shoelace experiments. Then $L_B=R_c\approx 0.9$ m corresponds to the major radius at the edge.

Now

$$\nabla\times\left(\frac{\mathbf{B}}{B^2}\right)=\frac{1}{B_0}\nabla\times\left(\hat{\mathbf{z}}\frac{1}{1-\frac{x}{L_B}}\right)=-\frac{1}{L_BB_0}\hat{\mathbf{y}}\left(1-\frac{x}{L_B}\right)^{-2}, \tag{3.28}$$

and so

$$\mathcal{K}(u) = \frac{1}{L_B B_0} \frac{1}{\left(1 - \frac{x}{L_B}\right)^2} \frac{\partial u}{\partial y} = \omega_B \frac{e}{T_e k_\perp} \frac{\partial u}{\partial y} = i\omega_B \frac{e}{T_e} u \tag{3.29}$$

where

$$\omega_B \equiv \frac{T_e}{e} \frac{k_\perp}{L_B B_0} \frac{1}{\left(1 - \frac{x}{L_B}\right)^2} \tag{3.30}$$

absorbs the length scale over which the magnetic field changes, L_B. In the present circumstances, at the edge, $\omega_B = 50\,\mathrm{eV} \cdot \frac{1}{0.9\,[\mathrm{m}] \cdot 2\,[\mathrm{T}]} \cdot 150\,\mathrm{m}^{-1} \approx 4200\,\mathrm{s}^{-1}$.

Reprising the quasineutrality and electron continuity equations, 3.24 and 3.25, after making the substitution for the diamagnetic divergence operator using Eq. 3.29, and moreover taking $\frac{\mathrm{d}_E}{\mathrm{d}t} \to -i\omega$ (ignoring nonlinear advection), $\nabla_\perp^2 \to -k_\perp^2$, $\nabla_\parallel \to 0$, and $x \to 0$,

$$\epsilon_0 \frac{\omega_{pi}^2}{\Omega_i^2} k_\perp^2 \omega \tilde{\Phi} = -\omega_B \frac{e\tilde{p}_e}{T_e} \tag{3.31}$$

and

$$\omega \frac{\tilde{p}_e}{p_e} = -\omega_B \frac{e\tilde{\Phi}}{T_e} + \omega_B \frac{\tilde{p}_e}{p_e} + \omega_* \frac{e\tilde{\Phi}}{T_e} \tag{3.32}$$

after dividing through by $\tilde{n}_e$ and letting T_e be uniform. The drift wave frequency, $\omega_* \equiv v_* k_\perp$, appears again, and we have taken $\frac{\partial}{\partial y} = ik_\perp$. (Compare with Eqs. 10.9 and 10.10 in [65].)

Rearranging Eq. 3.32 gives

$$\frac{\tilde{p}_e}{p_e} = \left(\frac{\omega_* - \omega_B}{\omega - \omega_B}\right) \frac{e\tilde{\Phi}}{T_e} \tag{3.33}$$

which, when inserted into Eq. 3.31, yields

$$\epsilon_0 \frac{\omega_{pi}^2}{\Omega_i^2} k_\perp^2 \omega = -\omega_B \frac{ep_e}{T_e} \left(\frac{\omega_* - \omega_B}{\omega - \omega_B}\right) \frac{e}{T_e} \tag{3.34}$$

The eigenfrequency is then estimated as

$$\omega^2 = -\frac{1}{k_\perp^2}\omega_*\omega_B\frac{e^2 n_e}{T_e}\frac{\Omega_i^2}{\omega_{pi}^2\epsilon_0} = -\frac{1}{k_\perp^2}\omega_*\omega_B\frac{1}{T_e}\frac{e^2B^2}{M_i} = -\frac{c_s^2}{L_pL_B}, \tag{3.35}$$

giving the ideal linear growth rate,

$$\boxed{\gamma_B = \Im\{\omega\} = \frac{c_s}{\sqrt{L_pL_B}} = \sqrt{\frac{T_e}{M_iL_pL_B}}} \tag{3.36}$$

after noting that $|\omega| \sim |\omega_*| \gg |\omega_B|$. This matches Eq. 10.22 in [65]. Using parameters from the experiment, $\gamma_B \approx 8.6\times10^5\ \mathrm{s}^{-1} = 2\pi\cdot 140\times10^3\ \mathrm{s}^{-1}$.

Note that the real part of the frequency is zero. This means that the mode is stationary in the plasma frame (its phase velocity is zero), and will typically appear to rotate at the $\mathbf{E}\times\mathbf{B}$ velocity in the laboratory frame (see Section 3.5).

Let us take this result and reexamine the relationship between $\tilde{\phi}$ and $\tilde{p}_e$, Eq. 3.33. With $|\omega| \sim |\omega_*| \gg |\omega_B|$, this relation becomes

$$\frac{\tilde{p}_e}{p_e} \approx -i\frac{\omega_*}{\gamma_B}\frac{e\tilde{\Phi}}{T_e}. \tag{3.37}$$

$\tilde{p}_e$ leads $\tilde{\Phi}$ by a phase angle of 90°. This result is preserved even in the steady-state turbulent case, when many eigenmodes oscillating at different wave numbers (distinct from the QCM, with its narrow spread in frequency and $\mathbf{k}$) interact with one another nonlinearly[13], although the nonlinear interactions tend to broaden the range of phase angles between $\tilde{p}_e$ and $\tilde{\Phi}$ [65, Chap. 10].

To summarize, ballooning modes are ideal MHD modes resulting from an interchange process in a toroidal geometry. They occur when a volume of plasma at higher field is interchanged with a volume of vacuum at lower field. They are unstable when the curvature drive defeats the resistance to the motion presented by compressing the plasma. Because tokamaks have good curvature, on average, on a flux surface, the interchange mode changes character in these devices, becoming localized on the low-field, bad-curvature side of the plasma, and favoring a high wave number.

[13] See Figure 10.7 in [65], and note that $\tilde{n}_e$ and $\tilde{p}_e$ have the same phase angle in this model since T_e is assumed constant.

Several properties of ballooning modes – a high $k_\perp$ relative to $1/a \approx 5$ m^{-1} (on C-Mod), a fluted character ($k_\perp \gg k_\parallel$), and localization to the bad-curvature side – are displayed by the QCM. Moreover, the laboratory-frame frequencies of the drift wave and ballooning modes can be similar, depending on the radial location of the mode (see Sec. 3.5), though the interchange model we examined produced a purely imaginary eigenfrequency[14]. A clear difference between the two modes, which appears in both linear and nonlinear, turbulent characterizations, is that for ballooning modes, the phase difference between $\tilde{p}_e$ and $\tilde{\Phi}$ is $\sim 90^\circ$, where it is close to zero for drift waves. Measurements of this parameter are consistent with a drift wave, rather than ballooning mode, label for the QCM.

3.4 Waves of the Cold, Homogeneous Plasma

The dielectric description of a cold, homogeneous plasma permits two waves – the "fast" and "slow" waves – each corresponding to a pair of roots in the full, biquadratic dispersion relation. In the low-frequency limit relevant to the present discussion, these waves form the pair of compressional and shear (or torsional) Alfvén waves. The former, with dispersion relation, $\omega^2 = k^2 v_A^2 \sim (2\pi \cdot 80 \text{ MHz})^2$, has a frequency range far in excess of the band around 100 kHz associated with the QCM and excited by the Shoelace antenna, and so it is not expected to play a role in the antenna response. However, the shear Alfvén wave continuum, characterized by $\omega^2 = k_\parallel^2 v_A^2$, can access such low frequencies by merit of the fact that $k_\parallel \ll k_\perp$.

The electrostatic approximation neglects the induced electric field (taking the electric field to be curl-free); its application to the cold plasma dielectric problem leads to a major simplification of the dispersion relation. However, we will see that its application in the present circumstance results in modes that are (a) in the wrong frequency range and (b) very strongly damped by electron-ion collisions.

Let us briefly introduce the plasma dielectric framework. The permittivity tensor

[14]This is a general result from ideal MHD theory - ω^2 is purely real, so that eigenfrequencies are either purely real or purely imaginary.

of the cold, homogeneous plasma medium is

$$\epsilon = \epsilon_0 \begin{bmatrix} S & iD & 0 \\ -iD & S & 0 \\ 0 & 0 & P \end{bmatrix}, \tag{3.38}$$

where $S \equiv 1 - \sum_s \frac{\omega_{ps}^2}{\omega^2 - \Omega_s^2}$, $D \equiv \sum_s \frac{\omega_{ps}^2}{\omega} \left[\frac{\Omega_s}{\omega^2 - \Omega_s^2}\right]$, and $P \equiv 1 - \sum_s \frac{\omega_{ps}^2}{\omega^2}$, with the summations ranging over all species, s, of charged particles, and treating Ω_s as *algebraic* (carrying the sign of the charge of species, s) [76, p. 7, Eqs. 1.18-1.22]. The coordinate system in use here is Cartesian, with $\hat{z}$ aligned with the background magnetic field, and taking the wave to propagate only in the (y, z)-plane.

The dispersion relation is obtained from requiring non-trivial solutions to the wave equation[15]:

$$\begin{aligned} &\frac{\omega^2}{c^2} \begin{vmatrix} S - n^2 & iD & 0 \\ -iD & S - n_z^2 & n^y n_z \\ 0 & n^z n_y & P - n_y^2 \end{vmatrix} = 0 \\ &= \left(S - n^2\right) \left[\left(S - n_z^2\right)\left(P - n_y^2\right) - n_y^2 n_z^2\right] - D^2 \left(P - n_y^2\right) \\ &= S n_\perp^4 + \left[\left(n_\parallel^2 - S\right)(P + S) + D^2\right] n_\perp^2 + P\left[\left(S - n_\parallel^2\right)^2 - D^2\right] = 0 \end{aligned} \tag{3.39}$$

where $n_y = n_\perp = \frac{k_y c}{\omega}$ is the y-component of the index of refraction, and $n_z = n_\parallel = \frac{k_\parallel c}{\omega}$ the z-component, with $n^2 = n_y^2 + n_z^2$, and $c \equiv \frac{1}{\sqrt{\mu_0 \epsilon_0}}$ is the vacuum speed of light.

In the low-frequency limit when $D \approx 0$,

$$0 = S n_\perp^4 + \left(n_\parallel^2 - S\right)(P + S) n_\perp^2 + P\left(S - n_\parallel^2\right)^2 \tag{3.40}$$

leading to

$$\boxed{n^2 = S} \leftarrow \text{Compressional Alfvén wave} \tag{3.41}$$

[15] In component form, the wave equation is $\left(k^i k_j - k^2 \delta_j^i + \omega^2 \mu_0 \epsilon^i{}_j\right) B^j = 0$.

and

$$\boxed{n_\perp^2 = P\left(1 - \frac{n_\parallel^2}{S}\right)} \leftarrow \begin{cases} \text{Shear Alfvén wave when } \left|\frac{n_\perp^2}{P}\right| \ll 1 \\ \text{Electrostatic wave when } 1 \ll \left|\frac{n_\parallel^2}{S}\right| \end{cases} \tag{3.42}$$

where

$$S \approx 1 + \frac{\omega_{pi}^2}{\Omega_i^2} = \frac{c^2}{v_A^2}. \tag{3.43}$$

In the following, we will analyze the results of the general dispersion relation in the context of particular waves.

3.4.1 The Shear Alfvén Wave

The shear Alfvén wave is among the most intensely studied oscillations in plasma physics [106]. Its special prominence owes partly to the fact that it is the first transverse wave identified for a magnetized plasma, illustrating a clearly distinct behavior from neutral gases, which support only longitudinal (sound) waves. But it is also ubiquitous in real plasmas, both in the astrophysical and laboratory settings, as well as in theoretical descriptions. Ideal MHD theory describes a single shear Alfvén wave [70]. The mode also appears as the "slow" wave when modeling a cold, homogeneous plasma as a dielectric medium [76, Chap. 2]. And in the drift-ordered plasma model, there are two shear Alfvén waves – the kinetic Alfvén waves [65, Chap. 4] – which display behavior not accounted for in the ideal MHD or cold plasma dielectric descriptions, including a coupling between pressure disturbances and the wave[16].

Conceptually, the shear Alfvén wave conjures the analogy of a vibration on a guitar string. The magnetic field provides the "tension" in the string, while the plasma, which is tied to the field line, provides the mass. The perturbed component of $\mathbf{B}$ is perpendicular to the background field. The wave can have any $k_\perp$ to complement its (nonzero) $k_\parallel$; however, the group velocity is always aligned with the background

[16]See also Section D.2 in the appendix for an investigation of the shear Alfvén waves in the drift-ordered system.

magnetic field.

The shear Alfvén wave arises from Eq. 3.42 when the root is approximated using $|n_\perp^2/P| \ll 1$. When $P \approx -\omega_{pe}^2/\omega^2$, $|n_\perp^2/P| = c^2k_\perp^2/\omega_{pe}^2 \sim 10^{-2} \ll 1$, and so the approximation is reasonable. In this case, Eq. 3.42 reduces to $n_\parallel^2 = S$, or

$$\omega^2 = \frac{c^2k_\parallel^2}{1+\frac{\omega_{pi}^2}{\Omega_i^2}} = k_\parallel^2 v_A^2, \tag{3.44}$$

where

$$v_A = \frac{c}{\sqrt{1+\frac{\omega_{pi}^2}{\Omega_i^2}}} = \frac{1}{\sqrt{\mu_0\epsilon_0}\sqrt{1+\frac{n_iM_i}{\epsilon_0B^2}}} \approx \frac{B}{\sqrt{\mu_0 n_i M_i}} = \frac{B}{\sqrt{\mu_0\rho}} \tag{3.45}$$

is the Alfvén speed, approximately $3.5\times10^6\,\mathrm{m/s} \sim \frac{c}{100}$ near the LCFS in these experiments. When the parallel wave number is estimated using the connection length as $k_\parallel \approx \pi/L_c \approx 0.35\ \mathrm{m}^{-1}$, the Alfvén wave dispersion relation gives $\omega \approx 2\pi\cdot 200$ kHz.

The most noteworthy result of this dispersion relation is that the frequency depends only on $k_\parallel$, and is completely independent of the perpendicular wave number. This is exactly the opposite situation from the drift wave. An additional implication of this is that the group velocity, $\mathbf{v}_g = \frac{\partial\omega}{\partial\mathbf{k}}$, is also parallel to the background field lines, as mentioned earlier: the wave energy is guided by the background magnetic field.

The compressional Alfvén wave is the branch with root, $\omega^2 = k^2v_A^2$, since $n = \frac{ck}{\omega}$. This is the "fast" wave. With $k^2 = k_\perp^2 + k_\parallel^2 \approx k_\perp^2$, this dispersion relation gives $|\omega| = kv_A \approx k_\perp v_A \approx 80$ MHz, well above the antenna frequency range.

The Alfvén wave is damped by resistivity, in contrast to the drift wave, which is destabilized by it. The most straightforward way to arrive at this result is to consider only parallel resistivity; the perpendicular resistivity will enter in the diagonal elements of $\bar{\bar{\epsilon}}$ as $\frac{\omega}{\Omega_i\Omega_e\tau_{ei}} \ll 1$, while the parallel resistivity enters as a modification to P as $\sim 0.51/(\omega\tau_{ei}) \sim 10$. Physically, this approach is reasonable since the parallel current is expected to be much larger than the perpendicular current, which is dominated in this case by the ion polarization contribution, and so resistivity should appear more prominently in the susceptibility component linking the parallel electric

field and current.

To derive a damping rate, start again from[17] Eq. 3.42,

$$n_\perp^2 = P\left(1 - \frac{n_\parallel^2}{S}\right). \tag{3.46}$$

Include the parallel resistivity through the term, $P \approx -\frac{\omega_{pe}^2}{\omega^2}\frac{1}{1+i\frac{1}{\omega\tau'_{ei}}} \approx i\frac{\omega_{pe}^2\tau'_{ei}}{\omega}$, with $\tau'_{ei} \equiv \tau_{ei}/0.51$. Assume also that the damping is small such that $\Im\{\omega\} = \omega_i \ll \Re\{\omega\} = \omega_r$, and that $\omega_r = k_\parallel v_A$ clears the term, $1 + \frac{\omega_{pi}^2}{\Omega_i^2} - n_\parallel^2$, and note that $S \approx 1 + \frac{\omega_{pi}^2}{\Omega_i^2} = c^2/v_A^2$. Then

$$\frac{n_\perp^2}{P} = -\frac{n_\perp^2}{\frac{\omega_{pe}^2}{\omega^2}\frac{1}{1+i\frac{1}{\omega\tau'_{ei}}}} \approx \left(1 - \frac{k_\parallel^2 v_A^2}{\omega^2}\right) \approx \omega^2\left(\omega_r^2 + 2i\omega_r\omega_i - \omega_i^2 - k_\parallel^2\omega^2\right) \approx \omega^2\left(2i\omega_r\omega_i\right) \tag{3.47}$$

or

$$-\frac{n_\perp^2}{\omega_{pe}^2\frac{1}{1+i\frac{1}{\omega\tau'_{ei}}}} \approx -i\frac{n_\perp^2}{\omega_{pe}^2\omega\tau'_{ei}} \approx 2i\omega_r\omega_i \tag{3.48}$$

so

$$\begin{aligned} &-\frac{\omega_{pe}^2}{\omega^2}\frac{1}{\left(1+i\frac{1}{\omega\tau'_{ei}}\right)}\left(2i\frac{\omega_i\omega_r}{v_A^2}\right) \approx -2\omega_i\frac{\omega_{pe}^2\tau'_{ei}}{v_A^2} \approx k_\perp^2\frac{c^2}{v_A^2} \\ &\Rightarrow \omega_i = -\gamma \approx -k_\perp^2\frac{c^2}{2\tau'_{ei}\omega_{pe}^2} = -\frac{\eta_s k_\perp^2}{2\mu_0}, \end{aligned} \tag{3.49}$$

where γ is the damping rate. Using typical parameters from experiment, the damping rate is approximated as $|\gamma/\omega_r| \sim 3\%$.

It is interesting that, when $k_\parallel$ is assumed to follow the shear Alfvén wave dispersion relation (Eq. 3.44) while ω still satisfies the drift-wave dispersion relation (Eq. 3.15), $k_\parallel = \omega_*/v_A$, then the drift-wave growth rate in Eq. 3.20 is simply twice the

[17] *cf.* [106, Eq. 1.17], $\omega^2 - \left(v_A^2 + \frac{i\omega\eta}{\mu_0}\right)k^2 = 0$, which applies to compressional Alfvén waves, and yields the same damping rate as for the shear Alfvén waves when $k_\perp \gg k_\parallel$. The damping rate for the kinetic shear Alfvén wave reported by Scott [65, p. 4.13] is $0.51\mu\Delta_\perp^{-2}/(\beta_e\tau_{ei}) = \eta_s/(\mu_0\Delta_\perp^2\rho_s^2)$, in the ρ_s-normalized perpendicular length scale, $\Delta_\perp$, which is identical to the damping rate given here when $\Delta_\perp^2\rho_s^2 = 2/k_\perp^2 \Rightarrow \Delta_\perp = \frac{\sqrt{2}}{k_\perp\rho_s} = \frac{\lambda_\perp}{\sqrt{2}\pi\rho_s}$

damping rate of the shear Alfvén wave (for which there are two roots) in Eq. 3.49. We will see in Section D.2 that the same Alfvén dispersion relation arises from the drift-ordered model for the real part of ω, but the damping rate is modified by the multiplicative factor, $\frac{1}{1\mp\omega_*/\omega_A}$, introducing a singularity at $\omega_* = \omega_A$ for one root. For the homogeneous plasma studied in this section, however, $\omega_* \propto \nabla p_e = 0$.

These results apply to a homogeneous plasma of infinite extent. Within the tokamak context, the spatial dependence on v_A through variation in B and ρ has a profound impact on the Alfvén spectrum, producing a continuum of modes that is strongly damped due to phase mixing, with decay $\propto \frac{1}{t}$ [106, 107]. Gaps in the Alfvén wave continuum develop, for example, by the coupling between different eigenmodes that results from the toroidal tokamak geometry. Discrete modes like the toroidicity-induced Alfvén eigenmode, or TAE, appear in the continuum gaps [107, 108]. Such gap modes suffer reduced continuum damping, and can be destabilized by energetic particles [108] – a point of concern for burning plasma devices, and the impetus for much active MHD research on this topic. A variety of mechanisms contribute to the damping of the Alfvén gap modes, including collisional (*e.g.* through collisions of trapped electrons), collisionless (*e.g.* through ion and electron Landau damping), and continuum coupling (albeit reduced) processes [92, Sec. 2.2.7].

In light of this complexity, we should not expect the damping rate expression in Eq. 3.49 to be useful for quantitative comparison with experiment. Rather, its utility is in demonstrating how resistivity affects the Alfvén wave, and in providing a point of comparison with the other simplified models of plasma waves discussed in this section.

In both the cold-plasma dielectric and ideal MHD formulations of the shear Alfvén wave in a homogeneous plasma, no pressure response accompanies the disturbance in field quantities, and vice versa. The coupling between $\tilde{p}_e$ and the shear Alfvén wave is recovered in the two-fluid drift-wave-ordered model, and when $k_\perp \rho_s \ll 1$, a similar Boltzmann (adiabatic) relation between potential and pressure, $e\tilde{\Phi}/T_e \sim \tilde{p}_e/p_e$, is expected as for drift waves [65, Sec. 4.5].

3.4.2 Electrostatic Modes

Many treatments of waves in plasmas ignore the displacement current in Ampère's law, $\nabla \times \mathbf{B} = \mathbf{J} + \frac{\partial \mathbf{D}}{\partial t} \approx \mathbf{J}$. When the induced electric field in Faraday's law is also ignored ($\nabla \times \mathbf{E} = -\frac{\partial(\nabla \times \mathbf{A})}{\partial t} = -\frac{\partial \mathbf{B}}{\partial t} = 0$), then $\mathbf{E} = -\nabla\Phi$. This is called the electrostatic approximation; it is justified for short wavelength modes for which the longitudinal component of $\mathbf{E}$ is much larger than the transverse component, $|\mathbf{E} \cdot \mathbf{k}/k| \gg |\mathbf{k} \times (\mathbf{k} \times \mathbf{E})/k^2|$. Section C.2 in the appendix applies a check on the applicability of the approximation, finding that it is robustly valid for the cold, homogeneous plasmas studied in this section.

The electrostatic approximation greatly simplifies the analysis of waves in plasmas, while still accessing a broad class of wave phenomena. Indeed, the drift wave dispersion relation – both as Eq. 3.15 and Eq. 3.18 – is most often derived taking $\mathbf{E} = -\nabla\Phi$. The focus of this section, however, is on only those modes permitted by the uniform and stationary electrostatic plasma medium, which excludes the drift wave.

The electrostatic dispersion relation under these conditions is contained within Eq. 3.42, which can be expressed as

$$\frac{n_\perp^2}{P} = 1 - \frac{n_\parallel^2}{S} = 1 - \frac{\omega_A^2}{\omega^2}. \tag{3.50}$$

For frequencies low relative to that of the shear Alfvén wave, $\omega_A^2/\omega^2 \gg 1$, the unity term may be neglected, yielding

$$n_\perp^2 S + n_\parallel^2 P = 0, \tag{3.51}$$

which is the desired electrostatic dispersion relation.

This result may also be derived directly from Gauss' law for the electric field,

$$\nabla \cdot \bar{\bar{\epsilon}} \cdot \mathbf{E} + \bar{\bar{\epsilon}} \cdot \nabla\mathbf{E} = \partial_i \left(\epsilon_j^i E^j\right) = (\partial_i \epsilon_j^i) E^j + \epsilon_j^i \partial_i E^j = 0, \tag{3.52}$$

where the middle expressions are in component form.

Fourier analyzing in space, $\partial_i \to ik_i$, and taking $E^j = -ik^j\Phi$,

$$(\partial_i \epsilon^i_j) E^j + \epsilon^i_j k_i k^j \Phi = 0. \tag{3.53}$$

When $\bar{\bar{\epsilon}}$ is homogeneous in space[18], then, making use of the cold plasma dielectric tensor in Eq. 3.38,

$$\begin{aligned} \mathbf{k}\cdot\bar{\bar{\epsilon}}\cdot\mathbf{k} = \epsilon^i_j k_i k^j &= \mathbf{k}\cdot\left[\hat{x}\left(Sk_x + iDk_y\right) + \hat{y}\left(-iDk_x + Sk_y\right) + \hat{z}Pk_z\right] \\ &= S\left(k_x^2 + k_y^2\right) + Pk_z^2 = Sk_\perp^2 + Pk_\parallel^2 = 0, \end{aligned} \tag{3.54}$$

which is the same as Eq. 3.51 after scaling by c^2/ω^2.

Now, $S = 1 - \sum_s \frac{\omega_{ps}^2}{\omega^2 - \Omega_s^2} \approx 1 + \frac{\omega_{pi}^2}{\Omega_i^2}$ and $P = 1 - \sum_s \frac{\omega_{ps}^2}{\omega^2} \approx -\frac{\omega_{pe}^2}{\omega^2}$, where the approximations are made in the low-frequency limit, $\omega \ll \Omega_i \ll \omega_{pi} \ll \Omega_e < \omega_{pe}$. In this case[19], the requirement, $Sk_\perp^2 = -Pk_\parallel^2$ becomes

$$\begin{aligned} & k_\perp^2\left(1 + \frac{\omega_{pi}^2}{\Omega_i^2}\right) = k_\parallel^2 \frac{\omega_{pe}^2}{\omega^2} \\ \Rightarrow\ & \omega^2 = \frac{k_\parallel^2}{k_\perp^2}\frac{\omega_{pe}^2}{1 + \frac{\omega_{pi}^2}{\Omega_i^2}} \approx \Omega_i^2 \frac{\omega_{pe}^2}{\omega_{pi}^2}\frac{k_\parallel^2}{k_\perp^2} \\ \Rightarrow\ & \boxed{\omega = \pm\sqrt{\Omega_i \Omega_e}\frac{k_\parallel}{k_\perp}}, \end{aligned} \tag{3.55}$$

revealing a hybrid electrostatic mode. For typical plasma parameters, and with $k_\perp \approx 150$ m^{-1} and $k_\parallel \approx 0.35$ m^{-1} (corresponding to $\lambda_\parallel \approx 2L_c$), $|\omega| \approx 2\pi \cdot 2.4$ MHz.

On the other hand, we have already seen that collisions cannot be ignored in the relatively-cold edge plasmas of interest here. This effect may be explored in the same

[18] which is certainly not true in the edge plasma, where strong gradients are expected; relaxing this assumption leads to drift waves, among other phenomena

[19] Using typical outer edge parameters for the discharges in the Shoelace experiments, $n_e \sim 10^{20}$ m^{-3} and $B = 2.3$ T (with deuterium as the main ion species), $\Omega_i = \frac{eB}{M_i} \sim 2\pi \cdot 20$ MHz, $\omega_{pi} = \sqrt{\frac{n_e e^2}{\epsilon_0 M_i}} \sim 2\pi \cdot 1.5$ GHz, $\Omega_e = \frac{eB}{m_e} \sim 2\pi \cdot 60$ GHz, and $\omega_{pe} = \sqrt{\frac{n_e e^2}{\epsilon_0 m_e}} \sim 2\pi \cdot 90$ GHz.

manner as for the shear Alfvén wave[20] by considering parallel electron-ion collisions through

$$P \equiv 1 - \sum_s \frac{\omega_{ps}^2}{\omega^2} \approx -\frac{\omega_{pe}^2}{\omega^2} \rightarrow -\frac{\omega_{pe}^2}{\omega^2}\frac{1}{1+i\frac{\nu'_{ei}}{\omega}} \approx i\frac{\omega_{pe}^2}{\nu'_{ei}\omega}, \tag{3.56}$$

since

$$\frac{\nu'_{ei}}{\omega} = \frac{1}{\omega\tau'_{ei}} \sim 10 \tag{3.57}$$

when $\omega \sim 2\pi \cdot 100$ kHz and τ'_{ei} is estimated from parameters measured at the LCFS in these experiments. Then Eq. 3.54 becomes

$$\omega\left(1 - i\frac{\omega}{\nu'_{ei}}\right) = \omega_0 \equiv -i\frac{\omega_{pe}^2}{\nu'_{ei}}\frac{\omega_A^2}{c^2k_\perp^2} = -i\frac{k_\parallel^2}{k_\perp^2}\frac{\Omega_i\Omega_e}{\nu'_{ei}}, \tag{3.58}$$

the roots of which are given by

$$\omega = \frac{\nu'_{ei}}{2}\left(-i \pm \sqrt{4i\frac{\omega_0}{\nu'_{ei}} - 1}\right), \tag{3.59}$$

noting that for these electrostatic modes, $|\omega| \sim \nu'_{ei} \approx 5\times10^6$, while $\omega_0 \approx -i5\times10^7$ s^{-1}. These roots correspond to strongly-damped modes[21], with the damping rate on the order of or larger than the real part of the frequency.

This somewhat heuristic treatment of electron-ion collisions is complemented by an investigation of finite, non-zero temperature effects after assuming Maxwellian distribution functions for ions and electrons. Such an analysis introduces important corrections to the electrostatic dispersion relation, Eq. 3.55 [109]. Figure 3-4 illustrates this point – here, one of four roots of the low-frequency, warm plasma, electrostatic dispersion relation are plotted for a mode oscillating at 170 kHz for five different electron temperatures between 0 and 100 eV (the dispersion relation is such that the full plot is symmetric about the $k_\parallel$ axis). The darkest blue line in the figure, with $T_e = 0.05$ eV, overlays the cold plasma result of Eq. 3.55, which is shown as a

[20] In general, this corresponds to using an effective electron mass, $m_{e,eff} \leftarrow m_e\left(1 + i\frac{1}{\omega\tau'_{ei}}\right)$.

[21] These are sometimes called "quasimodes."

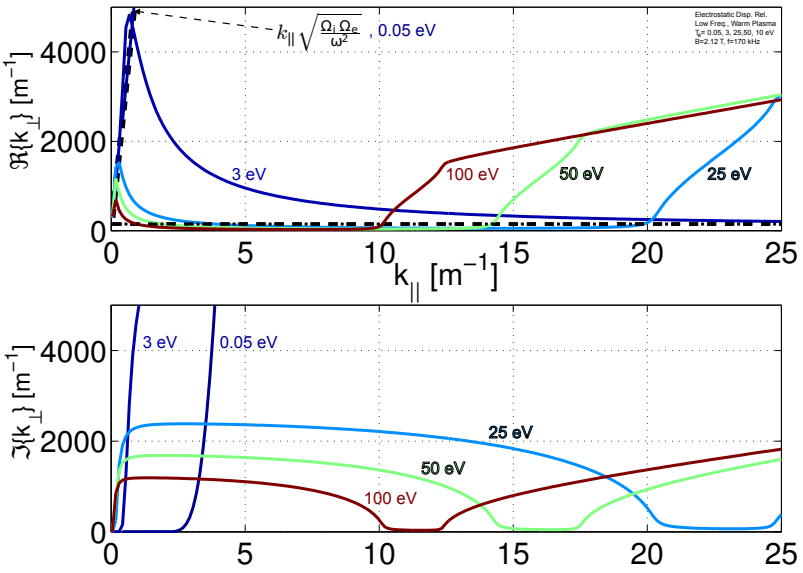

Figure 3-4: Relation between $k_\parallel$ and $k_\perp$ for one of the roots of the low-frequency electrostatic dispersion relation at $f = 170$ kHz for a warm, uniform, stationary Maxwellian plasma, as in Eqs. 1-5 of [109], where collisions are neglected; color of each line maps to the electron temperature. The Shoelace antenna perpendicular wave number is shown as a black dash-dotted line. The dispersion relation is symmetric reflected about the $k_\parallel$ axis.

thick dashed line. But at higher temperatures, a cutoff in $k_\parallel$ appears below which the electrostatic mode cannot propagate; with the electron temperature at the LCFS of $T_e \sim 50$ eV, the Shoelace antenna experiments reflect this situation. Not shown are the additional modes permitted by the warm plasma dispersion relation; these are at $|k_\perp| > 1000$ m^{-1}. For reference, the perpendicular wavenumber of the Shoelace antenna is shown as a horizontal dash-dotted line.

Resonance Cones

The group velocity for the electrostatic waves of Eq. 3.55 is

$$\mathbf{v}_g = \frac{\partial \omega}{\partial \mathbf{k}} = \pm \frac{\sqrt{\Omega_i \Omega_e}}{k_\perp} \left(\mathbf{e}_\parallel - \mathbf{e}_\perp \frac{k_\parallel}{k_\perp} \right). \tag{3.60}$$

where $\mathbf{e}_\parallel$ and $\mathbf{e}_\perp$ are the parallel and perpendicular basis vectors. Forming the dot product between $\mathbf{v}_g$ and $\mathbf{k}$ yields the interesting result,

$$\mathbf{v}_g \cdot \mathbf{k} = \pm \frac{\sqrt{\Omega_i \Omega_e}}{k_\perp} \left(\mathbf{e}_\parallel - \mathbf{e}_\perp \frac{k_\parallel}{k_\perp} \right) \cdot \left(\mathbf{e}_\parallel k_\parallel + \mathbf{e}_\perp k_\perp \right) = \pm \frac{\sqrt{\Omega_i \Omega_e}}{k_\perp} \left(k_\parallel - k_\parallel \right) = 0, \quad (3.61)$$

indicating that the group velocity is orthogonal to the direction of propagation. Moreover, Eq. 3.60 defines a cone of vectors which is coaxial with the background magnetic field, at an angle from the field line, $\tan(\theta) = k_\parallel / k_\perp$. This is an example of resonance cone behavior, which is associated with, but not exclusive to, electrostatic waves [110, 111, 112, 109, 113, 76].

The group velocity of shear Alfvén waves is also parallel to the background field, but this behavior does not represent a limit of the resonance cone, since $\mathbf{v}_g \cdot \mathbf{k} \neq 0$ for shear Alfvén waves.

3.5 Doppler Shift

It is important to note that the dispersion relations written above – Eqs. 3.15, 3.35, 3.44, and 3.55 – were derived in the plasma (co-rotating) frame. The frequency measured in the laboratory frame deviates from that in the plasma frame by the Doppler shift. If $\omega_{\ell f}$ is the laboratory-frame frequency and ω_{pf} the plasma-frame frequency (which applies to the dispersion relations derived above), then

$$\omega_{pf} = \omega_{\ell f} - \mathbf{k} \cdot \mathbf{u}, \quad (3.62)$$

where $\mathbf{u}$ is the velocity of the background plasma.

As an example, in the case of Alfvén waves, with the plasma moving at the $\mathbf{E} \times \mathbf{B}$ velocity, $\mathbf{u} = \mathbf{v}_E$, $(\omega_{\ell f} - \mathbf{k} \cdot \mathbf{v}_E)^2 = \omega_A^2 = k_\parallel^2 v_A^2$.

The Doppler shift is important in the context of experiments with the Shoelace antenna since $k_\perp$ is large and v_E is not only large, but rapidly varying with radial location, as discussed in Section 2.3. For example, at the LCFS, $v_E = 3$ km/s in the IDD; with $k_\perp = 150$ m^{-1} in the EDD, this results in a frequency shift of $\Delta\omega \approx -2\pi \cdot 70$ kHz from the plasma-frame value to that measured in the laboratory

frame – the Doppler shift is on the order of the QCM frequency, itself. 3 mm inside the LCFS, $v_E \approx 3$ km/s in the EDD, so that the corresponding frequency shift is $\Delta\omega \approx +2\pi \cdot 70$ kHz. If the frequency measured in the laboratory frame is 70 kHz, this means that the plasma-frame frequency resides somewhere between 0 and 140 kHz, depending upon the radial location of the mode. This spans the range of frequencies expected of ballooning modes, drift waves, and damped shear Alfvén waves, using the simplified models presented in this chapter.

Chapter 4

Experimental Method

> We should forget about small efficiencies, say about 97% of the time: premature optimization is the root of all evil.
>
> –Donald Knuth [114]

4.1 Introduction

This chapter seeks to describe the hardware employed in this study, as well as the methods of data collection and analysis. The design, construction, and operation of the antenna and its associated power system are discussed in detail, and the experimental procedure is motivated; readers may also refer to [115] for a description of the power system, and [116] for an outline of the experimental design. Signal processing techniques for the purposes of discovering the effect of the antenna are also introduced. Additional information on these topics appears in Appendices B and E.

4.2 Antenna Design

The basic constraints of the antenna design problem are to build a structure which produces a magnetic field perturbation mimicking that of the intrinsic quasi coherent mode, and which can survive the harsh conditions inside the tokamak vacuum vessel. A more precise statement of "mimicking" requires that the antenna match the QCM's

spatial structure and frequency. The first of these two statements is perhaps the defining feature of the Shoelace design. It is enormously restrictive, not only with regard to which spatial structures are allowed for the antenna, but also how robust the structure needs to be, and how much RF current must be driven to achieve a noticeable perturbation in the plasma. The second statement on frequency pertains to the RF power system, and will be covered in detail in Section 4.4.

The spatial structure of the QCM has been discussed in Chapter 2; to review, it is an approximately field-aligned ($k_\perp \gg k_\parallel$) mode with a relatively large perpendicular wave number, $k_\perp \sim 1.5$ cm^{-1} ($\lambda_\perp \sim 4.2$ cm), at the midplane, and localized to the low-field (bad-curvature) side.

To provide wave number matching, the antenna must either exhibit a self-similar structure, able to couple to a broad band in $\mathbf{k}$, or reproduce the same spatial periodicity as the mode. The latter of these two approaches is preferred here, since it is desired to couple to a single wave number (that of the QCM) rather than many.

The fact that $k_\perp$ is large deserves special attention, because it means that the spatial decay of the mode across the semi-vacuum scrape-off-layer (SOL) is rapid. To see this, it suffices to examine the constraints on the wave vector for a magnetostatic field perturbation in a charge-free region. In a uniform Cartesian geometry selected such that the wave vector has only $\hat{\mathbf{y}}$ (the slab proxy for the poloidal coordinate) and $\hat{\mathbf{x}}$ (corresponding to radial) components, Gauss' law gives

$$\nabla \cdot \mathbf{B} = 0 \rightarrow i\left(k_x B_x + k_y B_y\right) = 0, \tag{4.1}$$

and Ampère's law,

$$\begin{aligned} \nabla \times \mathbf{B} = 0 = \hat{\mathbf{x}}\left(\partial_y B_z - \partial_z B_y\right) - \hat{\mathbf{y}}\left(\partial_x B_z - \partial_z B_x\right) + \hat{\mathbf{z}}\left(\partial_x B_y - \partial_y B_x\right) \\ \rightarrow i\left[\hat{\mathbf{x}} k_y B_z - \hat{\mathbf{y}} k_x B_z + \hat{\mathbf{z}}\left(k_x B_y - k_y B_x\right)\right] = 0, \end{aligned} \tag{4.2}$$

for the plane wave solution, resulting in the constraints that $B_z = 0$, $\frac{B_x}{B_y} = -\frac{k_y}{k_x}$, and $k_x B_y = k_y B_x = -B_y \frac{k_y^2}{k_x} \Rightarrow k_x^2 = -k_y^2$, or $k_x = \pm i k_y$. Rejecting the growing

solution, this means that the perturbed field decays in x as $\mathbf{B} = \mathbf{B}_0 e^{ik_y y} e^{-k_y x}$, giving an e-folding length of $1/k_\perp = \lambda_\perp/(2\pi) = 0.67$ cm, using the value of $k_\perp$ for the QCM. Since the antenna must share the same perpendicular wave number as the QCM if it is to provide a good match, this means that the antenna must sit extremely close to the plasma if it is to have any measurable effect. The proximity to the plasma exposes the structure to high heat loads, while the rapid radial decay of the vacuum field also requires that the power system maximize the current driven in the antenna to offset this significant attenuation as much as possible.

The Shoelace antenna concept uses a wire to reproduce the filamentary structure attributed to the QCM. The antenna is wound from a single length of 1.5 mm-diameter lanthanum-doped molybdenum wire. The winding is in two layers, with the wire criss-crossing its way up the ceramic tension wheels in 19 rungs, and then retracing its path again on the top layer so as to reinforce the current from the bottom layer. The wire path gives the impression of a shoelace, from which the antenna takes its name. The interlayer spacing is 4.6 mm, close to the distance between the top layer and the LCFS at the point of closest approach – this is significant given the ∼6.7 mm e-folding length of the field through the SOL.

Table 4.1 lists a number of the geometrical parameters defining the antenna.

Figure 4-1 shows an annotated photograph of the antenna mounted in the Alcator C-Mod vacuum vessel, together with a plot of the approximate vacuum field, last closed flux surface (LCFS) location, and nominal QCM $\tilde{B}_\theta$ amplitude. Underneath the photograph, in Figure 4-1d, a cartoon schematic illustrates how the current in both layers of the antenna reinforce each other's induced magnetic field.

The wires are field-aligned when the safety factor at the 95% flux surface, q_{95}, is 3, the same value used in the discharges of the earlier characterization of the QCM by Snipes *et al.* [33] This, combined with the wire spacing, can be used to estimate the antenna's bandwidth in $k_\perp$ and toroidal mode number, n, as shown in Section B.2 of the appendix. The results of this analysis are summarized in the

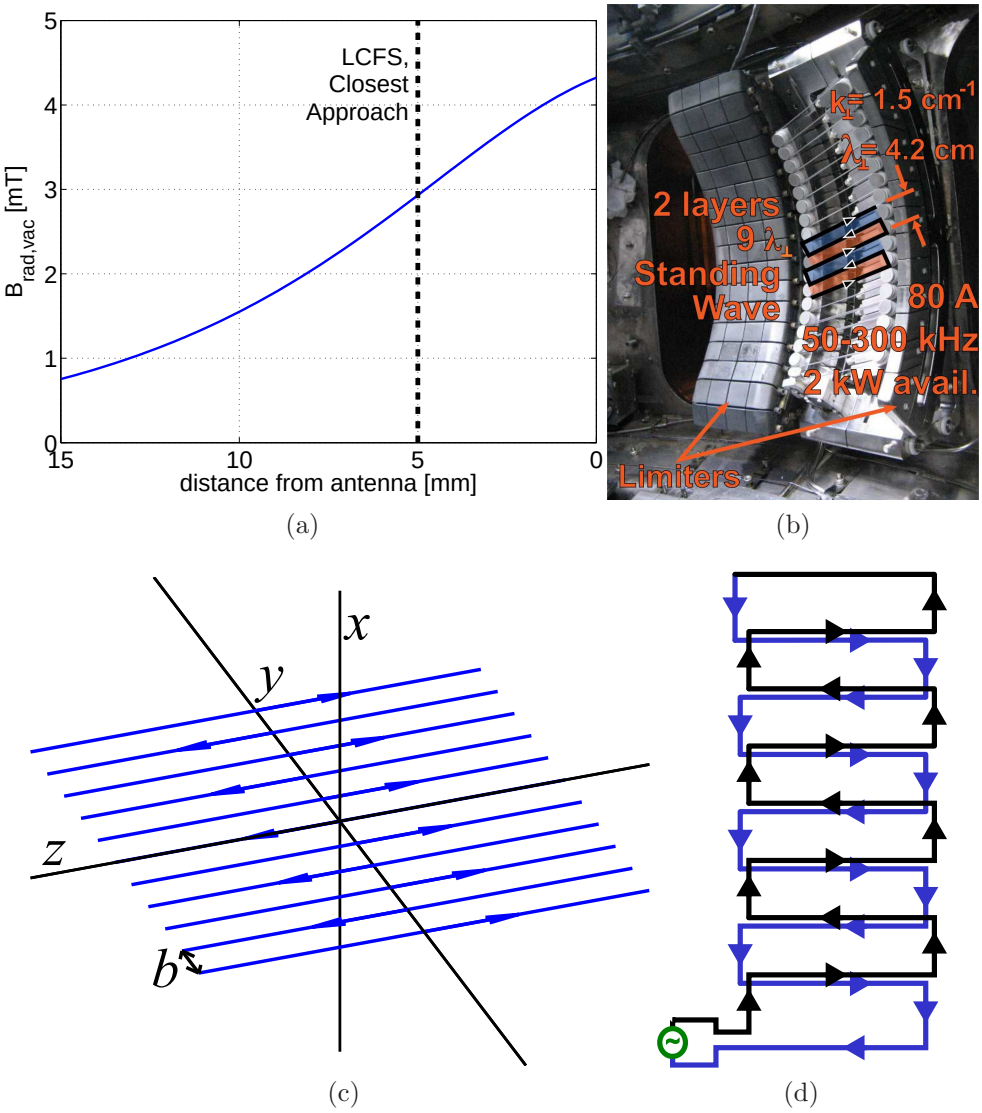

Figure 4-1: (a) Approximate radial vacuum field produced by the antenna; also shown are the LCFS at closest possible approach, as well as the nominal $\tilde{B}_\theta$ amplitude of the QCM. (b) Photograph of the Shoelace antenna mounted inside the Alcator C-Mod vacuum vessel. (c) Simplified schematic illustrating winding structure of Shoelace antenna; (d) Simplified planar geometry for modeling vacuum field of antenna.

Table 4.1: Shoelace Antenna Geometrical Parameters

Symbol	Value	Desc. [Units]
a	7.62×10^{-4} [m]	Radius of wire
A_c	1.82×10^{-6} [m^2]	Cross-sectional area of wire
b	0.0214 [m]	perpendicular spacing between rungs, $2b = \lambda_\perp$
d	4.6×10^{-3} [m]	distance between layers of windings [m]
h	0.41	Vertical height of antenna [m]
ℓ	$\sim$7	Total length of wire [m]
N_r	19	Number of rungs
N_c	18	Number of rectangular cells, or "turns"
V	1.29×10^{-5} [m^3]	Total volume of wire
w	0.153 [m]	length of horizontal wire segments
θ_p	14.5°	Pitch angle of windings; field aligned at $q_{95} \approx 3$
R_a	0.303 [m]	Radius of curvature of wire centers
$R_{a,0}, z_{a,0}$	0.613,0 [m]	Centroid of arc on which top-layer wire centers lie

following. The perpendicular spacing is $\Delta z_\perp = 2.1$ cm, giving $k_\perp = \pm 1.5 \pm 0.1$ cm^{-1}, with the spread corresponding to the full-width at half maximum (FWHM) of the $k_\perp$ spectrum calculated from the finite extent of the antenna in the perpendicular direction (e.g. (19 rungs-1)$\times\Delta z_\perp$). Since the antenna wires are angled at $\theta_w = 14.5°$, the Shoelace antenna's toroidal mode number, n, spectrum is centered on $n_0 = 2\pi R_0 / [2\Delta z_\perp / \tan(\theta_w)] \approx 35$, where $R_0 = 0.916$ m is the major radius of the top layer Shoelace rung at the midplane. The bandwidth of the n spectrum is limited by the width of the antenna, $w = 15.3$ cm; modeling the antenna as a tophat function in toroidal angle, ϕ, with an arc length of w gives a factor of sinc $\left(\frac{nw}{2R}\right)$ after a Fourier transform, or a span of $\Delta n \approx \pm 23$ from n_0 (FWHM). These values ensure a good match to the QCM, which typically has [33] $k_\perp = 1.5$ cm^{-1} and $n = 10 - 25$ (at higher safety factor), as well as to the WCM, which has a similar $k_\perp$ and n spectrum [5, 6]. It should be noted that the antenna has *no preferred direction*; it produces an RF vacuum field which is a standing wave in the (ϕ, θ) directions and decays rapidly in the radial dimension.

In a single poloidal cross section, the rungs of the antenna on the top layer fall on a circle centered at $R = 0.613$ m, $z = 0$ m, with a radius of 0.303 m. At closest approach, the rungs can be as little as 3 mm behind the main limiter. This proximity

is required to maximize the induced perturbation in the plasma given its rapid radial decay; however, it also risks damage to the antenna due to the large heat flux in the C-Mod edge. As seen in Figure 4-1, the antenna is sandwiched between and in the shadow of the main limiter as well as a smaller protection limiter. These provide a degree of shielding. Nonetheless, careful experimental planning, as well as a robust design of the Shoelace support structure, were needed to extend the longevity of the antenna in the harsh C-Mod edge environment.

By collapsing the winding in a single layer onto a plane, and extending the wire lengths such that they are of infinite extent, and assuming an infinite number of rungs, we arrive at the simplified geometry shown in Figure 4-1c. This is suitable for creating an analytical model of the perturbed vacuum field induced by the antenna. This analysis is carried out in Appendix B, and gives a radial field component (out of the plane of the antenna),

$$\boxed{B_x(\mathbf{r}) = -\frac{\mu_0 I_0}{2b}\frac{\sinh(k_\perp y)\cos(k_\perp x)}{\cosh^2(k_\perp y)-\cos^2(k_\perp x)} = -\frac{\mu_0 I_0}{2b}\frac{\sinh(k_\perp y)\cos(k_\perp x)}{\sinh^2(k_\perp y)+\sin^2(k_\perp x)}} \tag{4.3}$$

and a poloidal component (across the rungs of the antenna),

$$\boxed{B_y(\mathbf{r}) = \frac{\mu_0 I_0}{2b}\frac{\cosh(k_\perp y)\sin(k_\perp x)}{\cosh^2(k_\perp y)-\cos^2(k_\perp x)} = \frac{\mu_0 I_0}{2b}\frac{\cosh(k_\perp y)\sin(k_\perp x)}{\sinh^2(k_\perp y)+\sin^2(k_\perp x)}}. \tag{4.4}$$

where $k_\perp \equiv \frac{2\pi}{2b}$, I_0 is the current in the wire segment, and, of course, $B_z = 0$.

Figure 4-1a plots the total radial field, Eq. 4.3, summed from the upper and lower windings, and evaluated at a poloidal location in between two wire segments, as a function of distance from the top winding layer. A current of 80 A in each layer is assumed; such amplitudes were regularly achieved during antenna operation. The approximate location of the LCFS at closest approach is also shown.

Power is conducted to the antenna via a semi-rigid, vacuum-compatible coaxial cable with SiO_2 dielectric[1]. It is coupled to the external power source through a vac-

[1] 0.270-in (6.86 mm) outer diameter, maximum withstanding voltage V_{rms}=3.3 kV (Times Microwave)

uum feedthrough with a Threaded Neill-Concelman (TNC) connector. The antenna connects to the power system through a TNC connector with 3.0 kV breakdown rating (Times Microwave). A short ML alloy lead on this connector is joined electrically to the main antenna winding via a copper clamp housed in an alumina block. The winding runs up the antenna, and then back down, terminating at a clamp which grounds the wire to the antenna, and through the antenna, to the tokamak vacuum vessel.

A thermal analysis is carried out in Section B.5 in the appendix. This and more sophisticated analyses had indicated the antenna would survive the harsh environment inside Alcator C-Mod. This was largely true, but eventually, the antenna wire did fail due to excessive thermal loading, as discussed below in Section 4.3.

4.2.1 Antenna Pitch

The antenna pitch angle of 14.5° was chosen to match the field line pitch from an ohmic EDA H-mode plasma used in Snipes' earlier study of the QCM [33]. That the EDA H-mode used in Shoelace antenna experiments should be ohmic (meaning that only resistive heating is supplied to the plasma, and no auxiliary heating power is used) again is a result of the need to reduce the gap between plasma and antenna as much as possible, which requires the plasma to have lower heat exhaust in order to avoid damaging the antenna. As ohmic EDA H-modes are not routinely run on Alcator C-Mod, it was decided to design the antenna to match the field line pitch in the ohmic EDA experiments by Snipes *et al.*, for which the plasma was well-diagnosed, in order to maximize the chance of successfully reproducing such a confinement regime. This topic will be discussed in greater detail in the Experimental Design section, Section 4.5.3.

The effect of a mismatch between the antenna winding and the background magnetic field lines is investigated heuristically in Section B.4 of the appendix. This analysis results in an expectation that the antenna is unlikely to effectively couple to a QCM-like mode in the plasma beyond $q_{95} > 5$, while good coupling is expected in the lower range between $2 < q_{95} < 4$. Most C-Mod plasmas are run with $q_{95} \sim 5$,

which restricted the first round of experiments exploring the antenna's influence on the plasma to specialized discharges. However, future experiments with the Shoelace antenna will utilize a different pitch angle, as described in Chapter 6, which will increase the number of opportunities to make use of the structure.

4.2.2 Spring-Loaded Pulley System for Tensioning Antenna Wire

An intricate system of pulleys and tensioner blocks accommodates the thermal expansion of the wire, an inevitability given the antenna's proximity to the plasma. Figure 4-2 shows the assembly of the static and movable winding posts. The pulleys were fabricated by Ceramics Grinding Company from 99.8%-pure alumina. These are capped by molybdenum shields, whose support stalks penetrate through the center of the pulleys. Further information on these material selections is provided below.

A pretension of 50 lbs (220 N) is maintained across each wire segment. This is so in order to keep the wire from becoming slack at any location, which would risk the wire bowing inward toward the plasma, or becoming dislodged from the groove of the pulley. The pretension is achieved by pushing the movable post – that shown in Figure 4-2b – outward, pulling the wire taught while simultaneously compressing a stack of Belleville washers. As the wire expands in response to heating from the plasma, the Belleville washers also expand and continue to provide loading. Based upon the material properties of the ML wire, the temperature at which all 50 lbs of preload are relaxed by thermal expansion[2] is well above the recrystallization temperature of the ML wire (approximately 1300°C [117]).

The thermal expansion of the wire, and corresponding need to maintain a preload, makes it difficult to wind in more than two layers. The reason is that the top-most layer of the winding, nearest the plasma, will receive a much greater heat load during

[2]This is calculated from $\Delta T = \frac{F_0}{wK_b\alpha_E}\left(1+\frac{K_b}{2K_0}\right) \approx \frac{F_0}{wK_b\alpha_E}$, where $K_b \sim 10^5$ N/m is the spring constant of the Belleville washer stack, and $K_0 = EA_c/w \sim 4\times10^6$ N/m is the spring constant of the ML wire. With a 220 N preload, the approximate expression gives a temperature excursion of ΔT =2300°C before the preload is entirely relaxed by thermal expansion, while the more precise expression gives $\Delta T = 2000$.

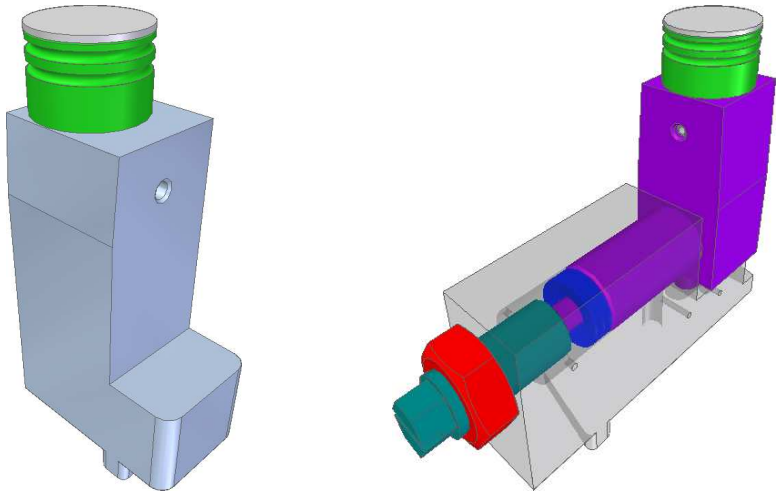

(a) (b)

Figure 4-2: CAD models of (a) fixed and (b) adjustable wire pulleys. Tensioning is accomplished by tightening the bolt on the adjustable pulley, pushing the pulley stand outward through a stack of Belleville washers, until $\sim$ 50 lbs ($\sim$ 220 N) of pretension has been applied. These and all other CAD drawings belonging to the Shoelace project were prepared by R. Leccacorvi.

the $\sim$1 s plasma flattop than will the windings underneath – much too short a time for the wire temperature to equilibrate. But the ML wire is also stiff – more like a bent paper clip than a rubber band – and the excess length cannot be spread uniformly throughout the structure. As a result, the top layer of winding will expand, but the bottom will not, preventing the adjustable posts from relaxing outward to maintain tension on the top layer. In the Shoelace design, however, with only two layers in the winding, each adjustable post maintains tension on *either* a pair of wire segments in the top or bottom layer, and so the two layers are adjusted independently.

More complicated designs decoupling the pretension in multiple layers may be imagined, but adding additional layers is of marginal benefit, since the added depth below the top layer means that the field contribution from these lower layers will be severely attenuated.

4.2.3 Material Selection

Table 4.2 provides a list of the materials used in the antenna construction. To limit the species of impurities in the plasma, it is standard practice on Alcator C-Mod that

all plasma-facing components be fabricated from molybdenum alloys, and this was followed here. The ML molybdenum alloy has good ductility and is suitable for wire drawing, motivating its selection for the antenna wire. Properties of the ML wire are listed in Table 4.3. The TZM molybdenum alloy, chosen for the pulley caps and Shoelace protection limiter tiles, is the material normally used for fabricating C-Mod limiters.

Alumina was selected for the pulley material due to its relatively high thermal conductivity, a requirement in order for the heat absorbed by the winding to be dissipated into the base structure (the pulley must, of course, be electrically insulating so as not to short out the winding). The pulley supports are fabricated from Inconel due to its high strength and stability under thermal loading; this material had also been planned originally for the Shoelace base structure, but examination of loading scenarios indicated that stainless steel would provide adequate strength, while being simpler to machine than Inconel.

The copper clamp connecting the wire to the TNC lead is sufficiently recessed from the plasma, and moreover insulated by an alumina shell, such that it is not at risk of damage from the plasma, but need only provide excellent electrical contact between the external power source and the antenna winding.

4.2.4 Construction

The Shoelace antenna components were machined at a number of external contractors. The Shoelace frame was cut from the stainless stock at Essex Engineering (Lynn, MA). BB&B Machine, Inc. (Wareham, MA) provided the molybdenum limiter tiles and wire termination block components (excluding the ceramic pieces), while Plus One Corporation (Peabody, MA) manufactured the supports and caps for the wire pulleys.

The alumina pulleys were machined by Ceramics Grinding Co., Inc. (Maynard, MA), as were inserts isolating the left and right halves of the base structure, and the

Table 4.2: List of Materials

Part	Material
Wire	ML (0.3% La by mass [117]) molybdenum alloy
Pulley	alumina, AL-998 (99.8%-pure Al_2O_3)
Shoelace limiter tiles	TZM (0.5% Ti, 0.08% Zr, 0.01-0.04% C by mass [117]) molybdenum alloy
Pulley Cap	TZM molybdenum alloy
Pulley Base	Inconel
Frame (housing)	304L stainless steel
Bolt, nut, washer hardware	304L stainless steel
Belleville washers	302L stainless steel
Plating material for some threaded surfaces	silver
Wire termination block	copper clamp, AL-998 insulator

Table 4.3: Material Properties of Molybdenum ML04 - See [117]

Property	Value	Desc.
E	320	Young's modulus (at 20 °C), [GPA]
σ	$1.79 \times 10^7 \approx \sigma_{Cu}/3.3$	Electrical conductivity [S/m]
ρ	1.038×10^4	Density [kg/m^3]
C_p	250.8	Specific heat capacity [J/(kg·K)]
k	138	Thermal Conductivity [W/(m·K)]
α	5.30×10^{-5}	Thermal diffusivity, $\alpha = k/(\rho C_p)$ [m^2/s]
α_E	5.2×10^{-6}	Coefficient of thermal expansion (at 20 °C), [m/(m K)]
T_R	1300°C	Recrystallization temperature

insulating shell around the copper termination block. This company also supplied the alumina for these parts.

The stainless steel stock was sourced from Alliant Metals (Hampstead, NH), while the Inconel was purchased from High Temp Metals (Sylmar, CA).

4.3 Antenna Damage

The Shoelace antenna was installed in August, 2011, and prior to the submission of this thesis, it completed two full C-Mod experimental campaigns. It survived the first without incident. However, the second campaign saw a number of high-performance discharges in the lead-up to an extended shutdown of Alcator C-Mod. In August of 2012, 34 days before the end of the second campaign, the antenna was severely damaged, with wire melting and breaking, as shown in Figure 4-3a. Incredibly, after this incident, the wire between the two layers reattached and melted together, effectively providing a current path for the lower half of the antenna. The antenna was operated in this state at normal current levels for all of the reverse-field discharges discussed in the next chapter. Eventually, even this self-patch failed, and a second fault developed, pictured in Figure 4-3b.

The fact that the antenna wire remained trapped on the device, rather than unwinding, is significant, and speaks to the efficacy of the winding posts' design to lock the windings from falling inward in this way. Were this not the case, operation on C-Mod would have been halted to allow for a manned access to remove the wire – a multi-week repair that would have canceled most of the run campaign subsequent to the antenna fault.

4.4 RF Power System

This section introduces the radio-frequency (RF) power system built to drive the antenna. The three original high-level design constraints of this system were as follows:

1. the antenna is characterized electrically as an inductor, $L \approx 6\ \mu$H, with a small

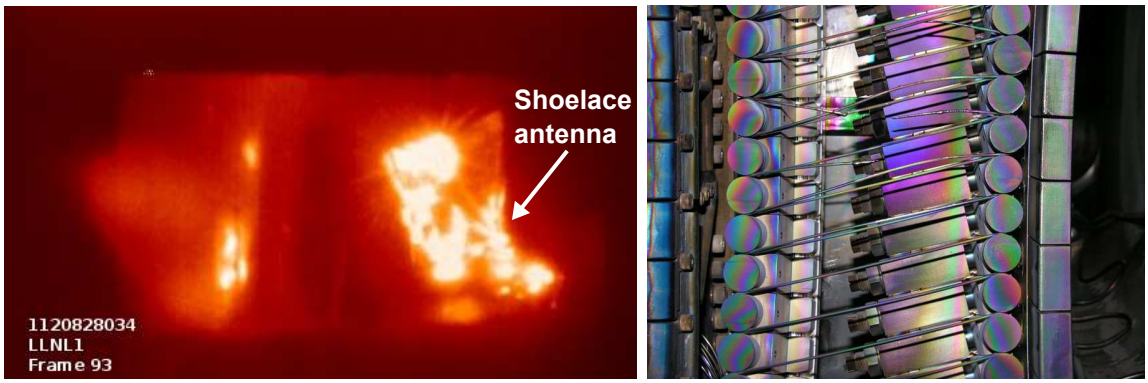

(a) (b)

Figure 4-3: (a) Image of antenna suffering a major fault, obtained from a 550.6 nm light imaging system [118]; the bright spot next to the antenna is the GH (main) limiter, which also experienced melt damage. (b) Close-up image of damaged antenna taken after the conclusion of the antenna's second campaign. The wire has melted through in two places near the midplane; the greater material removal on the upper fault suggests that it occurred first.

but variable resistance, $0.4 \lesssim R \lesssim 0.8\ \Omega$,

2. the power system must provide high and relatively constant current amplitude, $\gtrsim 60$ A across a wide ($50 < f < 300$ kHz) frequency range, and moreover be able to adjust the frequency rapidly (slew rate ~ 1 MHz/s or better) in real time, and

3. the RF power source should be provided by commercial 50-Ω amplifiers.

The design suggested by these constraints requires an agile matching network able to interface the commercial 50 Ω amplifiers to the inductive short presented by the antenna, and rapidly adjust in response to a variable frequency. This was, indeed, the approach followed for the Shoelace antenna, and it is described in detail below. In Sections 4.4.1, 4.4.2, and 4.4.4, the design and construction of the matching network, source, and phase lock systems are described in turn, while Section 4.4.3 gives an overview of the matching network calibration procedure. Finally, in Section 4.4.5, the overall performance is discussed. The reader is also referred to [115].

In general, the system met or exceeded design goals, and routinely provided $\gtrsim 80$ A of current in the lower-half of the frequency band, $50 < f < 150$ kHz, though current

availability tapered to 40 A at the 300 kHz level due to increased reflected power. The system also proved flexible, able to adapt to a major fault in the antenna which effectively halved its impedance, as described above. As this thesis is being prepared, the available power of the system is being expanded from 2 to $\geq$ 8 kW, nearing the upper threshold of allowed voltages and currents in the system. This upgrade is facilitated by the use of standard 50 Ω amplifiers which can essentially be swapped out in exchange for higher-power units.

4.4.1 Matching Network

Design

The low-frequency matching problem with inductive and resistive load is solved by the L-match configuration [119, Chap. 10]. This network makes use of two reactive elements, chosen to map the two components of an arbitrary complex load impedance to a particular source resistance. Collins *et al.* also employed an L-match network [82, 83] in their single-dipole antenna system, built for exciting shear Alfvén waves in a tokamak edge, though in that instance, the matching network had a low-Q and was broadband in the traditional sense (allowing all frequencies simultaneously through a wide passband), as opposed to the high-Q, narrow-but-rapidly-moveable passband approach pursued here. The low-loss requirement of the present context is necessary in order to maximize current throughput in the antenna, given the very rapid spatial decay of the antenna-driven vacuum field.

There are eight configurations of the L network, encompassing the combinations of the series leg being on the source- or load-sides of the parallel leg, and whether each leg is capacitive or inductive [119, Chap. 10]. Since the load presented by the antenna is mostly inductive, the L networks which provide a match over the largest frequency range are those with purely capacitive elements.

Figure 4-4 illustrates the L network implemented in the present work. This is combined with a two-input, single-output RF combiner built from two transformer cores, which completes the impedance match. In the discussion that follows, Z_{LI}

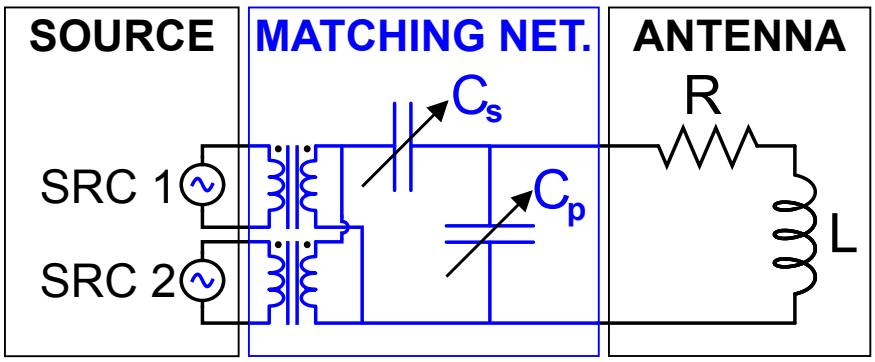

Figure 4-4: Schematic of antenna load, source power, and matching network interface used in this study. L and R are the antenna load inductance and resistance; C_s and C_p are the (discretely variable) series and parallel capacitors.

refers to the impedance looking in to the matching network at the source capacitor, on the load-side of the transformer/combiner. The desired values of the capacitors, C_s and C_p, are calculated from the constraint that Z_{LI} should match the transmission line characteristic impedance, Z_0, divided by the square of the effective transformer ratio, T, so that $\Re\{Z_{LI}\} = Z_0/T^2$ and $\Im\{Z_{LI}\} = 0$. Representing the load by $Z_L = R + jX$, with $X = \omega L$, and denoting the parallel combination of C_p and the load as $Z_1 = \left[j\omega C_p + (R+jX)^{-1}\right]^{-1}$, the matching constraints are

$$\begin{aligned}
\Re\{Z_{LI}\} = \frac{Z_0}{T^2} &= \Re\left\{\frac{1}{j\omega C_s} + Z_1\right\} = \Re\{Z_1\} \\
&= \frac{R}{(1-\omega X C_p)^2 + (\omega R C_p)^2} \\
&\Rightarrow C_p = \frac{X \pm \sqrt{(R^2+X^2)\frac{RT^2}{Z_0} - R^2}}{\omega\left(R^2+X^2\right)} \\
\Im\{Z_{LI}\} = 0 &= \Im\left\{\frac{1}{j\omega C_s} + Z_1\right\} \\
&\Rightarrow C_s = \frac{1}{\omega\Im\{Z_1\}} = \frac{(1-\omega X C_p)^2 + (\omega R C_p)^2}{\omega\left[X\left(1-\omega X C_p\right) - \omega R^2 C_p\right]} \\
&= \frac{C_p}{\frac{Z_0}{RT^2}\left(1-\omega X C_p\right) - 1}
\end{aligned} \tag{4.5}$$

In this application, the negative root for C_p is selected; otherwise, C_s must be replaced with an inductor.

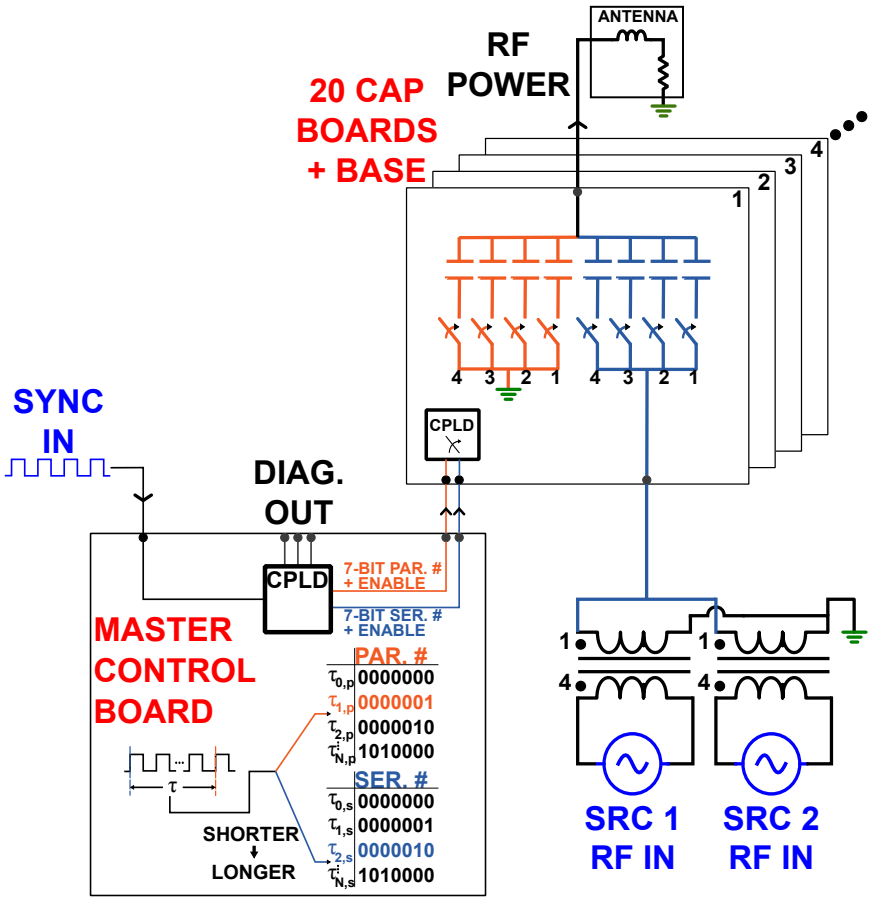

Figure 4-5: Matching network schematic showing capacitor switching boards, Master Control Board, and RF combiner.

An RF combiner accommodates multiple RF sources, as shown in Figures 4-4 and 4-5, and also further adjusts the look-in impedance of the L network to the line-matched value. Assuming the combiner consists of $M = 2$ identical transformers, each with individual winding ratio, $N_p/N_s = T_i = 4$, the effective winding ratio for the combiner is $T = \sqrt{M}T_i \approx 5.7$, such that the effective transformer ratio in Eq. 4.5 is $T^2 = MT_i^2 = 32$. A more precise matching condition may be further rendered by characterizing the transformers using a T equivalent network. Doing so, and neglecting the magnetizing and core losses, requires replacing Z_0 with $Z_0 - Z_{short}$, where Z_{short} is the short-circuit impedance presented by the transformer looking in from the high-voltage (source) side. The required function of the L-match network is then to map the antenna load impedance to $Z_{LI} = (Z_0 - Z_{short})/(MT_i^2)$.

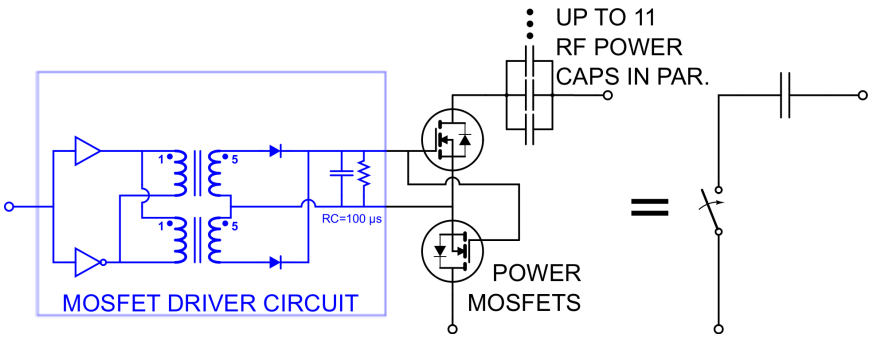

Figure 4-6: Schematic of capacitor with MOSFET switch. The input to the push-pull driver circuit is a 5 V, 500 kHz logic signal generated in a CPLD; the gate voltage to the MOSFETs is turned on and off via amplitude modulation of the logic signal, with modulation frequency typically not exceeding $\sim$ 12 kHz. The inverted square wave is actually produced directly by the CPLD, rather than by using an inverting buffer as shown in the figure.

Choosing Discrete Capacitor Levels

Because the power system must operate over a wide frequency range from 50-300 kHz, and the Q of the antenna is fairly high ($\omega L/R \sim 5-15$), the matching network capacitors must be variable, and set dynamically according to the RF frequency. To achieve this, a large number of discrete capacitor levels are arranged in parallel and switched into the network as needed to match the impedance at a particular frequency. In particular, 81 discrete capacitor levels for each of the series and parallel legs of the L network were chosen in the ranges, $3.3 \leq C_p \leq 694$ nF and $48.5 \leq C_s \leq 1385$ nF, according to a power law, with $C_{s,n+1} \approx 1.043 C_{s,n}$ and $C_{p,n+1} = 1.069 C_{p,n}$. This scheme provides current sharing between the discretized capacitors, so that no single capacitor channel carries more than $\sim 5\%$ of the total current running through the series or parallel pathway. This selection, in combination with the current limitation through the solid state switching, ultimately provides an upper bound on current that may be coupled to the antenna load; the design target for this bound was 200 A, based on heating considerations of the antenna winding.

An alternative distribution was considered which would have attempted to place the various resonant characteristics of each switching combination so as to minimize the reflection coefficient across the entire frequency band (see Figure 4-10). In prac-

tice, however, the antenna impedance is not static enough to merit such a high degree of optimization, and a more flexible capacitor distribution also allows more independent development of the matching network from other components in the system.

Implementation

The conceptual design described above is realized by the system outlined schematically in Figure 4-5. The completed system comprises 80 dynamically-switched, as well as one static "base load," discrete capacitance levels for each of the series and parallel matching legs. Solid state switching is used to add or subtract the appropriate capacitance to achieve a match. The static series and parallel capacitors are always in place. The capacitors are laid out on custom circuit boards; a photograph of one such board appears in Figure 4-7. The boards are 6U high (Eurocard dimension, 23.335 cm) and 22 cm deep. Each board provides four series and four parallel capacitors, as well as associated solid-state switching and control circuitry, so that a total of 20 boards provide all of the dynamically-switched capacitor channels. The static base load makes use of five additional boards, as described below.

Robust capacitors are needed to survive the high voltages (up to 1 kV) and currents (200 A maximum design target) produced within the power system. The components selected to meet these requirements were AVX Hi-Q, AVX High-Voltage (HV), and Kemet C-series multilayer ceramic (MLC) capacitors, all of which are ceramic, C0G (lowest thermal coefficient), low-equivalent-series-resistance capacitors. The inventory of capacitance values was 0.22, 0.39, 0.47, 0.68, 1.0, 4.7, and 8.2 nF; in all, 839 capacitors were used. Breakdown voltages ranged between 1 kV for the larger capacitance components and 3 kV for the smallest. All capacitors fit the surface mount 2225-case (0.22-in×0.25-in, 5763 metric) footprint.

Multiple capacitors are combined in parallel to produce the capacitance increment for a particular level. In the dynamic-switching boards, the capacitors were allotted in each discrete level according to the constraints that (a) no capacitor could account for more than 1/3 the total capacitance in the level while (b) no more than 11 capacitors were allowed in a level (leaving one spare solder pad in the channel), and (c) target

capacitance values were achieved to within half the smallest allowed capacitor for each level[3].

Each capacitor switch utilizes two ST Microelectronics STW13NK100Z power MOSFETs, connected drain-to-source so that the MOSFET body diodes do not short out the switch. These transistors were selected in part because of their high voltage rating (1 kV drain-to-source). The antenna sinks current from both the series and parallel branches; this, in conjunction with the 5% increment in the capacitor distributions, means that the 13 A rating of these FET's comfortably exceeds the 200 A antenna current design target. The 0.56-Ω drain-to-source on resistance is adequately low given the high-degree of current sharing, while intrinsic parasitic capacitance is low when the devices are fully in saturation [120], though not negligible (see Section 4.4.3).

Figure 4-6 shows the MOSFET driver circuit. A 500 kHz logic signal is generated on a compact programmable logic device (CPLD), divided down from a 4 MHz clock. This is driven by two buffers, exciting CoilCraft S5499-DL 1:5 transformers in a push-pull configuration. The stepped-up voltage undergoes full-wave rectification with a 100-μs RC filter and drives the MOSFET across the gate and source terminals. To turn the switch on and off, the 500 kHz control signal is amplitude-modulated by the CPLD, either at the full-amplitude ("on") state or the zero-voltage ("off") state. The actual driver circuit produces gate-source voltages of ∼14 V from the 5 V square wave input, fully turning on the MOSFET switches with sub-millisecond transition times.

Since the source terminals may float at RF voltages, the transformers in the driver circuit must also provide isolation between the logic circuitry and the RF power. The 1500 V_{rms} isolation afforded by the transformers selected for this role surpasses the design requirement [121].

Base level series and parallel channels replace dynamic switches with wire shorts to provide a static, minimum capacitance for each pathway, as seen in Figure 4-8.

[3]Due to inventory constraints and base load requirements, 0.22 and 0.39 nF capacitors were reserved for the smallest capacitance levels.

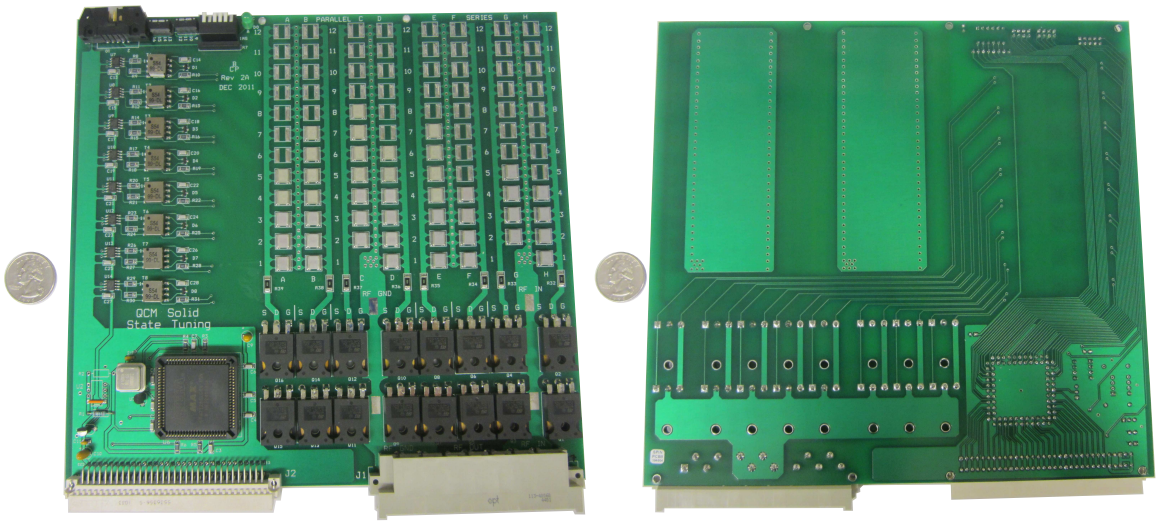

Figure 4-7: Photograph of a single dynamically-switched capacitor board, one of twenty in the system. (Left) The top and (right) bottom of the board are shown.

When all switched levels are disengaged, the base capacitor set must be able to carry the entirety of current running through the matching network, so its construction needs to be very robust. To satisfy this constraint, the current load is divided across many capacitors and board channels. The idealized design, based on the capacitance values given by Eq. 4.5 and neglecting all leakage capacitance, called for distributing the base capacitor components roughly uniformly across five circuit boards, using a total of 15 components for the C_p branch and 49 for the C_s. However, leakage capacitance through the boards and MOSFETs provides some base level capacitance, albeit amplitude-dependent in the case of the MOSFET contribution. The base boards, themselves, have no switching capability, and so in order to adjust for the leakage capacitance, only three of the original five boards were used in the final matching network, trimming the total static contribution to C_p and C_s to the correct values.

Diagnostics

High-voltage, high-current, low-loss probes are required both to monitor the power system performance and record antenna voltage and (crucially) current waveforms for referencing against plasma diagnostics. Moreover, the diagnostics must be compati-

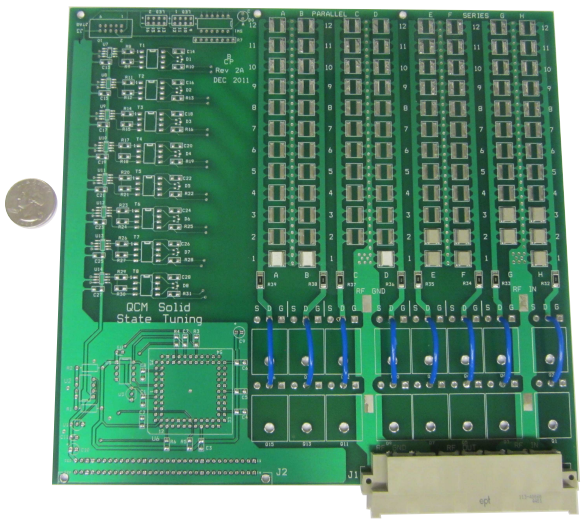

Figure 4-8: Photograph of top of base capacitor board, which replaces MOSFET switches with wire shorts, and spreads base capacitance over a number of circuit boards.

ble with the $\sim$ 10 kΩ input impedance presented by the D-tAcq ACQ216 digitizers available for data collection on Alcator C-Mod.

To address these needs, several current/voltage (I/V) probe units were constructed. These employ custom-built capacitive voltage dividers, nominally providing division of 200:1, as well as Pearson Model 101 current monitors with peak amplitude, 200 A, and an operational band from 0.25 Hz to 4 MHz [122]. The lower frequency bound of the voltage divider is determined by the resonance between the low-voltage leg capacitance and the magnetizing inductance of the isolation transformer, while the upper frequency bound results from the need to keep the impedance of the probe much larger than that of the antenna, which is in parallel. The circuit parameters were selected such that the phase shift in the voltage measurement resulting from the low-frequency resonance would be $\leq 5^\circ$ at 50 kHz, while the reflection coefficient, Γ, of the matching network would be increased by no more than 5% due to the modification of the load impedance by the voltage divider. Actual performance meets and exceeds these constraints.

Photographs of the voltage and current probes are shown in Appendix G (see Figures G-3 and G-4).

The voltage and current probes are housed in Compac SRF RF-shielded boxes.

These provide insulation against the noisy environment of the Alcator C-Mod experimental area, while also protecting against possible leakage of high-frequency signals which can be accidentally coupled from other antenna systems within the tokamak.

The capacitive voltage dividers are calibrated against 100:1 oscilloscope probes, using a high-input-impedance ($\sim$ 1 MΩ) digital oscilloscope to record the waveforms. The oscilloscope probes, themselves, were not suitable for typical operation because they require higher input impedance than that presented by the digitizers available during experiments ($\sim$ 10 kΩ). The Pearson current monitor's 100 A:1 V factory calibration is generally acceptable for interpreting current data. In fact, long cable lengths ($\sim$ 15 m) result in a phase drift in the current measurement from 1° to 5°, increasing with frequency across the system's operational band. Since we are typically interested in $\sim$ 180° phase shifts in transfer functions between the antenna current and plasma diagnostic signals, and over a fraction of the whole band, these phase errors are negligible in interpreting physics results. However, because the antenna resistance is so much smaller than its reactance, a careful accounting of this effect is required to extract the antenna impedance from current and voltage waveforms.

The antenna, itself, can also be used as a $k_\perp$-specific receiver to diagnose plasma fluctuations, as discussed in Section 5.2. In this operational mode, the power system is disengaged, and the voltage induced in the antenna by oscillations in plasma radial flux is coupled to a digitizer channel via an isolation transformer and a discretely-variable voltage divider. The antenna also picks up the 500 kHz beat frequency between two ICRF heating antennas, which operate at 78 and 78.5 MHz. The pickup is of sufficient amplitude that it can saturate the digitizer channel if left unmitigated. As such, it is suppressed with a simple LC notch filter. The digitized voltage is calibrated based on a characterization of the isolation transformer, divider, and filter to yield the voltage induced across the antenna.

Matching Network Control System

The matching network adjusts its tuning state according to the Sync signal, an output from the RF Generator Board described in Section 4.4.2 and Figures 4-5 and 4-9.

The period of this signal is measured in the Master Control Board (MCB), and this quantity is then mapped to two independent tuning numbers – one each for the series and parallel capacitor branches – using a lookup table. These two states are communicated to all dynamically-switched capacitor boards, which adjust their states accordingly to produce the desired total series and parallel capacitances.

The logic used to control the dynamic boards was programmed onto Altera EPM7128SLC84-15 CPLDs; a version of the Verilog code used for programming is available from GitHub[123]. A different CPLD, the Altera EPM2210F256C5, was used to accommodate the more complicated logic of the Master Control Board. The Verilog code used to program this device is also publicly available[124].

In the following, the logic flow is described briefly (see also Figure 4-5). The MCB's CPLD implements a period counter [125] to measure the Sync signal. The period is averaged over $M = 25$ Sync cycles at an $f_{clk} = 8$ MHz clock rate[4], resulting in a worst-case quantization error in frequency resolution of $\approx 2f_{sync,max}^2/(Mf_{clk}) = 900$ Hz. The minimum response time is $M/f_{sync,min} = 500$ μs, which occurs when the drive frequency is at the 50 kHz lower bound of the operational band.

Separate series and parallel capacitor lookup tables are programmed onto the MCB CPLD. The two lookup tables specify the bounds of each particular tuning state in terms of the Sync period, measured in clock counts. The period, rather than the frequency, is used in the bounds to avoid a division operation on the CPLD.

The state of the system is encoded in two independent, seven-bit binary numbers, one for the series capacitors and one for the parallel. These are broadcast from the MCB on a custom backplane feeding all capacitor boards, together with two separate enable bits to indicate changes in either the series or parallel states. These two states, together with the measured signal period, are also encoded in three serial bit streams which update on every change; these diagnostic outputs are recorded on digitizers during typical operation in order to monitor proper functioning of the matching network during experiments.

The capacitor boards' responses to the global tuning state are determined from

[4]In initial experiments, a 4 MHz clock averaging over 50 Sync cycles was used – see Sec. 4.4.4.

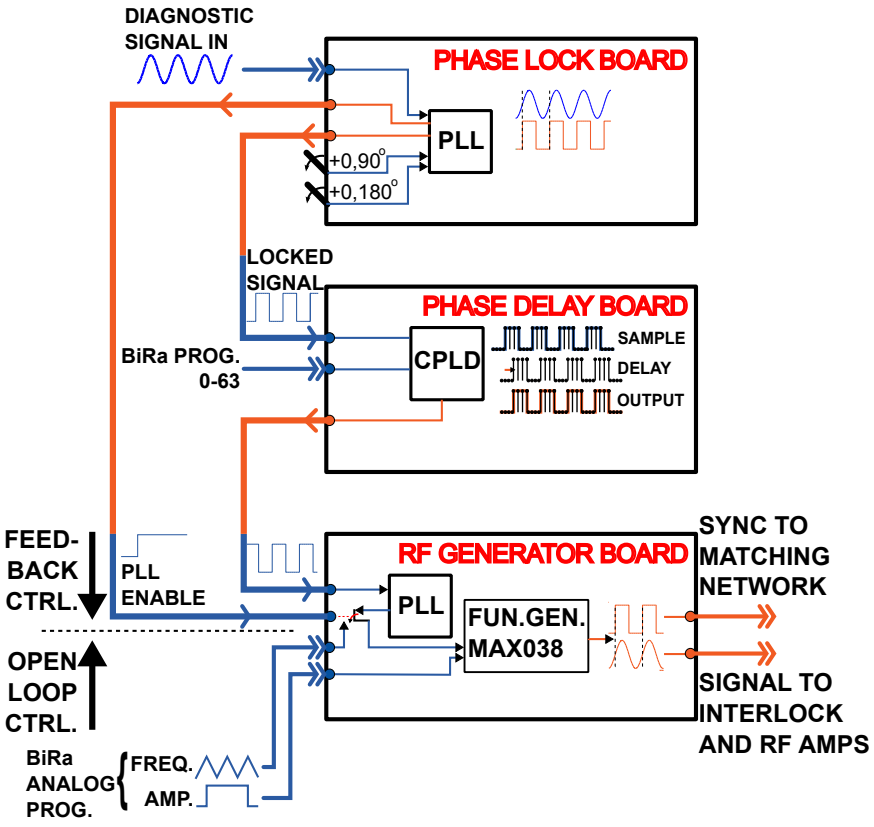

Figure 4-9: Source schematic illustrating generation of input signal to RF amplifiers.

each board's six-bit address number, which is parsed from a set of reconfigurable dip switches. State changes on the capacitor boards are triggered by the enable bits, with the series and parallel states controlled independently and in parallel.

4.4.2 Source and Control System

RF power is provided by two T&C AG1010 50-Ω, Class B amplifiers which provide 600 W continuous power and 1 kW pulsed power in the band from 20 kHz to 1 MHz [126]. Typical operation of the Shoelace antenna system is limited to 1 s with several minutes between pulses, so it is the 1 kW power limit that is relevant. The output from both amplifiers is combined in the matching network.

Figure 4-9 illustrates schematically the basic construction of the function generator which feeds the RF amplifiers, as well as its control system. The amplitude of the function generator output follows an open-loop program with a single analog control

signal, while the frequency and phase follow either open- or closed-loop (feedback) control. In the open-loop case, an analog input provides a control signal for the frequency of the output. In the closed-loop case, the function generator output is synchronized, with variable phase delay, to a real-time plasma density fluctuation signal via a phase-locked loop (PLL), as described in Section 4.4.4. The selection between the two frequency control pathways is carried out automatically by an enable bit which is set when the cross-power between the PLL output and plasma fluctuation signals is sufficiently high, with an auxiliary manual remote switch to disable phase locking. All analog control signals are generated on a remotely-programmable BiRa Systems, Inc., Model H910 function generator, which is part of Alcator C-Mod's CAMAC-based data acquisition system.

Besides the two RF power outputs, the source also provides an additional 5 V square wave – the "Sync" signal – that is generated with and synchronized to the sinusoidal input to the RF amplifiers. It is this signal that provides control of the matching network tuning state.

4.4.3 Calibration

The problem of assigning frequency ranges to discrete capacitance levels is manifested in Figure 4-10. Here, the fraction of power transmitted to the matching network is shown against frequency for many different combinations of discrete series and parallel capacitance levels. At a given frequency, a good calibration picks a capacitance configuration with a resonant curve whose power transmission is near 100%. However, it is infeasible to characterize all of the available resonance curves, not only due to the large number (81^2) of such curves and their variability with plasma conditions and power level, but also because mapping out the full curve at high power is not possible, since the RF sources will trip as reflected power increases off-resonance. Instead, calibrating the lookup tables requires careful characterization of the antenna load, the effective series and parallel capacitance, and the transformer, resolved across the entire frequency range of interest. These quantities are then integrated into the idealized models of Section 4.4.1 to synthesize initial tables, which are then optimized

manually with additional trials.

The most reliable technique for these operations is to excite the system under RF power, sweeping the frequency across the operational band and digitizing voltage and current waveforms across the components on an oscilloscope. The impedance over each component is then computed by processing the recorded signals; this frequency-dependent impedance data can be used directly, or parameterized in circuit models. Figure 4-11 compares the antenna impedance obtained with this procedure (at room temperature) against estimates provided by simple analytical models for resistance [127] and inductance. These models are derived in Section B.3 of the appendix. The transmission lines and vacuum feedthrough connecting the power system to the antenna contribute a non-negligible amount of impedance, and are included in load characterization.

In fact, the antenna impedance is not static; it varies with plasma conditions as heating from the plasma reduces the winding conductivity, and as antenna/plasma coupling changes. Fortunately, it is not necessary to retune the matching network between plasma discharges. Instead, characterizing the antenna impedance once under realistic conditions is sufficient, barring major faults developing in the antenna, and adequate results can also be obtained by assuming an unchanged inductance from the value with no plasma present, since antenna/plasma coupling has only a minimal effect, and a resistance increase commensurate with an estimated temperature rise of the antenna winding (in this case, R increases by approximately 50% during a plasma discharge).

With regard to characterizing the matching network's discrete capacitor levels, there are two non-ideal effects to consider. The first is the inclusion of stray capacitance between traces on the circuit boards. In each board, the static stray series and parallel capacitances are $\Delta C_s \approx 16$ and $\Delta C_p \approx 18$ pF. Totaling over the 20 dynamically-switched boards and five base level boards gives total static stray capacitances of $\Delta C_s \approx 400$ and $\Delta C_p \approx 450$ pF, both negligible values.

Leakage also occurs across the MOSFET switches. This is a nonlinear effect, as the drain-to-source parasitic capacitance drops off rapidly with increasing drain-to-source

voltage. Since the range of parasitic capacitance in these transistors spans hundreds to thousands of pF per device [120], this effect cannot be neglected, particularly for the higher frequencies, which require smaller capacitance values. This causes a complication in calibrating lookup tables. Initially, low power must be used to characterize the effective capacitances and load; otherwise, an abundance of reflected power will result in a trip at the RF sources. However, at higher powers, the nonlinear capacitance changes, detuning the system and again leading to high reflected power and trips at the source. As such, an iterative procedure is required, stepping the power up gradually while retuning the system after every step. In practice, three to four steps are adequate for the full frequency range.

Figure 4-12 shows one of the finished pairs of lookup tables used in the first round of antenna experiments.

4.4.4 Phase Locking to Real Time Fluctuation Measurement

The desire to explore feedback stabilization or destabilization of plasma oscillations motivated the development of a phase lock system. Figure 4-9 provides a simplified schematic of this system's operation. A phase-locked loop generates a square wave that follows a real-time analog output from the Phase Contrast Imaging (PCI) diagnostic [53], which resolves line-integrated plasma density fluctuations. When the cross-power between the diagnostic input and the locked square wave passes a threshold level, an enable bit is set to indicate a successful lock. If a second remote switch is also set, frequency control for the power system is changed from a pre-programmed evolution to the live lock.

The phase relationship between the locked square wave and the plasma signal can be adjusted in two ways: either via hardware switches to produce a 0, 90°, 180°, or 270° lag, or a separate phase delay circuit board. In the separate phase delay unit, the square wave is sampled at 16 MHz and stored in a cache. The input signal period (typically $\sim 6 - 20\,\mu$s) is also measured by counting the number of clock cycles, N_{clk}, between rising edges – an $M = 1$ period counter. From this measurement, a delay is calculated. The output of the phase delay board is the state of the input square wave

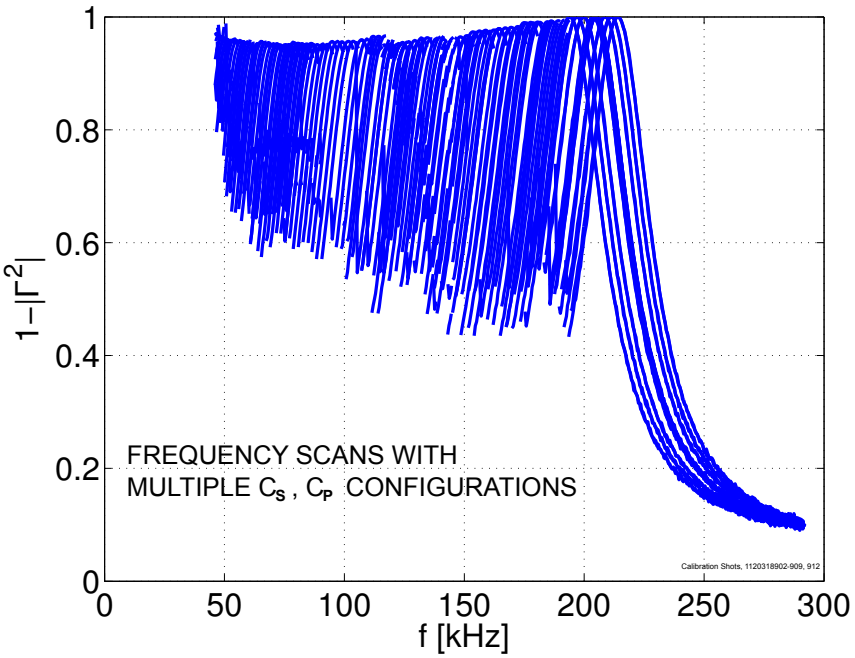

Figure 4-10: Test of matching network demonstrating a set of resonant curves obtained from different configurations of discrete C_s and C_p levels. Not all of the 81^2 possible resonant levels are shown. Source power of less than 100 W was used for the tests, making it possible to run far off match without overloading the amplifier, and no plasma was present. Moreover, a different amplifier was used, one which tolerated greater reflected power, but had a frequency range restricted to 9-250 kHz. Tracing out each individual resonant curve is impractical as a method of calibration, partly due to the large number of possible tuning configurations, and partly because it is not possible to access off-resonance frequencies at higher source power, since doing so would reflect an unacceptable level of power back to the amplifier.

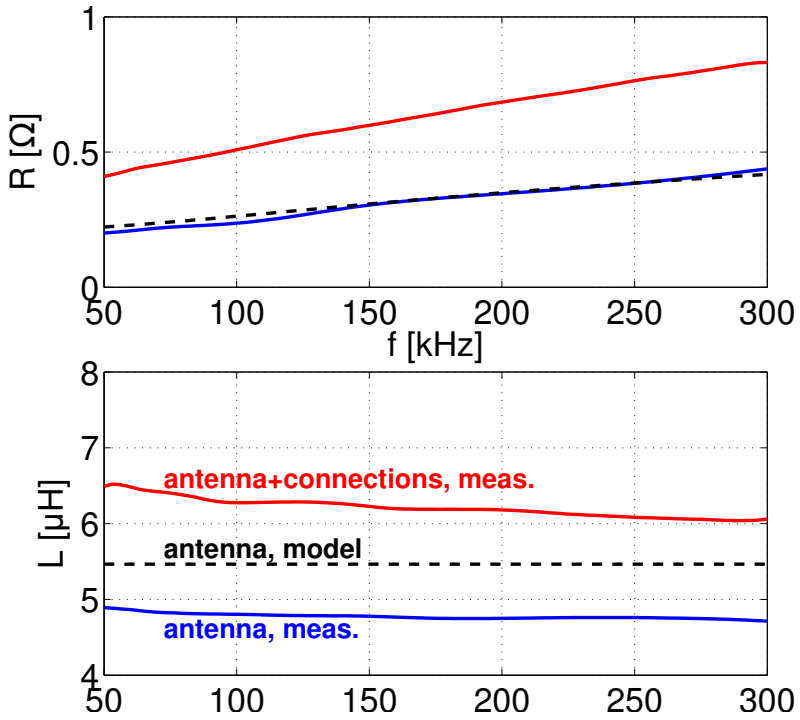

Figure 4-11: Antenna load, together with predicted value from model. The measured load characteristic is shown with and without the contribution from 4.3 m of transmission line and one vacuum feedthrough.

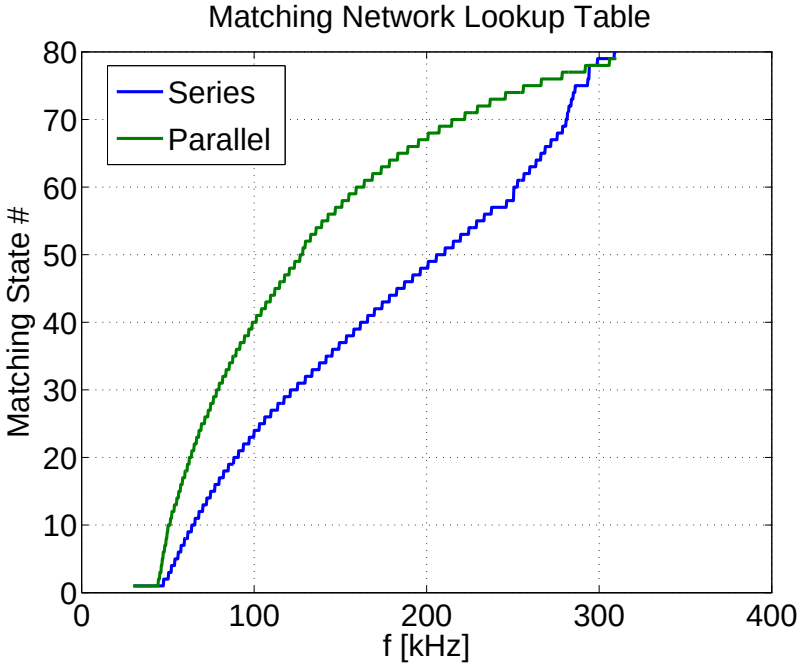

Figure 4-12: Lookup tables, mapping frequencies to series and parallel state numbers across the antenna operational band.

delayed by this amount, as retrieved from the cache. An Altera EPM2210F256C5 CPLD implements the required logic. The Verilog code used to program the CPLD has been made publicly available [128].

The challenges of locking to a plasma mode in this way are suggested by Figure 5-15, which shows actual performance of the locking system. The rapid evolution of the QCM – the fluctuation to which the power system must lock – is apparent from the PCI spectrogram in the top of the figure, where the time-evolving peak in the short-time spectra is due to the QCM. Building a phase-locked loop to track such a variable signal requires a careful balance between stability and response time. Moreover, rapid state changes in the matching network are required to provide a good impedance match over the duration of the antenna pulse. Indeed, the initial response time of the matching network state changes – 1 ms – was found to be too slow, such that the MCB clock rate was doubled to 8 MHz, and the period count halved to $M = 25$, in order to reduce the upper bound on the response time to a faster 500 μs.

4.4.5 Performance

Figure 4-13 summarizes the capability demonstrated by the Shoelace power system. The top frame shows the power fraction transmitted to the matching network across the entire frequency band during an actual plasma discharge, the middle frame shows the current amplitude in the antenna for the same discharge, while the bottom frame shows the total power output from the RF sources. At least 85% of source power reaches the antenna across the entire frequency band from 50-300 kHz, with better efficiency in the lower band from 50-150 kHz, which was of primary interest in experiments. Currents in excess of 80 A were achieved routinely in the lower frequency band, and the system operated reliably for hundreds of pulses. These performance characteristics exceed the design goals set forth at the project's inception.

Figure 4-14 shows results from a typical antenna experiment [129]. The top pane is a spectrogram of a PCI signal – it shows the evolution of the spectral content in line-averaged plasma density fluctuations. The distinctive, somewhat broad feature setting in at around 0.98 s and spinning down in frequency indicates the presence of

a quasi-coherent mode. The antenna-driven perturbation is visible as a triangle wave following the pre-programmed frequency waveform; it appears in the spectrogram just prior to the onset of the QCM. The antenna frequency is compared with the frequency of maximum spectral content in the middle pane of Figure 4-14, and the bottom pane shows the current driven in the antenna. The current varies between 68 and 83 A in this discharge; it tracks the antenna frequency, falling slightly with increasing frequency as the skin effect raises the antenna resistance. A slow droop in current over the duration of the pulse follows from the increase in the antenna temperature, and hence resistance.

Figure 5-15 shows the operation of the antenna with the phase-locked loop engaged. The format of the data is as in Figure 4-14. Initially, the source frequency remains at a stationary, pre-programmed value. At 1.128 s, the lock enable bit goes high, indicating that the cross power between the locked waveform and the real-time plasma signal from the PCI diagnostic has crossed a threshold value. Subsequently, control passes to the phase lock system, which successfully tracks the QCM frequency until the mode coherence drops around 1.4 s. However, more careful analysis shows that the phase lag between the antenna current and plasma signal is not fixed; this is lost when the function generator tries to lock to the output from the phase delay board. The square-wave envelope of the antenna current shows the amplitude modulation employed to help discern the antenna's effect on the fluctuation signal. Several very short trips at the RF source are visible, but the nominal current level stays constant despite the rapidly-varying frequency.

Phase-locked operation is discussed in Section 5.7.1.

It should be noted that the matching network calibration is adaptable. As noted above, at one point in the experimental campaign, a fault developed in the antenna: half of the windings were shorted out. This required a new calibration for the capacitor look-up table. Despite operating at roughly half the normal impedance, the system was still able to drive up to ~ 80 A in the antenna, albeit in a reduced band from 80 to 150 kHz.

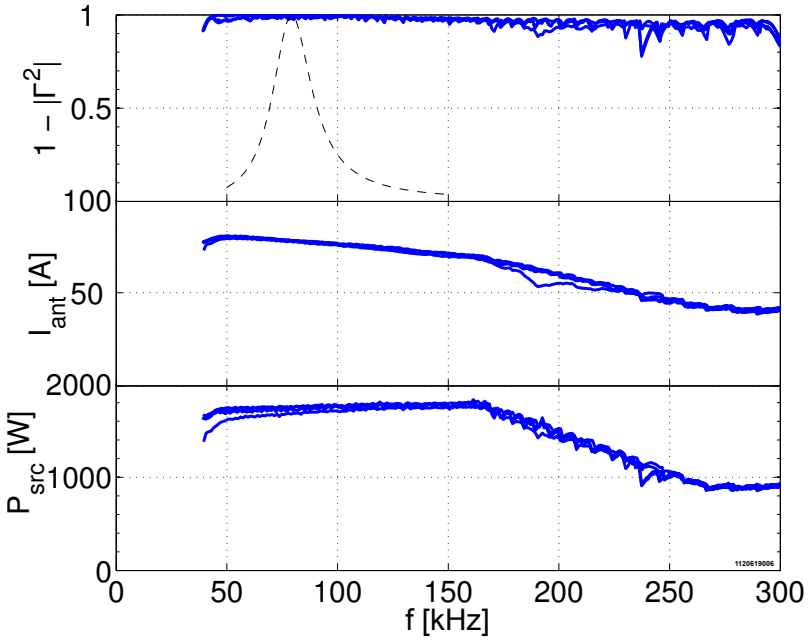

Figure 4-13: Matching network operational performance from an Alcator C-Mod discharge. The top curve shows the fraction of power entering the matching network. The dashed line highlights the power throughput expected from the idealized circuit model of the system for a particular configuration of capacitors; there are 81^2 such curves available, spanning the operational band. The plots underneath show the current and power entering the antenna. The power demand at higher frequencies is reduced in the system programming to avoid tripping the RF amplifiers.

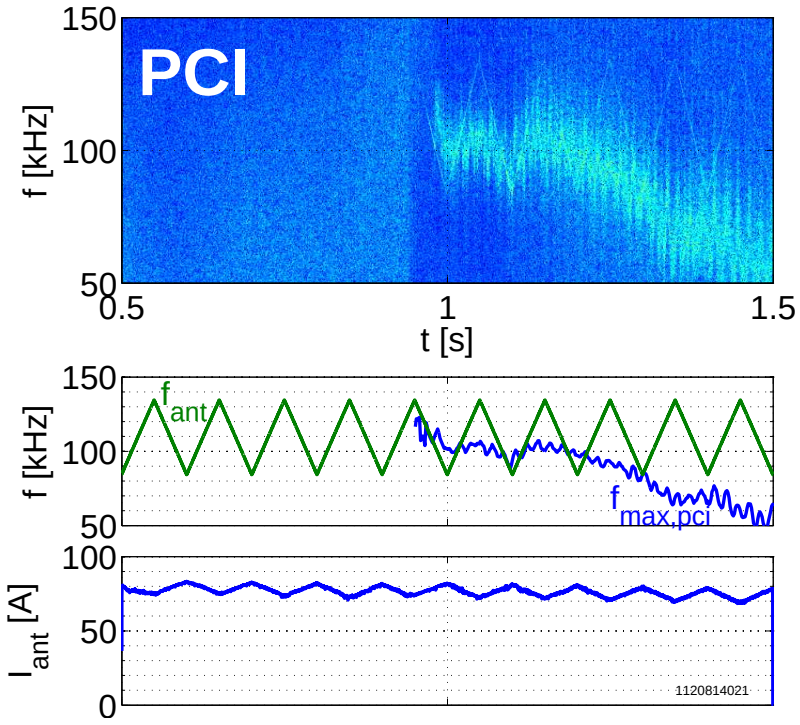

Figure 4-14: Typical operation of antenna system with open-loop frequency program. (Top) Spectrogram of plasma density fluctuation. (Middle) Antenna frequency and plasma mode nominal frequency. (Bottom) Antenna current.

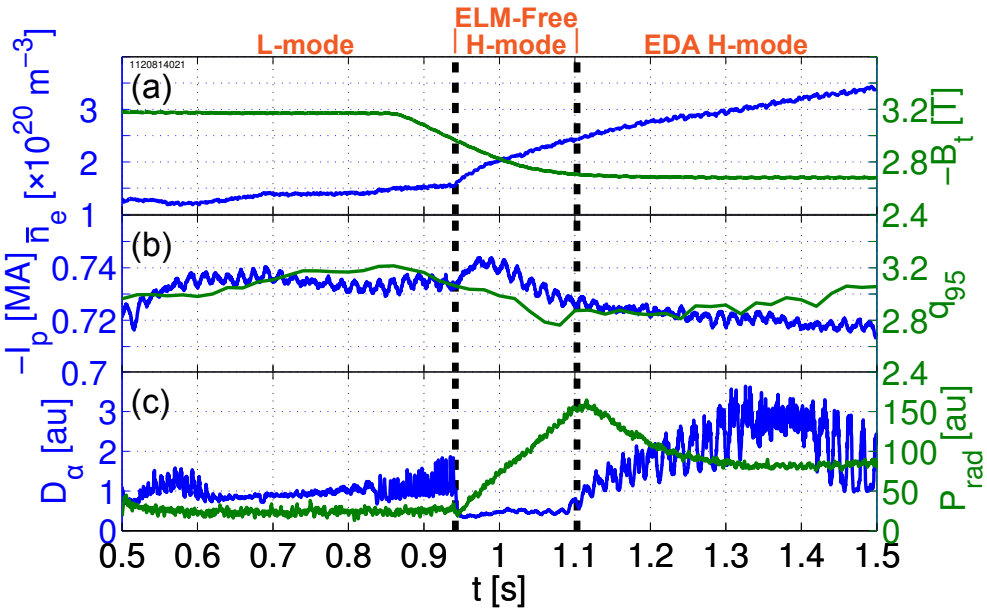

Figure 4-15: Traces of (a) line averaged electron density (left axis) and toroidal field (right axis), (b) plasma current (left axis) and safety factor at 95% flux surface (right axis), and (c) D_α light (left axis) and radiated power (right axis) for a typical forward-field discharge.

4.5 Experimental Setup

4.5.1 Discharge Development

Discharge parameters from the Shoelace experimental campaign approximated those used in the earlier examination of the QCM by Snipes *et al.* [33], since the Shoelace antenna was designed based upon the characterization of the QCM provided by this study. This choice was additionally motivated by the need to reduce the gap between plasma and antenna, as described above. The lack of auxiliary heating in these ohmic EDA H-modes achieved in these target discharges helps to avoid damaging the winding given its proximity to the plasma.

Departures from this base plasma equilibrium were made to increase the antenna response by minimizing antenna/plasma separation, survey the effect of different plasma parameters on the response, and attempt to map other diagnostics to the antenna. Details are described in Alcator C-Mod Mini Proposals 697 [130] and 719 [116].

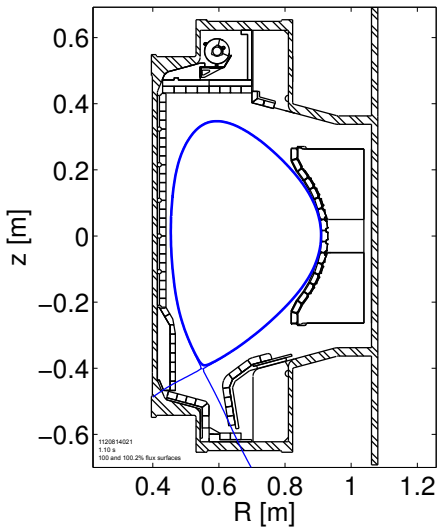

Figure 4-16: Reconstruction of the 100% and 100.2% flux surfaces in the R, z plane, together with the outline of the Alcator C-Mod vacuum vessel, limiter, and divertor tiles. The outer strike point hits the "slot" – the lower-right corner of the divertor.

Traces from a typical discharge are shown in Figure 4-15. Transition to H-mode was facilitated by ramping down the toroidal field to reduce the threshold heating power. Since EDA H-modes tend to favor higher q_{95} [26], it was expected that this parameter would have to be subsequently ramped up after the transition to ELM-free H-mode; in practice, this was not necessary, and q_{95} was maintained near the value that optimized the alignment between the Shoelace winding and the equilibrium field. However, creating an equilibrium field in which the outer strike point intersected the wall in outer corner of the divertor – the "slot" – proved to be particularly helpful in accessing the ohmic EDA H-mode. The LCFS and strike points from such an equilibrium are shown in Figure 4-16. In reverse-field discharges, the strike points intersect the upper divertor, which has no such recessed space, and so this technique was not available. Instead, ~ 30 ms ICRF pulses were used to help trigger transition to H-mode, though robust ohmic EDA H-modes proved difficult to produce[5].

The edge region of several ohmic EDA H-modes used in Shoelace antenna experiments was well-diagnosed by the Mirror Langmuir Probe (MLP), and its properties are discussed in detail elsewhere[32]. The MLP revealed that the LCFS in these dis-

[5]One was obtained on Discharge 1120926003.

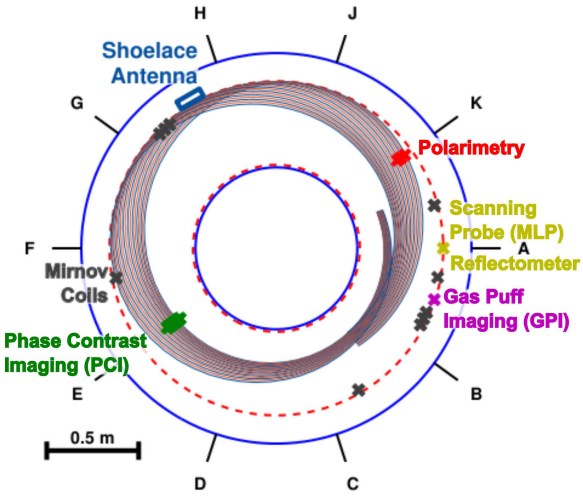

Figure 4-17: Plan view (R, ϕ) of Alcator C-Mod tokamak indicating locations of Shoelace antenna and fluctuation diagnostic measurements on the LCFS. Also plotted are magnetic field lines on the LCFS which map to rungs on the Shoelace antenna. Adjacent field lines alternate in color between blue and orange. The 10 equispaced horizontal ports are labeled A-K (skipping the letter, I).

charges is typified by $T_e \approx 50$ eV and $n_e \approx 1.5 \times 10^{20}$ m^{-3}, so that $\tau_{ei} \approx 100$ ns and $\tau_{ii} \approx 5$ μs, with $k_\perp \rho_s \approx 0.07$ for the antenna-imposed wave number.

4.5.2 Diagnostic Setup

Figure 4-17 shows a plan view (R, ϕ) of Alcator C-Mod, and indicates the placement of the Shoelace antenna relative to a number of fluctuation diagnostics; a (ϕ, z) view is shown in Figure 4-18, together with several poloidal cross sections of key diagnostics. Shown also are field lines along the last closed flux surface; these connect to the positions on the LCFS to which the antenna rungs project along rays to the antenna arc center. The mapping scheme is illustrated in Figure 4-19. The discussion in Chapter 5 reveals that, in fact, the antenna-driven fluctuation is guided by field lines, such that diagnostics which do not map to the antenna on a field line near the LCFS do not observe the driven mode. The diagnostics which are almost always mapped to the antenna include phase contrast imaging [53] (PCI), measuring line averaged density fluctuations, $\tilde{\bar{n}}_e$, with 32 vertical chords in a poloidal cross section uniformly spaced in major radius, ΔR =2.7 mm; three polarimetry [131] chords, sensitive to both density

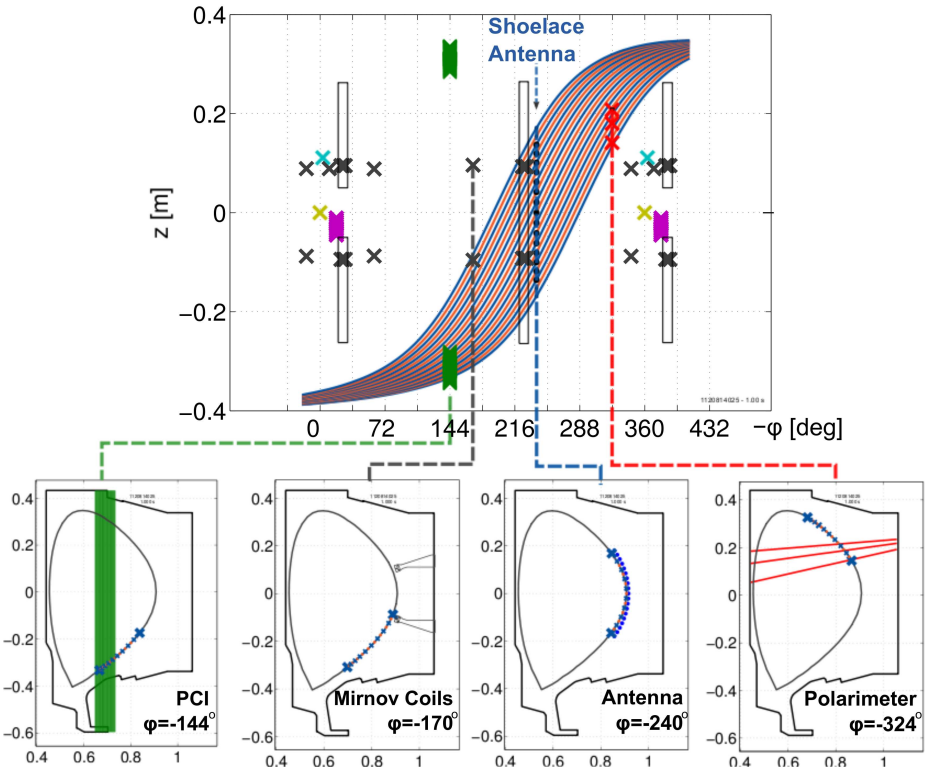

Figure 4-18: Field-line mapping projected onto (ϕ, z) plane, showing the projections of diagnostic measurements onto the LCFS ($\times$'s), as well as Shoelace rungs ($\bullet$'s) and limiters (boxes). Diagnostics and limiters are repeated as the view wraps around past 360° (toroidal). Breakout plots underneath are (R, z) cross-sections; units on axes are in meters.

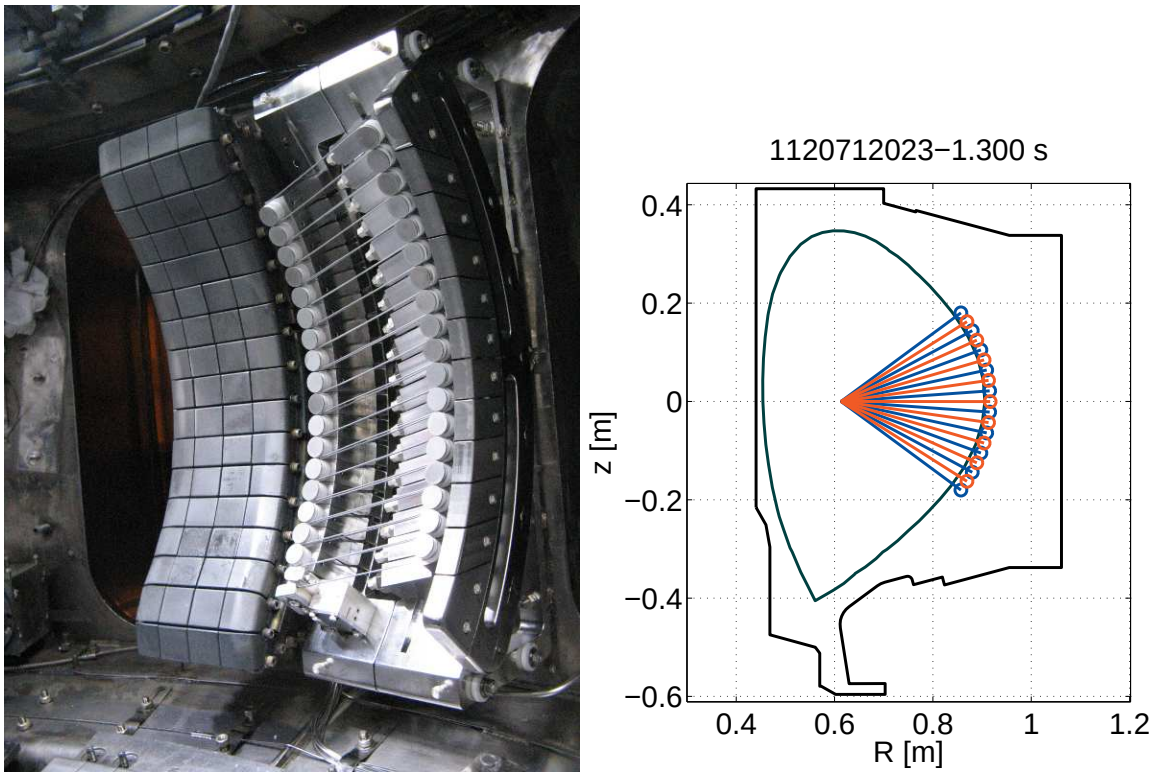

Figure 4-19: (a) Antenna and (b) mapping scheme, where rungs are projected onto LCFS along lines emanating from the antenna arc center.

and magnetic field fluctuations (though in the present work, the contribution from $\tilde{\mathbf{B}}$ is negligible); and wall-mounted Mirnov coils [92], measuring $\mathrm{d}B_\theta/\mathrm{d}t$ and sampled at f_s =2.5 MHz. The reflectometer [34], scanning Mirror Langmuir Probe [132], and gas puff imaging diagnostics [133] do not map to the antenna.

The reader is directed to the text on plasma diagnostics by Hutchinson for an overview on the operating principles of these and other measurement apparatus [134], as well as the references listed above for information specific to their implementation on Alcator C-Mod.

All fluctuation signals are recorded on Model ACQ216 digitizers manufactured by D-tAcq Solutions, Ltd. [135] The input impedance for these digitizers varies slightly, as the digitizers are customized for specific applications, but is typically around 10±2 kΩ. The analog signals of the Mirnov coils are sampled at f_s=2.5 MHz, while those of the PCI chords are sampled at f_s = 5 MHz. The polarimetry chords are oversampled at 20 MHz, and then processed onto a lower 4 MHz rate.

Ensuring that the timebases of different fluctuation diagnostics are aligned is crucial for cross-phase analysis, as explained in Section E.1 in the appendix. The synchronization procedure is described in [136]. However, faults in the synchronization hardware meant that this system was disabled for the PCI diagnostic during the Shoelace antenna experiments. Fortunately, the discrepancies between the PCI and global timebases are sufficiently small and repeatable that they can be calibrated out to adequate accuracy for the ∼100 kHz signals of interest. This procedure is described in Section E.2 of the appendix.

4.5.3 Shoelace Operation

As discussed above, open-loop amplitude control, as well as both closed- and open-loop frequency control, are available to the Shoelace antenna power system. In experiments, the Shoelace antenna amplitude was modulated in two ways: (1) a 100% gating, effectively turning the antenna on and off in order to discern its effect on the plasma from the intrinsic fluctuations, and (2) a smooth tapering of the amplitude at higher frequencies, especially > 200 kHz, to reduce the likelihood of a fault at the

power source due to increased reflected power.

Open-loop frequency modulation involved scanning the frequency linearly in a triangle wave, occasionally in a wide range from 45-300 kHz, but more typically in a narrower, 50 kHz scan, often between 85 and 135 kHz. The slew rate of these scans was typically limited to $\Delta f/\Delta t = 1$ MHz/s, which represents the lower bound on how fast the matching network can transition between every state in the lookup table. In fact, the matching network transition rate is usually faster than this, and when this limit does apply, it simply means that the matching network will skip over tuning configurations during the scan; it would still provide an adequate match at lower frequencies, for which the tuning configurations are spaced more closely together. However, the slew rate is also limited by the frequency resolution desired in the scan. As an example, with a 1 MHz/s slew rate and a nominal antenna drive frequency of 100 kHz, the frequency varies by approximately $(\Delta f/\Delta t)/f = 1$ MHz/s/100 kHz= 10 Hz over the course of a single period of the drive. Typically, a large number of cycles is desired to improve the statistical quality of the various estimates of spectral quantities being measured at a particular drive frequency. If 50 cycles is deemed an adequate number, then, with the same parameters, the antenna drive frequency scans through ∼500 Hz as these 50 cycles are recorded, putting an additional limit on the frequency resolution obtainable in spectral estimates.

A square wave frequency modulation envelope was also utilized in early experiments as a means to investigate exciting the plasma "on" and "off" resonance, though these plasmas were not in H-mode, had a larger spatial gap from the antenna, and exhibited a larger mismatch between field and winding pitch, so that no density response was achieved.

The antenna was operated under closed-loop frequency control for a limited number of discharges, as discussed in Sections 4.4.4 and 5.7.1.

4.6 Overview of Signal Processing Methods Employed in Data Analysis

The fluctuation diagnostics listed above provide digitally-sampled representations of analog signals. The analog signals are direct measurements of plasma fluctuations. Fluctuations in plasmas are typically "nonstationary," varying in both time and frequency. Because the underlying processes producing the oscillations are often either not well understood, chaotic, or both, the fluctuations are typically analyzed as random signals, and the associated suite of spectral analysis techniques for such signals are applied to extract information, including wave or mode numbers; the location, height, and width of spectral peaks; and the degree of coherence. What follows is a brief introduction to the particular analysis methods used in the following chapter, as well as some of the appendices. The emphasis is on explaining how the tools are used, rather than how they are crafted. For a comprehensive and standard resource on discrete time signal processing, the reader is referred to [137].

Despite the fact that all signal processing operations described below are applied to discrete signals, introducing them on continuous systems aids in their conceptualization. The cross power spectral density (shortened to cross power in the discussion below), P_{xy}, for continuous, stationary, and real signals, $x(t)$ and $y(t)$, is defined as

$$P_{xy}(j\omega) = \int_{-\infty}^{\infty} \mathrm{d}\tau \, e^{-j\omega\tau} \int_{-\infty}^{\infty} \mathrm{d}t \, x(t)y(t+\tau), \tag{4.6}$$

which is identified as the Fourier transform of the cross-correlation of two signals. The cross-correlation is closely related to the convolution operation, differing only in the fact that signal, y, is not flipped in time as it is slid past signal x, since the definition of this operation is motivated by a desire to characterize how far into the future a signal remains coherent, rather than summing the impulse response from prior input in order to retrieve the signal's present value. This, together with the convolution theorem, indicates that $P_{xy}(j\omega) = Y(j\omega)X^*(j\omega)$, where $Y(j\omega)$ and $X(j\omega)$ are the Fourier transforms of y and x, and the asterisk denotes complex conjugation. The

phase angle of P_{xy} is then the difference between the phases of Y and X, $\angle P_{xy}(j\omega) = \angle Y(j\omega) - \angle X(j\omega) = \angle\{Y(j\omega)X^*(j\omega)\}$.

The auto power spectrum, or spectral density, $P_{xx}(j\omega)$, of signal, $x(t)$, simply replaces $y(t)$ with $x(t)$ in Eq. 4.6.

The cross coherence spectral density estimate is given here by

$$C_{xy}(j\omega) = \frac{P_{xy}(j\omega)}{\sqrt{P_{xx}(j\omega)P_{yy}(j\omega)}}. \tag{4.7}$$

C_{xy} is normalized such that $0 \leq |C_{xy}| \leq 1$, and provides a measure of the correlation between two signals. Signal processing literature sometimes refers to the square of this quantity as the cross coherence spectral density, but the form in Eq. 4.7 is used here in order to make the phase of C_{xy} less ambiguous, since in this representation, $\angle C_{xy}(j\omega) = \angle P_{xy}(j\omega) = \angle Y(j\omega) - \angle X(j\omega)$, and especially, to simplify unwrapping of complex phases across multiple diagnostics. The magnitude squared coherence, $|C_{xy}|^2$, is labeled as such in the next chapter.

Similarly, the transfer function, or frequency response, is given by

$$H_{xy}(j\omega) = \frac{P_{xy}(j\omega)}{P_{xx}(j\omega)}. \tag{4.8}$$

The transfer function, $H(j\omega)$, can be thought of as the coherent output registered in the signal, y (*e.g.* output from a PCI chord or a Mirnov coil), caused by, and related linearly to, the input signal, x (the antenna current waveform). It is helpful in distinguishing peaks in the frequency response from excursions of the "input" amplitude. These peaks can then be characterized by their center frequency (corresponding to the natural resonant frequency of the mode), bandwidth (corresponding to the damping rate), and overall magnitude. Again, the phase is the difference of the phases of Y and X, $\angle H_{xy} = \angle C_{xy} = \angle P_{xy} = \angle Y(j\omega) - \angle X(j\omega)$.

Examining the plasma response to the antenna through the transfer function is a commonly employed analysis technique in the Active MHD literature [84, 90, 88, 92, 93]. There, the quantity is often calculated via "synchronous detection," appropriate to situations with a single peak in the spectrum. This time-domain method beats

(multiplies) the output signal with the input signal and its quadrature, low-pass filters the product, and then normalizes by the low-pass-filtered square of the input. Its operation in the time domain makes it amenable to real-time processing using analog, digital, or mixed-signal circuitry, while digital post-processing is also carried out with the aid of the Hilbert transform to provide the quadrature to the input. Synchronous detection analysis is not used in the following chapter, but was employed in some of the initial analysis of Shoelace antenna data.

Because the plasma fluctuation signals vary in both time and frequency, short-time spectral analysis is employed, not only for the spectral densities of individual signals, but for the pairwise estimates of the cross power, cross coherence, and transfer function, as well. In this case, the data is divided into short segments, or bins, and spectral analysis is performed within each segment. The Hamming window[6] [137, Eq. 5.17 and 7.60d] is used to select segments of the data; this is a moderately-tapered window that does not vanish at the endpoints, and provides reasonable spectral resolution and dynamic range.

The pairwise signal analysis performed here involves computing an estimate of the auto- and complex cross power using the Welch's modified[7] periodogram[8]; at a high level, this method divides a segment of data of length Q, into windowed subsequences of length, M, computes the spectral quantity in each subsequence, and then averages the result over all subsequences [137, Sec. 10.5.3].

All pairwise signal processing operations (*e.g.* calculations of cross coherence or cross power) are done at the slowest sampling rate – that of the Mirnov coils and Shoelace antenna voltage and current measurements ($f_s = 2.5$ MHz). The PCI and polarimetry diagnostics (with sampling frequencies, 5 and 4 MHz) are downsampled onto the 2.5 MHz rate. Since the polarimetry sampling rate is a non-integer multiple of this lowest rate, an interpolation step is required. The window length is chosen to be $M = 2^{10}$ (~ 0.41 ms), while the bin over which spectra are averaged has

[6] $w[n] = 0.54 - 0.46\cos\left(\frac{2\pi n}{M}\right)$, $0 \leq n \leq M$, and 0 otherwise.

[7] The designation, "modified," follows from the use of a non-rectangular window function.

[8] In this context, the periodogram refers to the method of estimating the spectral density, and cross spectral density, by direct discrete Fourier analysis of the signals, rather than on the cross- or autocorrelation functions.

$Q = 2^{13}$ samples (~ 3.3 ms). Hamming windows are applied both to the subsequence of length, M, and the larger bin of length, Q. The set of spectra that are averaged overlap by 50%; as such, $\frac{2Q}{M} - 1 = 15$ spectra are computed and averaged in each bin. Likewise, the bins of length, Q, are also overlapped by 50%. Then, for a typical 1 s data sequence, with $N = 2.5 \times 10^6$ samples, there are $609 \simeq \frac{2N}{Q} - 1$ pairwise spectral estimates, each corresponding to a bin $Q = 2^{13}$ samples ($\sim$3.3 ms) long, and with frequency resolution, $f_s/M \approx 2.4$ kHz.

The pairwise coherence and transfer function calculations presented in the next chapter and the appendices are most typically computed between a fluctuation signal and the digitized antenna current measurement, though other analyses between pairs of fluctuation signals are also presented.

Spectrograms of individual signals are computed using short-time Fourier analysis over segments of length, $Q = 2^{12}$ samples, for the Mirnov coil signals sampled at $f_s = 2.5$ MHz, and $Q = 2^{13}$ samples for the polarimetry ($f_s = 4$ MHz) and PCI ($f_s = 5$ MHz) signals. Hamming windows are also applied to these segments, and a 50% overlap is used. In the case of the Mirnov coil and PCI signals, this results in spectrograms with $1220 \approx \frac{2N}{Q} - 1$ temporal points and $f_s/M \approx 610$ Hz frequency resolution. For the polarimetry signals, there are 976 temporal points and ~ 488 Hz frequency resolution.

All signal processing operations presented in this text were carried out in the MATLAB ® environment with access to the Signal Processing Toolbox, though the `Python`-based `scipy` suite was employed during the course of the experiments. The results of the cross coherence, transfer function, and cross power calculations, along with several other pertinent signal processing quantities, are stored in the Alcator C-Mod `MDSplus` database in the `Magnetics` tree of the relevant discharges, under the `Shoelace` subtree.

Chapter 5

Results and Discussion

> We have to learn again that science without contact with experiments is an enterprise which is likely to go completely astray into imaginary conjecture.

–Hannes Alfvén

5.1 Introduction

This chapter presents data from the initial round of Shoelace antenna experiments, which were carried out between June and October of 2012. Use of the antenna as a fluctuation diagnostic is reviewed in Section 5.2 before the main results of active operation are discussed. Section 5.3 describes the Shoelace signature as observed on a number of fluctuation diagnostics, revealing that a strong field-aligned response is observed in $\tilde{n}_e$ and $\tilde{B}_\theta$ during H-mode, but only a $\tilde{B}_\theta$ is apparent in L-mode. Section 5.4 analyzes the relative phase between fluctuation measurements to estimate the wave number of the driven mode; as expected, the driven mode retains the precise mode number of the antenna winding, but while the antenna has no preferred perpendicular launch direction, the driven mode selects the electron diamagnetic drift (EDD) direction (in the laboratory frame). The transfer function between the antenna and fluctuation diagnostics is analyzed in Section 5.5, and is found to be well-described by the functional form of a simple pole with a damping rate, $\gamma/\omega \sim 5 - 10\%$. The field-line-guided behavior is revisited in Section 5.6 as part of the broader discus-

sion on the physical origin of the driven mode. Finally, efforts at examining possible interaction with the intrinsic QCM are examined in Section 5.7 from both a closed-loop (feedback) and open-loop perspective, though it is found that such interaction is marginal, at best, and further experimentation, especially at higher power, is needed before drawing conclusions on this topic.

The reader is also directed to reference [129], which covers much of the same material, as well as to [32] for a characterization of the intrinsic QCM from the set of discharges presented here.

5.2 Shoelace Antenna as a Receiver

Before discussing the results obtained from energizing the antenna, it is interesting to examine the voltage induced across the antenna by the fluctuating radial magnetic field associated with the QCM. Figure 5-1 shows a spectrogram of the short-time magnitude squared coherence between this induced voltage, measuring $\tilde{B}_r$, and the signal from a PCI chord, measuring $\tilde{\bar{n}}_e$; the high degree of coherence illustrates that the antenna, when used as a receiver highly selective in $k_\perp$, is sensitive to the QCM. The presence of a strong induced signal across the eighteen dipole loops of the antenna also indicates that the QCM has a long poloidal correlation length in this particular discharge.

Low-frequency, broadband turbulence may also be interrogated by the Shoelace antenna when it is used as a receiver. Figure 5-2 shows a spectrogram of the induced voltage over the antenna during a limited, L-mode discharge. This is compared with a spectrogram from a Mirnov coil, sensitive to $\dot{B}_\theta$. The antenna's selectivity in $k_\perp$ isolates a narrow slice of the broadband spectrum. The activity in this $k_\perp$ range is situated mostly between 200-400 kHz (the same frequency range typically associated with the WCM) in this discharge, and is modulated in frequency with the sawtooth crash.

It should be noted that the 500 kHz beat from the ICRF antennas[1] would have

[1] the D-port and E-port antennas, in particular, operating at 80.5 and 80 MHz

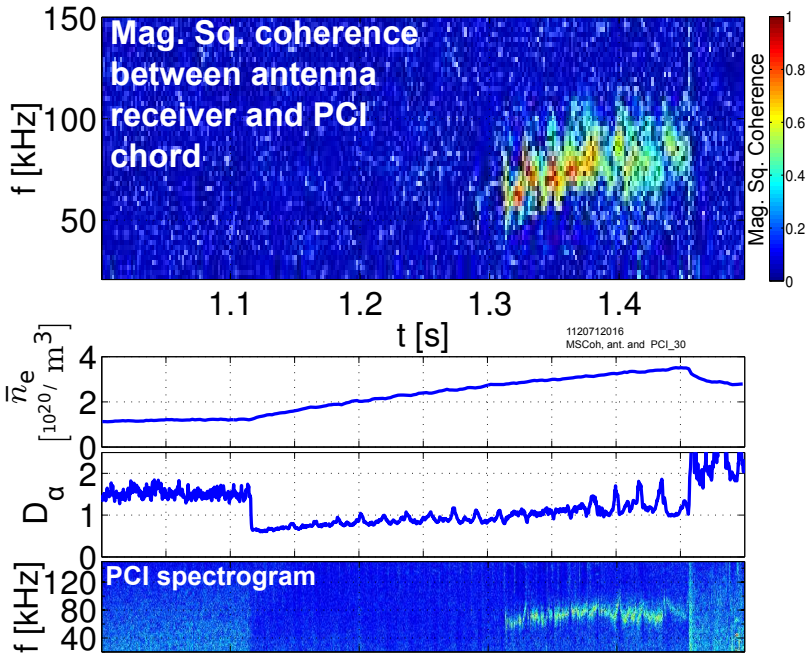

Figure 5-1: Short-time ($\sim$ 3.3 ms bins) magnitude squared coherence spectra between voltage induced over Shoelace antenna and PCI fluctuation signal showing that the Shoelace antenna can pick up the QCM fluctuation.

caused the Shoelace induced voltage to saturate the digitizer were it not for a notch filter employed to the suppress this signal. The filter's transfer characteristic was calibrated and removed from the signal analyzed in Figure 5-2.

It should also be mentioned that the antenna had developed a short across its winding before this discharge, effectively eliminating the antenna's upper half (see Section 4.3). Nonetheless, the antenna still measured plasma fluctuations, providing good selectivity in $k_\perp$ (though with a somewhat broader full-width-at-half-maximum by approximately a factor of two).

5.3 Antenna-Driven Edge Plasma Response

Figure 5-3a shows spectrograms from a PCI chord, a polarimeter chord, and a Mirnov coil, as well as $\bar{n}_e$ and D_α traces, from a discharge in which the Shoelace antenna was energized. Additional traces from this discharge are shown in Figure 4-15. A dashed line indicates the transition between ohmic L- and ohmic H-mode. A brief ELM-free

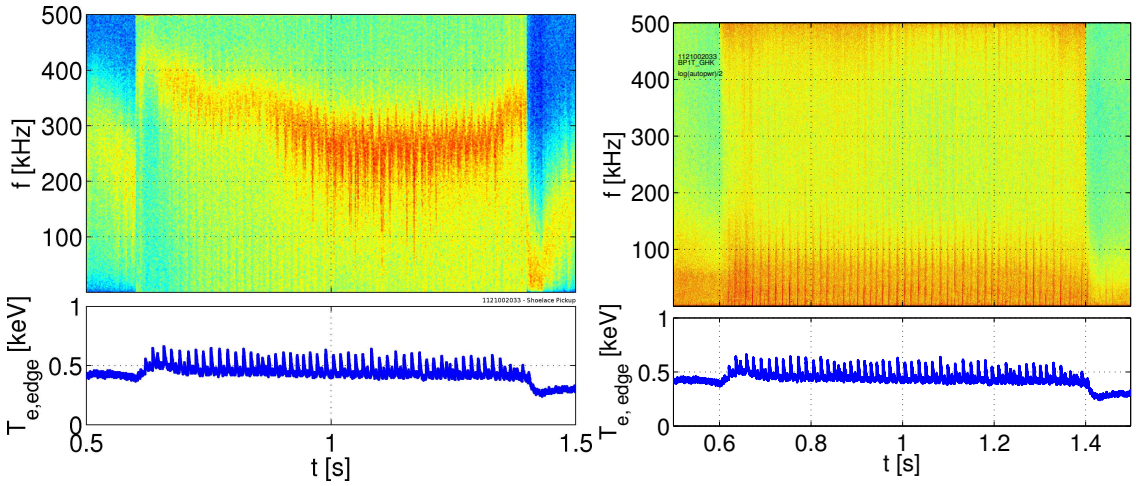

(a) (b)

Figure 5-2: Spectrograms (here, logarithm of autopower) of (a) voltage induced over Shoelace antenna when used as a receiver, characterizing a narrow slice in $k_\perp$ of the broadband turbulence spectrum in $\tilde{B}_r$, and (b) a Mirnov coil showing full broadband turbulence spectrum. The subplot in both figures is of the edge temperature, as provided by the electron cyclotron emission diagnostic, showing the characteristic inverse sawtooth crash.

H-mode gives way to an EDA H-mode, with a QCM visible in the spectra of all three diagnostics, and, after a short delay, an accompanying rise in D_α, consistent with a reduction in particle confinement.

Also visible in the spectrograms of all three diagnostics is a triangular waveform which precisely tracks the Shoelace antenna drive frequency. Several observations are noteworthy: (a) a $\tilde{B}_\theta$ perturbation at the antenna frequency is visible in both ohmic L- and H-mode, while the driven $\tilde{n}_e$ fluctuation only appears in H-mode; (b) the driven fluctuation appears strongest near the QCM center frequency, but is also present away from this frequency; (c) the driven $\tilde{n}_e$ appears early in the ELM-free H-mode phase, slightly preceding the QCM. These remarks are true in general for the perturbation driven by the Shoelace antenna.

A clearer view of the driven perturbation is offered by examining the magnitude squared coherence between the antenna current signal, I_a, and the fluctuation diagnostic signals, u, $|P_{I_a u}/\sqrt{P_{I_a I_a} P_{uu}}|^2$, computed over a short, running time window that spans about 3.3 ms. This short-time magnitude squared coherence is shown

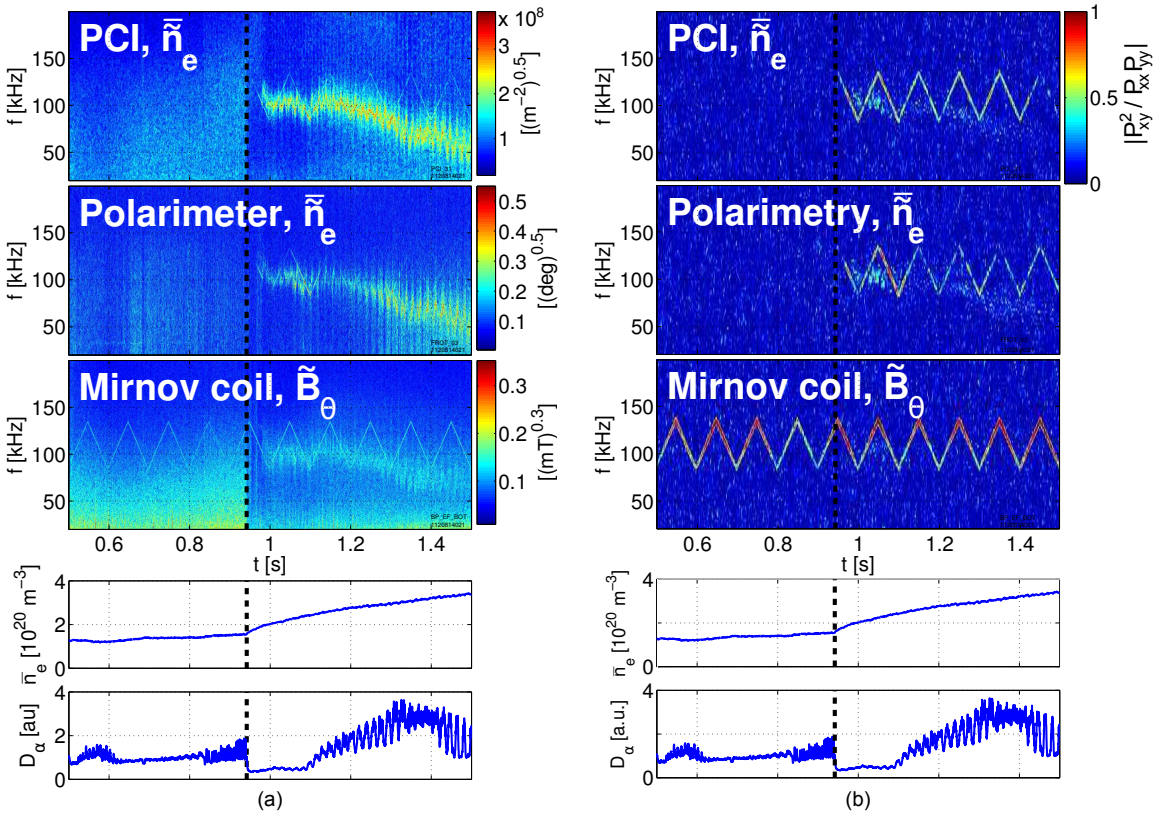

Figure 5-3: (a) Spectrograms of fluctuation signals from a PCI chord, a polarimeter chord, and a Mirnov coil during a discharge in which the Shoelace antenna was energized, together with density and D_α traces. The Shoelace response is seen in the triangle-wave feature in the spectrograms, which tracks the drive frequency and appears on top of the intrinsic QCM fluctuation. The spectral amplitudes are raised by an exponent to aid in visualizing the Shoelace response. The [deg] abbreviation in the polarimetry panel refers to degrees of Faraday rotation. The Mirnov coil measurement is given at the coil. The vertical dashed line marks the transition between L- and H-mode. (b) Short-time ($\sim$ 3.3 ms bins) magnitude squared coherence between the antenna current and PCI, Mirnov coil, and polarimeter fluctuation signals. The $\bar{n}_e$ and D_α traces are reproduced.

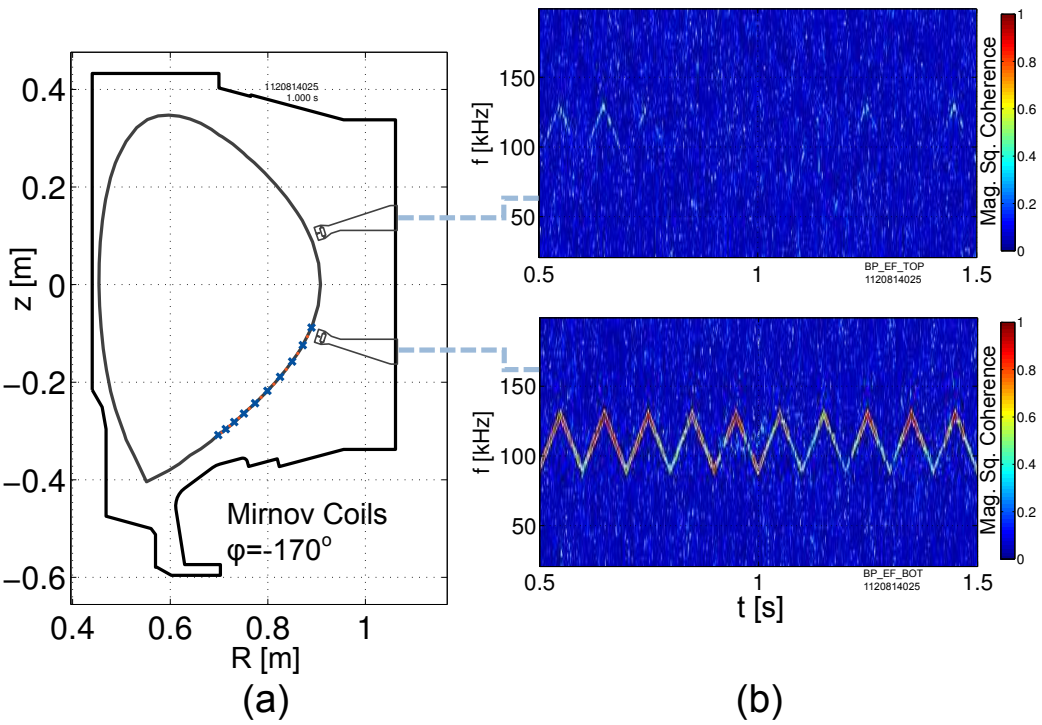

Figure 5-4: (a) Cross section showing location of two Mirnov coils, mounted on standoffs from the vacuum vessel, the LCFS (solid black line), and field lines ($\times$'s and $\bullet$'s) mapping Shoelace rungs on LCFS. (b) Short-time magnitude squared coherence for each coil; there is a strong coherent response on bottom coil, while there is almost none on top.

for the same three fluctuation signals in Figure 5-3b. We see now that the coherent perturbation in the PCI signal appears immediately after the transition to ELM-free H-mode, while a coherent $\tilde{B}_\theta$ signal is present throughout the entire Shoelace pulse.

Another feature of the driven perturbation is that it is not global. Rather, it is guided by field lines which map to antenna rungs. Figure 5-4 illustrates this point. Here, a poloidal cross section is shown which contains two Mirnov coils sitting on extensions from the vacuum vessel wall. The LCFS is also reproduced, together with the Shoelace antenna rung positions projected onto the LCFS and mapped to this toroidal location on field lines. Both coils pick up the QCM. However, while the bottom coil, which does map to the Shoelace antenna, shows strong cross coherence with the antenna current throughout the duration of the discharge, the top coil, which does not map to the antenna, has very little cross-coherence.

It should be pointed out that the Mirnov coils do not provide a point-localized

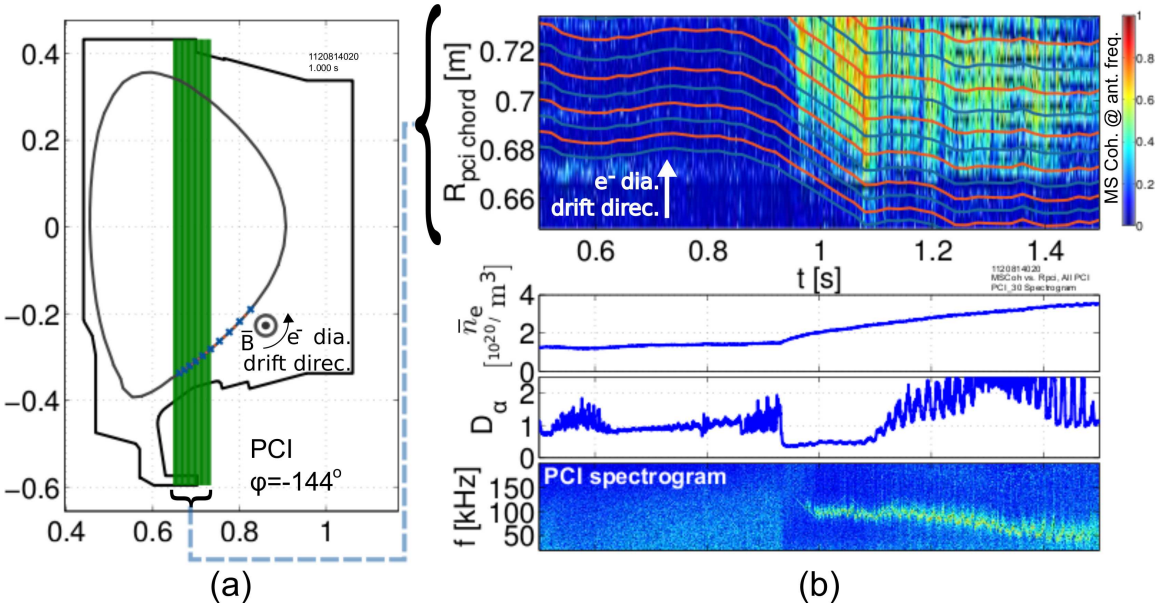

Figure 5-5: (a) Poloidal cross section containing PCI chords, as well as mapped locations of antenna rungs. While the PCI chords intersect the LCFS at two points, only the intersection below the midplane maps to the antenna. (b) The magnitude squared coherence at the antenna frequency is plotted in the color axis against major radius and time. This produces a one-dimensional image of the magnitude squared coherence across the major radial direction, which evolves as the discharge progresses. Overplotted in blue and orange lines are the antenna rung locations mapped on the LCFS to the plane containing the PCI chords. The subplots are $\bar{n}_e$ and D_α traces and a spectrogram from a single PCI chord.

measurement, and neither do the PCI or polarimetry chords. This complicates the mapping analysis, and also leads to uncertainty in the mode location. It has been assumed here and elsewhere in this work that the driven mode is localized to a narrow layer around the LCFS. This assumption is inspired by the recent measurements made with the Mirror Langmuir Probe (MLP) [32] described earlier, which show that the QCM, itself, is localized within a $\sim$ 3 mm layer spanning the LCFS. Moreover, the rapid-fall-off of the antenna vacuum field, and the experimental requirement of minimizing the gap between antenna and plasma in order to observe a strong driven response, limits the radial extent in which we expect to find the driven mode to the edge plasma. Nonetheless, at present, precise measurements of where the mode envelope is localized radially are not available; an experiment using the MLP to make these measurements has been planned, and will be run in the months following the completion of this thesis. However, because the field-line mapping between the antenna and these diagnostics remains sufficiently far from the single X-point, so that magnetic shear is low on the field line path, the results shown below pertaining to field-line mapping are robust against this uncertainty in the mode flux surface. This topic will be addressed again in the discussion of wave number estimates, Sec. 5.4.

Figure 5-5 provides a stronger indication of field-line guidance. The cross-section containing the PCI chords is shown, again with an illustration of the LCFS and the mapped Shoelace rung locations. In Figure 5-5b, a time-evolving, one-dimensional image of the induced perturbation is produced by stacking top-to-bottom the magnitude squared coherence at the antenna frequency for each PCI chord, and assembling all such images from each time slice, left-to-right. Overlaid on these images are the evolving locations of the Shoelace rungs mapped to the PCI cross section. The coherent signal is bounded in major radius by the extent reached by the Shoelace antenna rungs. Indeed, the four rungs that map to the smallest major radii mostly do not overlay with a perturbation, perhaps because of the increased gap between the plasma and the rungs at the lower portion of the antenna. Moreover, in the later part of the discharge, PCI seems to resolve very narrow lines of perturbation tracking closely the mapped rung locations. It should be noted that the electron diamagnetic drift

direction points toward the outward major radial direction (toward the top of the plot, as shown in the figure) at the location on the LCFS where the antenna maps to the PCI chords. One might conjecture that the lack of a driven fluctuation below the lowest rungs of the antenna in Figure 5-5 might be because the driven perturbation cannot propagate into this region. However, in reverse-field discharges, for which the electron diamagnetic drift velocity points in the opposite direction, the driven response is still restricted to mapped field lines, and the inner-most chords still do not observe a coherent response.

In fact, the field-line mapping criterion predicts accurately which diagnostics do and do not observe the driven perturbation. Figures 4-17 and 4-18 show top-down (R,ϕ) and unwrapped side-on (ϕ, z) views of the mapped field lines, together with the locations of a number of fluctuation diagnostics. Only the fluctuation diagnostics which map to the Shoelace antenna – namely, the PCI chords, one to three polarimeter chords, and a subset of Mirnov coils – ever observe a signal coherent with the antenna current.

Section 5.6 revisits the topic of the driven mode's field-line-guided nature in the context of identifying the physical origin of the observed plasma response to the antenna.

5.4 Driven Mode Wave Number and Propagation Direction

Thus far, the analysis has focused on the magnitude of the driven fluctuation. By examining its phase across several diagnostics, we may extract mode and wave numbers. Doing so shows that the driven mode has $k_\perp = 1.5$ cm^{-1} at the midplane, precisely the same value as imposed by the antenna winding structure; is approximately field-aligned; and has a phase velocity in the laboratory frame pointing in the same direction as the electron diamagnetic drift velocity, $\mathbf{v}_* = \nabla p_e \times \mathbf{B}/(n_e e B^2)$.

The PCI diagnostic provides a measurement of the major radial wave number, k_R,

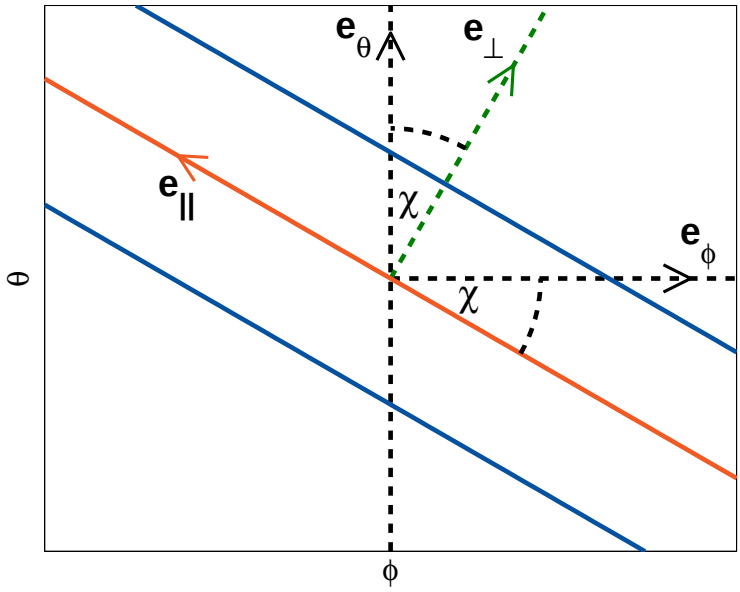

Figure 5-6: Schematic of field-aligned coordinate system when viewing inward toward the plasma core. Solid lines correspond to field lines. The directions of the unit vectors are indicated by arrows.

of the line-integrated density fluctuations. To derive wave numbers resolved within a flux surface, it is necessary to make an assumption about how the mode is localized. It is usually assumed [53, 33] that the mode exists in a narrow layer around a single flux surface, and that the PCI measurement, itself, can be localized to the point(s) where the chord intersects the mode's flux surface. Typically, the chords pass through a flux surface at an upper and lower point; however, only the lower intersection maps to the antenna on a field line, and so this ambiguity is removed. In the following, we first take the driven mode to lie nominally on the LCFS, and later explore what happens when this assumed mode layer is varied across other, nearby flux surfaces.

To aid in the calculation of wave numbers, we employ the ballooning coordinate system described by Dudson *et al.* [98] The coordinate[2], ζ, associated with a test point corresponds to the toroidal angle, ϕ, of the location at the outer midplane, $\theta = 0$, which maps on a field line to the test point. ξ is the poloidal angle, θ, of the test point; when ζ is held constant, varying ξ results in advancing along a field line. Here, the test points correspond to the intersections between the PCI chords and the

[2]This is denoted by z in the nomenclature of Dudson *et al.*, but ζ is used here to avoid confusion with the vertical component of the cylindrical coordinate system.

mode surface.

Figure 5-6 motivates a procedure for extracting a perpendicular wave number. The parallel direction corresponds to ξ, and the perpendicular direction to ζ. We relate the phase angle of the fluctuation signals, α, to the ξ and ζ coordinates associated with the PCI chords through the expression, $-\alpha_\ell = n\zeta_\ell + m\xi_\ell + \alpha_0$, for each chord, ℓ. The negative sign in front of α appears because α is derived from the phaser representation, $y(t) = \Re\left\{|A|\, e^{j(\omega t+\alpha)}\right\}$, while the mode number corresponds to the traveling wave, $e^{i(n\phi-\omega t)} = e^{j(\omega t-n\phi)}$ (taking $j = -i$). $n = -\frac{\partial\alpha}{\partial\zeta}$ is just the toroidal mode number. The corresponding wave number is $k_\phi = n/R$. Approximating the mode as field-aligned, $\mathbf{k} = k_\perp \hat{\mathbf{e}}_\perp$, and $-\alpha_\ell = n\zeta_\ell + \alpha_0$. To obtain $k_\perp$ given n, we take k_ϕ to be the projection of $\mathbf{k}$ onto the $\hat{\mathbf{e}}_\phi$ direction holding $\xi = \theta$ constant, such that

$$k_\perp = \frac{n}{\sin(\chi)\, R} \tag{5.1}$$

where $\tan(\chi) \equiv \frac{\sqrt{B^2 - B_\phi^2}}{B_\phi} = 1/\nu$, with $B_\phi = \mathbf{B}\cdot\hat{\mathbf{e}}_\phi$ the toroidal field strength, $\nu \equiv \frac{\mathbf{B}\cdot\nabla\phi}{\mathbf{B}\cdot\nabla\theta}$ the local field-line pitch [98], and χ and R are evaluated at the outer midplane.

The quality of the fit under the field-aligned approximation is apparent from Figure 5-7, which plots the phase angle, α, of each chord against the ζ coordinate, together with the least-squares fit to $-\alpha_\ell = n\zeta_\ell + \alpha_0$ from the outer 21 chords[3], using spectral analysis over a ~ 3 ms time slice. Note that α is "unwrapped" - differences between the phases of adjacent chords greater than or equal to π are eliminated by adding multiples of $\pm 2\pi$. The field-aligned approximation captures the phase progression across the PCI chords extremely well. As such, it may be concluded that taking $k_\perp \gg k_\parallel$ introduces a negligible error in the estimate for $k_\perp$.

It is also difficult to measure $k_\parallel$ using the PCI diagnostic. This is because the intersections between the chords and the lower LCFS span a poloidal range of $\theta_{32} - \theta_1 \approx 15^\circ$. By contrast, the range of ζ spans $\gtrsim 60^\circ$. These ranges, combined with the

[3]The outer 21 chords are selected from the full set of 32 because they reliably show a strong coherent signal with the antenna across a number of discharges. Not all of the inner PCI chords map to the antenna, as shown, for example, in Figure 5-5, and also the inner chords suffer greater attenuation in coherent signal because they map to points with increased gap between the antenna and the LCFS.

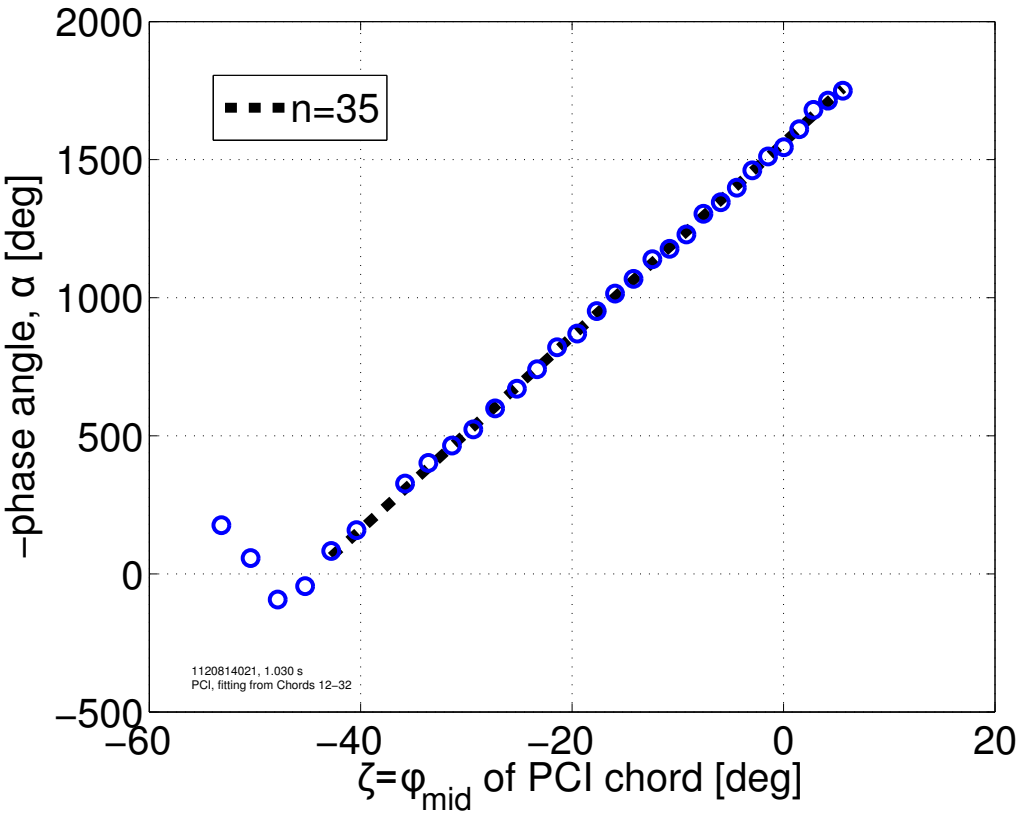

Figure 5-7: Quality of fit of expression, $-\alpha_\ell = n\zeta_\ell + \alpha_0$, across all PCI chords, ℓ. ζ_ℓ is the toroidal angle at the outer midplane (ϕ_{mid}) of the point which maps on a field line to the lower intersection of PCI chord, ℓ, with the LCFS.

expectation (derived from the QCM) that $k_\perp \gg k_\parallel$, means that the PCI diagnostic cannot provide a good measurement for $k_\parallel$, since most of the phase difference across the chords is due to the phase progression in the perpendicular direction. Diagnostic sets which cover a longer span along a field line, including the Mirnov coils, provide estimates for $k_\parallel$ which suffer from the fact that a small mapping error in ζ leads to a large discrepancy in phase, again a result of the fact that $k_\perp/k_\parallel \gg 1$. As such, a measurement of this quantity is not reported here. Instead, where an approximate value is needed, it is supplied as in Chapter 3 by assuming a parallel wavelength equal to twice the connection length, $L_c \approx 9$ m$\sim q_{95}\pi R$, which connects a point near the lower (upper) X-point to the top (bottom) of the plasma on a field line spanning the bad curvature region. Under this assumption, $k_\parallel \sim \pi/L_c = 0.0035$ cm$^{-1} \ll k_\perp = 1.5$ cm^{-1}.

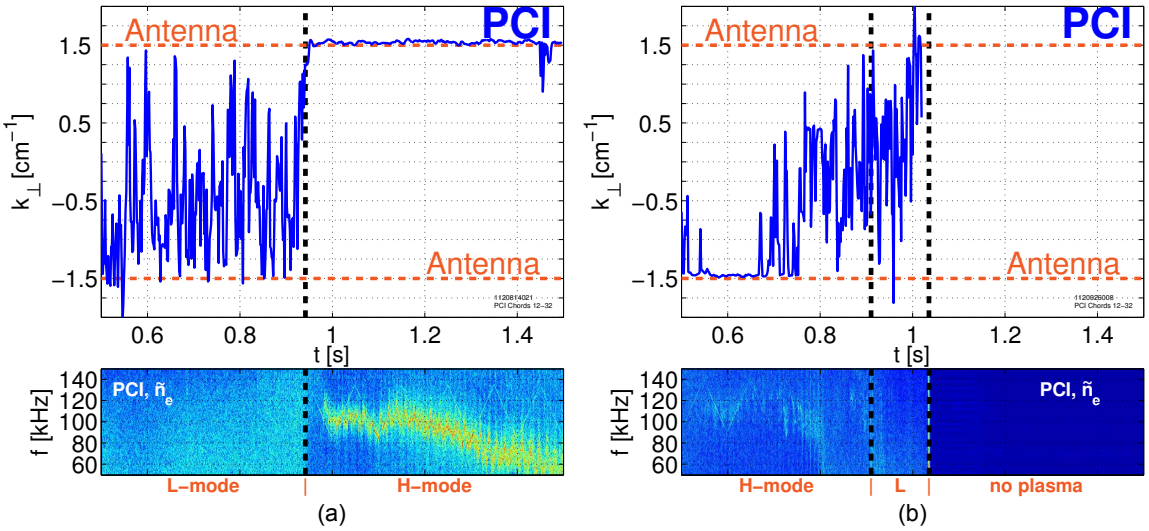

Figure 5-8: (a) Calculation of $k_\perp$ using the phase progression of the cross-power between the antenna current and the PCI chords from each time slice of the coherence spectrogram; a spectrogram from a PCI chord appears underneath, showing both the QCM and the Shoelace-driven perturbation. The sign of $k_\perp$ indicates propagation in the laboratory frame in the same direction as the electron diamagnetic drift velocity. (b) In this reversed field discharge, the value of $k_\perp$ for the driven fluctuation changes sign, consistent with the inversion of the electron diamagnetic drift direction. H-mode is lost just after 0.8 s, after which time the antenna produces no coherent density response.

Figure 5-8 shows the result of performing the calculation for $k_\perp$ using PCI data. Prior to the onset of H-mode, there is no coherent signal in the density fluctuation, and so the calculated value for $k_\perp$ varies randomly and rapidly. However, immediately after the H-mode transition, $k_\perp$ of the coherent signal locks to the value imposed by the antenna winding structure, namely, 1.5 cm^{-1}. Moreover, the sign corresponds to propagation in the laboratory frame in the same direction as the electron diamagnetic drift velocity.

Figure 5-8b reports data from a reverse-field discharge which had an early ELM-free H-mode (not EDA H-mode, and without an apparent QCM), followed by a back-transition to Ohmic L-mode, and finally terminating in a disruption. For reference, a spectrogram from this discharge of a single PCI chord is reproduced in Figure 5-10, accompanied by density and D_α traces. Here, again, during H-mode, $k_\perp$ settles precisely on the magnitude imposed by the antenna winding. However, now, the sign is negative, following the reversal of the field and electron diamagnetic drift directions.

It is prudent to examine how the assumption that the driven mode is localized to the LCFS affects the estimate for $k_\perp$. Figure 5-9a shows the result of repeating the $k_\perp$ calculation after assuming the mode is localized on each of 21 uniformly-spaced flux surfaces between $0.95 \leq \bar{\psi} = (\psi - \psi_0)/(\psi_{LCFS} - \psi_0) \leq 1.05$; at the midplane, this corresponds to a range from ~ 8 mm inside to ~ 8 mm outside the LCFS. The field-aligned approximation is still employed. The inset shows the value of $k_\perp$ obtained for each flux surface for a particular ~ 3 ms time slice around 1.20 s. The dashed lines highlight the FWHM band, $k_\perp = 1.5 \pm 0.1$ cm^{-1}, expected for the antenna's winding structure. The estimate for $k_\perp$ is robust against uncertainty in the identity of the flux surface to which the mode is localized. This is because the field lines that map the PCI chords to the midplane over this range of flux surfaces do not pass close enough to the X-point to experience significant magnetic shear. In fact, we might attempt to use this procedure to localize the driven fluctuation based on $k_\perp$-matching considerations; doing so would suggest that the driven mode sits in a layer between $0.98 \lesssim \bar{\psi} \lesssim 1.048$ ($-3 \lesssim R_{mid} - R_{mid,LCFS} \lesssim 7.5$ mm). However, this estimate is subject to error from the EFIT reconstruction. Nonetheless, it is consistent with the

expectation that the mode is localized in the edge, near the LCFS and overlapping with the QCM layer.

The phase information may also be reported directly as the toroidal mode number, n. This is done in Figure 5-9b. Here, the toroidal mode number obtained from the outer 21 chords of the PCI diagnostic is compared with that from two Mirnov coils spaced 4.8 toroidal degrees apart. Note that the field-aligned approximation is not applied to the analysis of the Mirnov coils, since they are displaced only in the toroidal angle. The values obtained from the two diagnostics are comparable, though there is a discrepancy between the stable value from PCI (between 31 and 34) and the Mirnov-supplied value prior to H-mode (during which time there is not a coherent $\tilde{n}_e$ fluctuation), and in the later part of the discharge. The lines labeled "antenna" correspond to the toroidal mode number for a field-aligned perturbation with $k_\perp = 1.5$ cm^{-1}; the positive line closely matches the measured toroidal mode number. Because the antenna drives a coherent $\tilde{B}_\theta$ response for the entire discharge, the Mirnov coils provide a measurement of n for the induced fluctuations prior to the onset of H-mode.

The fact that the toroidal mode numbers calculated from PCI (giving measurements of the driven mode below the midplane, and determined assuming $k_\parallel = 0$) and Mirnov coils (placed at a different poloidal angle above the midplane, and calculated without any assumption about $k_\parallel$) gives further confidence in approximating the driven mode as field-aligned, $k_\perp \gg k_\parallel$. This is consistent with a drift wave response, which tends to select the longest parallel wavelength, leading to the approximation using the connection length described above, $k_\parallel \sim \pi/L_c = 0.0035$ cm^{-1} $\ll k_\perp =$ 1.5 cm^{-1}.

The role of $\mathbf{E} \times \mathbf{B}$ flow also needs to be considered, as alluded to in Section 3.5. Recent measurements with the MLP [32] for ohmic EDA H-mode discharges like the ones discussed here have shown that in the QCM mode layer, the radial electric field points outward, so that the $\mathbf{E} \times \mathbf{B}$ and electron diamagnetic flows oppose one another (independent of the background field direction). As such, the QCM propagates in the electron diamagnetic drift direction in both the laboratory and

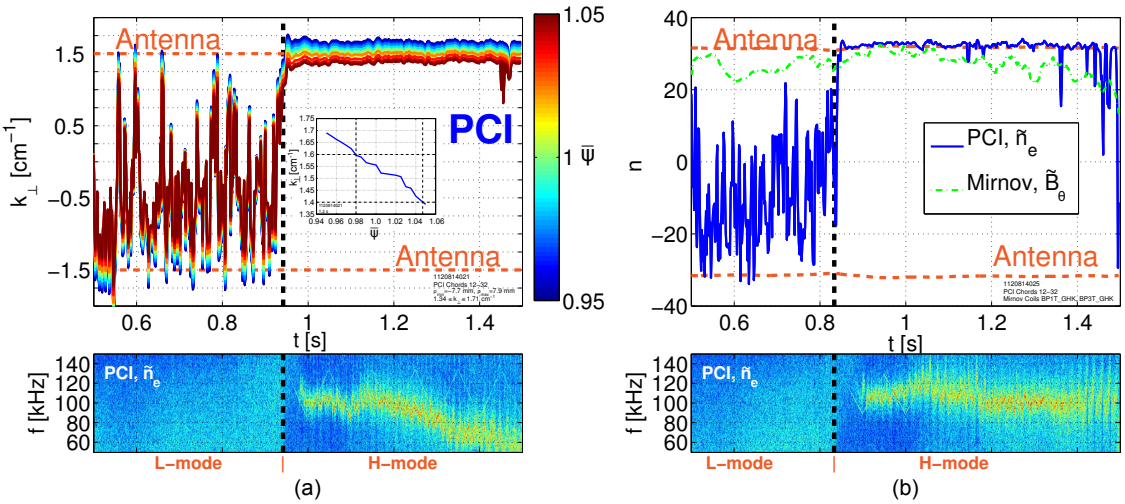

Figure 5-9: (a) Calculation of $k_\perp$ under field-aligned approximation, but taking the driven mode to be localized on any of 21 uniformly-spaced flux surfaces between $0.95 \leq \bar{\psi} = (\psi - \psi_0)/(\psi_{LCFS} - \psi_0) \leq 1.05$, as depicted by the line color; at the midplane, this corresponds to a range from ~ 8 mm inside to ~ 8 mm outside the LCFS. Inset: the value of $k_\perp$ obtained for each flux surface during a ~ 3 ms time slice around 1.20 s. The dashed lines highlight the FWHM band, $k_\perp = 1.5 \pm 0.1$ cm^{-1}, expected for the antenna's winding structure. (b) Toroidal mode number derived from Mirnov coils, as well as PCI measurements, from a different discharge. The Mirnov coils pick up a coherent response in $\tilde{B}_\theta$ for the entire antenna pulse, allowing a measurement of n for the driven fluctuations prior to the onset of H-mode. Also included is the antenna toroidal mode number corresponding to $k_\perp = \pm 1.5$ cm^{-1} for a field-aligned perturbation. The subplot shows a spectrogram from a single PCI chord.

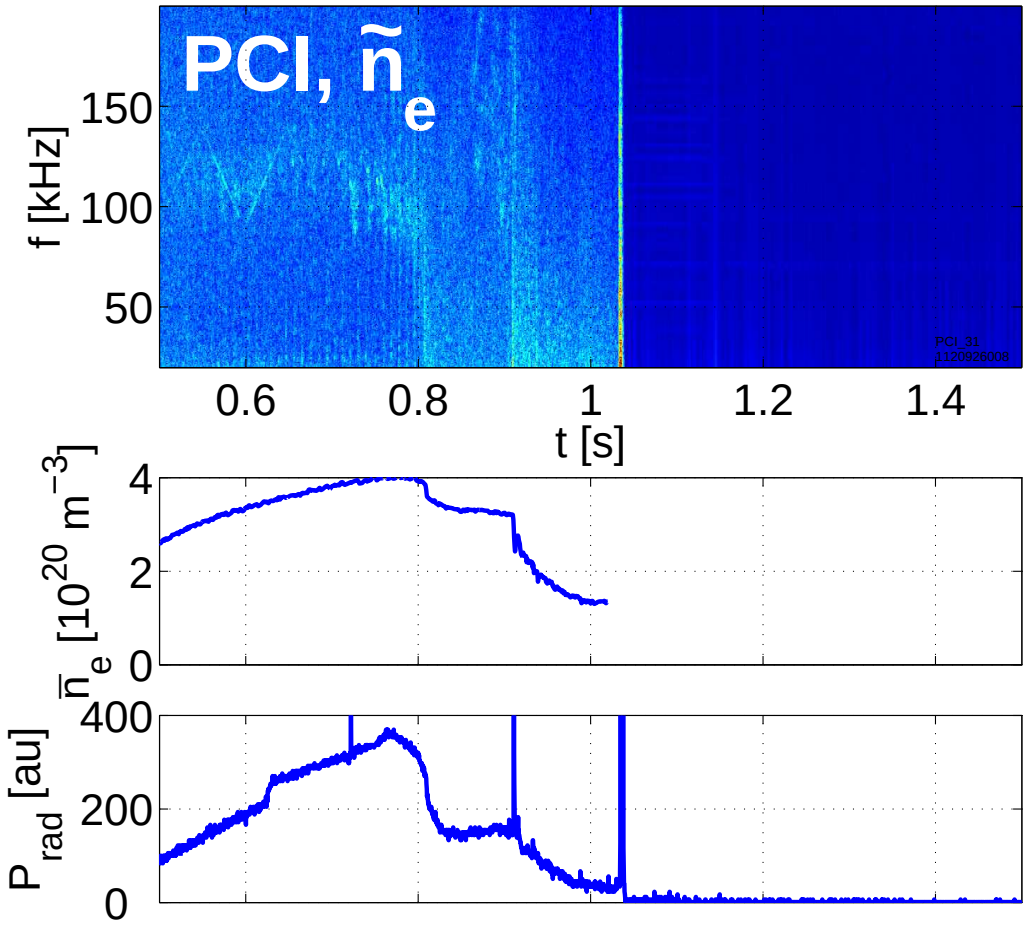

Figure 5-10: Spectrogram of reverse-field discharge in which a resonant response to the antenna appears on the diagnostic signals, but where there is no apparent intrinsic QCM.

plasma frames. But ~ 1 mm inward from the LCFS, the $\mathbf{E}\times\mathbf{B}$ flow changes directions, with $\mathbf{v_E} = \mathbf{v}_*$ at ~ 2 mm inside the LCFS. If the antenna-driven mode is confined to the same narrow radial layer as the QCM, as assumed above, then it also rotates in the electron diamagnetic drift direction in both the plasma as well as the laboratory frame. However, a precise measurement of the driven mode layer is necessary in order to make this statement with certainty; at present, this measurement is not available.

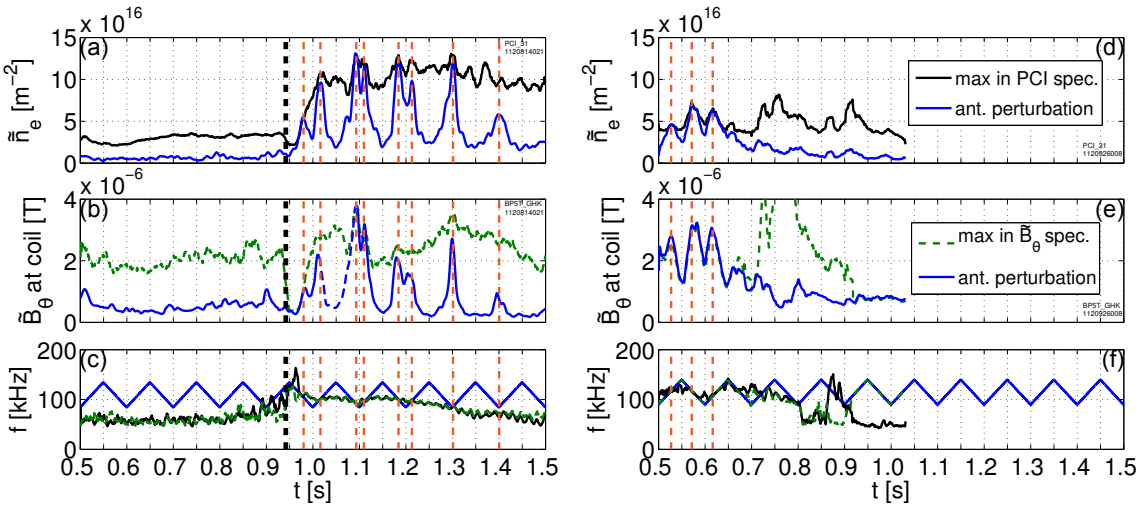

Figure 5-11: Magnitude of coherent response, $x|P_{xy}/P_{xx}|$, where x is the antenna current and y is the fluctuation signal, for (a,b,c) a forward-field shot with an intrinsic QCM and (d,e,f) a reverse-field shot with no prominent intrinsic QCM. The responses are from (a,d) a PCI chord and (b,e) a Mirnov coil. The bottom subplots (c,f) show the antenna drive frequency (blue solid line), together with the peak frequencies in the PCI (black solid) and Mirnov coil (green dashed) spectra. Orange vertical dashed lines highlight peaks in the coherent response.

5.5 Transfer Function Analysis

Up until now, we have focused on the coherence of fluctuations in short (∼3 ms) time slices. It is also instructive to examine the response across an entire frequency scan, typically covering ∼40 kHz, through the lens of the transfer function, a quantity introduced in Eq. 4.8 and the associated discussion.

Indeed, analysis of the transfer function reveals that the frequency response of the Shoelace antenna is strongly peaked in H-mode, but not in L-mode. Figure 5-11 illustrates this point. It shows an estimate for the absolute amplitude of the coherent response obtained by scaling the transfer function by the antenna current amplitude, $|H \cdot I_a|$. Both the line integrated density fluctuation, $\tilde{\bar{n}}_e$, from a PCI chord and the poloidal field fluctuation, $\tilde{B}_\theta$, measured at a Mirnov coil are shown[4]. For comparison, the amplitude of the maximum spectral component of the fluctuation signal in the band from 40 to 200 kHz is overplotted. The frequency of the maximum component for

[4]Extrapolating $\tilde{B}_\theta$ to the LCFS requires scaling by a factor $\sim 10^2$ that is very sensitive to the spacing between the LCFS and the wall-mounted coil.

each fluctuation signal is included in a subplot, together with the antenna frequency. The data on the left-hand side (Figure 5-11a-c) are from the same discharge as that shown in Figure 5-3, which had a fully-developed EDA H-mode with a QCM. The data on the right-hand side (Figure 5-11d-f) correspond to the discharge in Figure 5-10, which had a short-lived ELM-free H-mode and no prominent QCM.

Each time the antenna frequency crosses the peak in the PCI spectrum – a proxy for the QCM center frequency – there is a sharp peak in the coherent response, such that the amplitude of the coherent fluctuation matches the peak amplitude in the spectrum. This is true for both $\tilde{\tilde{n}}_e$ and $\tilde{B}_\theta$ measurements. We may wonder whether the antenna is driving a fluctuation of this amplitude, or is locking the intrinsic mode to its own phase. The second possibility might seem more plausible given that the total peak fluctuation amplitude increases only slightly when the antenna crosses the QCM frequency.

However, in experiments examining nonlinear interaction between a driven mode and a coherent drift wave structure on a linear device, Brandt *et al.* [80] observed frequency pulling and the appearance of sidebands in the fluctuation spectra. These features are, at best, hard to discern from the fluctuation spectra obtained during Shoelace antenna operation given the rapid variability of the intrinsic QCM, as evidenced by the analysis in Sections 5.7.2 and 5.7.3, though higher antenna power may be needed to access this behavior.

Appendix F investigates the possibility that the apparent peaks in the transfer function are simply the result of an artifact in the transfer function signal processing techniques causing the intrinsic peak in the QCM to appear as a driven feature. The analysis finds that while such erroneous peaks in the response can be generated, the driven peaks observed in this section are larger in magnitude by a factor of three to four, and are also characterized by a phase progression which reproduces the wave number and propagation direction observed above, a property that the smaller, erroneous peaks do not share.

In addition, in the case where there is no apparent QCM, the response is still peaked around a particular frequency, as shown in the data in Figure 5-11d-f, sug-

gesting a resonance. During the ELM-free H-mode, the coherent response dominates the PCI spectrum most of the time, and the Mirnov coil response all of the time. The peaks in the density response are shallower than, but still comparable to, those in the EDA case in 5-11a-c. This is a significant result, and suggests that, on mapped field lines, the antenna might be able to drive a fluctuation close to the level of an intrinsic QCM, even when no such intrinsic mode is present. Given the QCM's role in regulating the pedestal, we might also speculate that the antenna drives transport on mapped field lines similar to the intrinsic mode; future experiments have been planned to investigate this exciting possibility.

Before proceeding, it is important to point out that when the field pitch angle evolves during the discharge, it is necessary to remove a phase offset. This was not necessary in the calculation of mode numbers using the short-time spectral analysis because the time slices were on the order of ∼3 ms, and the pitch angle evolves on a longer time scale, as evidenced by the mapped rung locations overplotted on the time-evolving 1D coherence image in Figure 5-5. However, over the course of a complete frequency scan, lasting 50 ms in these experiments, the pitch angle can change appreciably. This effect may be accounted for in the transfer function as $H_c(j\omega) = H(j\omega)e^{-j\Delta\alpha} = H(j\omega)e^{jn\Delta\zeta}$, where the subscript, c, denotes calibration, and $\Delta\zeta = \zeta(t) - \zeta_0$ the change in the toroidal angle mapped to the outer midplane after an elapsed time, t.

Figure 5-12 shows the transfer function magnitude and phase over a single frequency scan from three mapped diagnostics: a PCI chord, a Mirnov coil, and a polarimeter chord. The data are from the same forward-field discharge described in Figure 5-11a-c. The magnitudes are normalized by the maximum value over the scan so that data from different diagnostics can be compared, while the phase is adjusted according to the discussion above. The peak frequency, FWHM, and relative phase transition match across the three diagnostics. The relative change in phase of 180° over the frequency scan further suggests that the response may be modeled as a

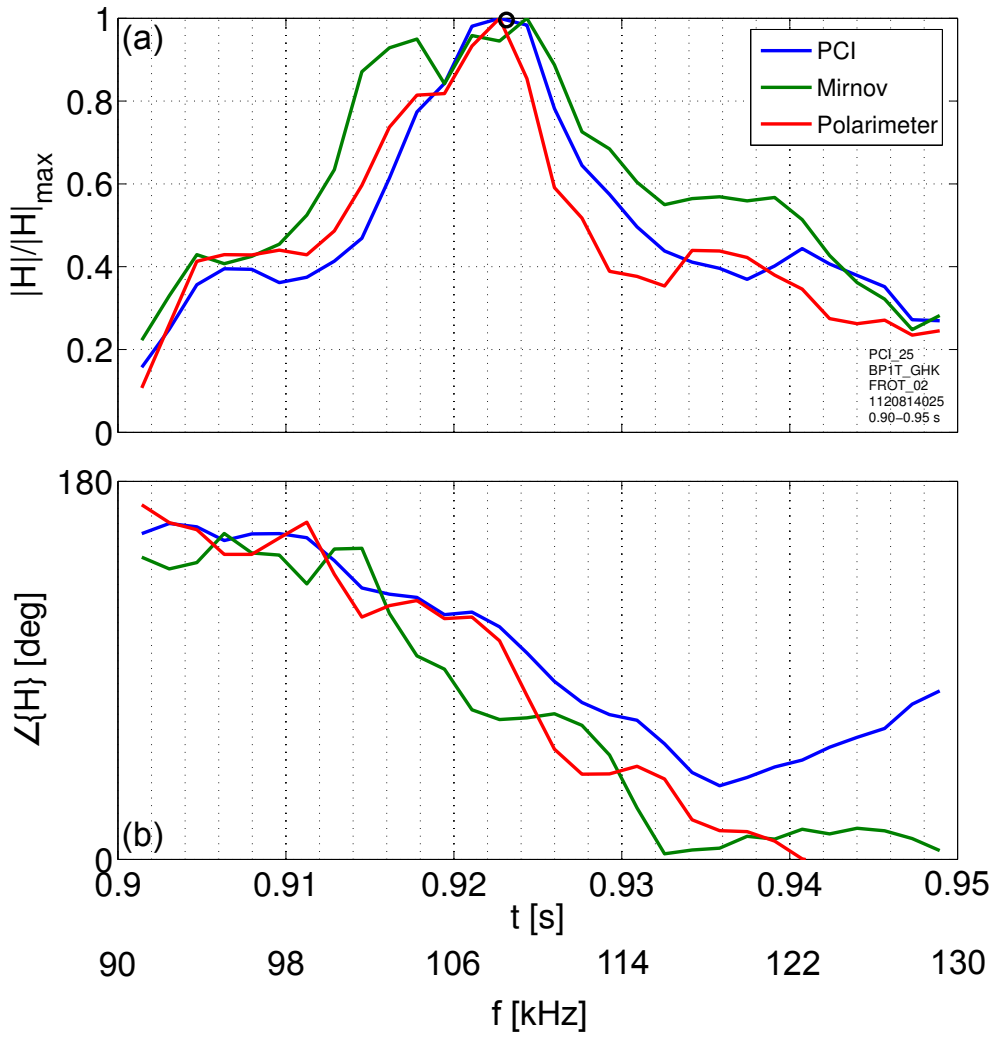

Figure 5-12: (a) Transfer function magnitude for a PCI chord, a Mirnov coil, and a polarimeter chord over a single frequency scan, normalized to the maximum value over the scan for each diagnostic in order to allow comparison. (b) Phase of the transfer function over the course of the same scan, adjusted by the phase offset, $n\Delta\zeta$, to account for the change in the mapped toroidal angle, $\Delta\zeta$, for each diagnostic, following the mapping procedure described in Section 5.4.

simple pole using an expansion of the form,

$$H_c(j\omega) = H_0 + \frac{A}{\gamma + j(\omega - \omega_0)} + \frac{A^*}{\gamma + j(\omega + \omega_0)} \tag{5.2}$$

where H_0 is a real constant offset, A is the complex residue, A^* its complex conjugate, γ the damping rate, ω_0 the resonant angular frequency, and the property that $H(-j\omega) = H^*(j\omega)$ ensures a purely real output signal. The residue, damping rate, and resonant frequency may then be used to characterize the peak.

Figure 5-13 examines the transfer function for a forward-field shot with a strong QCM (Figure 5-13a,b), as well as a reversed-field shot with no apparent QCM (Figure 5-13c,d). In both cases, the plot of the transfer function in the complex plane (the Nyquist plot), shown with a blue solid line, executes a circular trajectory, rotating in the clockwise direction for increasing frequency. The green solid line plots Eq. 5.2 with parameters fit to the same peak; this functional form always appears as a circle in the complex plane, circulating in the clockwise direction when $\gamma > 0$ (implying a damped response).

The phases, α, of the pole residues, A, used to fit the transfer function are also tracked and unwrapped, again revealing a major radial wave number, k_R, that (a) matches the antenna $k_\perp$ after assuming a field-aligned structure and mapping to the midplane, and (b) points in the direction of the electron diamagnetic drift direction, flipping sign between the forward- and reverse-field cases.

Having closely analyzed the phase of the residue, we may investigate the other fit parameters of Eq. 5.2. Figure 5-14a plots the resonant frequency, $f_0 = \omega_0/(2\pi)$, for each frequency scan, along with the peak in the PCI spectrum (black solid line) and the antenna drive frequency (black dashed line). f_0 is reproduced with little scatter across multiple PCI chords (blue solid lines), Mirnov coils (green solid lines), and polarimeter chords (red solid lines). Moreover, it tracks very closely the frequencies at which the antenna drive crosses the peak PCI frequency, recovering the result mentioned earlier that the peak frequency matches the QCM frequency when there is a QCM present.

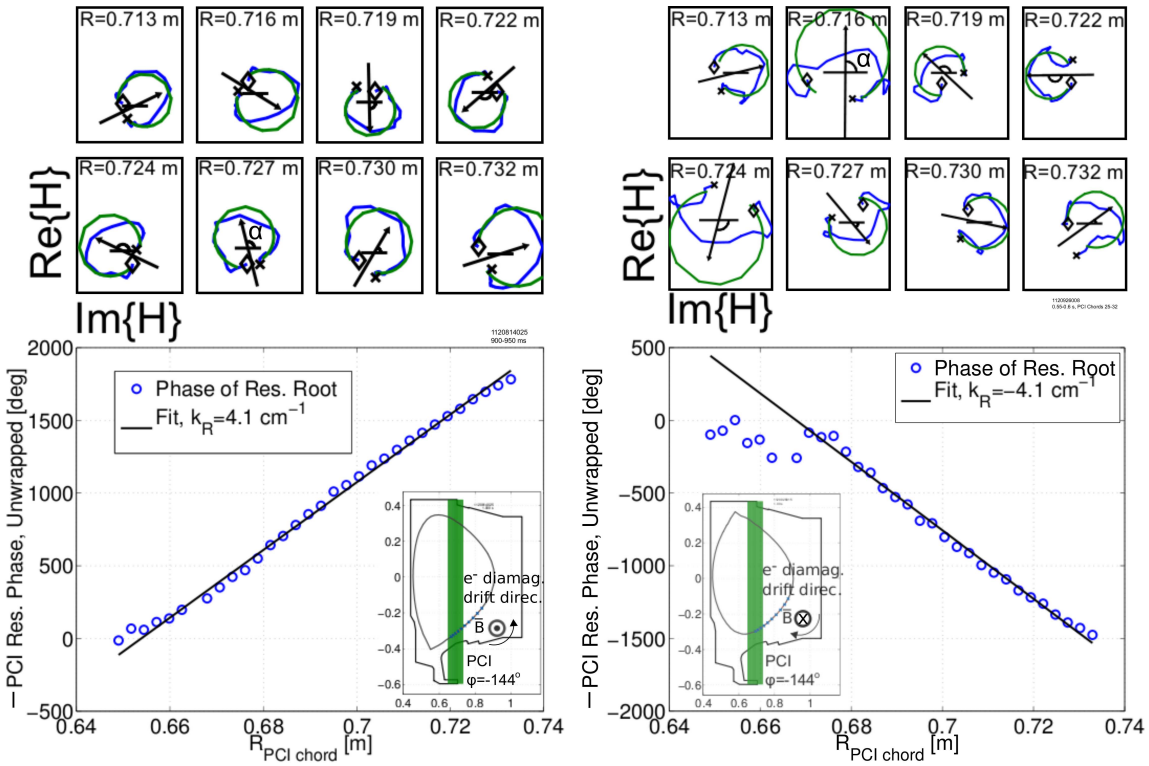

Figure 5-13: (a) Plot in complex plane of transfer function, H, for the eight outermost PCI chords (blue solid line), together with parameterized fit using Eq. 5.2 (green solid line). Arrows indicate phase angle of residue, A. The fact that circular trajectories of H are advancing in the clockwise direction for increasing frequency is indicative of a damped resonance. (b) Plot of -1 multiplied by the unwrapped phase angle of each pole residue from each chord versus corresponding chord major radius. The slope gives the major radial wave number, k_R. An inset shows Shoelace mapping on the LCFS in the PCI plane, as well as the B_ϕ and electron diamagnetic drift directions. (c,d) Here, the data is from a discharge with reversed field. Again, the sign of k_R is flipped, following the inversion of the electron diamagnetic drift direction. No QCM was present in this discharge, but the antenna response still appears to be a weakly-damped resonance.

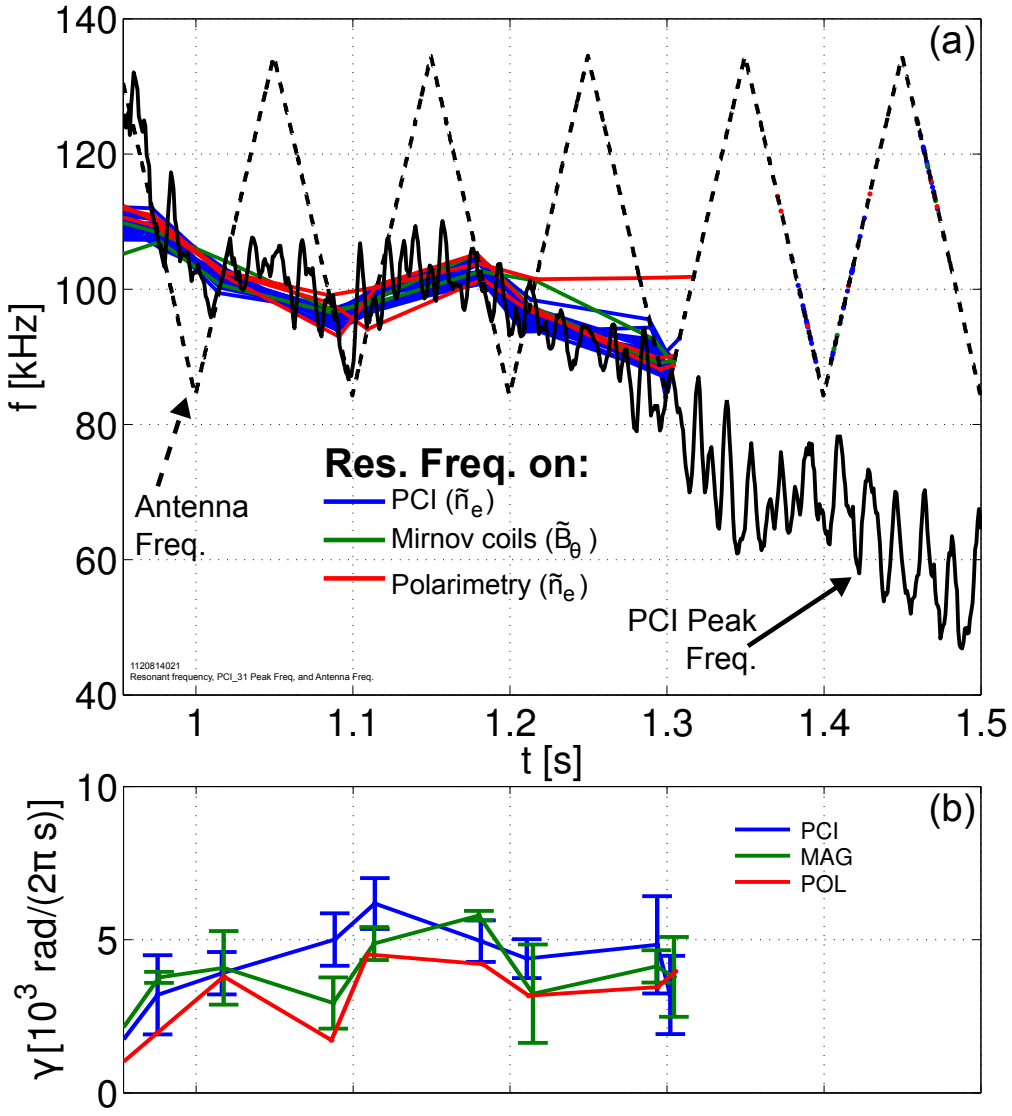

Figure 5-14: (a) Resonant frequency from PCI (blue solid lines), Mirnov coils (green solid), and polarimetry (red solid); antenna freq. (black dashed); peak PCI freq. (black solid). The resonant frequency tends to track the QCM frequency, whose proxy here is the peak in the PCI spectrum. (b) Damping rate across discharge, as determined by transfer function between antenna current and fluctuation signals from a Mirnov coil, a PCI chord, and a polarimeter chord. Damping rates from a wide variety of discharges are low, settling to a value between $\gamma/\omega_0 = 5 - 10\%$, where ω_0 is the resonant angular frequency.

Figure 5-14b shows the damping rate, γ, normalized by 2π for comparison with the resonant frequency. The error bars correspond to the standard deviation across independent measurements of an individual diagnostic. A damping rate of $\gamma/\omega \approx\sim 5\%$ appears across all diagnostics. The damping rate in the reversed field discharge shown in Figure 5-11d-f is higher - around 10% - and displays more scatter across the diagnostics. The range, $\gamma/\omega_0 = 5 - 10\%$, is typical of these experiments, indicating that the driven mode is only weakly damped.

The measured damping rate is discussed further in Appendix H in light of complications introduced by strong edge gradients and magnetic shear.

5.6 An Interpretation of the Field-Line-Guided Behavior

Now that the plasma response to the Shoelace antenna has been more fully described, let us return to the topic of the field-line-guided response of the Shoelace-induced perturbation. This observation is particularly interesting, since it is distinct from the QCM, which is global on the low-field side, and since it would otherwise be expected that the perturbation should propagate across field lines in the EDD if the mode is, indeed, of drift wave origin, like the QCM. A response strongly guided by magnetic field lines is reminiscent of resonance cones [110, 111, 112, 109, 113, 76]. This phenomenon was discussed in Section 3.4.2 in the context of electrostatic modes of a cold, homogeneous plasma, for which the wave energy was found to spread from the field line at an angle of $\tan(\theta) = k_\parallel/k_\perp$, a very small ratio in the present context. But such electrostatic modes were found to be strongly damped by electron-ion collisions. Moreover, accounting for warm plasma effects revealed the electrostatic modes with wave numbers in the vicinity of those expected of the driven mode to be in cutoff (see the $T_e = 50$ eV line of Figure 3-4, which corresponds to the temperature, density, field and approximate plasma-frame frequency of the driven mode at the LCFS). As such, resonance cones are not expected to play a role in the antenna response.

Section 3.4 showed that the group velocity of the shear Alfvén wave also runs parallel to the background field. Recall that a field-guided response was observed by Borg *et al.* in experiments on the TORTUS tokamak using a single dipole antenna driven below the ion cyclotron frequency and intended to excite shear Alfvén waves [81]. That dipole antenna essentially constitutes a single field-aligned rung on the Shoelace antenna. However, a shear Alfvén wave explanation for the antenna-driven mode does not, by itself, capture the observed resonance at the QCM frequency.

The simple interchange modes examined in Section 3.3 were found to have a purely imaginary frequency; since these are ideal MHD modes, ω^2 must be a real number, so we might presume that the modes do propagate when they are stable. However, the interchange mode analysis was carried out assuming $\nabla_\parallel \to 0$, and ballooning modes, the extension of the interchange mode to the tokamak topology, also share this fluted character. As such, $k_\parallel$ does not appear in the simplest descriptions of these modes, and it is not expected that their group velocity should be parallel to the background field, even using more advanced models.

Likewise, the group velocity of the drift wave is in the perpendicular direction, $\mathbf{v}_g = \partial\omega/\partial\mathbf{k} = \mathbf{e}_\perp v_*$, which seems in conflict with the observed field-line-guided behavior. Does the fact that the driven response is limited only to the flux bundle that maps directly to the Shoelace antenna on the LCFS sufficient to reject the drift wave hypothesis for the driven mode, or can we conjecture a scenario which is consistent with the driven mode having a drift wave character, while still displaying the field-line-guided behavior?

In formulating such a scenario, it should be noted that the antenna only overlaps with a short section of the field line on the LCFS, on the order of $w/L_c \approx 0.15\,\mathrm{m}/9\,\mathrm{m} \simeq 1.7\%$ of the connection length – nearly describing an impulse along the field line coordinate. While we expect an induced drift wave to propagate in the perpendicular direction, the fluted character of drift waves ($k_\perp \gg k_\parallel$) also implies parallel dynamics tend to rapidly equilibrate disturbances along a field line. We should look to shear Alfvén waves in attempting to understand the parallel dynamics to the narrow (along the field line) disturbance driven by the antenna, since the

coupling between a perturbation in pressure and the kinetic shear Alfvén wave is so closely associated with drift wave physics [65, p. 4.12]. This may then recover the field-guided response.

One possible interpretation is as follows: the antenna launches a drift wave in the plasma in the immediate vicinity in front of the winding, where the vacuum field perturbation is strong. This wave couples to a kinetic shear Alfvén wave[5], which then propagates in the parallel direction, signaling the presence of the antenna-driven drift wave on mapped diagnostics. The resonance around the QCM frequency belongs to the drift wave, and not the Alfvén wave, but the Alfvén wave response nonetheless traces out the peak, since its amplitude is tied to that of the drift wave, and is essentially in phase as measured on fluctuation diagnostics, since $\Delta\ell/v_A \lesssim 1\ \mu\text{s} \ll 1/f_{QCM}$, where $\Delta\ell$ is the distance along a field line on the LCFS between the antenna and a diagnostic. The density response measured by PCI and polarimetry would not be consistent with the ideal MHD picture of the shear Alfvén wave in a homogeneous plasma, but it is consistent with the kinetic shear Alfvén wave.

But if the pressure disturbance of the drift wave induced directly in front of the antenna launches kinetic shear Alfvén waves in the parallel direction, so, too, should any wave fronts which propagate off the antenna rungs in the perpendicular direction. Why don't these wave fronts, too, launch shear Alfvén waves along field lines, carrying the perturbation signal to fluctuation diagnostics not mapped to the antenna?

This may be reasoned as follows: the small amount of energy that is coupled to the drift wave spreads out almost instantaneously along the low-field side as a shear Alfvén wave, launched by the drift wave, transiently equilibrates the field line in response to the pressure disturbance in front of the antenna. On field lines which map to the antenna, the diagnostics intercept the disturbance as it is spread across the entire field line, "catching" the disturbance as it passes. On field lines beyond those which map to the antenna, the disturbance has already equilibrated over the whole field line and is too weak to measure.

[5]The reference to the "kinetic" shear Alfvén wave here is used capture the result from the drift-ordered model that pressure disturbances can excite shear Alfvénic activity, even in a plasma with a homogeneous background field and pressure [65, p. 4.6-4.7, 4.11-4.12].

Here, we are treating this system as though there were a single resonance to which the antenna couples, with the damping rate measured above of 5-10%. It is assumed that the wave actually propagates in the perpendicular direction for a number (∼10-20) of wavelengths before it is appreciably damped, but the wave energy is spread out too thinly to be measured. If this is the case, we should, in principle, be able to show a proportionally weaker driven mode signal as the distance along a field line is advanced. However, due to both mapping errors and limited diagnostic access, it is difficult to make such aligned measurements along a field line. Driving the mode harder such that the fully-equilibrated field line still contains a sufficient disturbance to be measurable might be another way to justify this interpretation. Such higher-power experiments are being planned as of the preparation of this thesis (see Section 6).

However, another possibility is that all of the wave energy is damped at the upper and/or lower bounds of the plasma, especially at the X-point, where significant magnetic shear is strongly stabilizing for a drift wave. But if this is the case, then we would expect that the driven mode should be strongly, rather than weakly, damped, with a damping rate closer to γ/ω ∼100% (strong damping over a single perpendicular wavelength) than 5-10%. It is conceivable that spatial dependence of the driven mode dispersion relation, in addition to shear in the magnetic topology, might lead to a discrepancy between the actual damping rate and the value of 5-10% reported above. This issue is explored in Appendix H, where it is shown that the measured damping rate is not likely to be suffering from these kinds of errors.

Unfortunately, without a measurement of the phase difference between the induced $\tilde{n}_e$ and $\tilde{\Phi}$ fluctuations, it is not possible to conclusively identify the driven mode as having a drift wave character; the discussion in this section merely addresses whether such a physical origin is consistent with the observed plasma response to the antenna. It is expected that this data will become available in the months following the submission of this thesis.

5.7 Does the Shoelace Antenna Interact with the Intrinsic Mode?

In their study of open-loop control of drift waves by internal and external actuators, Brandt *et al.* and Schröder *et al.* observe two signs of nonlinear interaction between the exciter and the intrinsic coherent mode: (a) a sideband structure developing at the sum and difference frequencies between the exciter and intrinsic mode when the exciter is driven off-peak, and (b) locking (synchronization) and frequency pulling between the drive and the intrinsic mode [78, 79, 80]. They also differentiate between density perturbations driven by the exciter, but not constituting a drift wave, and driven perturbations which couple to a coherent drift wave. The phase difference between the density and potential perturbations provides the distinguishing feature between the two cases, as alluded to in Chapter 3. In the former case, where the driven fluctuations do not couple to a drift wave, the phase difference between $\tilde{n}_e$ and $\tilde{\Phi}$ is $\pi/2$. When coupling to a drift wave is achieved, the phase difference is nearly 0, as expected.

The ideal tool on Alcator C-Mod to measure the phase difference between $\tilde{n}_e$ and $\tilde{\Phi}$ is the mirror Langmuir probe, which performed this very characterization of the intrinsic QCM [32]. However, because this diagnostic did not map to the Shoelace antenna, such measurements were not possible for the driven mode.

Spectral analysis comparing fluctuations measured on field lines which do map to the antenna with measurements on those that do not may determine whether these sideband or locking phenomena occur. Two elements of this analysis are shown below: a comparison of power spectra over a narrow time range (Section 5.7.2), and comparison of the peak frequency in the spectra over the duration of the H-mode (Section 5.7.3). Broadly speaking, while there are hints that sidebands and frequency locking do occur, it is hard to clearly identify either behavior, as the apparent observations of this nonlinear interaction might simply be an imagined interpretation of the natural variability in spectral structure, as well as the frequency modulation, of the intrinsic mode.

In addition to this open-loop approach, the antenna power system was built to explore closed-loop, feedback control of the intrinsic mode. However, only preliminary work was carried out using this functionality. This topic is discussed below in Section 5.7.1.

5.7.1 Antenna Operation with Phase Lock to QCM

As described in Section 4.4.4, the Shoelace antenna power system has the capability to lock in real-time to an analog fluctuation diagnostic signal with a coherent feature in the QCM band, 50-150 kHz, adding a phase delay tunable in 64 steps between 0 and 360 degrees. The phase lock system was built to explore whether the antenna may feedback stabilize, or further destabilize, the intrinsic QCM, and whether it may also impart a torque to the plasma, in an analogous manner to an AC motor, where the antenna plays the role of the stator and the current filaments of the QCM, the rotor. However, as of the preparation of this thesis, only four useful discharges were executed under this line of inquiry. Further experiments are needed to determine the efficacy of this closed-loop control.

Nonetheless, the functionality of the phase lock system was successfully demonstrated in initial experiments, as shown in Figure 5-15. Here, a spectrogram of a PCI signal is accompanied by traces of the PCI peak (blue solid line) and antenna drive (green solid line) frequencies, as well as the antenna current. The antenna frequency closely tracks the rapidly-varying PCI peak frequency, while the antenna current remains near 80 A throughout the discharge as the matching network continually adjusts its tuning following the changing frequency. Pre-programmed amplitude modulation was applied to the current to help distinguish the antenna-driven fluctuation from the intrinsic QCM.

Figure I-10 in the appendix shows additional data obtained during operation of the phase lock system.

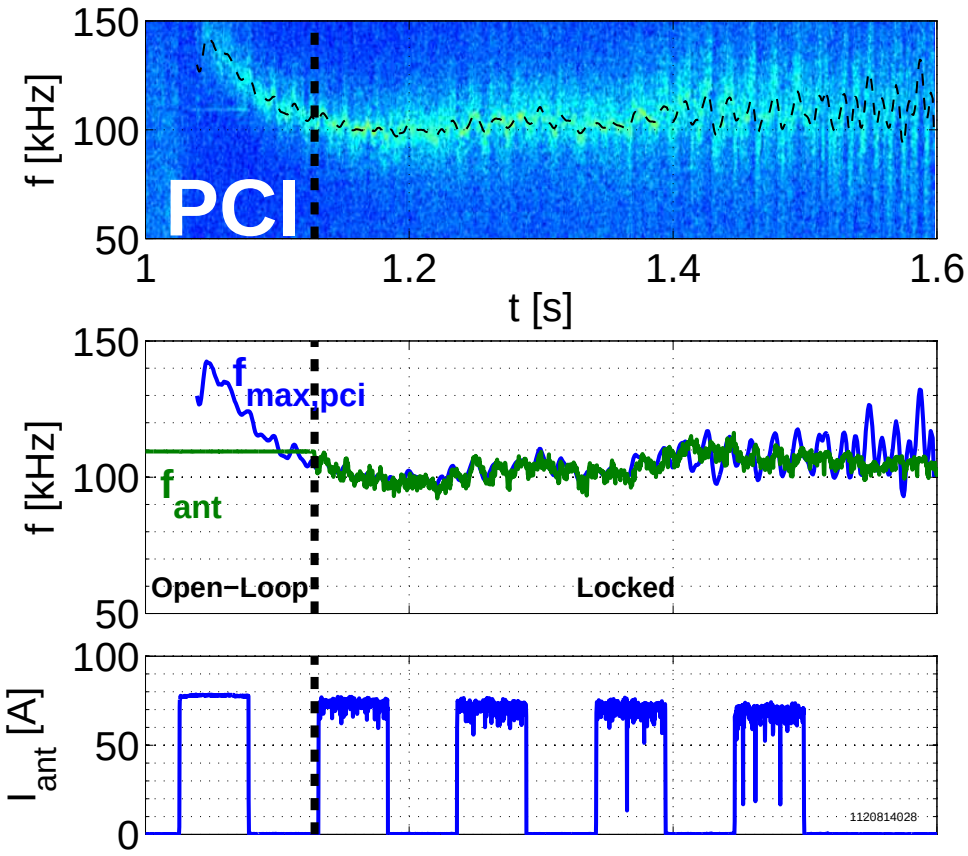

Figure 5-15: Demonstration of phase lock. (Top) Spectrogram of PCI diagnostic; thin dashed black line highlights peak frequency in PCI spectrum, thick black dashed line indicates transition from open- to closed-loop control. (Middle) PCI peak frequency ($f_{max,pci}$, blue) overplotted with antenna frequency (f_{ant}, green). The cross-power between the phase-locked-loop-generated signal and the PCI diagnostic signal surmounts a logic threshold at 1.128 s, so that control is automatically switched from a pre-programmed (open-loop) constant frequency to the locked signal, whereupon f_{ant} closely tracks f_{peak}. (c) Antenna current remains high, despite rapid frequency modulation. The current is intentionally amplitude-modulated at 9.5 Hz.

5.7.2 Comparing Mapped and Unmapped Power Spectra

To understand whether the antenna affects the intrinsic QCM, it is useful to make a comparison between perturbed and unperturbed fluctuations. Fluctuation spectra measured on field lines which are far from being mapped to the antenna may provide a good reference for the "unperturbed," background spectrum. These may be compared against "perturbed" spectra measured on field lines that do map to the antenna. This analysis is carried out below, where power spectra are presented for three pairs of "mapped" and "unmapped" Mirnov coils, as well as one pair of mapped and unmapped polarimeter chords.

The locations of the Mirnov coils and polarimeter chords used in this comparison are shown in Figure 5-16. Note that the vertical component of the electron diamagnetic drift velocity points upward in these figures for this forward-field discharge. The two Mirnov coils in each pair are essentially displaced only toroidally; axisymmetry implies that such pairings ought to have a good parity in the background spectrum. On the other hand, all available polarimeter chords intersect the plasma in a single toroidal section, and so the measurements for this diagnostic are displaced only poloidally. The unmapped Mirnov coils are far from field lines which map to the Shoelace antenna, while the lower polarimeter chord is only displaced from the bundle of mapped field lines by a small perpendicular distance. Nonetheless, for both the Mirnov coil and polarimeter chord pairs, only the fluctuation measurements which map to the antenna show a strong coherent response, as seen in the magnitude squared coherence spectrograms of Figure 5-17.

The power spectra shown below are computed over 3 ms bins[6], and have roughly 500 Hz frequency resolution. The magnitudes of these spectra are then smoothed with a ∼3 kHz (six-point) moving average, normalized again by the peak in the frequency range between 50 and 150 kHz, so the spectra between different coils and chords may

[6]the signal sampling rate is f_s =2.5 MHz for the Mirnov coils, and 4 MHz for the polarimeter chords, and the size of the Hamming window used in the discrete spectral analysis is $n_w = 2^{12}$ samples for the Mirnov coils and 2^{13} for the polarimeter chords, so the spacing between frequency points in the spectra is $f_s/n_w \approx 610$ Hz for the Mirnov coils, and ~ 490 Hz for the polarimeter chords.

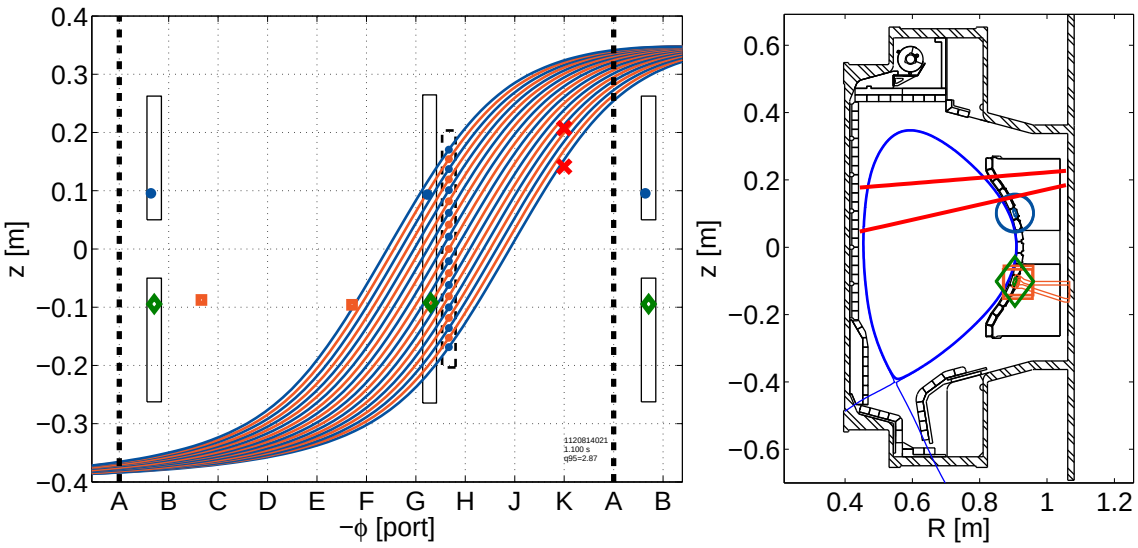

(a) (b)

Figure 5-16: Location of diagnostics used in comparison of power spectra, together with magnetic reconstruction of plasma at 1.100 s on the same discharge. (a) Unwrapped view of ϕ, z plane, showing field lines mapping to antenna rungs on LCFS, together with the positions of three pairs of Mirnov coils and the pair of polarimeter chords, projected onto the LCFS as discussed in Section 4.5.2. Pairs of coils have the same shape and color; the red X's correspond to the polarimeter chords, while the other markers signify the Mirnov coils. The toroidal angle is indicated by the port label, with each port separated by 36° toroidally. The wall and diagnostics are wrapped across the vertical black dashed lines. (b) Locations of diagnostics collapsed onto a single R, z cross section, superimposed on the outline of the vacuum vessel, as well as the limiter and divertor tiles. Colors and shapes are as in (a) (the full polarimeter chord paths are drawn here, rather than their intersections with the LCFS as in (a)). Outlines of the Mirnov coils, themselves, are also drawn, together with supporting hardware. The LCFS is drawn (thick blue line), together with the 100.2% flux surface (thin blue line) to indicate the strike points.

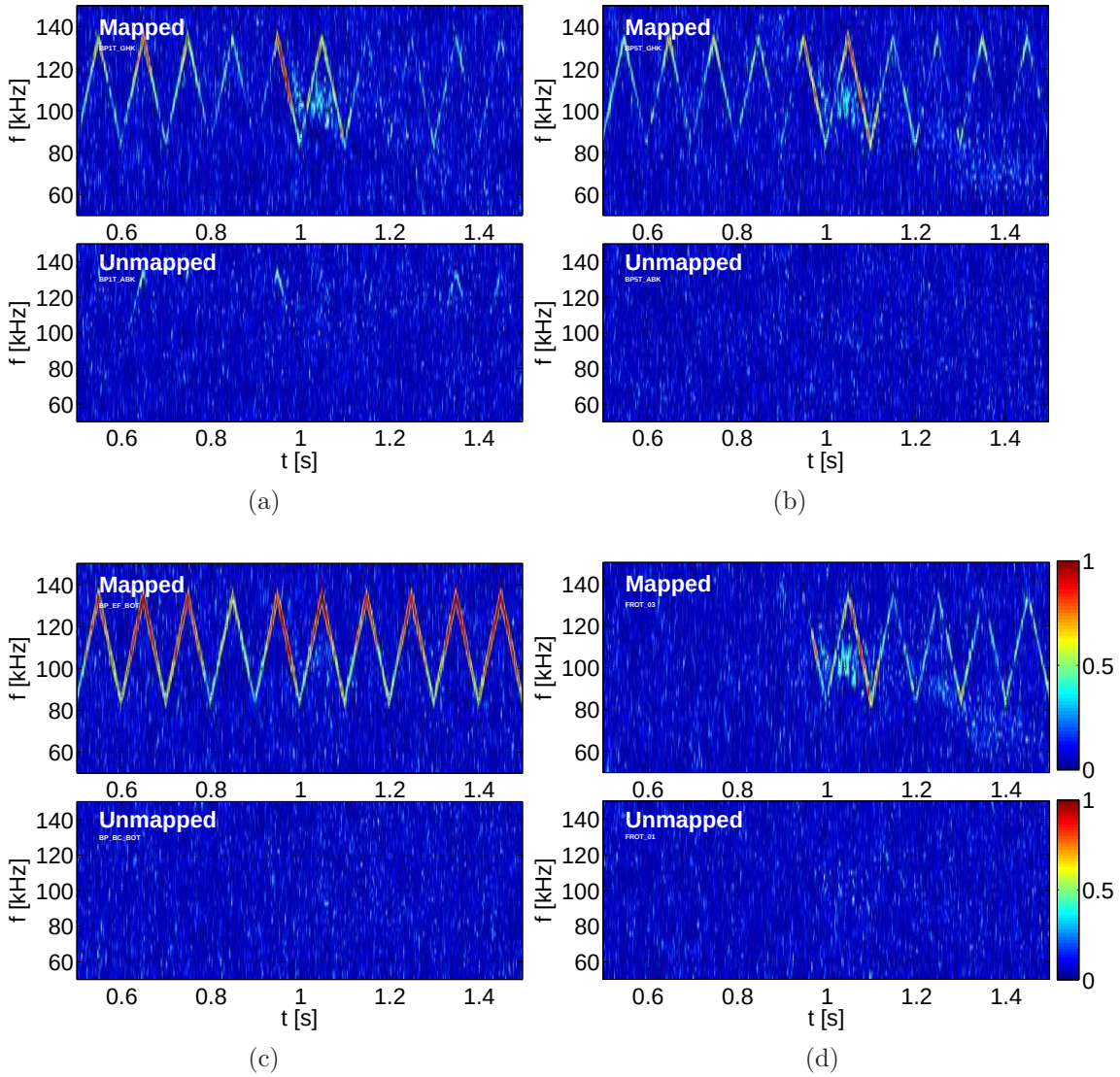

Figure 5-17: Magnitude squared coherence between the fluctuation signals and the Shoelace antenna current for pairs of (a) Mirnov coils corresponding to blue circles, (b) green diamonds, and (c) orange squares, as well as (d) polarimeter chords corresponding to red X's, in Figure 5-16. Only the mapped coils have strong coherence with the antenna.

be more readily compared, and plotted on a linear scale. The complex spectra of the Mirnov coils are first normalized by $j\omega$ so that they correspond to the poloidal magnetic field fluctuation, rather than its derivative. The antenna frequency scans through 3 kHz over the 3 ms time segment of each bin; the initial, middle, and final frequencies in this scan are depicted in Figures 5-18 and 5-19 by vertical dashed black lines.

In the first time bin, Figures 5-18a, d, g, and j, it appears that there are two primary peaks in the background spectrum (though the higher-frequency peak is much more prominent in the polarimetry data in the bottom row), and the antenna drive frequency misses them both. Interestingly, the spectra of the mapped Mirnov coils and polarimeter chord are quite different from those of the unmapped coils and chord. Indeed, the peak in the mapped spectra at the antenna frequency is dominant in Figures 5-18d and j; the similarity between these two particular spectra might be expected since the measurements almost map to each other on a field line (see the green diamond around G port and the upper red X around K port in Figure 5-16a). In the case of the Mirnov data set, axisymmetry would suggest that the background spectra of the paired coils, which have the same poloidal angle, should have a similar structure. Is the antenna responsible for this difference, and is it responsible for the sidebands in the mapped spectra? Is the background mode not axisymmetric? It should be noted that, over the 3 ms bin size over which these spectra are calculated, the plasma normally executes several complete toroidal transits due to its intrinsic rotation.

In the second time bin, the peak in the mapped spectra aligns precisely with the antenna frequency; the peak is also quite narrow and with minimal appearance of sidebands. In the Mirnov coil data, there appear to be two peaks in the background spectra, one below the antenna frequency, and one above. The lower peak is more prominent in the background spectra of Figures 5-18b and h, while the upper peak is more prominent in 5-18e. But there is only one peak in the mapped spectrum. Does this alignment of peak, suppression of a secondary peak, and disappearance of sidebands indicate that the antenna has locked to the QCM?

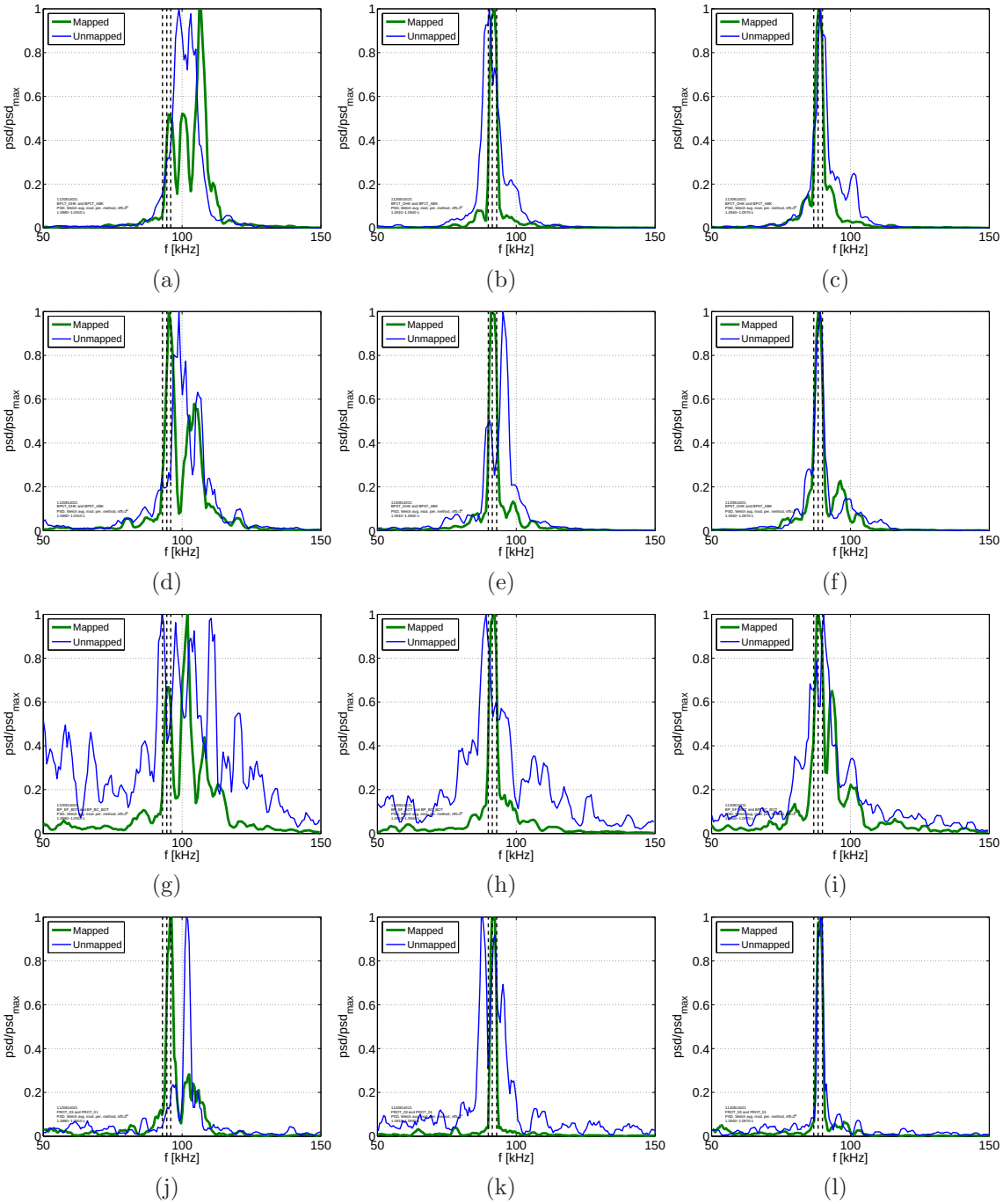

Figure 5-18: Comparison of power spectra, normalized to the maximum spectral power for each signal, of pairs of diagnostics, with one mapped (thick green line) and one unmapped (thin blue line) diagnostic in each pair. The frames from the top row, (a)-(c), correspond to the Mirnov coils represented by the large blue circles in Figure 5-16, (d)-(f) to the green diamonds, and (g)-(i) to the orange squares. The bottom row, (j)-(l), shows spectra from two polarimeter chords, the red X's in Figure 5-16. The 3 ms time bin is the same down a column, with start times for each column, 1.088 (a,d,g,j), 1.091 (b,e,h,k), and 1.094 s (c,f,i,l). The vertical dashed lines show the antenna frequency at the beginning, middle, and end of the time bin.

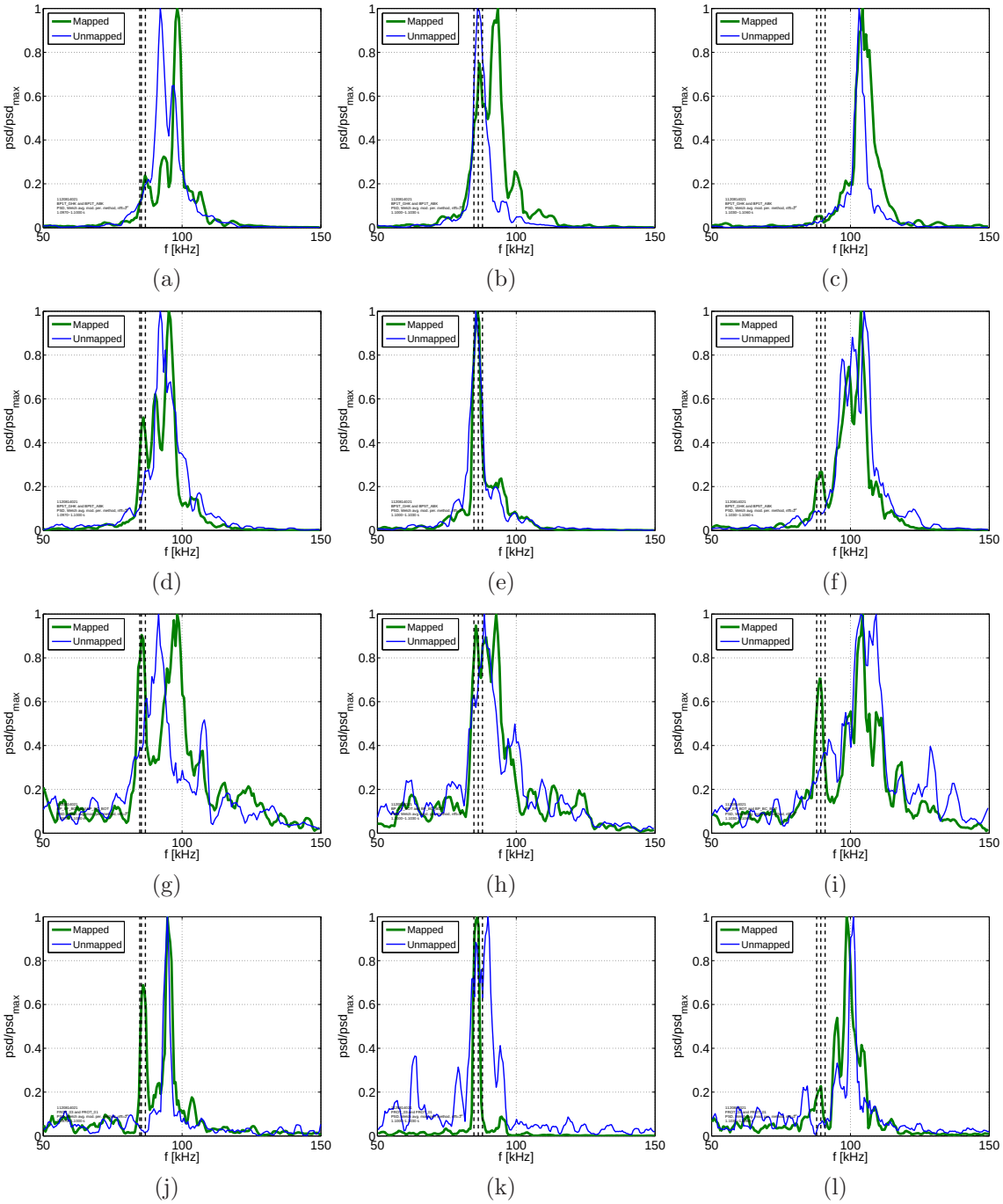

Figure 5-19: The start times for each column are 1.097 (a,d,g,j), 1.100 (b,e,h,k), and 1.103 s (c,f,i,l), and the width of each bin is 3 ms.

Moreover, the spectrum from the unmapped polarimeter chord in Figure 5-18k has three peaks arranged symmetrically about the driven peak. Is this the shape of the intrinsic spectrum, or is the chord only marginally "unmapped" – is it close enough to mapping to the antenna such that side bands are induced on the field line it samples? There is no indication of a coherent response from the antenna in the fluctuation measurement of this chord.

In the next frame, the alignment between the antenna drive and peak in the the mapped measurements persists. Now, however, the spectra on the unmapped coils and chord align fairly closely to those of the mapped signals, apart from a small shift between the peaks of the unmapped and mapped spectra in Figure 5-18i, and a more prominent sideband structure on the mapped coil, as well. Does this contact between the mapped and unmapped spectra mean that the antenna has locked the mode globally, or is it simply a coincident synchronization due to the natural variability of the background spectrum? Certainly, the signals in the mapped and unmapped spectra are not strongly coherent at any time in the discharge, as evidenced by the cross coherence spectrograms in Figure 5-20 (see also Figure I-10 in the appendix) – only the antenna organizes a fluctuation over perpendicular distances larger than several $\lambda_\perp$. This might be expected, since the coherence time[7] of $\sim 13\ \mu s \sim 1/f$ implies that the mode dephases over a few perpendicular wavelengths[8].

In the subsequent frame, the peak in the unmapped spectra jumps upward, off of the antenna frequency. Interestingly, for the Mirnov coils, the peak in the mapped spectrum jumps further by approximately the difference in frequency between the antenna drive and the unmapped peak. In the following frame, both the unmapped and mapped spectra appear "locked" in Figure 5-19e. In Figure 5-19b, however, the *unmapped* spectrum appears more "locked" than the mapped spectrum, whose dominant peak is at a higher frequency. If the background spectra in the unmapped and mapped measurements are different – the QCM is not axisymmetric – then it

[7]This is determined here from the e-folding envelope of the autocorrelation function from a Mirnov coil, BP6T_ABK, that did not map to the Shoelace antenna.

[8]The coherence time of the QCM can be larger, on the order of 10 periods – see Mirnov coil data from Alcator C-Mod discharge 1110201023, for example, for which the autocorrelation function e-folds on a time scale of 155 μs, while the QCM has a mean frequency around 86 kHz.

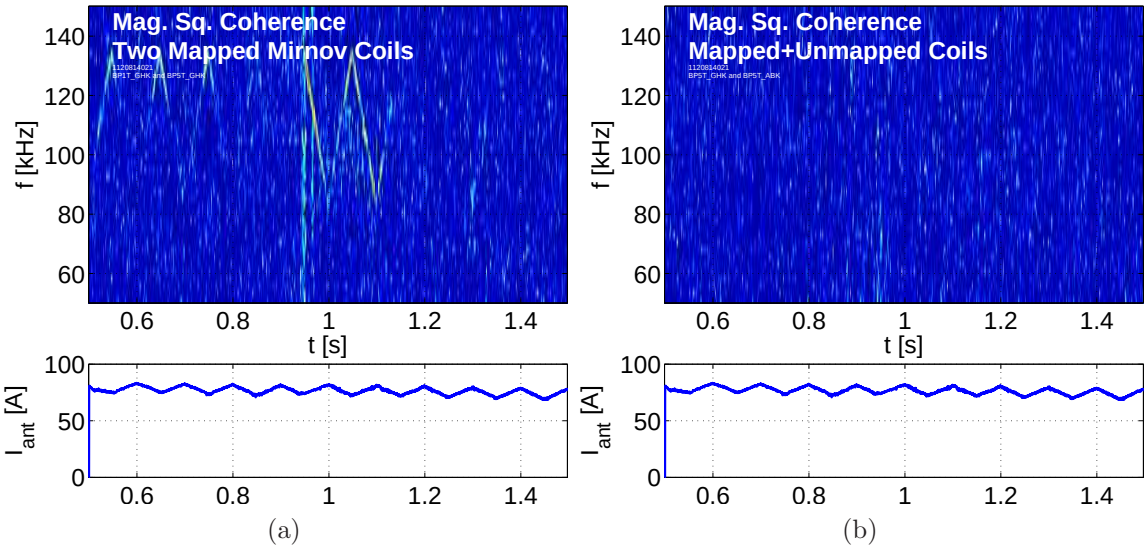

Figure 5-20: Magnitude squared coherence between (a) two coils which map to the antenna, but not to one another (corresponding to the mapped blue circle and mapped green diamond in Figure 5-16), and (b) a pair of coils, one of which maps to the antenna, and one which does not (the green diamonds in Figure 5-16). The discharge is the same as that analyzed throughout this section. The subplot is the antenna current.

is possible that the antenna is driven "off-resonance" on this field line, creating the sideband around 100 kHz. Of course, in this case, comparing spectra between these pairs of diagnostics is of dubious usefulness. The "unmapped" polarimeter chord again displays what appear to be sidebands appearing symmetrically about the driven peak, while the mapped spectrum is dominated by the component at the antenna frequency.

In the final frame, the peak in both the mapped and unmapped spectra jumps again, and is far from the antenna frequency. A small peak at the antenna frequency appears in Figures 5-19f, i, and l; there are multiple peaks in Figure 5-19f and l, where there are not in 5-19c.

The pair of Mirnov coils whose spectra appear in the third-from-the-top rows of Figures 5-18 and 5-19 have the largest gap between coil and plasma by about 1 cm. These coils correspond to the orange boxes in Figure 5-16. This increased distance acts as a low-pass filter in $k_\perp$, since the field perturbation in the minor radial direction is attenuated roughly as $e^{-k_\perp r}$, such that longer wavelength modes suffer less attenuation. As a result, the QCM feature in these spectra is less dominant.

It is also interesting that the antenna peak is usually more prominent on the mapped coil of this pair than it is on the others; this could suggest that there are significant currents driven by the antenna further out radially into the SOL from the intrinsic mode.

Examining these data, it is clear that the spectrum of the QCM evolves rapidly. The frames are separated by only 3 ms, but the peak in the spectrum can jump by $\sim$ 20 kHz in this short span of time. It also seems that the structure of spectra on different field lines can differ from one another, even if the measurements are made at the same poloidal angle, and that there can be multiple peaks around the QCM frequency in a single 3 ms background spectrum. Given this intrinsic variability, it is hard to determine whether the behavior on mapped field lines constitutes locking or displays sidebands resulting from the Shoelace antenna.

Figures I-1-I-7 in Section I.1 of the appendix show additional frames of power spectra. Section I.3 compares cross coherence calculated between pairs of Mirnov coils which both map to the Shoelace antenna (but not to each other) during a discharge in which the antenna current was amplitude modulated.

5.7.3 Comparing the Peak Frequency in Mapped and Unmapped Spectra

Let us reexamine Figure 5-14, which shows the peak in the PCI spectrum superimposed with the antenna and resonant frequencies during an H-mode. When the antenna frequency approaches the peak in the PCI spectrum, the PCI peak seems to track the drive briefly. To explore whether this constitutes frequency pulling, we might track the peak in spectra in pairs of mapped and unmapped measurements.

If, when the antenna frequency crosses that of the QCM, the trajectory of the peak from the mapped diagnostic follows the antenna, while that on the unmapped diagnostic does not, it might suggest that the QCM on the flux bundle tied to the antenna exhibits frequency pulling. Again, with a coherence time on this discharge of $\sim$13 μs, or about 1.3 QCM periods (with a mean QCM frequency around 98 kHz), and

given that the induced perturbation is only seen on mapped field lines, this scenario is plausible. However, in fact, it is hard to distinguish any such locking from the rapid ($\sim$ 60 Hz), natural variability of the background spectral peak locations, as will be seen shortly.

Figure 5-21 shows the peak spectral frequencies for the pair of Mirnov coils corresponding to the green diamonds in Figure 5-16, and the middle row of Figures 5-18 and 5-19, one which maps to the antenna (the thick green line), and one which does not (the thin blue line). Also shown are the evolving spectral peaks of two polarimetry chords, one which maps to the antenna (thick green), and one which does not (thin blue) – these correspond to the red X's in Figure 5-16, and the bottom row of Figures 5-18 and 5-19. The plasma discharge is the same as that analyzed in the last section. The spectral peak of the mapped Mirnov coil in Figure 5-21a is similar to that of the unmapped coil for most of the discharge. The Shoelace frequency crosses that of the intrinsic QCM (on the unmapped diagnostic) six times during the 0.5 s time segment shown (discounting the last crossing, which is marginal). The QCM peak evolves in time, and the antenna frequency also varies following its pre-programmed sweep. During most of the instances where the QCM peak and antenna frequencies cross, the trend of the evolving QCM frequency follows that of the scanning antenna frequency, but this tracking does not last for longer than half a period of the QCM frequency modulation, nor does this period seem to be affected by the antenna. Around 1.09 s (the nominal time of the power spectra shown in Section 5.7.2), the QCM peak first moves in the opposite direction as the Shoelace frequency scan, before reversing direction shortly afterward, and then following the peak in the mapped spectrum.

The spectral peaks of the mapped and unmapped polarimetry chords also follow one another closely, and deviate only slightly from one another at instances when the Shoelace antenna frequency nears that of the intrinsic QCM. The largest deviations occur during the first and second frequency crossings around 1.02 s and 1.09 s, at which times the mapped chord hugs the Shoelace frequency slightly longer than the unmapped peak.

Note also that for these discharges, the sawtooth crash cycle does not synchronize

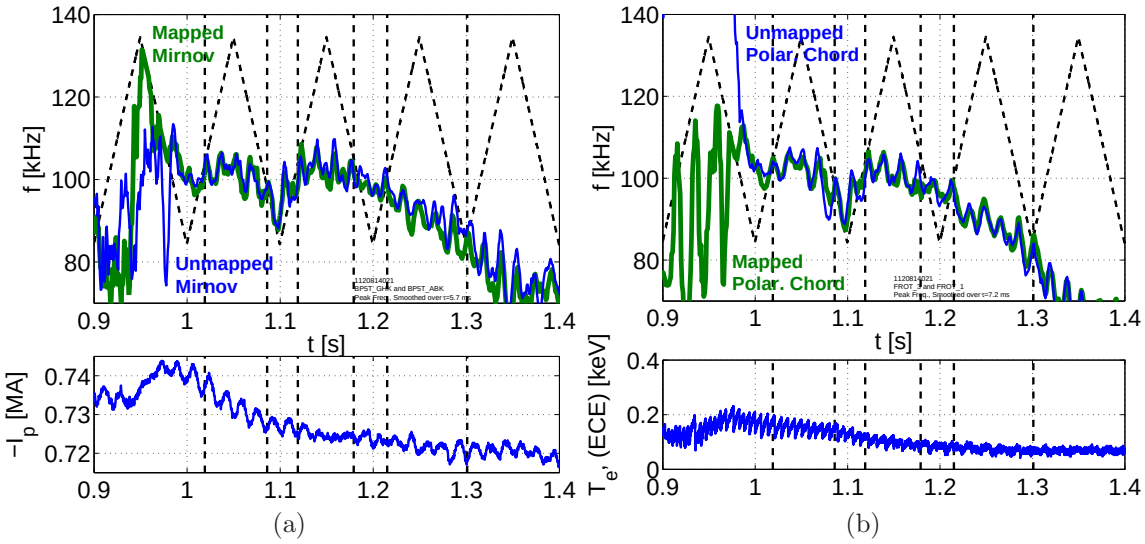

Figure 5-21: Peak frequency in spectrum for (a) two Mirnov coils, one which connects on a field line to the antenna (thick green line) and one which does not (thin blue line), and (b) two polarimeter chords, one which maps to the antenna (the top-most chord; thick green line) and one which does not (the bottom-most chord; thin blue line). The black dashed triangle wave is the antenna drive frequency. The vertical black dashed lines point out frequency crossings between the antenna and background QCM frequencies. The subplot of (a) is the plasma current, while that of (b) is the temperature as measured by the ECE diagnostic.

with the frequency modulation of the intrinsic mode, where it has been observed to do so elsewhere [53, p. 104]. This fact may be observed in Figure I-9a. The plasma current has an amplitude modulation at ∼60 Hz which is nearer the modulation frequency of the QCM peak, as shown in Figure I-9b, though even this does not align perfectly with the peak's movement.

The temperature trace carries the caveat that a non-stationary and relatively low (for Alcator C-Mod) nominal field, meant that it was difficult to calibrate the electron cyclotron emission (ECE) diagnostic providing temperature data on these discharges. Nonetheless, the observation still holds that the sawtooth cycle, at a frequency of ∼ 135 Hz, is much more rapid than the frequency, ∼ 60 Hz, of QCM frequency modulation.

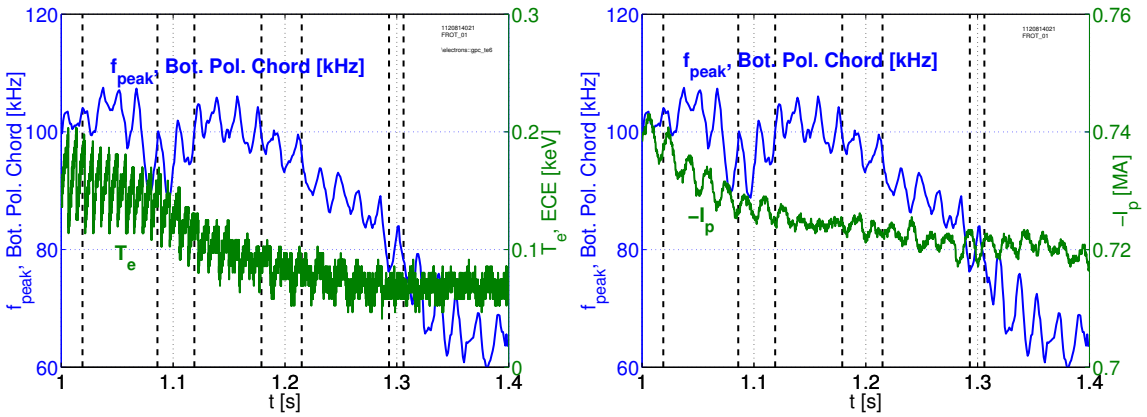

Figure 5-22: Peak spectral frequency of the bottom (unmapped) polarimeter chord referred to in Figure 5-21, plotted together with (a) the electron temperature from an ECE chord and (b) the plasma current. Note that the ECE diagnostic, which provided the temperature measurement, faced difficulties from a low and rapidly varying field.

Chapter 6

Conclusions and Future Work

Am I happy, or sad?

–The canonical question from Professor Jeffrey Freidberg to students of the PSFC at the end of their seminars

6.1 Summary

A new "Shoelace" antenna was used for the first time to drive fluctuations in the Alcator C-Mod tokamak edge. The field-aligned antenna winding imposes a particular $k_\perp = \pm 1.5 \pm 0.1$ cm^{-1}, with toroidal mode number, $n = \pm 35 \pm 23$, while a custom-built wide-band matching network allows operation in a broad frequency range from 45-300 kHz. These wave number and frequency ranges were chosen primarily to cover the parameters normally observed for the quasi-coherent mode, which regulates the pedestal in the ELM-free, steady-state EDA H-mode regime. However, they also cover part of the parameter range of the WCM, which accompanies the I-mode regime. In this initial round of experiments, 2 kW of RF power were provided by two commercial 50 Ω amplifiers.

The antenna was energized during a number of ohmic L- and H-mode plasmas. In H-mode plasmas, the antenna drove density and magnetic field perturbations in the edge, while in L-mode plasmas, only magnetic field perturbations were induced. The driven mode always propagated in the electron diamagnetic drift direction in the

laboratory frame in both forward- and reverse-field operation, and was approximately field-aligned, with $k_\perp$ and n matching the values imposed by the antenna winding. The driven fluctuations were also guided by field lines.

Moreover, the driven response was strongly peaked around a specific frequency in H-mode, but not in L-mode. In EDA H-mode discharges with an intrinsic QCM, the resonance fell precisely on the QCM center frequency. However, even in ELM-free H-mode discharges without a prominent QCM, the antenna response was still peaked. In both cases, the damping rate was weak, with $\gamma/\omega_0 \approx 5 - 10\%$, with the lower end of the range corresponding to EDA H-mode discharges. At the resonant frequency, a large fraction of the total $\tilde{n}_e$ and $\tilde{B}_\theta$ fluctuation was strongly coherent with the antenna current. In discharges with a QCM, it is possible that the antenna locked the intrinsic mode phase to its own. However, if this occurred, it only did so for short ($\sim$3-6 ms) periods, and a comparison between spectra on diagnostics which do and do not map to the antenna does not indicate prolonged frequency locking or sideband generation. In discharges without a strong QCM, the antenna-induced fluctuation seemed to dominate the QCM range of the $\tilde{n}_e$ and $\tilde{B}_\theta$ spectra. This is significant, causing us to ask the question: does the driven mode induce transport in a similar fashion to, but in the absence of, the intrinsic QCM?

The antenna-driven mode shares the same $k_\perp$, frequency, and laboratory-frame propagation direction as the QCM, with $k_\perp \gg k_\parallel$, is localized to the edge, only exhibits a density fluctuation after the development of steep edge gradients in H-mode, and is guided by field lines. The guided behavior is reminiscent of resonance cones predicted for low-frequency electrostatic waves, as well as shear Alfvén waves, but these scenarios, alone, are not consistent with the high collisionality ($\tau_{ei}^{-1}/\omega \approx 20 \gg 1$) of the edge, nor the driven resonance around the QCM.

Experiments in linear devices have shown that exciting mode-selective parallel currents is the essential ingredient for coupling to drift waves, and that this may be done inductively [79, 80]. As such, it is tempting to associate the driven mode with the QCM, which has been identified as an electron drift wave with additional interchange and electromagnetic character [32]. The field-line guided property of

the driven response may then be a result of the disturbance spreading along a field line via a kinetic shear Alfvén wave launched by the pressure disturbance of the drift wave. Since the antenna is much narrower than the connection length, roughly delimiting the parallel extent of the drift wave, we may conjecture that the disturbance is greatly attenuated after it has spread over the field line, and so any cross-field propagation beyond the last rung of the antenna cannot be detected. However, at present, we do not have the same detailed diagnostic information of the driven mode as is available for the intrinsic QCM – in particular, simultaneous, co-located fluctuations measurements and background profiles of plasma potential, electron density, and electron temperature – and so it is difficult to conclusively verify this scenario.

From another perspective, we might also ask: what implication does the existence of a weakly-damped resonance at the QCM frequency have on the globally-unstable intrinsic QCM? What makes the intrinsic mode unstable? One possibility is that, further up the pedestal, an interchange-driven process releases free energy from the pressure gradient, and then couples this to, or becomes manifested as, a drift wave further down the pedestal. In this description, the interchange mode is then an internal analog to the Shoelace antenna (or vice versa): both release free energy into a drift wave, in which it is slowly damped while driving transport across the LCFS. This suggests the need to extend measurements of the QCM deeper into the plasma, where its dynamics may change (as might be registered by a changing relative phase angle between $\tilde{\Phi}$ and n_e). It also implies that, while the intrinsic QCM is limited to the LFS by ballooning mode dynamics, the Shoelace antenna might excite a drift wave either on the high- or low-field sides. However, once again, without additional experiments are needed before this picture of the QCM system can be either validated, clarified, or rejected.

6.2 Shoelace Rewind, Upgrades, and Future Work

It is clear that a better experimental characterization of the mode driven by the Shoelace antenna is needed before its nature is understood, as well as its relationship

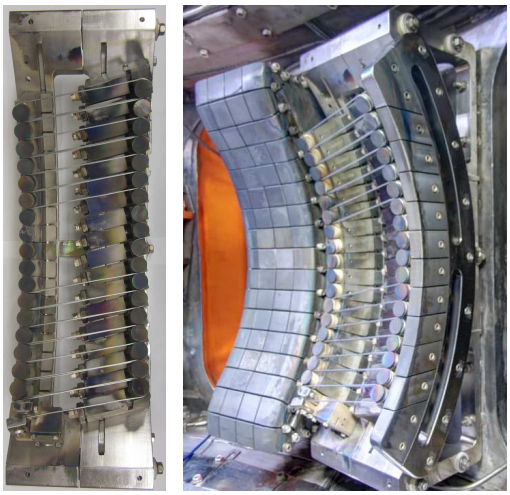

(a) (b)

Figure 6-1: Photographs of the Shoelace antenna, rewound at a shallower pitch angle and without the four middle rungs (the 9th-12th rungs). (a) Benchtop view, (b) image of the rewound Shoelace antenna mounted in-vessel. (Photo credits: (a) T. Golfinopoulos; (b) R. Mumgaard)

to the QCM. The Mirror Langmuir Probe (MLP) has been identified as the diagnostic best-suited for this purpose. But it did not yield data for the Shoelace antenna for the experiments presented in this thesis due to the fact that it was not mapped to the antenna along a field line on the LCFS.

To change this situation, the pitch angle of the Shoelace antenna winding was modified by shifting the adjustable wire posts (those on the right-hand side when facing the antenna wires) downward on a new set of bolt holes. Moreover, the four central rungs – the 9th through the 12th counting from the bottom – have been skipped in the new winding, since this region receives the highest heat load from the plasma, and failed in two places during the initial round of experiments. The new configuration is shown in Figure 6-1.

The new, shallower pitch angle is aligned to the background field lines when $q_{95} \sim 4$, and is reasonably matched over the range, $3 \leq q_{95} \leq 5$. This allows the original equilibrium conditions used in the study of the Shoelace antenna to be revisited, but also, crucially, at the upper end of this q_{95} range, the antenna maps to the MLP, as demonstrated in Figure 6-2.

Examining the driven mode using the MLP will (a) identify the degree of spatial

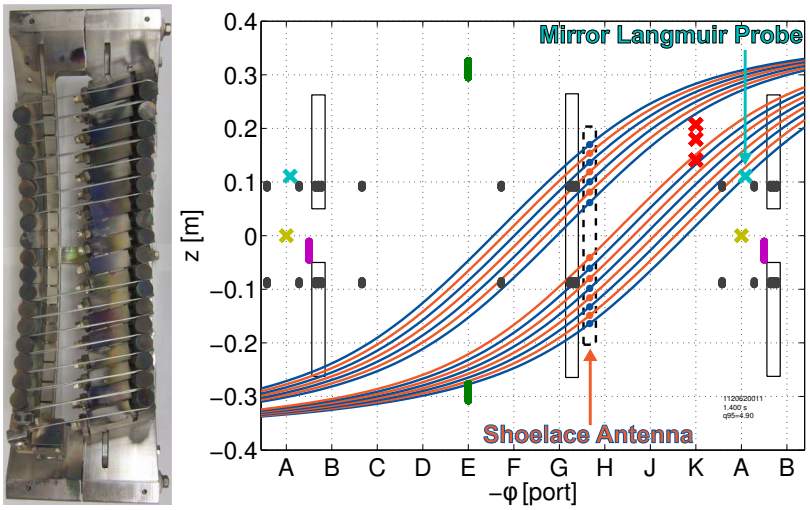

(a) (b)

Figure 6-2: (a) Benchtop view of rewound antenna and (b) field lines on LCFS that map to projections of Shoelace rungs onto this surface, calculated from an EFIT equilibrium field reconstruction for a discharge with $q_{95} = 4.90$. The lower rungs of the antenna map to the MLP.

overlap between the intrinsic QC and driven modes, (b) determine the phase difference between the different fluctuation quantities (especially electron pressure, $\tilde{p}_e$, and potential, $\tilde{\Phi}$) to characterize the driven mode physics, (c) examine via local measurements whether the antenna affects the amplitude, phase, or stability of the intrinsic mode, (d) determine whether the antenna imparts torque to the plasma, and (e) learn whether the antenna-induced mode independently drives transport.

In addition, the recent purchase of two Tomco Technologies BT04000-AlphaA Class AB amplifiers will expand the available Shoelace RF power supply from 2 kW to better than 8 kW, approaching the breakdown voltage design limit of the matching network. This upgrade, combined with the slightly-lower resistance of the antenna, will more than double the driven current, though, of course, the flux coupled to the plasma is proportionately reduced by the loss of four rungs.

Since any interaction between the antenna and the intrinsic QCM – particularly frequency pulling, sideband generation, and feedback stabilization/destabilization – is more apparent with a larger driven excitation, the power upgrade will help to identify whether such behavior appears in the plasma response, especially when the power is

scanned over many levels. In addition, the increased power means that the antenna will be able to impart a detectable perturbation to the plasma with a greater standoff than is presently possible (currently, the gap between the plasma and the antenna is restricted to $0 < R_{gap} \lesssim 5$ mm in order to observe a strong driven perturbation). This will make it possible to run useful Shoelace antenna experiments in most C-Mod discharges, including those with high RF heating and current drive input (*i.e.* I-mode discharges, QCM discharges with the lower hybrid antenna operating, etc.). Lastly, increasing the antenna power maximizes the likelihood of detecting antenna-driven transport, as well as effects on the global confinement regime resulting from antenna operation.

The power system upgrade is expected to be completed in June, 2014, in time for use during the summer Alcator C-Mod experimental campaign. Experiments during the 2014 campaign will target ELM-free H-modes, in addition to EDA H-modes. In this way, the plasma response to the antenna may be investigated in the absence, as well as the presence, of an intrinsic QCM. The antenna will also be energized into I-mode plasmas to determine whether it may induce a response in the lower portion of the frequency band, $200 < f < 500$ kHz, belonging to the Weakly Coherent Mode (WCM), which plays a similar role in I-mode as the QCM in H-mode.

Complementing the experimental effort is an attempt to model the antenna/plasma interaction using `BOUT++`, a highly-adaptable framework for performing plasma fluid simulations in arbitrary, three-dimensional, curvilinear coordinate systems [98]. Initial work has utilized a three-field slab model evolving pressure (p_e), parallel vorticity, $\bar{\omega} = \mathbf{b}\cdot\nabla\times\tilde{\mathbf{u}}$, and parallel ion velocity, $u_\parallel$, and incorporating magnetic and flow shear; however, the model will be expanded to include electromagnetic and curvature effects. A plasma dielectric description has also been prepared for use in the `COMSOL` ® finite element package, offering an alternative route to exploring the antenna-plasma interaction numerically. Appendix D discusses the initial work carried out in `BOUT++`, while Appendix C derives a permittivity tensor appropriate to simulations in `COMSOL`. It should be pointed out that, as of the preparation of this thesis, simulation of the QCM using `BOUT++` remains an active area of research [77], and the precise behavior

measured in experiment has not yet been fully captured in the model.

6.3 Am I Happy or Sad?

A few words are in order to address Professor Freidberg's wise and pithy question. The high-level goal which inspired the Shoelace antenna was to learn whether confinement regimes like the QCM can be conjured at will via the use of an external actuator. The results of Shoelace antenna experiments satisfy conditions that might be considered "necessary" for this to be true: the antenna did, indeed, drive a fluctuation similar to, and resonant at the frequency of, the QCM, insofar as this could be verified by the set of diagnostics which registered a response. However, the results are not a sufficient proof of concept for the approach of controlling edge transport by active stimulation of edge modes, as no direct measurements of antenna-driven transport were available, beyond the fact that the antenna is not thought to have changed the confinement regime globally in the discharges in which it operated. A set of experiments and theoretical investigations have been outlined above which will help to provide a more definitive answer to this question.

However, even assuming a positive result for this additional work, the Shoelace antenna, itself, is still not a viable approach for a real reactor. The reason is evident already from Figure 4-3. The high wave number of the QCM requires an inductive structure to be very close to the plasma at the precise location where the greatest fluxes of heat and particles "come out" – the outer midplane. Alcator C-Mod already produces the highest heat fluxes of any of the world's tokamak devices, and a real reactor's heat flux will be somewhat greater, still. As such, it is unlikely that an antenna like the Shoelace would survive for continuous operation in a power-producing tokamak.

Instead, the driven current filaments must be produced a different way. An example of such a different approach is to employ radio-frequency current drive to reproduce the filamentary currents associated with the QCM. Here, a phased array on a lower hybrid (LH, f ~several GHz) "grill" or set of electron cyclotron range of frequency

(ECRF, $f \sim$100 GHz) horn antennas might be envisaged as the "carrier" waves which drive a drift-wave-like mode through a nonlinear, indirect, and likely low-efficiency mechanism[1], but one whose excitation structures can be placed far from the plasma. At the same time, work should be done to investigate whether the plasma may be excited at a longer perpendicular wavelength, such that an inductive, "flux-coupling" antenna like the Shoelace may be further recessed behind a limiter, while still achieving a desired transport response. Likewise, the antenna might be moved to a safer location (for example, the high-field side) with a reduced heat flux, where perhaps it could coax particles out of the plasma without increasing local heat output. This approach faces the obvious difficulty of trying to excite a transport-regulating fluctuation where it does not normally occur (following up on the same example, due to the stabilizing effect of good curvature on the high-field side, though note that exciting a drift wave on the HFS may still be possible).

As is typically the case in fusion research, and applied science, generally, we are part happy and part sad, and there's lots more work to do, but at the least, we are further along than we were before.

[1]The Manley-Rowe relations constrain a three-wave coupling process to transfer power from the high-frequency pump to the low-frequency target mode as the ratio of the frequencies[89], ordering down the transfer by six orders of magnitude from the ECRF to the QCM frequencies, and four from LH to QCM; however, the three-wave process may not be the relevant transfer mechanism in this case.

Appendix A

Key of Symbols and Abbreviations

Table A.1: List of Symbols

Symbol	Name	Description
β	Normalized pressure	Plasma pressure normalized by magnetic pressure, $\beta \equiv 2\mu_0 p/B^2$. Unitless.
γ	Damping or growth rate	Depending on the context, γ is the linear damping or growth rate of a mode. In all analysis of the Shoelace antenna data, γ is a damping rate. Units: [1/s]
$\bar{\bar{\epsilon}}$	Electric permittivity	Electric permittivity dyadic tensor in the plasma medium. Units: [F/m]
ϵ_0	Electric permittivity of vacuum	Electric permittivity of vacuum, $\epsilon_0 \approx 8.854 \times 10^{-12}$ [F/m].
ζ	Toroidal angle mapped to outer midplane	ζ is a coordinate in the field-aligned coordinate system employed in this thesis. It is the toroidal angle of the location on the outer midplane which maps to the test point along a field line; the angle is referenced to the toroidal location of the Shoelace antenna (-240° from Port A in the cylindrical coordinate system). Units: [degrees] or [radians].
η	Resistivity	Plasma resistivity. Can appear as dyadic tensor, $\bar{\bar{\eta}}$, components of this tensor, Spitzer resistivity, $\eta_s = 0.51\frac{m_e}{n_e e^2 \tau_{ei}}$, etc. Units: [$\Omega$·m]
θ	Poloidal angle	Poloidal angle of a point; $\tan(\theta) = (z - z_0)/(R - R_0)$ for a test point at R, z, where R_0 and z_0 specify the R, z location of the magnetic axis. The Mirnov coils primarily measure the fluctuating field component in the $\hat{\theta}$ direction. Units: [degrees] or [radians].
μ_0	Magnetic permeability of vacuum	Magnetic permeability of vacuum, $\mu_0 = 4\pi \times 10^{-7}$ [H/m] $\approx 1.257 \times 10^{-6}$ [H/m]

List of Symbols

Symbol	Name	Description
μ_e	Mass ratio	Ratio of electron mass to main ion species mass, $\mu_e \equiv m_e/M_i \approx 2.724 \times 10^{-4}$ for these deuterium plasmas.
ξ	Field-aligned coord. along field line	ξ is equal to the poloidal angle, θ, of a test point, but is used to refer to the location along a field line. In the field-aligned coordinate system, when the flux surface, ψ, and the field line label, ζ, are held constant, advancing ξ slides a test point along a field line. Units: [degrees] or [radians]
ρ	Mass density	Mass density, given by $\rho = n_i M_i + n_e m_e \approx n_i M_i$. Units: [kg/m^3]
ρ_c	Charge density	Charge density, given by $\rho_c \equiv Z e n_i - e n_e$. Units: [C/m^3]
ρ_s	Drift wave dispersion length scale	Drift wave dispersion length scale, $\rho_s \equiv c_s/\Omega_i \approx 4.5 \times 10^{-4}$ [m] at the LCFS in the present experiments. Plays similar role as ion gyro radius, replacing ion thermal speed with sound speed.
ϕ	Toroidal angle	Toroidal angle coordinate. Note the lower case. Units: [radians], [degrees].
Φ	Potential	Electrostatic potential, related to the electric field through $\mathbf{E} = -\frac{\partial \mathbf{A}}{\partial t} - \nabla\Phi$. Note the upper case. Units: [V]
$\bar{\bar{\chi}}$	Susceptibility	Tensor quantity defined through $\mathbf{J} = \frac{\partial \bar{\bar{\chi}} \cdot \mathbf{E}}{\partial t}$, such that $\nabla \times \mathbf{H} = \frac{\partial (\bar{\bar{\epsilon}} \cdot \mathbf{E})}{\partial t}$, where $\bar{\bar{\epsilon}} = \epsilon_0 (1 + \bar{\bar{\chi}})$. Unitless.
ω	Angular frequency	Angular frequency, $\omega = 2\pi f$. Units: [rad/s]
ω_{ps}	Plasma frequency	Plasma frequency of species, s, where $s = i$ (ions) or e (electrons). Given by $\omega_{ps}^2 = n_s Z_s^2 e^2/(m_s \epsilon_0)$.
Ω_s	Cyclotron (gyro) frequency	Cyclotron (gyro) frequency of species, s, where $s = i$ (ions) or e (electrons). Given by $\Omega_s = Z_s e B/m_s$. Units: [radians/s]
$\mathbf{A}$	Vector magnetic potential	Vector magnetic potential, related to the electric field through $\mathbf{E} = -\frac{\partial \mathbf{A}}{\partial t} - \nabla\Phi$, and the magnetic field through $\mathbf{B} = \nabla \times \mathbf{A}$. Units: [V·s/m]=[T·m]
$\mathbf{B}$	Magnetic flux density	Magnetic flux density, $\mathbf{B} = \mu_0 H = \nabla \times \mathbf{A}$. Units: [T]
c	Vacuum speed of light	Speed of light in vacuum, $c = 1/\sqrt{\mu_0 \epsilon_0} \approx 2.998 \times 10^8$ [m/s].
c_s	Sound speed	Sound speed in plasma, $c_s = \sqrt{\frac{T_e}{M_i}} \approx 49$ km/s at the LCFS in the present experiments. Units: [m/s]
C_{xy}	Cross coherence	The cross coherence is the cross power of two signals normalized by the square root of the product of their auto powers, $C_{xy}(j\omega) = P_{xy}(j\omega)/\sqrt{P_{xx}(j\omega)P_{yy}(j\omega)}$. It is sometimes define as the square of this ratio. The quantity gives an indication of whether two signals are linearly correlated and is normalized such that $0 \leq |C_{xy}| \leq$. The magnitude squared value, $|C_{xy}|^2$, and the phase of C_{xy}, are used extensively in analysis in this work.
e	Electron charge	Fundamental electron charge, $e \approx 1.602 \times 10^{-19}$ C.

List of Symbols

Symbol	Name	Description
H_{xy}	Transfer function, frequency response	The transfer function (or frequency response) of a system relates the output, y, obtained as a linear operation on the input x. It is defined through $H_{xy}(j\omega) = P_{xy}(j\omega)/P_{xx}(j\omega)$, such that the phase is $\angle Y(j\omega) - \angle X(j\omega) = \angle(Y(j\omega)X^*(j\omega)$. It is used in this work to look for poles in the plasma response to the antenna.
$\mathbf{J}$	Current density	Electric current density. Units: [A/m^2]
$\mathbf{k}$	Wave vector	Wave vector. The perpendicular wave number is $k_\perp$, and is the component of $\mathbf{k}$ perpendicular to the magnetic field. The component parallel to the magnetic field is denoted $k_\parallel$. Units: [radians/m], [radians/cm].
L_c	Connection length	The distance traveled along a magnetic field line in order to connect the upper and lower limits of a flux surface (typically the LCFS) across the bad-curvature side. This can be used to estimate the longest-possible, and most typical, parallel wavelength, $\lambda_\parallel \approx 2L_c \Rightarrow k_\parallel \approx \pi/L_c$. In the straight-tokamak approximation, $L_c \approx 2\pi Rq/2 = \pi Rq$, since only half a poloidal transit is completed on the field line path. For typical Shoelace experiments, $q \approx 3$; using a mean value between $R_0 \approx 0.68$ m and $R_0 + a \approx 0.9$ m on C-Mod, $L_c \approx 7.5$ m. EFIT reconstructions give a somewhat larger value, nominally $L_c \approx 9$ m.
L_p	Pressure gradient length scale	Pressure gradient length scale $L_p = \lvert\nabla p/p\rvert^{-1}$. Units: [m]
m_e	Electron mass	Electron mass, $m_e \approx 9.109 \times 10^{-31}$ kg.
M_i	Ion mass	Mass of main ion species. In the experiments described in this work, this is deuterium, with $M_i \approx 2.014\,\text{amu} = 3.344 \times 10^{-27}$ [kg].
$\mathbf{n}$	Index of refraction	Index of refraction, $\mathbf{n} = c\mathbf{k}/\omega$. Unitless.
n_e	Electron density	Total electron density; occasionally meant in the sense of the equilibrium density, $\langle n_e \rangle$. Units: [m^{-3}]
p_e	Electron pressure	Electron pressure, typically related to temperature from isotherm, $p_e = n_e T_e$. Units: [Pa], [atm]
P_{xy}	Cross power spectral density	Cross power spectral density (shortened to cross power) between two signals, x and y, where the phase angle of $P_{xy}(j\omega)$ is the difference between the phase angle of the Fourier transforms of y and x, $\angle P_{xy}(j\omega) = \angle\mathcal{F}\{y(t)\} - \angle\mathcal{F}\{x(t)\} = \angle Y(j\omega) - \angle X(j\omega) = \angle(Y(j\omega)X^*(j\omega))$. The cross power is the Fourier transform of the cross correlation between $y(t)$ and $x(t)$, and is used in the definitions of the cross coherence and transfer functions.
q	Safety factor	Safety factor, describing the number of toroidal revolutions required to execute one poloidal revolution when following a magnetic field line. In the "straight-cylinder" tokamak, $q = \frac{rB_\phi}{RB_\theta}$. Unitless.

List of Symbols

Symbol	Name	Description
R	Major radial coordinate	Major radial coordinate in the cylindrical coordinate system, measured from the axis of symmetry to a point along the horizontal. R_0 is the major radius of the the plasma at the magnetic axis; for Alcator C-Mod, $R_0 \approx 0.68$ m. Units: [m]
T_e	Electron temperature	Electron temperature. When no additional subscripts are used, assumed isotropic. Otherwise, components of a dyadic tensor. Units: Boltzmann constant is absorbed, so units are energy: [J], [eV].
$\mathbf{u}$	Ion velocity	Ion velocity. Units: [m/s]
$\mathbf{u}_*$	Ion diamagnetic drift velocity	Ion diamagnetic drift velocity, $\mathbf{u}_* = \mathbf{B}\times\nabla p_i/(n_i Z_i e B^2)$. Runs in opposite direction to electron diamagnetic drift velocity. Units: [m/s]
$\mathbf{v}$	Electron velocity	Electron velocity. Units: [m/s]
$\mathbf{v}_E$	$\mathbf{E}\times\mathbf{B}$ velocity	$\mathbf{E}\times\mathbf{B}$ drift velocity, $\mathbf{v}_E = \mathbf{E}\times\mathbf{B}/B^2$. Magnitude of several km/s in the Alcator C-Mod edge plasma. Units: [m/s]
$\mathbf{v}_*$	Electron diamagnetic drift velocity	Electron diamagnetic drift velocity, $\mathbf{v}_* = \nabla p_e\times\mathbf{B}/(n_e e B^2)$, with $\lvert v_*\rvert = c_s\rho_s/L_p$ for the isothermal case. In the present experiments, $v_* \approx 6.1$ km/s at the LCFS. Units: [m/s]
v_A	Alfvén speed	Alfvén speed, $v_A = \frac{c}{1+\frac{\omega_{pi}^2}{\Omega_i^2}} = \frac{1}{\sqrt{\mu_0\epsilon_0}\left(1+\frac{n_i M_i}{\epsilon_0 B^2}\right)} \approx \frac{B}{\sqrt{\mu_0 n_i M_i}} = \frac{B}{\sqrt{\mu_0\rho}} \approx 2.9\times10^6$ [m/s] at LCFS in the present experiments. Implicated in dispersion relation of shear and compressional Alfvén waves. Units: [m/s]
$v_{th,e}$	Electron thermal velocity	Electron thermal velocity; when the temperature is isotropic, $\frac{3}{2}m_e v_{th,e}^2 = T_e$. When there are different parallel and perpendicular temperatures, $\frac{1}{2}m_e v_{th,e,\parallel}^2 = T_{e,\parallel}$ and $m_e v_{th,e,\perp}^2 = T_{e,\perp}$. Units: [m/s]
z	Vertical coordinate	Typically refers to the vertical coordinate in the cylindrical coordinate system. In a slab (Cartesian) geometry, it also typically refers to the coordinate pointing along the field line. Units: [m]
Z	Atomic number, charge number	Atomic number, which is also the charge number or state for the fully-ionized species in the fusion plasmas of the present experiments. In this case, with deuterium as the main ion species, $Z = 1$.

Table A.2: List of Abbreviations

Abbrev.	Expanded	Description

List of Abbreviations

Abbrev.	**Expanded**	**Description**
Alcator	High-field torus (Latin: *ALto CAmpus TORus*)	The name of a series of tokamaks operated at MIT's plasma Science and Fusion Center, comprising Alcator A (1973-1979), Alcator C (1978-1987), and the current iteration, Alcator C-Mod (1991-present). As of the preparation of this thesis, Alcator C-Mod is the highest-field tokamak in the world, reaching a maximum on-axis field of about 8 T.
ASDEX	Axially Symmetric Divertor EXperiment	Tokamak that operated in Garching, Germany, from 1980-1990; succeeded by ASDEX-Upgrade. Pioneer of the use of a divertor, and discoverer of the H-mode.
AUG	ASDEX-Upgrade	Tokamak research facility located in Garching, Germany. Operating since 1991, and succeeding the original ASDEX experiment (1980-1990)
EDA	Enhanced D_α	Steady-state, high-confinement, usually ELM-free operating regime routinely used at Alcator C-Mod
EDD	Electron Diamagnetic Drift	The electron diamagnetic drift velocity is given by $\mathbf{v}_* = \nabla p_e \times \mathbf{B}/(n_e e B)$. It corresponds to the electron contribution to the diamagnetic current, which provides MHD force balance in the presence of a pressure gradient. It points in the opposite sense as the ion diamagnetic drift (IDD) direction.
EHO	Edge Harmonic Oscillation	The continuous, low-to-intermediate-n, $6-15$ kHz edge fluctuation associated with the QH mode which performs the role of ELMs in this steady-state, ELM-free operating regime.
ELM	Edge-Localized Mode	Periodic, bursting instabilities, typically peeling-ballooning in nature, which relax the edge pressure gradient in H-mode, expelling impurities.
FA	Field-Aligned	Property of a fluctuation whereby the oscillation is uniform along field lines, so that the wave vector is perpendicular to field lines. This is a common feature of lower-frequency ($\omega \ll \Omega_{ci}$) modes, since Alfvénic dynamics along field lines tend to smooth out perturbations relatively rapidly. In a cylindrical device, this constrains the eigenmode to be located on the rational surface with safety factor, $q = m/n$.
H-mode	High-confinement mode	Confinement regime of tokamaks and other toroidal magnetically-confined plasmas, characterized by an internal transport barrier which improves confinement over L-mode. Typically found in diverted experiments. First discovered on the ASDEX experiment. Can be steady-state or transient.

List of Abbreviations

Abbrev.	Expanded	Description
HFS	High-field side	The inner half (in major radius) of the toroidal plasma tends to have a higher field strength than the outer half, since the field falls as $\|\mathbf{B}\| \propto \frac{1}{R}$ in a toroidal geometry. The high-field side refers to this inner half. This is also the side with "good" curvature. The plasma tends to be fairly quiescent on this side due to these stabilizing properties.
ICRF	Ion Cyclotron Range of Frequency	Pertaining to RF waves in a plasma around the cyclotron frequency, usually in the context of providing RF heating power to the plasma.
IDD	Ion diamagnetic drift	The ion diamagnetic drift velocity is given by $\mathbf{u}_* = \mathbf{B} \times \nabla p_i/(Zn_ieB)$. It is the ion component of the diamagnetic current, which provides MHD force balance in the presence of a pressure gradient. It points in the opposite sense as the electron diamagnetic drift (EDD) direction.
ITER	(ITER is not an acronym)	ITER is the name of a machine under construction (as of the preparation of this thesis) by an international consortium of nations, involving the US, EU, Russia, China, Japan, South Korea, and India. At a major radius of ~ 6 m, it would be the world's largest tokamak. It has been designed to achieve $Q = 10$ operation. ITER means "the way" in Latin.
JET	Joint European Torus	A tokamak located in Oxfordshire, UK, operating since 1984. With a major radius of $R = 2.96$ m, it is the world's largest tokamak as of the preparation of this thesis.
LCFS	Last-Closed Flux Surface	The last closed flux surface is the outermost flux surface on which field lines do not come into contact with a material surface. For diverted plasmas with an x-point, this surface has a null in the poloidal or toroidal field, and the safety factor, q, becomes singular. Field lines inside the LCFS are called "closed," while field lines outside are called "open." Since closed field lines have significantly better confinement, the LCFS defines the boundary of the plasma, with density and temperature falling off very rapidly across it.
LFS	Low-field side	The outer half (in major radius) of the toroidal plasma tends to have a lower field strength than the inner half, since the field falls as $\|\mathbf{B}\| \propto \frac{1}{R}$ in a toroidal geometry. The low-field side refers to this outer half. This is also the side with "bad" curvature. Heat and particles tend to exit the plasma on this side.
LH	Lower Hybrid	A plasma oscillation whose dynamics involves both the ion plasma ($\omega_{pi}^2 = n_iZ^2e^2/(\epsilon_0 m_i)$) and cyclotron ($\Omega_i = ZeB/m_i$) oscillations, hence the name, hybrid. LH waves are frequently used on tokamaks to drive plasma current non-inductively.

List of Abbreviations

Abbrev.	Expanded	Description
L-mode	Low-confinement mode	Steady-state tokamak confinement regime characterized by poorer confinement (more rapid thermal, as well as particle, loss), with transport increasing with auxiliary heating power. Transport is dominated by broadband turbulence.
MAST	Mega-Amp Spherical Tokamak	A large spherical tokamak operated in Culham, UK.
MHD	Magneto Hydrodynamic	A fundamental fluid theory used to describe plasmas. The most typical model, "ideal MHD," treats the plasma as a perfect, single-fluid, current-carrying conductor. The displacement current in Maxwell's equations is neglected. A number of texts treat this subject.
NBI	Neutral Beam Injection	Method for providing auxiliary heating to the confined plasma whereby a beam of energetic neutral particles is injected, either perpendicularly or tangentially, into the plasma. Less effective in higher-density plasmas, in which beam does not penetrate as deeply.
PLL	Phase-Locked Loop	A type of feedback circuit which adjusts the frequency of the output signal to minimize the phase difference between the output and input signals, as might be used, for example, to demodulate an FM radio signal.
PFC	Plasma Facing Components	Machine components which are exposed directly to the plasma, with no material structures placed in between. Examples include limiters and divertors.
QCM	Quasi-Coherent Mode	Edge fluctuation with $50 \lesssim f \lesssim 150$ kHz, $k_\perp \sim 1.5$ cm^{-1}, accompanying EDA H-mode and providing enhanced particle transport.
QH	Quiescent H(-mode)	A steady-state, ELM-free H-mode first found on DIII-D, with similar regimes found on other tokamaks (AUG, JT-60U, JET); characterized by a continuous EHO which flushes impurities from the plasma.
SOL	Scrape Off Layer	The quasi-vacuum region in a plasma outside the LCFS whose field lines are "open," intersecting material surfaces. The region is named because the field lines and flux surfaces appear to be scraped off at the x-point from the LCFS.
tokamak	toroidal chamber with magnetic coils (Russian transliteration: *toroidal'naya kamera s magnitnymi katushkami*)	A device for confining fusion plasmas originating in Soviet Union in the 1950's. In this concept, an externally-applied axial magnetic field is combined with the poloidal field resulting from the plasmas own axial current, producing the helical field which gives the rotational transform required for stability. Additional vertical field coils are also needed for stability and shaping.

Appendix B

Analytical Calculations for Antenna

B.1 Derivation of Antenna Vacuum Field Model

Figure 4-1 shows a photograph of the antenna, as well as the geometry used in the model below.

The derivation of the vacuum field relations for the Shoelace antenna proceeds as follows. First, flatten the geometry of the antenna onto a single plane. Next, let the wires be of infinite extent in length, of alternating sign but equal magnitude in current, $I = \pm I_0$, and with an infinite number of filaments in an equispaced array. b represents the spacing between filaments. The radius of each filament is a, but for the present, a is considered to be infinitesimally small, $a \to 0$.

The magnetostatic vacuum field produced by a single current filament may be calculated by the Biot-Savart law,

$$\mathbf{B}(\mathbf{r}) = \int \frac{\mu_0}{4\pi} \frac{I \mathrm{d}\vec{\ell} \times \mathbf{r}}{|\mathbf{r}|^3} \tag{B.1}$$

where $\mathbf{r}$ represents the position at which the field is to be evaluated, $\mathrm{d}\vec{\ell}$ the infinitesimal path length along the current-bearing interval, and the integral is over all such

intervals on the filament.

Choose an orthonormal coordinate system such that the z coordinate is colinear with a current element, the xz plane contains the current elements, and the y coordinate extends away from the elements. In this case, z corresponds to the toroidal ϕ coordinate, x corresponds to the poloidal angle, θ, and y to the minor radial or flux surface coordinate.

Then the current density associated with the n^{th} current filament is

$$\mathbf{J} = (-1)^n I_0 \delta(y)\,\delta(x - nb) \tag{B.2}$$

where δ is the Dirac delta.

Applying the Biot-Savart law, Eq. B.1, to each filament produces a sum,

$$\mathbf{B}(\mathbf{r}) = \sum_{n=-\infty}^{\infty} I_0 \int \frac{\mu_0}{4\pi} \frac{(-1)^n \mathrm{d}\vec{\ell} \times \mathbf{r}_n}{|\mathbf{r}_n|^3} \tag{B.3}$$

where $\mathbf{r}_n = \mathbf{r} - \hat{\mathbf{x}} nb = \hat{\mathbf{x}}(x - nb) + \hat{\mathbf{y}} y + \hat{\mathbf{z}}(z - \ell)$ is the vector between infinitesimal interval on the n^{th} current filament and the point, $\mathbf{r}$, where the field is being evaluated. This may be rewritten as

$$\begin{aligned}
\mathbf{B}(\mathbf{r}) &= \sum_{n=-\infty}^{\infty} (-1)^n \frac{\mu_0 I_0}{4\pi} \int_{-\infty}^{\infty} \mathrm{d}\ell \frac{\hat{\mathbf{z}} \times [\hat{\mathbf{x}}(x - nb) + \hat{\mathbf{y}} y + \hat{\mathbf{z}}(z - \ell)]}{|(x - nb)^2 + y^2 + (z - \ell)^2|^{3/2}} \\
&= \sum_{n=-\infty}^{\infty} (-1)^n \frac{\mu_0 I_0}{4\pi} \int_{-\infty}^{\infty} \mathrm{d}\ell \frac{\hat{\mathbf{y}}(x - nb) - \hat{\mathbf{x}} y}{|(x - nb)^2 + y^2 + (z - \ell)^2|^{3/2}} \\
&= \sum_{n=-\infty}^{\infty} (-1)^n \frac{\mu_0 I_0}{4\pi} [\hat{\mathbf{y}}(x - nb) - \hat{\mathbf{x}} y] \int_{-\infty}^{\infty} \mathrm{d}\ell \frac{1}{|r_\perp^2 + (\ell - z)^2|^{3/2}}
\end{aligned} \tag{B.4}$$

where $r_\perp^2 \equiv (x - nb)^2 + y^2$ is the distance in the xy plane between the infinitesimal current element and the test point, $\mathbf{r}$. To evaluate the integral, substitute $\zeta^2 \equiv (z - \ell)^2$, with $\mathrm{d}\zeta = \mathrm{d}\ell$, and with the same limits of integration. Then

$$\int_{-\infty}^{\infty} \mathrm{d}\zeta \frac{1}{(r_\perp^2 + \zeta^2)^{3/2}} = \frac{2}{r_\perp^2} \tag{B.5}$$

and

$$\mathbf{B}(\mathbf{r}) = \frac{\mu_0 I_0}{2\pi} \sum_{n=-\infty}^{\infty} (-1)^n \frac{\hat{\mathbf{y}}(x - nb) - \hat{\mathbf{x}}y}{(x - nb)^2 + y^2} \tag{B.6}$$

The $\hat{\mathbf{x}}$-component of $\mathbf{B}$ is

$$B_x(\bar{\mathbf{r}}) = -\frac{\mu_0 I_0 \bar{y}}{2\pi b} \sum_{n=-\infty}^{\infty} (-1)^n \frac{1}{(\bar{x} - n)^2 + \bar{y}^2} \tag{B.7}$$

while the $\hat{\mathbf{y}}$-component is

$$B_y(\bar{\mathbf{r}}) = \frac{\mu_0 I_0}{2\pi b} \sum_{n=-\infty}^{\infty} (-1)^n \frac{(\bar{x} - n)}{(\bar{x} - n)^2 + \bar{y}^2} \tag{B.8}$$

where $\bar{x} \equiv x/b$, $\bar{y} \equiv y/b$, and $\bar{\mathbf{r}} = \mathbf{r}/b$.

Now,

$$\sum_{n=-\infty}^{\infty} \frac{1}{(\bar{x} - n)^2 + \bar{y}^2} = \frac{\pi \cosh(\pi\bar{y}) \sinh(\pi\bar{y})}{\bar{y}\left[\cosh^2(\pi\bar{y}) - \cos^2(\pi\bar{x})\right]} \tag{B.9}$$

and

$$\begin{aligned}
&\sum_{n=-\infty}^{\infty} (-1)^n \frac{1}{(\bar{x} - n)^2 + \bar{y}^2} = \sum_{n=-\infty}^{\infty} \frac{1}{(\bar{x} - 2n)^2 + \bar{y}^2} - \sum_{n=-\infty}^{\infty} \frac{1}{[\bar{x} - (2n+1)]^2 + \bar{y}^2} \\
&= \frac{1}{4} \sum_{n=-\infty}^{\infty} \frac{1}{(\frac{\bar{x}}{2} - n)^2 + \left(\frac{\bar{y}}{2}\right)^2} - \frac{1}{4} \sum_{n=-\infty}^{\infty} \frac{1}{\left(\frac{\bar{x}-1}{2} - n\right)^2 + \left(\frac{\bar{y}}{2}\right)^2} \\
&= \frac{1}{4} \left[\frac{\pi \cosh\left(\pi\frac{\bar{y}}{2}\right) \sinh\left(\pi\frac{\bar{y}}{2}\right)}{\frac{\bar{y}}{2}\left[\cosh^2(\pi\frac{\bar{y}}{2}) - \cos^2(\pi\frac{\bar{x}}{2})\right]} - \frac{\pi \cosh\left(\pi\frac{\bar{y}}{2}\right) \sinh\left(\pi\frac{\bar{y}}{2}\right)}{\frac{\bar{y}}{2}\left[\cosh^2(\pi\frac{\bar{y}}{2}) - \cos^2(\pi\frac{\bar{x}-1}{2})\right]} \right] \\
&= \frac{\pi \cosh\left(\pi\frac{\bar{y}}{2}\right) \sinh\left(\pi\frac{\bar{y}}{2}\right)}{2\bar{y}} \left[\frac{1}{\cosh^2(\pi\frac{\bar{y}}{2}) - \cos^2(\pi\frac{\bar{x}}{2})} - \frac{1}{\cosh^2(\pi\frac{\bar{y}}{2}) - \sin^2(\pi\frac{\bar{x}}{2})} \right] \\
&= \frac{\pi \cosh\left(\pi\frac{\bar{y}}{2}\right) \sinh\left(\pi\frac{\bar{y}}{2}\right)}{2\bar{y}} \left[\frac{\cos^2(\pi\frac{\bar{x}}{2}) - \sin^2(\pi\frac{\bar{x}}{2})}{\left[\cosh^2(\pi\frac{\bar{y}}{2}) - \cos^2(\pi\frac{\bar{x}}{2})\right]\left[\cosh^2(\pi\frac{\bar{y}}{2}) - \sin^2(\pi\frac{\bar{x}}{2})\right]} \right] \\
&= \frac{\pi \cosh\left(\pi\frac{\bar{y}}{2}\right) \sinh\left(\pi\frac{\bar{y}}{2}\right)}{2\bar{y}} \left[\frac{\cos(\pi\bar{x})}{\cosh^4(\pi\frac{\bar{y}}{2}) - \cosh^2(\pi\frac{\bar{y}}{2}) + \cos^2(\pi\frac{\bar{x}}{2})\sin^2(\pi\frac{\bar{x}}{2})} \right] \\
&= \frac{\pi \cosh\left(\pi\frac{\bar{y}}{2}\right) \sinh\left(\pi\frac{\bar{y}}{2}\right)}{2\bar{y}} \left[\frac{\cos(\pi\bar{x})}{\cosh^4(\pi\frac{\bar{y}}{2}) - \cosh^2(\pi\frac{\bar{y}}{2}) + \frac{1}{4}\sin^2(\pi\bar{x}))} \right]
\end{aligned} \tag{B.10}$$

noting that $\cos(\pi\frac{\bar{x}-1}{2}) = \cos(\frac{\pi\bar{x}}{2}-\frac{\pi}{2}) = \sin(\frac{\pi\bar{x}}{2})$. But $\cosh^4(x)-\cosh^2(x) = \left[\frac{\cosh(2x)+1}{2}\right]^2 - \frac{\cosh(2x)+1}{2} = \frac{1}{4}\left[\cosh^2(2x)+2\cosh(2x)+1\right] - \frac{1}{2}\left[\cosh(2x)+1\right] = \frac{1}{4}\left(\cosh^2(2x)-1\right)$, so the sum is

$$\begin{aligned}\sum_{n=-\infty}^{\infty}(-1)^n\frac{1}{(\bar{x}-n)^2+\bar{y}^2} &= \frac{2\pi\sinh\left(\pi\frac{\bar{y}}{2}\right)\cosh\left(\pi\frac{\bar{y}}{2}\right)}{\bar{y}}\left[\frac{\cos(\pi\bar{x})}{\cosh^2(\pi\bar{y})+\sin^2(\pi\bar{x})-1)}\right] \\ &= \frac{\pi\sinh\left(\pi\bar{y}\right)}{\bar{y}}\left[\frac{\cos(\pi\bar{x})}{\cosh^2(\pi\bar{y})-\cos^2(\pi\bar{x}))}\right]\end{aligned} \tag{B.11}$$

and

$$B_x(\bar{\mathbf{r}}) = -\frac{\mu_0 I_0\bar{y}}{2\pi b}\sum_{n=-\infty}^{\infty}(-1)^n\frac{1}{(\bar{x}-n)^2+\bar{y}^2} = -\frac{\mu_0 I_0}{2b}\frac{\sinh\left(\pi\bar{y}\right)\cos(\pi\bar{x})}{\cosh^2(\pi\bar{y})-\cos^2(\pi\bar{x}))} \tag{B.12}$$

or

$$\boxed{B_x(\mathbf{r}) = -\frac{\mu_0 I_0}{2b}\frac{\sinh\left(k_\perp y\right)\cos(k_\perp x)}{\cosh^2(k_\perp y)-\cos^2(k_\perp x))} = -\frac{\mu_0 I_0}{2b}\frac{\sinh\left(k_\perp y\right)\cos(k_\perp x)}{\sinh^2(k_\perp y)+\sin^2(k_\perp x))}} \tag{B.13}$$

where $k_\perp \equiv \frac{2\pi}{2b}$.

But in a vacuum region with no currents, and neglecting displacement current, Ampère's law becomes

$$\nabla\times\mathbf{B} = \hat{\mathbf{z}}\left(\frac{\partial B_y}{\partial x}-\frac{\partial B_x}{\partial y}\right) = 0 \Rightarrow B_y = \int \mathrm{d}x\,\frac{\partial B_x}{\partial y} \tag{B.14}$$

after noting that $B_z = 0$ and the field is uniform in z by symmetry. Performing this calculation leads to

$$\boxed{B_y(\mathbf{r}) = \frac{\mu_0 I_0}{2b}\frac{\cosh(k_\perp y)\sin(k_\perp x)}{\cosh^2(k_\perp y)-\cos^2(k_\perp x)} = \frac{\mu_0 I_0}{2b}\frac{\cosh(k_\perp y)\sin(k_\perp x)}{\sinh^2(k_\perp y)+\sin^2(k_\perp x)}}. \tag{B.15}$$

B.2 Antenna Bandwidth in k-Space

The **k**-space bandwidth of the vacuum field induced by the antenna is the same as the bandwidth for vacuum perturbations to which the antenna is sensitive when operating as a receiver. Consider the flux linked by the antenna by a vacuum-field perturbation,

$$\Phi = \iint \mathbf{B} \cdot \mathrm{d}\mathbf{A} = \iint \mathbf{B} \cdot \hat{\vec{\nu}} \mathrm{d}A = \iint \mathrm{d}x\mathrm{d}y\, B_x \hat{\nu} \tag{B.16}$$

where the unit normal, $\hat{\nu}$, of the differential surface area is given by

$$\hat{\nu}(y,z) = \mathrm{sgn}\left[\cos(k_a y)\right]\left[\,\mathrm{u}(y+h/2) - \mathrm{u}(y-h/2)\right]\left[\,\mathrm{u}(z+w/2) - \mathrm{u}(z-w/2)\right], \tag{B.17}$$

with k_a the perpendicular wavenumber of the antenna (~ 1.5 cm^{-1}), w the width of antenna (~ 15.3 cm, in the z direction), $h \approx 39$ cm the height of the antenna, $\mathrm{sgn}(x)$ the signum function, and $\mathrm{u}(x)$ the Heaviside step function. $\hat{x}$ is the direction normal to the plane of the antenna; y varies crossing the rungs of the antenna (the long windings), and z varies moving along the rungs. Here, the width of the antenna wire is neglected, since it is much smaller than h.

In the Fourier domain,

$$\Phi = \left(\frac{1}{2\pi}\right)^2 \iint \mathrm{d}k_y \mathrm{d}k_z e^{i(k_y y + k_z z)} \tilde{B}_x * \tilde{\hat{\nu}} \tag{B.18}$$

where $\tilde{A} \equiv \iint \mathrm{d}y\mathrm{d}z\, e^{-i(k_y y + k_z z)} A$ is the Fourier transform of the quantity, A, and $*$ is the convolution operator, $\left(\tilde{A} * \tilde{B}\right)\Big|_u = \int \mathrm{d}v A(v) B(u-v)$.

The Fourier transform of $\hat{\nu}$ in **k** is

$$\tilde{\hat{\nu}} = \iint \mathrm{d}y\mathrm{d}z\, e^{-i(k_y y + k_z z)}\, \mathrm{sgn}\left[\cos(k_a y)\right] \left[\,\mathrm{u}(y+\frac{h}{2}) - \,\mathrm{u}(y-\frac{h}{2})\right] \left[\,\mathrm{u}(z+\frac{w}{2}) - \,\mathrm{u}(z-\frac{w}{2}\right]$$
$$= \left(\int \mathrm{d}z e^{-ik_z z} \left[\,\mathrm{u}(z+\frac{w}{2}) - \,\mathrm{u}(z-\frac{w}{2})\right]\right)$$
$$\left(\int \mathrm{d}y\, e^{-ik_y y}\, \mathrm{sgn}\left[\cos(k_a y)\right] * \int \mathrm{d}y\, e^{-ik_y y} \left[\,\mathrm{u}(y+\frac{h}{2}) - \,\mathrm{u}(y-\frac{h}{2})\right]\right) \tag{B.19}$$

The first term is

$$\int_{-\infty}^{\infty} \mathrm{d}z\, e^{-ik_z z}\, [\,\mathrm{u}(y+h/2) - \,\mathrm{u}(y-h/2)] = -\frac{1}{ik_z} e^{-ik_z z}\Big|_{-w/2}^{w/2}$$
$$= -\frac{1}{ik_z}(e^{-ik_z w/2} - e^{ik_z w/2}) = 2\frac{\sin(k_z w/2)}{k_z}\frac{w/2}{w/2} = w\,\mathrm{sinc}\left(\frac{k_z w}{2}\right) \tag{B.20}$$

and similarly,

$$\int \mathrm{d}y\, e^{-ik_y y}\, [\,\mathrm{u}(y+w/2) - \,\mathrm{u}(y-w/2)] = h\,\mathrm{sinc}(\frac{k_y h}{2}) \tag{B.21}$$

Also,

$$\int \mathrm{d}y\, e^{-ik_y y}\, \mathrm{sgn}\left[\cos(k_a y)\right] = \sum_{\mu=-\infty}^{\infty} \delta(k_y - \mu k_a)\frac{4\sin(\mu\pi/2)}{\mu} - 1, \tag{B.22}$$

since the Fourier series of the square wave is $\sum_{\mu=-\infty}^{\infty} c_\mu e^{i2\pi\mu y/\lambda_a}$, with $\lambda_a = 2\pi/k_a$ and

$$
\begin{aligned}
c_\mu &= \frac{1}{\lambda_a}\int_{-\lambda/2}^{\lambda_a/2} \mathrm{d}y\, e^{-i\mu 2\pi y/\lambda_a}\,\mathrm{sgn}\left[\cos(2\pi y/\lambda_a)\right] \\
&= -\frac{1}{\lambda_a}\int_{-\lambda/2}^{-\lambda_a/4} \mathrm{d}y\, e^{-i\mu 2\pi y/\lambda_a} + \frac{1}{2\pi}\int_{-\lambda/4}^{\lambda_a/4} \mathrm{d}y\, e^{-i\mu 2\pi y/\lambda_a} - \frac{1}{2\pi}\int_{\lambda_a/4}^{\lambda_a/2} \mathrm{d}y\, e^{-i\mu 2\pi y/\lambda_a} \\
&= -\frac{1}{\lambda_a}\frac{\lambda_a}{i2\pi\mu}\left(-e^{-i\mu 2\pi(\lambda/2)/\lambda} + e^{-i\mu 2\pi/4} + e^{-i\mu 2\pi/4} - e^{i\mu 2\pi/4} - e^{i\mu 2\pi/4} + e^{i\mu 2\pi/2}\right) \\
&= -\frac{1}{i2\pi\mu}\left[-(e^{-i\mu 2\pi(\lambda/2)/\lambda} - e^{-i\mu 2\pi(\lambda/4)/\lambda}) + (e^{-i\mu 2\pi(\lambda/4)/\lambda} - e^{i\mu 2\pi(\lambda/4)/\lambda})\right. \\
&\quad \left. -(e^{i\mu 2\pi(\lambda/4)/\lambda} - e^{i\mu 2\pi(\lambda/2)/\lambda})\right] \\
&= -\frac{1}{i2\pi\mu}\left(-e^{-i\mu\pi} + e^{-i\mu\pi/2} + e^{-i\mu\pi/2} - e^{i\mu\pi/2} - e^{i\mu\pi/2} + e^{i\mu\pi}\right) \\
&= -\frac{1}{i2\pi\mu}\left(2i\sin(\mu\pi) - 4i\sin(\mu\pi/2)\right) \\
&= \boxed{\frac{2\sin(\mu\pi/2)}{\pi\mu}},
\end{aligned}
\tag{B.23}
$$

$\mu \neq 0$, and $c_0 = 0$, and noting for a periodic function, $f(y)$, with period, $\lambda_a = 2\pi/k_a$,

$$
f(y) = \frac{1}{2\pi}\int \mathrm{d}k_y e^{ik_y y}\tilde{f}(k_y) = \sum c_\mu e^{i2\pi\mu y/\lambda_a} \Rightarrow \tilde{f}(k_y) = 2\pi\sum_{\mu=-\infty}^{\infty}\delta(k_y - \mu k_a)c_\mu \tag{B.24}
$$

Then

$$
\tilde{\tilde{\nu}}(k_y, k_z) = \left[w\,\mathrm{sinc}\left(\frac{k_z w}{2}\right)\right]\left[h\,\mathrm{sinc}\left(\frac{k_y h}{2}\right) * \left(\sum_{\mu=-\infty}^{\infty}\delta(k_y - \mu k_a)\frac{4\sin(\mu\pi/2)}{\mu} - 1\right)\right] \tag{B.25}
$$

To estimate the full width at half maximum in k_y for the first harmonic, look for

$$
\mathrm{sinc}\left(\frac{k_y^* h}{2}\right) = 2\frac{\sin(k_y^* h/2)}{k_y^* h} == \frac{1}{2} \Rightarrow \sin(k_y^* h/2) = k_y h/4, \tag{B.26}
$$

or $k_y \approx \frac{3.7910}{h}$. We may also expand the sinc function for small argument, giving

$$1 - \frac{(k_y^* h/2)^2}{6} \approx= \frac{1}{2} \Rightarrow k_y^* \approx \frac{2\sqrt{3}}{h} \approx 3.46/h \tag{B.27}$$

As such, the primary k_y band of the antenna is $\approx k_a \pm \frac{2\sqrt{3}}{h} \approx 1.5 \pm 0.05$ cm^{-1}. Similarly, the band in k_z space is 0 ± 0.2475 cm^{-1}.

Since the antenna wires are angled at $\theta_w = 14.5°$ from the toroidal direction, the Shoelace antenna's toroidal mode number, n, spectrum is centered on $n_0 = 2\pi R_0 / [2\Delta z_\perp / \tan(\theta_w)] \approx 35$, where $R_0 = 0.916$ m is the major radius of the top layer Shoelace rung at the midplane. The bandwidth of the n spectrum is limited by the width of the antenna in the toroidal direction, $w_\phi = 15.3\cos(14.5°)$ cm. Modeling the antenna as a tophat function in toroidal angle, ϕ, with an arc length of w_ϕ gives a factor of $\text{sinc}\left(\frac{n w_\phi}{2R}\right)$ in the transform, or a span of $\Delta n \approx \pm 23$ from n_0 (FWHM).

B.3 Lumped Element Circuit Parameters of Antenna

B.3.1 Resistance

The DC resistance of the wire is

$$R_{dc} = \frac{\ell}{\sigma A_c} = 0.206\,\Omega \tag{B.28}$$

The skin depth – the e-folding length of the attenuation for a plane wave incident upon a planar slab of a conducting material – is, for a good conductor[1],

$$\delta = \sqrt{\frac{2}{\omega \sigma \mu_0}} \tag{B.29}$$

For the ML molybdenum alloy, at 100 kHz, $\delta = 376$ μm, smaller than the wire radius of 762 μm. As such, the skin effect must be considered when calculating

[1]This follows simply from $\nabla \times \mathbf{B} = \mu_0 \mathbf{J} = \mu_0 \sigma \mathbf{E} \Rightarrow \nabla \times \nabla \times \mathbf{B} = -\mu_0 \sigma \frac{\partial \mathbf{B}}{\partial t} \rightarrow \mathbf{B}k^2 = i\omega\mu_0\sigma\mathbf{B}$ after Fourier decomposition, so $k = \sqrt{i\omega\mu_0\sigma} = (1+i)\sqrt{\frac{\omega\mu_0\sigma}{2}}$, the imaginary part of which defines the decay through the conductor with an e-folding length, $1/\Im\{k\} = \sqrt{\frac{2}{\omega\mu_0\sigma}}$.

the resistance. Neher and McGrath provide the following framework for wires of cylindrical cross section [127]: take the ratio of the AC resistance to that of the DC resistance for a bare, solid, uninsulated cylindrical wire to be

$$R_{ac}/R_{dc} = 1 + Y_c. \tag{B.30}$$

Y_c is divided into two components - one due to the skin effect in a single conductor, and one due to the proximity effect when multiple conductors are present. In the present case, only the single conductor model is needed. The loss due to the skin effect is given by $Y_{cs} = F(x_s)$. Here, $F(x)$ is a tabulated skin effect function, and $x_s = 1.585\sqrt{fk_s/R'_{dc}}$, where f is the frequency, $k_s = 1$ is a geometric factor equal to unity for a conductor of solid circular section, and R'_{dc} is the DC resistance per unit length[2] in units of Ω/m. $R_{dc} = 1/(\sigma A_c) = 0.0306$ for the ML wire used on the Shoelace antenna. Then $x_s = 2.86$, and $Y_{cs} = F(x) = 0.275$.

The result of the resistance calculated in this way is shown in 4-11.

B.3.2 Self Inductance

In order to visualize how to perform the inductance calculation, it is helpful to imagine stretching the rectangular-cell antenna into a continuous linkage of figure-eights, as shown in B-1. Here, it is plainly seen that the total magnetic flux linked by the antenna is equal to the number of cells multiplied by the flux linked in each cell[3]. In the planar model introduced in Section B.1, symmetry implies that the flux linked by each cell is identical.

If the field distribution from the antenna is known, the self inductance may be calculated by direct integration. Using the planar model results, Eqs. B.13 and B.15, for the field, and integrating in the plane of the wires, $x = 0$, *between* the wire segments (limiting the integration at the outer radius, a, of the wire) yields the

[2] in [127], the formula is provided as $Y_{cs} = 0.875\sqrt{fk_s/R'_{dc}}$, with R'_{dc} in $\mu\Omega$/foot.

[3] Similarly, the EMF voltage resulting from the line integral of $\nabla \times \mathbf{E}$ in Faraday's law may be carried out by integrating around cell in separately and adding all of the results, rather than integrating along the entire meandering path.

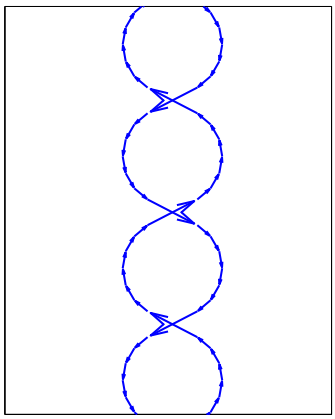

Figure B-1: Conceptual cartoon stretching the antenna winding from rectangular to circular cells. The actual antenna wire does not follow this path, but has the same topology, and the flux linked by the antenna is simpler to visualize in this picture since the wires do not lie one on top of the other.

enclosed flux per unit length along the wire (in the z coordinate),

$$\begin{aligned}\frac{\Phi_1}{w} &= \int_{\frac{a}{b}}^{1-\frac{a}{b}} B_x(\bar{y}, x=0)\mathrm{d}\bar{y} = \frac{\mu_0 I_m}{2}\int_{\frac{a}{b}}^{1-\frac{a}{b}} \frac{\sin(\pi\bar{y})}{1-\cos^2(\pi\bar{y})}\mathrm{d}\bar{y} = \frac{\mu_0 I_m}{2}\int_{\frac{a}{b}}^{1-\frac{a}{b}} \frac{1}{\sin(\pi\bar{y})}\mathrm{d}\bar{y} \\ &= \frac{\mu_0 I_m}{2\pi}\left\{\ln\left[1+\cos(\pi\frac{a}{b})\right] - \ln\left[1-\cos(\pi\frac{a}{b})\right]\right\},\end{aligned} \tag{B.31}$$

with Φ_1 representing the total flux linked by a single cell and $\bar{y} = y/b$. Then the self inductance is[4]

$$L = \mathcal{P}N_c w\frac{\Phi_1}{I_a w} = \mathcal{P}^2 N_c w\frac{\mu_0}{\pi}\left\{\ln\left[1+\cos(\pi\frac{a}{b})\right] - \ln\left[1-\cos(\pi\frac{a}{b})\right]\right\} \tag{B.32}$$

where we have evaluated $I_m/I_a = 2\mathcal{P}$, and $N_c = 18$ is the number of cells, equal to one less than the number of wire segments. $\mathcal{P}$ is the number of round-trip passes made by the winding (bottom to top and back). For the Shoelace antenna, $\mathcal{P} = 1$.

[4] A similar calculation gives an expression for the mutual inductance between two such filamentary arrays displaced only vertically, as for for the antenna and its mirror currents, $M_{12} = \frac{V_{emf,21}}{\mathrm{d}I_1/\mathrm{d}t} = \frac{\mathrm{d}N_c\Phi_{21}/\mathrm{d}t}{\mathrm{d}I_1/\mathrm{d}t} = \frac{j\omega N_c\Phi_{21}}{j\omega I_1} = \frac{\mu_0 N_c w}{2\pi}[\ln(\cosh(k_\perp\Delta x)+1) - \ln(\cosh(k_\perp\Delta x)-1)]$, where Δx is the distance between the arrays.

Notice the logarithmic singularity when $\frac{a}{b} \to 0$.

End effects tend to reduce the inductance; this is especially true when $b \sim w$. To account for end effects in the $\hat{z}$ direction, an effective width, $w_e = w - b$, might be used in Equation B.32. Moreover, the vertical separation (in x) between the two layers of the winding tends to reduce the flux enclosed in the antenna windings. This effect might be approximated by evaluating B_x at a height, $x = d/2$, intermediate between the layers of wrappings, instead of $x = 0$, as in B.31, where d is the distance between the winding layers. These two approximations give

$$L \approx \mathcal{P}^2 N_c w_e \frac{\mu_0}{\pi} \left\{ \ln \left[\cosh(\frac{\pi d}{2}) + \cos(\pi \frac{a}{b}) \right] - \ln \left[\cosh(\frac{\pi d}{2}) - \cos(\pi \frac{a}{b}) \right] \right\}. \quad \text{(B.33)}$$

When $d/b \ll 1$, this reduces the simple calculation for L by an amount, $\mathcal{P} \frac{\mu_0}{2\pi} \frac{\pi \cos(\pi a/b)}{1-\cos^2(\pi a/b)} \frac{d^2}{4b^2}$.

Equation B.31 gives $L \approx 6.3$ μH, while Equation B.33 gives $L \approx 5.4$ μH.

B.4 Matching Antenna Pitch to Background Field Lines

Since the QCM is field-aligned, it is expected that the perturbation induced by the antenna will be greatest when it is also field-aligned; indeed, experience in experiment confirmed this expectation. The effect of mismatch on the antenna response may be heuristically quantified by a simplified geometric model, as illustrated in Figure B-2. First, assume two planes containing current filaments - one modeling the antenna, and one the plasma. Within each plane are current filaments that are parallel but of alternating direction. The planes share the same normal vector, but the current filaments in one plane are rotated relative to those in the other plane. The horizontal extent of the planes is limited to the width of the antenna. Our goal is to estimate the net flux enclosed by the field lines that is produced by the windings. If we assume that the flux produced by the windings is all directed out of the plane, then the integral of

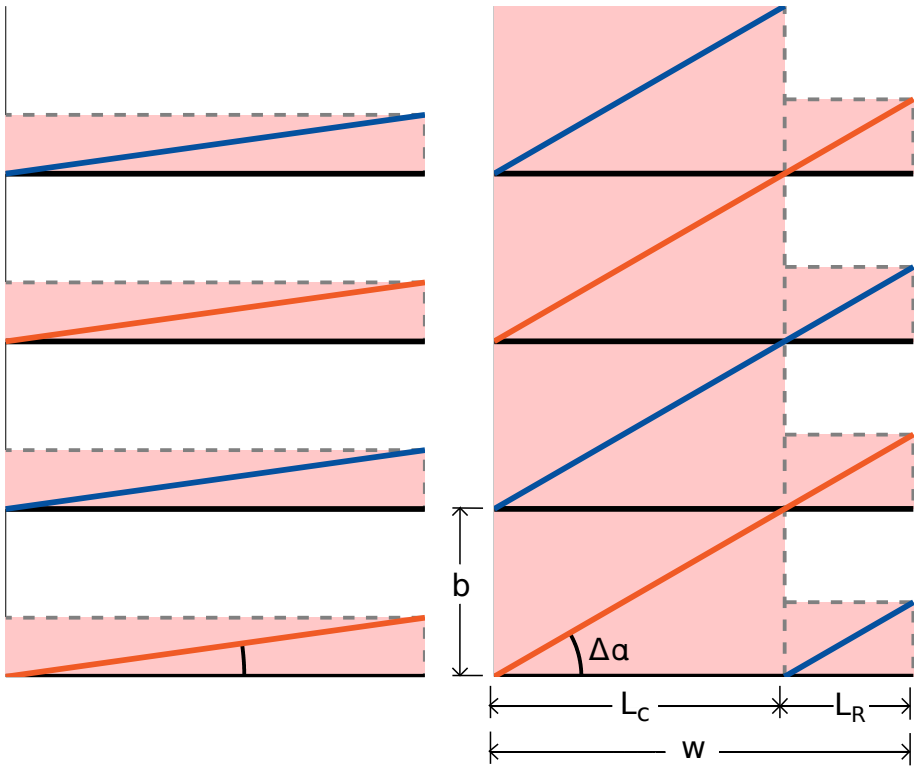

Figure B-2: Illustration of simplified geometry for quantifying pitch mismatch for (a) small angle mismatch and (b) large angle mismatch. The case in (a) is more typical of the actual situation. The annotations in (b) correspond to Eq. B.34 below. Horizontal black lines represent antenna windings; angled blue and orange lines represent field lines. Shaded regions are subject to complete flux cancellation, and the formula in Eq. B.34 gives the ratio of unshaded to total area.

the flux may be determined by geometric considerations, alone. Noting that the flux alternates direction into and out of the page across alternating antenna rungs, the net flux may be determined by subtracting from the total area those regions which sample equal regions of opposite flux, such that they are completely canceled. These regions are shaded in Figure B-2.

The effective fractional antenna coupling is then determined by the geometric ratio, $\mathcal{R}$, of coupled flux area to the total flux area of the antenna, which is the same as the ratio of unshaded to total area in Figure B-2. This is calculated as

$$\mathcal{R} = \left[1 - \frac{L_R}{b}\tan(\Delta\alpha)\right](-1)^N \tag{B.34}$$

where $\Delta\alpha$ is the angle between the antenna and plasma lines, $L_R = w - NL_c$ is the effective width of the antenna after fully canceled regions are removed, $L_c = b/\tan(\alpha)$ is the length along the antenna wire between points where the angled "plasma" line intersects the "flat" antenna line, and $N = floor(L_c/w)$ is the number of intersections that occur over the length of the antenna (i.e. the number of fully canceled flux regions, each of width, L_c).

For $\Delta\alpha < \tan^{-1}(b/w)$ such that $N = 0$, $L_c > w$, and $L_R = w$, $R = 1 - w\tan(\Delta\alpha)/b$. At $\Delta\alpha = \tan^{-1}(b/w) = \tan^{-1}(2.1/14.6) = 8^\circ$, $\mathcal{R} = 0$; at $\Delta\alpha = \tan^{-1}[b/(2w)] = \tan^{-1}(2.1/29.2) = 4^\circ$, $\mathcal{R} = 1/2$.

Several operational examples may serve to gauge the effectiveness of the chosen winding pitch angle, 14.5°, in aligning to background field. In a plasma from an antenna experiment, with $q_{95} \approx 3.2$, the field line pitch was about 13° at the midplane and 13.5°at the bottom of the antenna, corresponding to $0.8 < \mathcal{R} < 0.9$. For a $q_{95} \approx 4.0$ plasma, these angles were both approximately 10.7°, corresponding to $\mathcal{R} \approx 0.55$. At $q_{95} \approx 5.0$, they are about 8.9°, with $R \approx 0.33$. As such, the range of q_{95} over which the antenna was effectively matched to the pitch of the plasma was[5] $q_{95} < 5$, with best match at $q_{95} \approx 3$.

[5]the lower bound of q_{95} from the perspective of the acceptable range of R is irrelevant, as it is MHD unstable

B.5 Thermal Loading

The ML wire alloy used for the Shoelace winding recrystallizes at 1300 °C. Since the wire is the component exposed to the greatest heat flux, and has a low thermal mass, it is the component most likely to fail due to thermal loading (as, indeed, occurred – see Section 4.3), and so analysis of such loading should concentrate on the wire.

The relevant partial differential equation is parabolic,

$$\frac{\partial T}{\partial t} = \alpha \nabla^2 T + q/(C_p \rho) \tag{B.35}$$

where T is the wire temperature, α is the wire thermal diffusivity, and q is the heat input source per unit volume, ([W/m^3]). It is convenient to work in terms of the heat input per unit length; this quantity is denoted by Q', and may be used by substituting $q = Q'/A_c$ in Equation B.35.

The two primary sources of thermal loading are (1) the incident power flux from the plasma and the Joule (resistive) heating of the wire during an antenna pulse. In both cases, it is adequate to assume the heat flux to be uniform over the length of the wire; however, the resistive heating in the wire is not radially uniform as a result of the skin effect. Moreover, the heat flux due to the plasma is highly variable from experiment to experiment. The antenna must survive a range of conditions even when not used actively in experiments, since access to the interior of the vacuum vessel occurs infrequently, with several months of experimental run days occurring during the intervening periods.

There are two problems of interest: the transient heat rise during an experiment, and the transient cooling during the roughly ten-minute period between shots, during which time there is neither plasma nor resistive heating of the wire. Several simplifications of the problem geometry arise from the following considerations. Firstly, the decay constant for Fourier harmonics of the solution to the one-dimensional version of Equation B.35 is $\tau_n = \lambda^2/(\alpha n^2 \pi^2)$, where λ is the length of wire between the boundary points. If there is no heat-flow across the turning points in the wire path, then $\lambda = \ell$, and the longest-lived harmonic ($n = 1$) has $\tau_1 = 4.1^2/(5.3 \times 10^{-5} \cdot \pi^2) = 32 \times 10^3$ s ≈ 9

hours. If, on the other hand, the turning points provide a good contact to thermal ground, then the pertinent length is $\lambda = w$, and $\tau_1 \approx 45$ s.

As such, heat is expected to be dissipated from the wire through the ceramic pulleys to the posts. Moreover, over the course of the 1 s plasma flattop, there will be little thermal diffusion along the length of the wire, while the wire is sufficiently thin such that the temperature equilibrates across the wire radius, even for nonuniform resistive heating in light of the skin effect. As such, the transient cooling problem can be viewed as one-dimensional across the length of the wire (though complications arise in accounting for cooling through the ceramic pulley), while the heat loading can be approximated as a zero-dimensional problem.

The temperature evolution of the hottest point along the wire is then given by

$$\Delta T = \frac{Q' w}{C_p \rho w A_c} t = \frac{Q'}{C_p \rho A_c} t, \tag{B.36}$$

with t the duration of the experimental shot and ΔT the change from the initial temperature.

The heat input per unit length may be then be modeled simply as

$$Q' = (2awS_p + I^2 Rw/\ell)/w = 2aS_p + I^2 R/\ell, \tag{B.37}$$

where S_p is the incident heat flux due to the plasma, and I is the antenna current. In design work, S_p was approximated at 1 MW/m^2; a nominal current value of 150 A was selected for calculating the contribution from resistive heating; this amplitude was never achieved in the experiments presented in this thesis, but an ongoing upgrade to the power system is expected to produce outputs of this magnitude.

With these heating levels, $Q' = 1.5 \times 10^3 + 0.88 \times 10^3 = 3.1 \times 10^3$ [W/m], where $\Delta T \approx 500[\frac{\mathrm{K}}{\mathrm{s}}] \times t$. For a two-second pulse, this would result in a temperature rise of 1000 K, pushing the antenna wire near its recrystallization temperature. In practice, however, the antenna is never pulsed for more than 1 s, and the plasma flattop is typically 1 s (though occasionally longer), with plasma current ramp-up and ramp-down involving lower-power plasmas.

In the cooling problem, the critical figure of interest is the amount of time, τ, necessary for the hottest point on the wire to cool sufficiently so that it will not ratchet up, from one discharge to the next, past the recrystallization temperature over the course of an experimental run day. The interval between discharges is typically about ten minutes: $\tau < 600$ s.

Modeling the thermal diffusion in one-dimensional,

$$\frac{\partial T}{\partial t} = \alpha \frac{\partial^2}{\partial y^2} T \tag{B.38}$$

with boundary conditions, $T(0) = T(w) = T_\infty$, and the solution is

$$T = T_\infty + \sum_{n=1}^{n\to\infty} c_n e^{-t/\tau_n} \sin\left(\frac{n\pi y}{w}\right) \tag{B.39}$$

where $T_0 \equiv T(y, t = 0)$ is the uniform initial temperature on the wire,

$$c_n = \begin{cases} 0 & \text{when } n \text{ is even} \\ \dfrac{4(T_0 - T_\infty)}{\pi n} & \text{when } n \text{ is odd} \end{cases}, \tag{B.40}$$

and

$$\tau_n = \frac{L^2}{n^2 \pi^2 \alpha}. \tag{B.41}$$

The hottest point on the wire is in the middle, $y = w/2$, where the sine term is ± 1. Its decay is shown by the black dashed line in Figure B-3 using molybdenum ML wire parameters and $T_0 = 1300$ °C, $T_\infty = 400$ °C. The cooling is 99% complete after $\tau_{99} \approx 220$ s (3 min 40 s).

The actual transient will decay more slowly because of the ceramic insulation at the endpoints of the wire. To analyze this, a simplified model may be introduced as follows:

- Simplify the geometry of the heat conduction problem in the ceramic tension wheel to a toroidal disc of rectangular cross with imposed temperature on the curved boundaries and a no-flux condition on the flat surfaces.

- Examine the timescale of the decay time for the transient solution in the temperature profile in the ceramic.
- If the transient in the ceramic may be ignored, use the steady-state solution to derive an imposed-flux boundary condition for the thermal diffusion problem in the wire. This boundary condition will depend on the instantaneous boundary temperature.
- Solve the one-dimensional heat diffusion problem in the wire numerically.

The thermal diffusion problem in the ceramic is written in cylindrical coordinates as

$$\frac{\partial T}{\partial t} = \alpha \nabla^2 T = \alpha \left[\frac{1}{r} \frac{\partial}{\partial r} \left(r \frac{\partial T}{\partial r} \right) + \frac{1}{r^2} \frac{\partial^2 T}{\partial \theta^2} + \frac{\partial^2 T}{\partial z^2} \right]. \tag{B.42}$$

For simple boundary conditions, separation of variables suggests a trial solution (enforcing temperature decay),

$$T(r, \theta, z; t) = R(r)\Theta(\theta)Z(z)e^{-\omega t}. \tag{B.43}$$

Substitution of B.43 into B.42 yields

$$\begin{aligned}
Z_n(z) &= \cos\left(\frac{n\pi}{h_c} z\right) \\
\Theta_m(\theta) &= A_m e^{im\theta} + B_m e^{-im\theta} \\
R_{mn}(r) &= \mathrm{Y}_m\left(\sqrt{\frac{\omega_{mn}}{\alpha} - \frac{n^2\pi^2}{h_c^2}} r\right) - \frac{\mathrm{Y}_m\left(\sqrt{\frac{\omega_{mn}}{\alpha} - \frac{n^2\pi^2}{h_c^2}} r_i\right)}{\mathrm{J}_m\left(\sqrt{\frac{\omega_{mn}}{\alpha} - \frac{n^2\pi^2}{h_c^2}} r_i\right)} \mathrm{J}_m\left(\sqrt{\frac{\omega_{mn}}{\alpha} - \frac{n^2\pi^2}{h_c^2}} r\right) \\
T_t(r, \theta, z; t) &= \sum_{m=0}^{\infty} \sum_{n=0}^{\infty} R_{mn}(r)\Theta_m(\theta)Z_n(z)e^{-\omega_{mn}t} \\
T(r, \theta, z; t) &= T_{ss}(r, \theta, z) + T_t(r, \theta, z; t),
\end{aligned} \tag{B.44}$$

where J_m is the mth-order Bessel function of the first kind, and Y_m of the second kind; r_i is the inner radius of the ceramic tension wheel, r_o the outer radius, and h_c

is the height of the part. T_{ss} is the steady-state solution which will be determined shortly, and T_t is the transient solution. The boundary conditions,

$$\begin{aligned} T_t(r = r_i) &= 0 \text{ provides constant factor in } R_{mn} \\ T_t(r = r_o) &= 0 \text{ specifies } \omega_{mn} \\ \left.\frac{\partial T}{\partial z}\right|_{z=0} &= 0 \text{ eliminates quadrature component in } Z_n(z) \\ \left.\frac{\partial T}{\partial z}\right|_{z=h_c} &= 0 \text{ specifies eigenvalue, } \frac{n\pi}{h_c}, \end{aligned} \tag{B.45}$$

and the initial conditions,

$$T_t(r, \theta, z; t = 0) = T_0 - T_{ss}(r, \theta, z), \tag{B.46}$$

determine the constants, A_{mn} and B_{mn}, through the orthogonality relation,

$$\begin{aligned} A_{mn} &= \frac{\int_{z=0}^{z=h_c} \mathrm{d}z \cos(\frac{n\pi}{h_c} z) \int_0^{2\pi} \mathrm{d}\theta\, e^{im\theta} \int_0^{r_o} \mathrm{d}r\, r R_{mn}(r)[T(r, \theta, z; t = 0) - T_{ss}(r, \theta, z)]}{\pi h_c \int_0^{r_o} \mathrm{d}r\, r R_{mn}^2(r)} \\ B_{mn} &= \frac{\int_{z=0}^{z=h_c} \mathrm{d}z \cos(\frac{n\pi}{h_c} z) \int_0^{2\pi} \mathrm{d}\theta\, e^{-im\theta} \int_0^{r_o} \mathrm{d}r\, r R_{mn}(r)[T(r, \theta, z; t = 0) - T_{ss}(r, \theta, z)]}{\pi h_c \int_0^{r_o} \mathrm{d}r\, r R_{mn}^2(r)} \end{aligned} \tag{B.47}$$

h_c requires further comment: the geometry of this simplified problem corresponds to a uniform boundary condition at $r = r_o$ (the second condition in B.45). In the real geometry, the contact between the wire and the ceramic is much smaller than the total height of the tension wheel. h_c in this simplified problem is therefore not on the scale of the height of the ceramic as much as the diameter of the wire. However, making $h_c \backsim a$ greatly increases the thermal resistance in the simplified problem from that of the real problem. As such, the simplified problem has been posed in such a way as to be very conservative (more than compensating for the fact that the contact between wire and wheel is made only between $0 < \theta < \pi$, rather than 2π, as implied by the axisymmetry of the boundary conditions).

Table B.1: Transient decay times, τ_{mn}, for ceramic pulley cooling [s]

n \ m	0	1	2	3
0	1.4866	1.1027	0.6667	0.4347
1	0.3040	0.4344	0.6002	1.5007
2	0.0898	0.0985	0.1051	0.1174
3	0.0413	0.0430	0.0442	0.0463

The eigenvalues, ω_{mn}, are the quantity of interest from this analysis. If it is shown that $\max_{mn}(\tau_{mn}) \equiv 1/\min_{m,n}(\omega_{mn}) \ll \tau_{decay} > 100$ s, then it is safe to assume that steady-state heat-conduction through the ceramic pulley is sufficiently accurate in modeling the boundary conditions of the wire.

Numerical determination of the first several values of ω_{mn} with $r_i = 1.3$ mm, $r_o = 10$ mm, $h_c = 6a = 4.6$ mm, and $\alpha_{\mathrm{Al_2O_3}} = 5.54 \times 10^{-6}$ m^2/s yields the entries in Table B.1.

The longest-lived mode is $\tau_{00} \approx 1.5$ s$\ll \tau_{wire\,decay} > 100$ s. As such, it is, indeed, justifiable to approximate the temperature across the ceramic pulley as instantaneously at equilibrium.

The axisymmetric steady-state solution for the temperature profile across the ceramic pulley is

$$\begin{aligned} T_{ss}(r) &= a_0 \ln(r) + a_1 \\ a_0 &= \frac{T_o - T_i}{\ln(r_o/r_i)} \\ a_1 &= T_i - a_0 \ln(r_i) \end{aligned} \tag{B.48}$$

where T_i is the fixed disc temperature at the inner radius and T_o at the outer radius. This solution is used to specify one of the two boundary conditions for the wire cooling problem posed in B.38,

$$\left.\frac{\partial T_{wire}}{\partial y}\right|_{y=endpoint} = -\frac{\kappa_a}{\kappa_m}\frac{T(y_{end};t) - T_i}{r_o \ln(r_o/r_m)}, \tag{B.49}$$

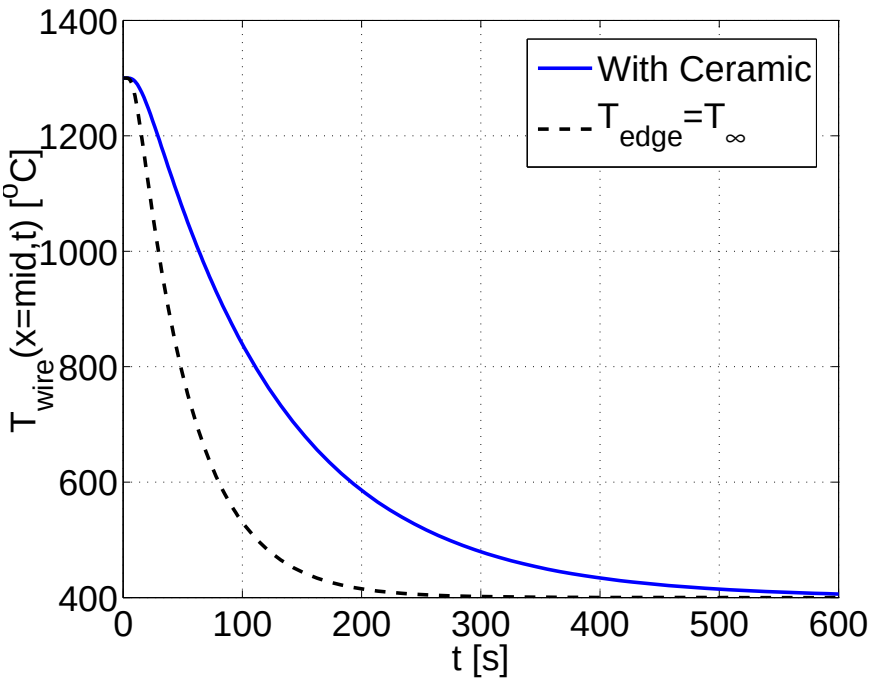

Figure B-3: Evolution of wire temperature at the hottest point of the wire (the midpoint) for the case with boundary conditions provided by the steady-state ceramic pulley model (blue solid line) and a fixed endpoint temperature (black dashed line). The initial temperature was set at 1300℃, and the temperature at the inner radius of the ceramic was fixed at 400℃.

where $\kappa_a \approx 18$ W/(m·K) is the thermal conductivity of the alumina tension wheel and $\kappa_m \approx 138$ W/(m·K) is the thermal conductivity of the ML wire.

The numerical solutions to B.38 with the boundary conditions in B.49 as well as with the original boundary conditions are shown in Figure B-3. The wire takes longer to cool using this model of the ceramic, but is still about 99% equilibrated just at the ten-minute mark. Again, the actual geometry of the ceramic tension wheel is not captured here; the additional thermal mass and contact area with the wheel's inner heat sink would likely reduce the cooling time.

Prior to the construction of the antenna, more precise thermal calculations were carried out with roughly the same heat loading parameters, finding similar, and slightly more favorable, results. Despite this, the experimental reality proved harsher than what were thought to be conservative design estimates, and the antenna wire still failed under thermal loading (see Section 4.3).

Appendix C

Low-Frequency Waves in Inhomogeneous Plasmas from the Plasma Dielectric Perspective

The cold, homogeneous plasma model does not give rise to a drift wave. However, with the inclusion of a finite, non-zero parallel electron temperature, as well as a density gradient, the drift wave branch appears with the familiar dispersion relation. This will be shown in the following. Moreover, several derivations useful for interpreting theory shown in the main body of the text are also included.

C.1 Introducing the Dielectric Tensor

First, we will describe the dielectric formalism in which the plasma response is subsumed into the dielectric tensor, $\bar{\bar{\epsilon}}$. Starting with Maxwell's equations (in SI units),

$$\begin{aligned}
\nabla \cdot \mathbf{D} &= \rho \\
\nabla \times \mathbf{E} &= -\frac{\partial \mathbf{B}}{\partial t} \\
\nabla \cdot \mathbf{B} &= 0 \\
\nabla \times \mathbf{H} &= \mathbf{J} + \frac{\partial \mathbf{D}}{\partial t}.
\end{aligned} \tag{C.1}$$

To proceed, we make use of the constitutive relation between the electric displacement and field intensity quantities. In vacuum, this is

$$\mathbf{D} = \epsilon_0 \mathbf{E}. \tag{C.2}$$

and in a general medium, it is

$$\mathbf{D} = \bar{\bar{\epsilon}} \cdot \mathbf{E} = \epsilon_0 \left(\bar{\bar{1}} + \bar{\bar{\chi}} \right) \mathbf{E}, \tag{C.3}$$

introducing $\bar{\bar{\chi}}$ as the electric susceptibility[1].

The plasma may be viewed as a dielectric medium by absorbing the current into the dielectric tensor's action on $\mathbf{E}$ in Ampère's law,

$$\mathbf{J} = \epsilon_0 \frac{\partial}{\partial t} \left(\bar{\bar{\chi}} \cdot \mathbf{E} \right), \tag{C.4}$$

so that

$$\nabla \times \mathbf{H} = \frac{\partial}{\partial t} \left(\bar{\bar{\epsilon}} \cdot \mathbf{E} \right) = \epsilon_0 \frac{\partial}{\partial t} \left[\left(\bar{\bar{1}} + \bar{\bar{\chi}} \right) \cdot \mathbf{E} \right] = \mathbf{J} + \epsilon_0 \frac{\partial \mathbf{E}}{\partial t}. \tag{C.5}$$

With

$$\mathbf{B} = \mu_0 \mathbf{H} \tag{C.6}$$

Maxwell's equations may then be expressed as

[1]The notation adopted here represents vectors with boldface, $\mathbf{u}$, and dyadics (second order tensors) with two overbars, $\bar{\bar{u}}$.

$$\begin{aligned}
\nabla \cdot (\bar{\bar{\epsilon}} \cdot \mathbf{E}) &= 0 \\
\nabla \times \mathbf{E} &= -\frac{\partial \mathbf{B}}{\partial t} \\
\nabla \cdot \mathbf{B} &= 0 \\
\nabla \times \mathbf{B} &= \mu_0 \frac{\partial \left(\bar{\bar{\epsilon}} \cdot \mathbf{E}\right)}{\partial t}.
\end{aligned} \tag{C.7}$$

C.2 Electrostatic Approximation

The electrostatic approximation results from taking the electric field to be curl-free, so that the inductive contribution to the field is negligible. In this case, $\mathbf{E} = -\nabla\tilde{\Phi} = -i\mathbf{k}\tilde{\Phi}$. This means that $\mathbf{E}$ is purely longitudinal, since the displacement in this quantity is exactly parallel to $\mathbf{k}$. Labeling the longitudinal and transverse components of $\mathbf{E}$, relative to $\mathbf{k}$, as E_ℓ and E_t, then it is clear that for the electrostatic approximation is valid when $E_\ell \gg E_t$. A sufficient condition for this to be the case is that $|n|^2 = \left|\left(\frac{ck}{\omega}\right)\right|^2 \gg \left|\frac{\epsilon^i{}_j}{\epsilon_0}\right|$ [76, Sec. 3.4]. Now, assuming a homogeneous cold plasma, and restricting the analysis to low frequencies,

$$\bar{\bar{\epsilon}} = \epsilon_0 \begin{bmatrix} S & 0 & 0 \\ 0 & S & 0 \\ 0 & 0 & P \end{bmatrix} \tag{C.8}$$

Using the free parameters from these experiments, $n^2 = \frac{c^2k^2}{\omega^2} \approx \frac{c^2k_\perp^2}{\omega^2} \sim (10^5)^2$, while $S \approx \frac{c^2}{v_A^2} \sim (10^2)^2$. Neglecting collisions, $P \approx -\frac{\omega_{pe}^2}{\omega^2} \sim -(10^6)^2$, but when $(\omega\tau'_{ei})^{-1} \gg 1$, $P \approx i\frac{\omega_{pe}^2\tau'_{ei}}{\omega} \sim i(3\times10^5)^2$. This means that n^2 is much larger than all of the components of $\bar{\bar{\epsilon}}$ except $\epsilon_{\parallel,\parallel}$.

However, the ratio of E_t and E_ℓ is rendered more precisely as [76, Eq. 3.34]

$$\frac{E_t}{E_\ell} = \frac{\hat{\mathbf{t}} \cdot \bar{\bar{\epsilon}} \cdot \hat{\mathbf{n}}}{n^2 - \hat{\mathbf{t}} \cdot \bar{\bar{\epsilon}} \cdot \hat{\mathbf{t}}} \approx \frac{-S\frac{k_\perp k_\parallel}{k^2} + P\frac{k_\perp k_\parallel}{k^2}}{n^2 - \left(\frac{k_\parallel^2 S + k_\perp^2 P}{k^2}\right)} \approx \frac{\frac{k_\parallel}{k_\perp}P}{n^2 - P} \leq \frac{k_\parallel}{k_\perp} \ll 1, \tag{C.9}$$

where the transverse unit vector, $\hat{\mathbf{t}}$, is defined through

$$-\frac{\mathbf{k}\times(\mathbf{k}\times\mathbf{E})}{k^2}=\hat{\mathbf{t}}E_t. \tag{C.10}$$

As such, the electrostatic approximation is robustly valid for the cold, homogeneous plasma which shares the density, field, and frequency range from the experiments discussed here.

We have seen in Section 3.4.2 that the electrostatic modes of the cold, homogeneous plasma are strongly damped by electron-ion collisions, and are not likely to appear in the frequency range driven by the Shoelace antenna. However, introducing an inhomogeneity in the plasma density opens a new branch – the drift wave. In the following, drift waves will be analyzed from the plasma dielectric perspective, first under electrostatic conditions, and then relaxing the electrostatic approximation.

C.3 Fluid Model

To obtain expressions for the components of $\bar{\bar{\chi}}$, we must model the plasma current response to a disturbance in $\mathbf{E}$. In the present study, we are interested in low frequencies (~ 100 kHz$\ll \Omega_{ci}/(2\pi)$), with electron collision frequencies $\nu_e \sim 10^7$. Fluid models are successful in this parameter range, and we will use one here. The model will treat electrons and ions (deuterons, in particular) as separate fluids, but quasineutrality will ensure that $\tilde{n}_e = \tilde{n}_i$. The species' temperatures are assumed equal and homogeneous. However, the density profile is taken to be inhomogeneous, varying slowly in the x coordinate[2]. This gives rise to drift waves, which appear as a result of the perturbed $\mathbf{E}\times\mathbf{B}$ velocity advecting the density gradient. The resulting density perturbations travel at the electron diamagnetic drift velocity because the forms of the $\mathbf{E}\times\mathbf{B}$ and electron diamagnetic drift velocities are similar.

[2]The coordinate system is that of the Cartesian slab, with x corresponding to the radial (or flux) coordinate, y to the perpendicular direction in a flux surface (roughly the "poloidal" coordinate), and the z direction aligned with the equilibrium magnetic field (roughly the "toroidal" coordinate).

The electron momentum equation is written as

$$m_e n_e \frac{\partial \mathbf{v}_e}{\partial t} = -e n_e \left(\mathbf{E} + \mathbf{v}_e \times \mathbf{B}\right) - \nabla p_e + m_e n_e \nu_e' \left(\mathbf{u}_i - \mathbf{v}_e\right) \tag{C.11}$$

and the ion momentum equation is

$$m_i n_i \frac{\partial \mathbf{u}_i}{\partial t} = e n_i \left(\mathbf{E} + \mathbf{u}_i \times \mathbf{B}\right) - \nabla p_i - m_e n_e \nu_e' \left(\mathbf{u}_i - \mathbf{v}_e\right). \tag{C.12}$$

The parameter, $\nu_e' \equiv \frac{0.51}{\tau_{ei}}$, is the electron collisionality that appears in the Spitzer resistivity as $\eta_s = \frac{m_e \nu_e'}{n_e e^2} = \frac{\nu_e'}{\epsilon_0 \omega_{pe}^2}$, which is equal to the parallel resistivity in the Braginskiĭ model.

To construct Ohm's law, we multiply the ion momentum equation by $\mu_e \equiv m_e/m_i$ and subtract from this the electron momentum equation. Assuming $n_i = n_e$ and $p_i = p_e$, and neglecting terms of order μ_e, this gives

$$m_e n_e \frac{\partial}{\partial t}\left(\mathbf{u}_i - \mathbf{v}_e\right) = e n_e \left(\mathbf{E} + \mathbf{v}_e \times \mathbf{B}\right) + \nabla p_e - m_e n_e \nu_e' \left(\mathbf{u}_i - \mathbf{v}_e\right). \tag{C.13}$$

Multiplying by e/m_e and permuting factors of n_e with differentials at will when multiplying a dynamic quantity gives

$$\frac{\partial \mathbf{J}}{\partial t} = \frac{e^2 n_e}{m_e}\left(\mathbf{E} + \mathbf{v}_e \times \mathbf{B}\right) + \frac{e}{m_e}\nabla p_e - \nu_e' \mathbf{J}. \tag{C.14}$$

Clearing the coefficient of $(\mathbf{E} + \mathbf{v}_e \times \mathbf{B})$ gives Ohm's Law,

$$\frac{m_e}{e^2 n_e}\frac{\partial \mathbf{J}}{\partial t} = \left(\mathbf{E} + \mathbf{v}_e \times \mathbf{B}\right) + \frac{1}{n_e e}\nabla p_e - \frac{m_e \nu_e'}{e^2 n_e}\mathbf{J}. \tag{C.15}$$

With $\omega_{pe}^2 \equiv \frac{e^2 n_e}{\epsilon_0 m_e}$ and generalizing $\eta_s = \frac{m_e \nu_e'}{e^2 n_e}$ to a diagonal tensor,

$$\frac{1}{\epsilon_0 \omega_{pe}^2}\frac{\partial \mathbf{J}}{\partial t} = \left(\mathbf{E} + \mathbf{v}_e \times \mathbf{B}\right) + \frac{1}{n_e e}\nabla p_e - \bar{\bar{\eta}} \cdot \mathbf{J}. \tag{C.16}$$

The parallel component of this equation is

$$\boxed{\frac{1}{\epsilon_0 \omega_{pe}^2}\frac{\partial J_\parallel}{\partial t} = E_\parallel + \frac{1}{n_e e}\nabla_\parallel p_e - \eta_\parallel J_\parallel} \tag{C.17}$$

where $\nabla_\parallel \equiv \hat{\mathbf{b}} \cdot \nabla$.

To retrieve a susceptibility from the parallel Ohm's law, it is necessary to eliminate p_e and express the parallel pressure drive in terms of the current and electric field components. This may be accomplished with the aid of the electron continuity condition,

$$\boxed{\frac{\partial n_e}{\partial t} + \nabla \cdot n_e \mathbf{v}_e = 0}. \tag{C.18}$$

The contributions to the electron velocity vector, $\mathbf{v}_e$, are from parallel motion and drifts,

$$\mathbf{v}_e = \hat{\mathbf{b}} v_\parallel + \mathbf{v}_* + \mathbf{v}_E, \tag{C.19}$$

where $\mathbf{v}_* = \frac{\nabla p_e \times \mathbf{B}}{n_e e B^2}$ is the electron diamagnetic drift velocity and $\mathbf{v}_E = \frac{\mathbf{E}\times\mathbf{B}}{B^2}$ is the $\mathbf{E} \times \mathbf{B}$ drift velocity.

Expanding the terms for $\mathbf{v}_e$ in Eq. C.18,

$$\frac{\partial n_e}{\partial t} + \nabla \cdot \left(n_e v_\parallel \hat{b}\right) + \nabla \cdot (n_e \mathbf{v}_*) + \nabla \cdot (n_e \mathbf{v}_E) = 0 \tag{C.20}$$

Next, we make use of the *diamagnetic divergence operator*, also known as the *magnetic curvature operator*, $\mathcal{K}$, according to [65]. This operator is discussed in Section C.6.

The diamagnetic drift flux can be expressed with $\mathcal{K}$ as

$$\nabla \cdot (n_e \mathbf{v}_*) = \nabla \cdot \left(n_e \frac{\nabla p_e \times \mathbf{B}}{n_e e B^2}\right) = -\frac{1}{e}\nabla \cdot \left(\frac{1}{B^2}\mathbf{B} \times \nabla p_e\right) = \frac{1}{e}\mathcal{K}\left(p_e\right) \tag{C.21}$$

Using the electrostatic approximation for $\mathbf{E}$ in the perpendicular direction,

$$\nabla \cdot \mathbf{v}_E = \nabla \cdot \left(\frac{\mathbf{E} \times \mathbf{B}}{B^2}\right) = \nabla \cdot \left(\frac{-\nabla\Phi \times \mathbf{B}}{B^2}\right) = \nabla \cdot \left(\frac{1}{B^2}\mathbf{B} \times \nabla\Phi\right) = -\mathcal{K}\left(\Phi\right) \tag{C.22}$$

so that

$$\nabla \cdot (n_e \mathbf{v}_E) = n_e \nabla \cdot \mathbf{v}_E + \mathbf{v}_E \cdot \nabla n_e = -n_e \mathcal{K}(\Phi) + \mathbf{v}_E \cdot \nabla n_e. \tag{C.23}$$

Returning to Eq. C.20, and making use of the diamagnetic divergence operator, we have

$$\frac{\partial n_e}{\partial t} + \nabla \cdot \left(n_e v_\parallel \hat{\mathbf{b}} \right) + \mathbf{v}_E \cdot \nabla n_e + \frac{1}{e} \mathcal{K}(p_e) - n_e \mathcal{K}(\Phi) = 0 \tag{C.24}$$

This equation is accurate to all orders under the electrostatic approximation.

Let us now turn our attention to $\mathbf{E} \times \mathbf{B}$ advection of the density gradient. Using the identity, $\mathbf{A} \cdot (\mathbf{B} \times \mathbf{C}) = (\mathbf{A} \times \mathbf{B}) \cdot \mathbf{C} = \mathbf{B} \cdot (\mathbf{C} \times \mathbf{A})$,

$$\boxed{\begin{aligned} \mathbf{v}_E \cdot \nabla n_e = \nabla n_e \cdot \mathbf{v}_E = \nabla n_e \cdot \frac{\mathbf{E} \times \mathbf{B}}{B^2} = \mathbf{E} \cdot \frac{\mathbf{B} \times \nabla n_e}{B^2} = -\frac{n_e e}{T_e} \mathbf{E} \cdot \frac{T_e \nabla n_e \times \mathbf{B}}{n_e e B^2} \\ = -\frac{n_e e}{T_e} \mathbf{E} \cdot \mathbf{v}_* \end{aligned}} \tag{C.25}$$

where the last equality holds when T_e is homogeneous and so can be commuted inside the gradient of n_e, using the isotherm, $p_e = n_e T_e$. It is this result, in fact, which gives drift waves a phase velocity equal to the electron diamagnetic drift velocity, even though no diamagnetic drift physics need be invoked, as we shall see.

Let us next (a) neglect the terms bearing $\mathcal{K}$ and (b) carry out an ordered expansion of n_e and $\mathbf{v}_e$, $n_e = n_{e,0} + \tilde{n}_e$ and $\mathbf{v}_e = \mathbf{v}_{e,0} + \tilde{\mathbf{v}}$, with $\frac{\partial}{\partial t} \to 0$ for equilibrium quantities (those with a "0" subscript),

$$\begin{aligned} &\nabla \cdot (n_{e,0} \mathbf{v}_{e,0}) = 0 \\ &\frac{\partial \tilde{n}_e}{\partial t} + \nabla \cdot (\tilde{n}_e \mathbf{v}_{e,0} + n_{e,0} \tilde{\mathbf{v}}_e) = 0. \end{aligned} \tag{C.26}$$

The gradient of the background density profile is assumed to vary only in one direction, $\nabla n_{e,0} = \frac{\partial n_e}{\partial x}$, $\hat{\mathbf{x}} \equiv -\nabla n_e / |\nabla n_e|$, which is orthogonal to the background magnetic field, $\mathbf{B} \cdot \hat{\mathbf{x}} = 0$.

We can approximate the $\mathcal{O}\{1\}$ equation as

$$\frac{\partial \tilde{n}_e}{\partial t} + n_{e,0}\nabla_\parallel v_\parallel + \tilde{\mathbf{v}}_E \cdot \nabla n_{e,0} + \mathbf{v}_{E,0} \cdot \nabla \tilde{n}_e = 0. \tag{C.27}$$

The diamagnetic velocity has disappeared[3] since we have taken $\mathcal{K} \to 0$. Having already ignored the curvature operator, $\mathcal{K}$, $\nabla \cdot \left(n_e v_\parallel \hat{\mathbf{b}} \right) \approx \hat{\mathbf{b}} \cdot \nabla \left(n_e v_\parallel \right) = \nabla_\parallel \left(n_e v_\parallel \right) = v_\parallel \nabla_\parallel n_e + n_e \nabla_\parallel v_\parallel \approx v_{\parallel,0} \nabla_\parallel \tilde{n}_e + n_{e,0} \nabla_\parallel \tilde{v}_\parallel$, since the equilibrium quantities are assumed uniform along field lines. Then

$$\frac{\mathrm{d}_E \tilde{n}_e}{\mathrm{d}t} + v_{\parallel,0}\nabla_\parallel \tilde{n}_e + n_{e,0}\nabla_\parallel \tilde{v}_\parallel + \tilde{\mathbf{v}}_E \cdot \nabla n_{e,0} = 0, \tag{C.28}$$

using the convective derivative, $\frac{\mathrm{d}_E U}{\mathrm{d}t} = \frac{\partial U}{\partial t} + \mathbf{v}_E \cdot \nabla U$ for an arbitrary scalar field, U. Now, in light of Eq. C.25,

$$\tilde{\mathbf{v}}_E \cdot \nabla n_{e,0} = -\frac{n_{e,0} e}{T_e} \tilde{\mathbf{E}} \cdot \mathbf{v}_* \tag{C.29}$$

As such, again taking T_e to be homogeneous in space[4],

$$\left(\frac{\mathrm{d}_E}{\mathrm{d}t} + v_{\parallel,0}\nabla_\parallel \right) \tilde{n}_e = -n_{e,0}\nabla_\parallel \tilde{v}_\parallel - \tilde{\mathbf{v}}_E \cdot \nabla n_{e,0} = -n_{e,0}\nabla_\parallel \tilde{v}_\parallel + \frac{n_{e,0} e}{T_e} \tilde{\mathbf{E}} \cdot \mathbf{v}_* \tag{C.30}$$

$$\tilde{n}_e = \left(\frac{\mathrm{d}_E}{\mathrm{d}t} + v_{\parallel,0}\nabla_\parallel \right)^{-1} \left(-n_{e,0}\nabla_\parallel \tilde{v}_\parallel + \frac{n_{e,0} e}{T_e} \tilde{\mathbf{E}}_\perp \cdot \mathbf{v}_* \right) \tag{C.31}$$

and $\mathbf{E} \cdot \mathbf{v}_* = \mathbf{E}_\perp \cdot \mathbf{v}_*$, since $\hat{\mathbf{b}} \cdot \mathbf{v}_* = 0$.

$$\tilde{n}_e = \left(\frac{\mathrm{d}_E}{\mathrm{d}t} + v_{\parallel,0}\nabla_\parallel \right)^{-1} \left(-n_{e,0}\nabla_\parallel \tilde{v}_\parallel + \frac{n_{e,0} e}{T_e} \mathbf{E}_\perp \cdot \mathbf{v}_* \right) \tag{C.32}$$

Because $n_{e,0}$ is at equilibrium, and $\nabla n_{e,0}$ is orthogonal to $\mathbf{v}_E$ and $\hat{\mathbf{b}}$, $n_{e,0}$ may be

[3] Independently, advection by the diamagnetic velocity is canceled by the diamagnetic momentum flux – this is the diamagnetic cancellation.

[4] although this is not the case for the QCM; ultimately, we must involve additional energy conservation equations to account for temperature fluctuations, though this is not done here.

factored out of the quantities under the inverted operator,

$$\boxed{\tilde{n}_e = n_{e,0}\left(\frac{\mathrm{d}_E}{\mathrm{d}t} + v_{\parallel,0}\nabla_\parallel\right)^{-1}\left(-\nabla_\parallel\tilde{v}_\parallel + \frac{e}{T_e}\mathbf{E}_\perp\cdot\mathbf{v}_*\right)}. \tag{C.33}$$

Fourier transforming and neglecting $\mathbf{v}_E$ advection in the convective derivative[5], $\frac{\mathrm{d}_E}{\mathrm{d}t} \to \frac{\partial}{\partial t}$, and taking $\mathbf{E}_\perp = -\nabla_\perp\Phi$

$$\tilde{n}_e = n_{e,0}\frac{1}{i\omega}\left(ik_\parallel\tilde{v}_\parallel + i\frac{e}{T_e}\frac{k_\parallel}{k_\parallel}k_\perp\tilde{\Phi}v_*\right) \tag{C.34}$$

where $k_\perp = k_y$ and $v_* = \hat{\mathbf{e}}_y\cdot\mathbf{v}_*$ (and so v_* can be positive or negative). Now, making use of the electrostatic approximation, $E_\perp = -i\frac{k_\parallel}{k_\parallel}k_\perp\Phi = \frac{k_\perp}{k_\parallel}E_\parallel$, and so

$$\boxed{\tilde{n}_e = -in_{e,0}\frac{k_\parallel}{\omega}\left(i\tilde{v}_\parallel - \frac{e}{T_e}\frac{k_\perp v_*}{k_\parallel^2}\tilde{E}_\parallel\right)}. \tag{C.35}$$

Using the same isotherm for the electron pressure, $p_e = n_eT_e$, Eq. C.33 can be used to eliminate p_e from the parallel Ohm's law, Eq. C.17, reprised below

$$\frac{1}{\epsilon_0\omega_{pe}^2}\frac{\partial\tilde{J}_\parallel}{\partial t} = \tilde{E}_\parallel + \frac{1}{n_ee}\nabla_\parallel\tilde{p}_e - \eta_\parallel\tilde{J}_\parallel. \tag{C.36}$$

Again, we will assume that the temperature is spatially homogeneous. Then $\tilde{p}_e = \tilde{n}_eT_e$, and

$$\boxed{\begin{aligned}\frac{1}{\epsilon_0\omega_{pe}^2}\frac{\partial\tilde{J}_\parallel}{\partial t} =& \tilde{E}_\parallel + \frac{T_e}{e}\nabla_\parallel\left[\left(\frac{\mathrm{d}_E}{\mathrm{d}t} + v_{\parallel,0}\nabla_\parallel\right)^{-1}\left(\frac{1}{n_ee}\nabla_\parallel\tilde{J}_\parallel - \nabla_\parallel u_\parallel + \frac{e}{T_e}\mathbf{E}_\perp\cdot\mathbf{v}_*\right)\right] \\ &- \eta_\parallel\tilde{J}_\parallel\end{aligned}} \tag{C.37}$$

after commuting the equilibrium density outside of the parallel gradient operator and taking $n_{e,0}/n_e \approx 1$.

To derive the simplest drift wave dispersion relation, (a) Fourier transform in time and space using plane waves, $e^{i(\mathbf{k}\cdot\mathbf{r}-\omega t)}$, (b) assume no equilibrium flows, $v_{\parallel,0} =$

[5] Compare this equation with Eq. C.52 for the result from the ion continuity equation.

$\mathbf{v}_{E,0} = 0$ and (c) no parallel ion velocity perturbation, $\tilde{u}_\parallel = 0$, and (d) use the electrostatic approximation in both the parallel and perpendicular directions, such that $\tilde{E}_\parallel = -ik_\parallel\tilde{\Phi}$ and $E_y = -ik_y\tilde{\Phi} = -ik_y\frac{k_\parallel}{k_\parallel}\tilde{\Phi} = \frac{k_y}{k_\parallel}\tilde{E}_\parallel$. Then Eq. C.37 becomes

$$-i\omega\frac{1}{\epsilon_0\omega_{pe}^2}\tilde{J}_\parallel = \tilde{E}_\parallel + i\frac{T_e}{e}k_\parallel\left[\frac{1}{-i\omega}\left(ik_\parallel\frac{1}{n_e e}\tilde{J}_\parallel + \frac{e}{T_e}\frac{k_\perp}{k_\parallel}\tilde{E}_\parallel v_*\right)\right] - \eta_\parallel\tilde{J}_\parallel \tag{C.38}$$

and, solving for $\tilde{J}_\parallel$

$$\boxed{\tilde{J}_\parallel = \frac{\epsilon_0\omega_{pe}^2}{-i\omega}\frac{\left(1-\frac{k_\perp v_*}{\omega}\right)}{\left(1-k_\parallel^2\frac{T_e}{m_e\omega^2}+i\frac{\nu_e'}{\omega}\right)}\tilde{E}_\parallel} \tag{C.39}$$

noting that $\eta_\parallel = \frac{\nu_e'}{\epsilon_0\omega_{pe}^2} = \frac{0.51}{\epsilon_0\omega_{pe}^2\tau_{ei}}$ (the Spitzer resistivity).

Referring to Eq. C.4, we identify the component of the susceptibility tensor, χ_{zz}, as

$$\boxed{\chi_{zz} = -\frac{\omega_{pe}^2}{\omega^2}\frac{\left(1-\frac{k_\perp v_*}{\omega}\right)}{\left(1-k_\parallel^2\frac{T_e}{m_e\omega^2}+i\frac{\nu_e'}{\omega}\right)}} \tag{C.40}$$

where $\chi_{zz} = \bar{\bar{\chi}}\cdot\hat{\mathbf{e}}_z\cdot\hat{\mathbf{e}}_z$.

The electrostatic dispersion relation for a homogeneous plasma (which this is not) is given by $\mathbf{k}\cdot\bar{\bar{\epsilon}}\cdot\mathbf{k} = 0$, but since $\epsilon_{zz} = 1+\chi_{zz} \approx \chi_{zz}$, and this is the largest element of $\bar{\bar{\epsilon}}$, the dispersion relation may be well-approximated by $\chi_{zz} = 0$, leading to

$$\boxed{\omega = k_\perp v_*}. \tag{C.41}$$

The effect of the pressure gradient on the cold plasma model is to modify $P = 1-\frac{\omega_{pe}^2}{\omega^2}$. This opens a new branch in the dispersion relation: the drift wave (*cf.* Eq. 3.15).

As seen in Eq. C.25, the appearance of the diamagnetic drift velocity, v_*, is a result of $\mathbf{E}\times\mathbf{B}$ advection of the density gradient, combined with the fact that density and potential perturbations track each other closely, $\frac{e\tilde{\Phi}}{T_e} \sim \frac{\tilde{n}_e}{n_e}$, as suggested by the parallel Ohm's law, treating resistive ($\eta_\parallel J_\parallel$), electron inertial ($\frac{m_e}{n_e e^2}\frac{\partial\tilde{J}_\parallel}{\partial t}$), and electromagnetic

$(-\frac{\partial A_\parallel}{\partial t})$ contributions are small corrections.

The physical interpretation of the drift wave is described in Section 3.2.2.

Note that diamagnetic drift physics need not be invoked for this velocity to appear – indeed, we took $\nabla \cdot (n_e \mathbf{v}_*) = \frac{1}{e}\mathcal{K}(p_e) \to 0$ in a homogeneous field[6]. Even with a purely parallel thermal velocity, for which there is no diamagnetic drift, the same drift wave dispersion relation appears [76].

The denominator of χ_{zz} hints at Landau damping [76], since, if $\nu_e' \to 0$, causality implies a deviation of the pole in χ_{zz} to the positive imaginary half-plane.

C.4 Polarization Drift and Dispersion

The polarization drift was defined in Eqs. 3.6 and 3.7, and its importance was explained in the context of quasineutrality in the discussion around Eq. 3.17. Let us briefly revisit the quasineutrality approximation. The divergence of Ampère's law, $\nabla \times \mathbf{B} = \mu_0 \mathbf{J} + \mu_0 \frac{\partial \mathbf{D}}{\partial t}$, is

$$0 = \nabla \cdot \mathbf{J} + \mu_0 \frac{\partial \nabla \cdot \mathbf{D}}{\partial t} = \nabla \cdot \mathbf{J} + \mu_0 \frac{\partial \rho_s}{\partial t} \tag{C.42}$$

after permuting spatial and temporal derivatives. The quasineutral approximation[7], appropriate at low frequencies, sets $\frac{\partial \rho}{\partial t} \to 0$, such that

$$\boxed{\nabla \cdot \mathbf{J} \approx 0}. \tag{C.43}$$

Under this approximation, static space charge is permitted, giving rise to background flows, but it is not permitted to accumulate or diminish over time.

The polarization drift is proportional to the species mass through $u_{p,s} \propto \frac{\omega}{\Omega_{cs}}$. The small electron inertia obviates the need to include the electron polarization drift at low frequencies. However, the ion inertia is sufficient to produce a non-negligible ion

[6] Of course, if there is a pressure gradient, then the equilibrium field cannot truly be homogeneous, but must also have a spatial dependence, though small in magnitude in the present case. This is seen from MHD equilibrium, which holds that $\nabla(p_e + p_i) = \mathbf{J}_* \times \mathbf{B}$, where $\mathbf{J}_*$ is the diamagnetic current and implies a non-zero curl in $\mathbf{B}$.

[7] Note that this is the same approximation that leads to Kirchoff's current law.

polarization drift which balances the parallel gradient in the parallel current,

$$\begin{aligned}\nabla\cdot\mathbf{J}=0&=\nabla\cdot\left(-n_e e v_\parallel\hat{\mathbf{b}}+n_e e\mathbf{u}_p+n_e e\left(\mathbf{v}_*+\mathbf{u}_*\right)\right)\\&=\nabla\cdot\left(-n_e e v_\parallel\hat{\mathbf{b}}+n_e e\mathbf{u}_p\right)+\mathcal{K}\left(p_e+p_i\right)\end{aligned}\tag{C.44}$$

with $n_e = n_i$. Neglecting the contribution to the divergence from the diamagnetic drifts, $\mathcal{K}\to 0$, we can identify that $v_\parallel = u_p$.

The most straightforward way to include the effect of the polarization current into the drift-wave dispersion relation is to use the ion continuity equation, rather than the electron, in the elimination of $\nabla_\parallel\tilde{n}_e$ from the parallel Ohm's law. This is possible since quasineutrality ensures that $\tilde{n}_e = \tilde{n}_i$. The ion continuity equation is

$$\begin{aligned}\frac{\partial n_i}{\partial t}+\nabla\cdot\left(n_i\mathbf{u}\right)=0&=\frac{\partial n_i}{\partial t}+\nabla\cdot\left[n_i\left(\mathbf{v}_E+\mathbf{u}_*+\mathbf{u}_p\right)\right]\\&=\frac{\partial\tilde{n}_i}{\partial t}+\nabla\cdot\left[n_i\left(\mathbf{v}_E+\mathbf{u}_*\right)\right]+\nabla\cdot\left[n_i\frac{1}{\Omega_{ci}}\frac{\mathbf{B}}{B}\times\frac{\mathrm{d}_E}{\mathrm{d}t}\left(\mathbf{v}_E+\mathbf{u}_*\right)\right]\end{aligned}\tag{C.45}$$

noting that the $\mathbf{E}\times\mathbf{B}$ velocity is the same for both species, $\mathbf{u}_E = \mathbf{v}_E$. Now,

$$\frac{\partial\tilde{n}_i}{\partial t}+\nabla\cdot\left[n_i\left(\mathbf{v}_E+\mathbf{u}_*\right)\right]=\frac{\mathrm{d}_E n_i}{\mathrm{d}t}-n_i\mathcal{K}\left(\Phi\right)+\frac{1}{e}\mathcal{K}\left(p_i\right)\tag{C.46}$$

as before, with the electrostatic approximation used in the perpendicular direction, $\mathbf{E}_\perp = -\nabla_\perp\Phi$. However,

$$\begin{aligned}\nabla\cdot\left(n_i\mathbf{u}_p\right)&=\nabla\cdot\left[n_i\frac{1}{\Omega_{ci}}\frac{\mathbf{B}}{B}\times\frac{\mathrm{d}_E}{\mathrm{d}t}\left(\mathbf{v}_E+\mathbf{u}_*\right)\right]\approx\nabla\cdot\left[n_i\frac{1}{\Omega_{ci}}\frac{\mathrm{d}_E}{\mathrm{d}t}\left[\frac{\mathbf{B}}{B}\times\left(\mathbf{v}_E+\mathbf{u}_*\right)\right]\right]\\&=\nabla\cdot\left[n_i\frac{1}{\Omega_{ci}}\frac{\mathrm{d}_E}{\mathrm{d}t}\left(\frac{\mathbf{E}_\perp}{B}-\frac{\nabla_\perp p_i}{n_e e B}\right)\right]\\&=-\nabla\cdot\left[\frac{1}{\Omega_{ci}}\frac{n_i}{B}\frac{\mathrm{d}_E}{\mathrm{d}t}\left(\nabla_\perp\Phi+\frac{\nabla_\perp p_i}{n_e e}\right)\right]\end{aligned}\tag{C.47}$$

where $\nabla_\perp u = \nabla u - \hat{\mathbf{b}}\cdot\nabla u$. Then the ion continuity equation (neglecting parallel ion

flow) becomes

$$\frac{\mathrm{d}_E n_i}{\mathrm{d}t} - n_i \mathcal{K}\left(\Phi\right) + \frac{1}{e}\mathcal{K}\left(p_i\right) - \nabla \cdot \left[\frac{1}{\Omega_{ci}}\frac{n_i}{B}\frac{\mathrm{d}_E}{\mathrm{d}t}\left(\nabla_\perp \Phi + \frac{\nabla_\perp p_i}{n_e e}\right)\right] = 0. \tag{C.48}$$

Letting $\mathcal{K} \to 0$ (by taking $\mathbf{B}$ to homogeneous), keeping only first-order terms, ignoring the contribution of diamagnetic flows in the divergence of the polarization current, and lastly ignoring background advection by $\mathbf{v}_{E,0}$,

$$\frac{\partial n_i}{\partial t} + \tilde{\mathbf{v}}_E \cdot \nabla n_{i,0} - \frac{1}{\Omega_{ci}}\frac{n_{i,0}}{B}\frac{\partial}{\partial t}\left(\nabla_\perp^2 \tilde{\Phi}\right) = 0. \tag{C.49}$$

Again making use of Eq. C.25,

$$\frac{\partial n_i}{\partial t} + \frac{n_{i,0} e}{T_i}\mathbf{E} \cdot \mathbf{u}_* - \frac{1}{\Omega_{ci}}\frac{n_{i,0}}{B}\frac{\partial}{\partial t}\left(\nabla_\perp^2 \tilde{\Phi}\right) = 0. \tag{C.50}$$

Fourier transforming,

$$-i\omega\tilde{n}_i + \frac{n_{i,0} e}{T_i}\frac{k_\perp}{k_\parallel}\tilde{E}_\parallel u_* - ik_\perp^2 \omega \frac{1}{\Omega_{ci}}\frac{n_{i,0}}{B}\tilde{\Phi} = 0. \tag{C.51}$$

Then, solving for $\tilde{n}_i = \tilde{n}_e$,

$$\boxed{\tilde{n}_i = -i\frac{n_{i,0}}{\omega}\frac{e}{T_i}\frac{k_\perp u_*}{k_\parallel}\left(1 + \frac{k_\perp \omega}{u_*}\rho_s^2\right)\tilde{E}_\parallel} \tag{C.52}$$

where, as before, $u_* = \mathbf{u}_* \cdot \hat{\mathbf{e}}_y$ is the y component (where $\hat{y}$ is perpendicular to the flux surface and the background field) of the diamagnetic flow (this time, for the ions), and $\mathbf{u}_* = \frac{\mathbf{B}\times\nabla p_i}{n_e e B^2}$ is the ion diamagnetic velocity, which runs in the opposite direction as $\mathbf{v}_*$. We have also introduced the parameter,

$$\boxed{\rho_s \equiv \frac{c_s}{\Omega_i}}, \tag{C.53}$$

the drift dispersion scale length, so named because it controls the degree of dispersion in the drift wave phase velocity, as will become apparent shortly. This parameter is similar to the ion gyro radius, with the sound speed, $c_s = \sqrt{T_e/M_i}$, replacing the ion

thermal speed.

Eq. C.52 may be compared with Eq. C.35 describing electron continuity.

Using Eq. C.52 to eliminate $\tilde{n}_e$ from the parallel Ohm's law, Eq. C.17,

$$-i\omega\frac{1}{\epsilon_0\omega_{pe}^2}\tilde{J}_\parallel = \tilde{E}_\parallel + ik_\parallel\frac{T_e}{n_e e}\left[-i\frac{n_{i,0}}{\omega}\frac{e}{T_i}\frac{k_\perp u_*}{k_\parallel}\left(1+k_\perp\omega\frac{\rho_s^2}{u_*}\right)\tilde{E}_\parallel\right] - \eta_\parallel\tilde{J}_\parallel. \tag{C.54}$$

Taking $T_i = T_e$ and $n_{e,0} = n_{i,0}$, so that $u_* = -v_*$,

$$\tilde{J}_\parallel = i\frac{\epsilon_0\omega_{pe}^2}{\omega}\frac{\left[1-\frac{k_\perp v_*}{\omega}\left(1-k_\perp\omega\frac{\rho_s^2}{v_*}\right)\right]}{\left(1+i\frac{\nu_e'}{\omega}\right)}\tilde{E}_\parallel, \tag{C.55}$$

so that

$$\boxed{\chi_{zz} = -\frac{\omega_{pe}^2}{\omega^2}\frac{\left[1-\frac{k_\perp v_*}{\omega}\left(1-k_\perp\omega\frac{\rho_s^2}{v_*}\right)\right]}{\left(1+i\frac{\nu_e'}{\omega}\right)}} \tag{C.56}$$

which may be compared to Eq. C.40. The new drift wave dispersion relation obtained from setting $\chi_{zz} = 0$ is

$$1-\frac{k_\perp v_*}{\omega}\left(1-k_\perp\omega\frac{\rho_s^2}{v_*}\right) = 0. \tag{C.57}$$

But we expect the dispersive correction to the basic drift wave dispersion relation, Eq. C.41, to be small. Then $k_\perp\omega\frac{\rho_s^2}{v_*} \approx k_\perp\omega_d\frac{\rho_s^2}{v_*} = k_\perp^2\rho_s^2 \ll 1$, $\omega_d \equiv k_\perp v_*$, resulting in the dispersion relation[8],

$$\boxed{\omega = \frac{k_\perp v_*}{1+k_\perp^2\rho_s^2}}. \tag{C.58}$$

For the case of interest here, $\rho_s \equiv \frac{c_s}{\Omega_{ci}} = \sqrt{\frac{T_e}{M_i}}\frac{1}{\Omega_{ci}} = \sqrt{\frac{T_{e,eV}}{B\Omega_{ci}}} \approx \sqrt{\frac{50}{2\cdot 2\pi 20\times 10^6}} = 5\times\sqrt{\frac{1}{2\pi 20\times 10^6}} \approx 0.45$ mm, where $B \approx 2$ T at the outer edge for the $B_0 \approx 3$ T, while $T_e \approx 50$ eV at the LCFS, so $k_\perp^2\rho_s^2 \approx 0.0045$ in the discharges of interest (low field for Alcator C-Mod). As such, the dispersion in the phase velocity is mild.

[8] *cf.* Eq. 5.16 in [65]

In the following section, we will explore what happens when the electrostatic approximation is relaxed. However, before doing so, it is instructive to examine the cold plasma model, modifying $\epsilon_{zz} = P \to P'$ to incorporate the susceptibility in Eq. C.56. This is appropriate to the case where there exists only a parallel temperature [76]. The cold plasma dielectric tensor under these conditions is

$$\bar{\bar{\epsilon}} = \epsilon_0 \begin{bmatrix} S & iD & 0 \\ -iD & S & 0 \\ 0 & 0 & P' \end{bmatrix} \tag{C.59}$$

where

$$\begin{aligned} S &= \frac{1}{2}(R+L) \\ D &= \frac{1}{2}(R-L) \\ P' &= 1 + \chi_{zz} \approx 1 - \frac{\omega_{pe}^2}{\omega^2} \frac{1 - \frac{1}{\omega}\frac{k_\perp v_*}{1+k_\perp^2\rho_s^2}}{1 + i\frac{\nu_e'}{\omega}} \end{aligned} \tag{C.60}$$

where, again, the $k_\perp^2\rho_s^2$ term arises from approximating $\omega \approx k_\perp v_*$ in $k_\perp \rho_s^2 \omega / v_*$. The R and L parameters are given by

$$\begin{aligned} R &= 1 - \sum_s \frac{\omega_{ps}^2}{\omega(\omega + \Omega_s)} \\ L &= 1 - \sum_s \frac{\omega_{ps}^2}{\omega(\omega - \Omega_s)}. \end{aligned} \tag{C.61}$$

In the case under study[9], with $\omega \sim 2\pi \times (100\,\text{kHz})$, $\omega \ll \Omega_i$, and ω resides firmly in the low-frequency limit, where

[9] $\Omega_i = \frac{eB}{M_i} \sim 2\pi \times (17\,\text{MHz})$, $\omega_{pi} = \sqrt{\frac{n_e e^2}{\epsilon_0 M_i}} \approx 2\pi\,(1.5\,\text{GHz})$, $\Omega_e = -\frac{eB}{m_e} \approx -2\pi\,(63\,\text{GHz})$, $\omega_{pe} = \sqrt{\frac{n_e e^2}{\epsilon_0 m_e}} \approx 2\pi\,(90\,\text{GHz})$ for a deuterium main ion species with $B = 2.27$ T and $n_e = 10^{20}$ m^{-3}.

$$
\begin{aligned}
S &= \frac{1}{2}\left(2 - \sum_s \frac{\omega_{ps}^2}{\omega}\left[\frac{1}{(\omega+\Omega_s)} + \frac{1}{(\omega-\Omega_s)}\right]\right) = 1 - \sum_s \frac{\omega_{ps}^2}{\omega^2-\Omega_s^2} \approx 1 + \frac{\omega_{pi}^2}{\Omega_i^2} \\
D &= \frac{1}{2}\left(\sum_s \frac{\omega_{ps}^2}{\omega}\left[\frac{2\Omega_s}{\omega^2-\Omega_s^2}\right]\right) \approx -\sum_s \frac{\omega_{ps}^2}{\omega\Omega_s}.
\end{aligned}
\tag{C.62}
$$

But note that in this representation, Ω_s carries the sign of the charge of species, s,

$$
D \approx -\sum_s \frac{\omega_{ps}^2}{\omega\Omega_s} = -\left(-\frac{n_e e^2}{\epsilon_0 m_e}\frac{m_e}{\omega e B} + \frac{n_i e^2}{\epsilon_0 m_i}\frac{m_i}{\omega e B}\right) = -\frac{e^2}{\epsilon_0 \omega e B}\left(-n_e + n_i\right) = 0,
\tag{C.63}
$$

where the last equality follows from setting $n_i = n_e$. The modified low-frequency cold plasma dielectric tensor is then

$$
\bar{\bar{\epsilon}} = \epsilon_0 \begin{bmatrix} 1 + \frac{\omega_{pi}^2}{\Omega_i^2} & 0 & 0 \\ 0 & 1 + \frac{\omega_{pi}^2}{\Omega_i^2} & 0 \\ 0 & 0 & P' \end{bmatrix}
\tag{C.64}
$$

where P' is given in Eq. C.60.

If we naïvely take $\bar{\bar{\epsilon}}$ to be homogeneous (which, at this point, would be unjustified), then we arrive at a wave equation in component form, $\left(k^i k_j - k^2\delta_j^i + \omega^2\mu_0\bar{\bar{\epsilon}}\right)B^j = 0$. Setting the determinant of the coefficient of B^j gives a dispersion relation. If we take modes to propagate only in the y and z directions, then

$$
\begin{aligned}
&\frac{\omega^2}{c^2}\begin{vmatrix} 1 + \frac{\omega_{pi}^2}{\Omega_i^2} - n^2 & 0 & 0 \\ 0 & 1 + \frac{\omega_{pi}^2}{\Omega_i^2} - n_z^2 & n^y n_z \\ 0 & n^z n_y & P' - n_y^2 \end{vmatrix} = 0 \\
&= \frac{\omega^2}{c^2}\left(1 + \frac{\omega_{pi}^2}{\Omega_i^2} - n^2\right)\left[\left(P' - n_y^2\right)\left(1 + \frac{\omega_{pi}^2}{\Omega_i^2} - n_z^2\right) - n_y^2 n_z^2\right]
\end{aligned}
\tag{C.65}
$$

where $n_y = \frac{k_y c}{\omega}$ is the y-component of the index of refraction, and likewise for n_z,

with $n^2 = n_y^2 + n_z^2$, and, as per the usual notation, $c \equiv \frac{1}{\sqrt{\mu_0 \epsilon_0}}$ is the vacuum speed of light. This dispersion relation supports compressional Alfvén waves in the root, $1 + \frac{\omega_{pi}^2}{\Omega_i^2} - n^2 = 0$, as well as shear Alfvén waves through $1 + \frac{\omega_{pi}^2}{\Omega_i^2} - n_z^2 = 0$ when $P' \gg n_y^2 \left(1 + \omega_{pi}^2/\Omega_i^2\right)$, which will typically occur at frequencies well above $\omega_d = k_y v_*$. However, if P' becomes much larger than the other terms, then forcing it, and in particular, χ_{zz}, to vanish independently also gives an approximate root to the dispersion relation, and it is this scenario that gives rise to the drift wave.

C.5 Relaxing the Electrostatic Approximation

In the preceding two sections, we derived the drift wave dispersion relation under the electrostatic approximation. However, since the focus of this study is to examine how an antenna external to the plasma may couple *inductively* to a drift wave, we expect that we will have to relax the electrostatic approximation to understand how this coupling might take place. This is done below.

We start again from the momentum balance equations. The electron momentum equation is, after Fourier transforming in time,

$$iB\frac{\omega}{\Omega_{ce}}\mathbf{v}_e = (\mathbf{E} + \mathbf{v}_e \times \mathbf{B}) + \frac{1}{n_e e}\nabla p_e - \bar{\bar{\eta}} \cdot \mathbf{J}. \tag{C.66}$$

Likewise, the ion momentum equation is

$$iB\frac{\omega}{\Omega_{ci}}\mathbf{u}_i = -(\mathbf{E} + \mathbf{v}_e \times \mathbf{B}) + \frac{1}{n_i e}\nabla p_i + \bar{\bar{\eta}} \cdot \mathbf{J}. \tag{C.67}$$

The $\mathbf{v}_e \times \mathbf{B}$ and $\mathbf{u}_i \times \mathbf{B}$ terms on the right-hand sides of Eq.'s C.66-C.67 clear the *perpendicular* components of the momentum equations up to terms of order of the polarization current, proportional to $\frac{\omega}{\Omega_{ci}} \sim 6 \times 10^{-3}$ for ions and $\frac{\omega}{\Omega_{ce}} \sim 2 \times 10^{-6}$ for electrons. We retain the polarization current per the discussion of quasineutrality above, and write the perpendicular components of $\mathbf{J}$ directly from the diamagnetic and polarization drifts.

To proceed, we treat the parallel dynamics as before, forming the *parallel* Ohm's

law by subtracting the parallel component of Eq. C.66 from $\mu_e \equiv \frac{m_e}{M_i}$ times the parallel component of Eq. C.67 and dividing through by $n_e e$:

$$\begin{aligned}\frac{m_e n_e}{n_e e}\frac{\partial}{\partial t}\left(u_\parallel - v_\parallel\right) &= \frac{1}{\epsilon_0 \omega_{pe}^2}\frac{\partial J_\parallel}{\partial t} \\ &= E_\parallel + \frac{1}{n_e e}\nabla_\parallel p_e - \eta^\parallel_{\ j} J^j + \mu_e\left[\frac{n_i}{n_e}E_\parallel - \frac{1}{n_e e}\nabla_\parallel p_i - \eta^\parallel_{\ j} J^j\right] \\ &\approx E_\parallel + \frac{1}{n_e e}\nabla_\parallel p_e - \eta_\parallel J_\parallel\end{aligned} \tag{C.68}$$

neglecting terms of order, μ_e, and taking $\bar{\bar{\eta}}$ to be diagonal.

However, the *perpendicular* components of $\mathbf{J}$ are written directly from the polarization and diamagnetic currents. Including these two contributions,

$$\mathbf{J}_\perp = \mathbf{J}_p + \mathbf{J}_*. \tag{C.69}$$

For the ions, $q_i = +e$, and

$$\mathbf{u}_p \approx \frac{1}{\Omega_i B}\frac{\partial}{\partial t}\left(\mathbf{E}_\perp - \frac{\nabla_\perp p_i}{n_i e}\right). \tag{C.70}$$

$\mathbf{u}_p$ is larger than the electron polarization velocity, $\mathbf{v}_p$, by the inverse mass ratio, M_i/m_e, so $\mathbf{J}_p = n_e e(\mathbf{u}_p - \mathbf{v}_p) \approx n_e e \mathbf{u}_p$.

The diamagnetic current is

$$\mathbf{J}_* = \frac{\mathbf{B} \times \nabla\left(p_i + p_e\right)}{B^2} \tag{C.71}$$

For simplicity, we assume that $T_i = T_e$ and $p_i = p_e$. Also, let $\vec{\alpha}$ be defined through

$$\tilde{n}_e = \vec{\alpha} \cdot \mathbf{E}. \tag{C.72}$$

The perpendicular components of $\mathbf{J}_\perp$ are then

$$\begin{aligned}\mathbf{J}_\perp = \mathbf{J}_p + \mathbf{J}_* &\approx \frac{n_e e}{\Omega_i B}\frac{\partial}{\partial t}\left(\mathbf{E}_\perp - \frac{\nabla_\perp p_i}{n_i e}\right) + \frac{\mathbf{B}\times\nabla_\perp\left(p_i+p_e\right)}{B^2} \\ &= \epsilon_0\frac{\omega_{pi}^2}{\Omega_i^2}\frac{\partial}{\partial t}\left(\mathbf{E}_\perp - \frac{\nabla_\perp p_i}{n_i e}\right) - \frac{\nabla_\perp\left(p_i+p_e\right)\times\mathbf{B}}{B^2}.\end{aligned} \tag{C.73}$$

In component form,

$$\begin{aligned}J_\perp^j &= \epsilon_0\frac{\omega_{pi}^2}{\Omega_{ci}^2}\frac{\partial}{\partial t}\left(\delta^i{}_j E^j - T_e\frac{\partial_i\left(\alpha_j E^j\right)}{n_i e}\right) - \frac{\varepsilon_{ik\ell}\partial_k\left(p_i+p_e\right)B^\ell}{B^2} \\ &= \epsilon_0\frac{\omega_{pi}^2}{\Omega_{ci}^2}\frac{\partial}{\partial t}\left(\delta^i{}_j E^j - \frac{T_e}{n_i e}\left(E^j\partial_i\alpha_j + \alpha_j\partial_i E^j\right)\right) - \frac{2T_e}{B}\varepsilon_{ikz}\left(E^j\partial_k\alpha_j + \alpha_j\partial_k E^j\right) \\ &= \left[\epsilon_0\frac{\omega_{pi}^2}{\Omega_{ci}^2}\frac{\partial}{\partial t}\left(\delta^i{}_j - \frac{T_e}{n_i e}\left(\partial_i\alpha_j + \alpha_j\partial_i\right)\right) - \frac{2T_e}{B}\varepsilon_{ikz}\left(\partial_k\alpha_j + \alpha_j\partial_k\right)\right]E^j\end{aligned} \tag{C.74}$$

choosing $\mathbf{B} = B\hat{\mathbf{e}}_z$ and with

$$\varepsilon_{ikz} = \begin{bmatrix} 0 & 1 \\ -1 & 0 \end{bmatrix}. \tag{C.75}$$

Fourier transforming with plane waves, $e^{i(\mathbf{k}\cdot\mathbf{r}-\omega t)}$, we replace ∂_i with ik_i when acting on E^j, and ∂_t with $-i\omega$ everywhere, so that

$$J_\perp^j = \left[-i\omega\epsilon_0\frac{\omega_{pi}^2}{\Omega_{ci}^2}\left(\delta^i{}_j - \frac{T_e}{n_i e}\left(\partial_i\alpha_j + i\alpha_j k_i\right)\right) - \frac{2T_e}{B}\varepsilon_{ikz}\left(\partial_k\alpha_j + i\alpha_j k_k\right)\right]E^j \tag{C.76}$$

or

$$\begin{aligned}J_\perp^j = \Bigg\{ &-i\omega\epsilon_0\frac{\omega_{pi}^2}{\Omega_{ci}^2}\left(\begin{bmatrix}1 & 0\\ 0 & 1\end{bmatrix} - \frac{T_e}{n_i e}\left(\begin{bmatrix}\partial_x\alpha_x & \partial_x\alpha_y\\ \partial_y\alpha_x & \partial_y\alpha_y\end{bmatrix} + i\begin{bmatrix}\alpha_x k_x & \alpha_y k_x\\ \alpha_x k_y & \alpha_y k_y\end{bmatrix}\right)\right) \\ &-\frac{2T_e}{B}\left(\begin{bmatrix}\partial_y\alpha_x & \partial_y\alpha_y\\ -\partial_x\alpha_x & -\partial_x\alpha_y\end{bmatrix} + i\begin{bmatrix}\alpha_x k_y & \alpha_y k_y\\ -\alpha_x k_x & -\alpha_y k_x\end{bmatrix}\right)\Bigg\}E^j.\end{aligned} \tag{C.77}$$

When $\vec{\alpha}$ has only a y-component and depends only on x,

$$J_\perp^j = \left\{ -i\omega\epsilon_0 \frac{\omega_{pi}^2}{\Omega_{ci}^2} \left(\begin{bmatrix} 1 & 0 \\ 0 & 1 \end{bmatrix} - \frac{T_e}{n_i e} \left(\begin{bmatrix} 0 & \partial_x \alpha_y \\ 0 & 0 \end{bmatrix} + i \begin{bmatrix} 0 & \alpha_y k_x \\ 0 & \alpha_y k_y \end{bmatrix} \right) \right) \right. \\ \left. - \frac{2T_e}{B} \left(\begin{bmatrix} 0 & 0 \\ 0 & -\partial_x \alpha_y \end{bmatrix} + i \begin{bmatrix} 0 & \alpha_y k_y \\ 0 & -\alpha_y k_x \end{bmatrix} \right) \right\} E^j. \tag{C.78}$$

This provides the four "perpendicular" components (xx, xy, yx, and yy) of the susceptibility, $\bar{\bar{\chi}}$. The remaining components derive from C.68, noting that $\chi_{xz} = \chi_{yz} = 0$ under the assumptions made so far. This gives

$$\left(\frac{1}{\epsilon_0 \omega_{pe}^2} \frac{\partial}{\partial t} + \eta_\parallel \right) J_\parallel = E_\parallel + \frac{1}{n_e e} \nabla_\parallel p_e. \tag{C.79}$$

Fourier transforming in time and space for evolving quantities and using $n_e = \vec{\alpha} \cdot \mathbf{E}$, with $p_e = n_e T_e$ and T_e constant,

$$\begin{aligned} J_\parallel &= \frac{\epsilon_0 \omega_{pe}^2}{-i\omega} \frac{E_\parallel + \frac{1}{n_e e} \nabla_\parallel \left(\vec{\alpha} \cdot \mathbf{E} \right)}{1 + i \frac{\nu'_{e,\parallel}}{\omega}} \\ &= \frac{\epsilon_0 \omega_{pe}^2}{-i\omega} \frac{\left(\hat{\mathbf{b}} + i k_\parallel \frac{T_e}{n_e e} \vec{\alpha} \right)}{1 + i \frac{\nu'_{e,\parallel}}{\omega}} \cdot \mathbf{E} \end{aligned} \tag{C.80}$$

after taking $\nabla_\parallel \alpha \to 0$, since this ought to be an equilibrium quantity which is unlikely to have non-uniformities along a field line in the case with no curvature and with sufficiently simple boundary conditions.

Using the ion continuity equation, Eq. C.50,

$$\tilde{n}_i = i \frac{1}{\omega} \frac{n_{i,0} e}{T_i} \left(\mathbf{v}_* - \rho_s^2 \mathbf{k}_\perp \omega \right) \cdot \mathbf{E}. \tag{C.81}$$

after taking $\mathbf{u}_* = -\mathbf{v}_*$. If $\omega \approx \mathbf{k} \cdot \mathbf{v}_* = \mathbf{k}_\perp \cdot \mathbf{v}_*$,

$$\tilde{n}_i \approx i\frac{1}{\omega}\frac{n_{i,0}e}{T_i}\left(1-k_\perp^2\rho_s^2\right)\mathbf{v}_*\cdot\mathbf{E} \approx i\frac{1}{\omega}\frac{n_{i,0}e}{T_i}\frac{1}{1+k_\perp^2\rho_s^2}\mathbf{v}_*\cdot\mathbf{E} \tag{C.82}$$

so that

$$\boxed{\alpha_j = i\frac{1}{\omega}\frac{n_{i,0}e}{T_i}\frac{1}{1+k_\perp^2\rho_s^2}v_{*,j}}. \tag{C.83}$$

Taking $\mathbf{v}_* = v_*\hat{\mathbf{e}}_y$ and $\nabla\alpha_y = \frac{\partial\alpha_y}{\partial x}\hat{\mathbf{e}}_x$,

$$\boxed{\alpha_y = i\frac{1}{\omega}\frac{n_{i,0}e}{T_i}\frac{1}{1+k_\perp^2\rho_s^2}v_*}. \tag{C.84}$$

We may now rewrite Eq.'s C.85 and C.80 as

$$\begin{aligned} J_\perp^j = &-i\omega\epsilon_0\frac{\omega_{pi}^2}{\Omega_{ci}^2}\left\{\begin{bmatrix}1&0\\0&1\end{bmatrix} - \frac{1}{1+k_\perp^2\rho_s^2}\left(i\frac{\partial_x v_*}{\omega}\begin{bmatrix}0&1\\0&0\end{bmatrix} - \frac{v_*}{\omega}\begin{bmatrix}0&k_x\\0&k_y\end{bmatrix}\right)\right. \\ &\left. +2\frac{\Omega_{ci}}{\omega}\frac{1}{1+k_\perp^2\rho_s^2}\left(\frac{\partial_x v_*}{\omega}\begin{bmatrix}0&0\\0&-1\end{bmatrix} + i\frac{v_*}{\omega}\begin{bmatrix}0&k_y\\0&-k_x\end{bmatrix}\right)\right\}E^j \end{aligned} \tag{C.85}$$

and

$$J_\parallel = \frac{\epsilon_0\omega_{pe}^2}{-i\omega}\frac{\left(\hat{\mathbf{b}} - \frac{k_\parallel\mathbf{v}_*}{\omega\left(1+k_\perp^2\rho_s^2\right)}\right)}{1+i\frac{\nu'_{e,\parallel}}{\omega}}\cdot\mathbf{E} \tag{C.86}$$

so that

$$\begin{aligned} \bar{\bar{\chi}} = &\frac{\omega_{pi}^2}{\Omega_{ci}^2}\left\{\begin{bmatrix}1&0&0\\0&1&0\\0&0&0\end{bmatrix} - \frac{1}{1+k_\perp^2\rho_s^2}\left(i\frac{\partial_x v_*}{\omega}\begin{bmatrix}0&1&0\\0&-2i\frac{\Omega_{ci}}{\omega}&0\\0&0&0\end{bmatrix}\right.\right. \\ &\left.\left. -\frac{v_*}{\omega}\begin{bmatrix}0&k_x+2i\frac{\Omega_{ci}}{\omega}k_y&0\\0&k_y-2i\frac{\Omega_{ci}}{\omega}k_x&0\\0&0&0\end{bmatrix}\right)\right\} - \frac{\omega_{pe}^2}{\omega^2}\frac{1}{1+i\frac{\nu'_{e,\parallel}}{\omega}}\begin{bmatrix}0&0&0\\0&0&0\\0&-\frac{k_\parallel v_*}{\omega\left(1+k_\perp^2\rho_s^2\right)}&1\end{bmatrix}. \end{aligned} \tag{C.87}$$

When the density has an exponential profile, $n_e = n_{e,0}e^{-x/L_n}$, the term, $\partial_x v_* = 0$, so

$$\begin{aligned}\bar{\bar{\chi}} = \frac{\omega_{pi}^2}{\Omega_{ci}^2}&\left(\begin{bmatrix}1&0&0\\0&1&0\\0&0&0\end{bmatrix} + \frac{v_*}{\omega\left(1+k_\perp^2\rho_s^2\right)}\begin{bmatrix}0&k_x+2i\frac{\Omega_{ci}}{\omega}k_y&0\\0&k_y-2i\frac{\Omega_{ci}}{\omega}k_x&0\\0&0&0\end{bmatrix}\right)\\ &-\frac{\omega_{pe}^2}{\omega^2}\frac{1}{1+i\frac{\nu'_{e,\parallel}}{\omega}}\begin{bmatrix}0&0&0\\0&0&0\\0&-\frac{k_\parallel v_*}{\omega\left(1+k_\perp^2\rho_s^2\right)}&1\end{bmatrix}\end{aligned} \tag{C.88}$$

and the dielectric tensor is $\bar{\bar{\epsilon}} = \epsilon_0\left(\bar{\bar{1}} + \bar{\bar{\chi}}\right)$.

It is instructive to compute the electrostatic dispersion relation for comparison with the previous section. Neglecting the spatial dependence of $\bar{\bar{\epsilon}}$, this is accomplished by

$$\begin{aligned}0 &= \mathbf{k}\cdot\left(\bar{\bar{1}}+\bar{\bar{\chi}}\right)\cdot\mathbf{k} = k^2 + \left(\mathbf{k}\cdot\bar{\bar{\chi}}\cdot\mathbf{k}\right)\\ &= k^2 + \mathbf{k}\cdot\left\{\frac{\omega_{pi}^2}{\Omega_{ci}^2}\left(\begin{bmatrix}1&0&0\\0&1&0\\0&0&0\end{bmatrix} + \frac{v_*}{\omega\left(1+k_\perp^2\rho_s^2\right)}\begin{bmatrix}0&k_x+2i\frac{\Omega_{ci}}{\omega}k_y&0\\0&k_y-2i\frac{\Omega_{ci}}{\omega}k_x&0\\0&0&0\end{bmatrix}\right)\right.\\ &\left.-\frac{\omega_{pe}^2}{\omega^2}\frac{1}{1+i\frac{\nu'_{e,\parallel}}{\omega}}\begin{bmatrix}0&0&0\\0&0&0\\0&-\frac{k_\parallel v_*}{\omega\left(1+k_\perp^2\rho_s^2\right)}&1\end{bmatrix}\right\}\cdot\mathbf{k}\\ &= k^2 + k_\perp^2\frac{\omega_{pi}^2}{\Omega_{ci}^2}\left(1+\frac{k_y v_*}{\omega\left(1+k_\perp^2\rho_s^2\right)}\right) - \frac{\omega_{pe}^2}{\omega^2}\frac{k_\parallel^2}{1+i\frac{\nu'_{e,\parallel}}{\omega}}\left(1-\frac{k_y v_*}{\omega\left(1+k_\perp^2\rho_s^2\right)}\right).\end{aligned} \tag{C.89}$$

At the low frequencies ($f \sim 100$ kHz) of interest, the last term is expected to dominate, since $\frac{k_\parallel^2}{k_\perp^2}\frac{\omega_{pe}^2}{\omega^2}\frac{\Omega_{ci}^2}{\omega_{pi}^2}\frac{\omega}{\nu'_{e,\parallel}} \sim 55$ (noting $\left|i\nu'_{e,\parallel}/\omega\right| \approx |i11| \gg 1$). Keeping only this term results in

$$0 \approx \frac{\omega_{pe}^2}{\omega^2} \frac{k_\parallel^2}{1 + i\frac{\nu'_{e,\parallel}}{\omega}} \left(1 - \frac{k_y v_*}{\omega\left(1 + k_\perp^2 \rho_s^2\right)}\right) \tag{C.90}$$

which is exactly the same dispersion relation as found from setting χ_{zz} in Eq. C.56 to zero, with a real part of the frequency given by Eq. C.58.

Let us examine the first-order correction to ω. Let $\omega_0 \equiv \frac{k_y v_*}{1+k_\perp^2 \rho_s^2} \approx k_y v_*$. Also, let $\omega = \omega_0 + \omega_1$, with $\frac{\omega_1}{\omega_0} \ll 1$. Then the dispersion relation from Eq. C.89 can be rewritten as

$$\begin{aligned} 0 &= k^2 + k_\perp^2 \frac{\omega_{pi}^2}{\Omega_{ci}^2}\left(1 + \frac{\omega_0}{\omega_0 + \omega_1}\right) - \frac{\omega_{pe}^2}{\omega^2}\frac{k_\parallel^2}{1 + i\frac{\nu'_{e,\parallel}}{\omega}}\left(1 - \frac{\omega_0}{\omega_0 + \omega_1}\right) \\ &\approx 2k_\perp^2 \frac{\omega_{pi}^2}{\Omega_{ci}^2} - \frac{\omega_{pe}^2}{\omega^2}\frac{k_\parallel^2}{1 + i\frac{\nu'_{e,\parallel}}{\omega}}\left(\frac{\omega_1}{\omega_0}\right) \\ \Rightarrow \frac{\omega_1}{\omega_0} &\approx 2\frac{k_\perp^2}{k_\parallel^2}\frac{\omega_{pi}^2}{\Omega_{ci}^2}\frac{\omega^2}{\omega_{pe}^2}\left(1 + i\frac{\nu'_{e,\parallel}}{\omega}\right). \end{aligned} \tag{C.91}$$

With $\nu'_e = \frac{0.51}{\tau_e} = 0.51\frac{\sqrt{2}n_e e^4 \ln(\Lambda)}{12\pi^{3/2}\epsilon_0^2\sqrt{m_e}T_e^{3/2}} \approx 6.8 \times 10^6$ s^{-1}, $\nu'_e/\omega \approx 11$, and the factor, $\frac{k_\perp^2}{k_\parallel^2}\frac{\omega_{pi}^2}{\Omega_{ci}^2}\frac{\omega^2}{\omega_{pe}^2} \approx 1.7 \times 10^{-3}$, $\omega_1 \ll \omega_0$.

C.6 Diamagnetic Divergence, or Magnetic Curvature, Operator

The diamagnetic divergence operator [65, p. 3.11], also called the magnetic curvature operator [65, p. 11.4], is defined as [65, p. 3.11, p. 11.4]

$$\mathcal{K}(u) = -\nabla \cdot \left(\frac{1}{B^2}\mathbf{B} \times \nabla u\right) = -\left(\nabla \times \frac{\mathbf{B}}{B^2}\right) \cdot \nabla u \tag{C.92}$$

which applies the drift operator, $\frac{\mathbf{B}}{B^2}\times$, to the gradient of a scalar, u, followed by applying the divergence operator to the result, and negating this quantity. The second equality in Eq. C.92 follows from the identity, $\nabla\cdot(\mathbf{A} \times \mathbf{B}) = (\nabla \times \mathbf{B})\cdot\mathbf{A} + (\nabla \times \mathbf{A})\cdot\mathbf{B}$,

with $\mathbf{A} \leftarrow \mathbf{B}/B^2$ and $\mathbf{B} \leftarrow \nabla u$, and the additional identity, $\nabla \times \nabla \mathbf{u} = 0$. On a homogeneous background field, the diamagnetic divergence operator vanishes, $\mathcal{K} \rightarrow 0$.

Let us examine the factor, $\left(\nabla \times \frac{\mathbf{B}}{B^2}\right)$:

$$\nabla \times \left(\frac{\mathbf{B}}{B^2}\right) = \frac{1}{B^2}\nabla \times \mathbf{B} - \mathbf{B} \times \nabla(\mathbf{B}\cdot\mathbf{B})^{-1} = \frac{1}{B^2}\left(\nabla \times \mathbf{B} + \frac{1}{B^2}\mathbf{B} \times \nabla\left(\mathbf{B}\cdot\mathbf{B}\right)\right) \tag{C.93}$$

The first term is approximated as

$$\frac{1}{B^2}\nabla \times \mathbf{B} = \frac{\mu_0}{B^2}\left(\mathbf{J} + \frac{\partial \mathbf{D}}{\partial t}\right) \approx \frac{\mu_0 \mathbf{J}}{B^2}, \tag{C.94}$$

while the second term inside the parentheses is manipulated as

$$\begin{aligned}
\frac{1}{B^2}\mathbf{B} \times \nabla\left(\mathbf{B}\cdot\mathbf{B}\right) &= \frac{2}{B^2}\mathbf{B} \times \left[\mathbf{B} \times \left(\nabla \times \mathbf{B}\right) + \left(\mathbf{B}\cdot\nabla\right)\mathbf{B}\right] \\
&= \frac{2}{B^2}\mathbf{B} \times \left[\left(\mathbf{B}\cdot\nabla\right)\mathbf{B}\right] \\
&= 2\hat{\mathbf{b}} \times \left[\left(\hat{\mathbf{b}}\cdot\nabla\right)\left(\hat{\mathbf{b}}B\right)\right] \\
&= 2\mathbf{B} \times \left[\left(\hat{\mathbf{b}}\cdot\nabla\right)\hat{\mathbf{b}}\right] + 2\hat{\mathbf{b}} \times \left[\hat{\mathbf{b}}\left(\hat{\mathbf{b}}\cdot\nabla\right)B\right] \\
&= 2\mathbf{B} \times \left[\left(\hat{\mathbf{b}}\cdot\nabla\right)\hat{\mathbf{b}}\right] \\
&= 2\mathbf{B} \times \vec{\kappa}
\end{aligned} \tag{C.95}$$

where $\vec{\kappa} \equiv \hat{\mathbf{b}}\cdot\nabla\hat{\mathbf{b}}$ is the curvature vector. Then

$$\nabla \times \left(\frac{\mathbf{B}}{B^2}\right) = \frac{1}{B^2}\left[\nabla \times \mathbf{B} + 2\mathbf{B} \times \vec{\kappa}\right] \approx \frac{\mu_0 \mathbf{J}}{B^2} + \frac{2}{B}\mathbf{b} \times \vec{\kappa}, \tag{C.96}$$

so that the diamagnetic divergence operator acting on u is

$$\mathcal{K}\left(u\right) = \left[\frac{\mu_0}{B^2}\left(\mathbf{J} + \frac{\partial \mathbf{D}}{\partial t}\right) + \frac{2}{B}\hat{\mathbf{b}} \times \vec{\kappa}\right] \cdot \nabla u \approx \frac{\mu_0}{B^2}\left[\mathbf{J} + \frac{2}{\mu_0}\mathbf{B} \times \vec{\kappa}\right] \cdot \nabla u. \tag{C.97}$$

Typically [65, p. 11.4], it is the second term, proportional to the curvature, which is relevant for flute-like modes in toroidal plasmas with small β.

The diamagnetic divergence operator is expected to be small next to the other terms. To rationalize this, consider $\mathcal{K}(p_e)$. The curvature is small, while the remaining term is small because it involves the multiplication of a pair of lower-order terms, since $\nabla p_{e,0}$ is orthogonal to $\mathbf{J}$, while $\nabla \tilde{p}_e$ is largely perpendicular to $\mathbf{J}_0$. For the near-adiabatic case expected of drift-like waves, $\tilde{T}_e \sim e\tilde{\Phi}$, so that $\frac{1}{e}\mathcal{K}(p_e) \sim n_e \mathcal{K}(\Phi)$, where $p_e = n_e T_e$. As such, both $n_e\mathcal{K}(\Phi)$ and $\frac{1}{e}\mathcal{K}(p_e)$ are expected to be small. However, the ballooning nature of the QCM suggests that curvature plays an important role in the relevant physics, and as such, a more complete model must include the diamagnetic divergence terms, particularly near the X-point.

C.7 Quasineutrality Condition

The quasineutrality condition,

$$\nabla \cdot \mathbf{J} = 0, \tag{C.98}$$

may be rendered in a form useful for inclusion in the ballooning model as follows. Firstly, split $\mathbf{J}$ into parallel and perpendicular components, $\mathbf{J} = \hat{\mathbf{b}} J_\parallel + \mathbf{J}_\perp$; then, applying Gauss' law,

$$\nabla \cdot \mathbf{J} = \nabla \cdot \left(\hat{\mathbf{b}} J_\parallel\right) + \nabla \cdot \mathbf{J}_\perp = \nabla \cdot \left(\frac{\mathbf{B}}{B} J_\parallel\right) + \nabla \cdot \mathbf{J}_\perp = B\nabla_\parallel \left(\frac{J_\parallel}{B}\right) + \nabla \cdot \mathbf{J}_\perp. \tag{C.99}$$

Now,

$$\mathbf{J}_\perp = en_i \mathbf{u}_* - en_e \mathbf{v}_* + en_i \mathbf{u}_p, \tag{C.100}$$

and

$$\nabla \cdot \mathbf{J}_\perp = \mathcal{K}(p_i + p_e) + \nabla \cdot en_i \mathbf{u}_p \tag{C.101}$$

where $\mathcal{K}(u) = -\nabla \cdot \left(\frac{\mathbf{B}\times\nabla u}{B^2}\right)$ is the diamagnetic divergence operator. Using the ion

polarization drift from Eq. 3.6, the divergence of the perpendicular current is

$$\begin{aligned}\nabla\cdot\mathbf{J}_\perp &= \nabla\cdot\left(en_i\mathbf{u}_p\right)+\mathcal{K}\left(p_i+p_e\right)\\ &= -\nabla\cdot\left(\epsilon_0\frac{\omega_{pi}^2}{\Omega_i^2}\frac{\mathrm{d}_E}{\mathrm{d}t}\left(\nabla_\perp\Phi+\frac{\nabla_\perp p_i}{n_ie}\right)\right)+\mathcal{K}\left(p_i+p_e\right).\end{aligned} \tag{C.102}$$

Inserting this back into the quasineutrality condition,

$$\boxed{\nabla\cdot\left[\epsilon_0\frac{\omega_{pi}^2}{\Omega_i^2}\frac{\mathrm{d}_E}{\mathrm{d}t}\left(\nabla_\perp\Phi+\frac{\nabla_\perp p_i}{n_ie}\right)\right]=B\nabla_\parallel\left(\frac{J_\parallel}{B}\right)+\mathcal{K}\left(p_i+p_e\right).} \tag{C.103}$$

Following only the perturbed variables,

$$\boxed{\nabla\cdot\left[\epsilon_0\frac{\omega_{pi}^2}{\Omega_i^2}\frac{\mathrm{d}_E}{\mathrm{d}t}\left(\nabla_\perp\tilde{\Phi}+\frac{\nabla_\perp\tilde{p}_i}{n_ie}\right)\right]=B\nabla_\parallel\left(\frac{\tilde{J}_\parallel}{B}\right)+\mathcal{K}\left(\tilde{p}_i+\tilde{p}_e\right).} \tag{C.104}$$

C.8 Electron Continuity Condition

The electron continuity equation is manipulated in a similar fashion to the quasineutrality condition:

$$\begin{aligned}0 &= \frac{\partial n_e}{\partial t}+\nabla\cdot n_e\mathbf{v}_e=\frac{\partial n_e}{\partial t}+\nabla\cdot\left(n_e\mathbf{v}_E\right)+\nabla\cdot\left(n_e\mathbf{v}_*\right)+B\nabla_\parallel\left(n_e\frac{v_\parallel}{B}\right)\\ &= \frac{\mathrm{d}_E}{\mathrm{d}t}\left(n_e\right)+\tilde{\mathbf{v}}_E\cdot\nabla n_e+B\nabla_\parallel\left(n_e\frac{v_\parallel}{B}\right)-n_e\mathcal{K}\left(\Phi\right)+\frac{1}{e}\mathcal{K}\left(p_e\right)\end{aligned} \tag{C.105}$$

or

$$\frac{\mathrm{d}_En_e}{\mathrm{d}t}=n_e\mathcal{K}\left(\Phi\right)-\frac{1}{e}\mathcal{K}\left(p_e\right)-\tilde{\mathbf{v}}_E\cdot\nabla n_e+\frac{B}{e}\nabla_\parallel\left(\frac{J_\parallel}{B}\right)-B\nabla_\parallel\left(\frac{n_eu_\parallel}{B}\right) \tag{C.106}$$

Tracking the evolution of the perturbed quantity, $\tilde{n}_e$,

$$\boxed{\frac{\mathrm{d}_E\tilde{n}_e}{\mathrm{d}t} = n_e\mathcal{K}\left(\tilde{\Phi}\right) - \frac{1}{e}\mathcal{K}\left(\tilde{p}_e\right) - \tilde{\mathbf{v}}_E\cdot\nabla n_e + \frac{B}{e}\nabla_\parallel\left(\frac{\tilde{J}_\parallel}{B}\right) - B\nabla_\parallel\left(\frac{n_e\tilde{u}_\parallel}{B}\right)}, \quad \text{(C.107)}$$

ignoring zeroth-order parallel ion flow.

Appendix D

Framework for BOUT++ Simulations

D.1 Drift Waves in Slab Geometry with Homogeneous Field

The drift ordering is a simplification of the fluid plasma dynamic model for situations where $\omega \ll \Omega_i$ and $k_\perp \gg k_\parallel$, and orders perturbations on the scale, $\delta \equiv \rho_s/L_p \ll 1$ [65, Chap. 3]. The drift wave dispersion scale, $\rho_s \equiv c_s/\Omega_i = \frac{\sqrt{T_e/M_i}}{\Omega_i}$, was introduced in Chapter 3 in Section 3.2.2. It is similar to the ion Larmor (or gyro) radius, but replaces T_i with T_e. $L_p \equiv \left|\frac{1}{p_e}\frac{\mathrm{d}p_e}{\mathrm{d}dx}\right|^{-1}$ is the pressure gradient length scale, and was introduced in the discussion after Eq. 3.16. When $\rho_s \ll L_p$, finite Larmor radius effects may be neglected, as ions and electrons essentially sample a uniform plasma in their gyro orbits; this greatly simplifies the analysis. Compressional dynamics (*e.g.* compressional Alfvén waves) are eliminated, and parallel and perpendicular dynamics largely decouple. The amplitudes of the perturbed quantities are further presumed to scale as $e\tilde{\Phi}/T_e \sim \tilde{n}_e/n_e \sim \tilde{u}_\parallel/c_s \sim \tilde{\mathbf{B}}_\perp/B \sim \delta$.

A conceptual frame work for the drift wave was introduced in Section 3.2. Below, a simple model is introduced appropriate to a slab geometry in a homogeneous field, with uniform and equilibrated electron and ion temperatures, $T_i = T_e = constant$.

This is the starting point for the initial simulations conducted in BOUT++. The equations are a simplified version of Eqs. 5.19-23 in[65, p. 5.8].

The set is

$$\frac{\partial}{\partial t}\rho_s^2\nabla_\perp^2\frac{e\tilde{\Phi}}{T_e} = c_s\nabla_\parallel\frac{\tilde{J}_\parallel}{nec_s} \quad \leftarrow \nabla\cdot\mathbf{J}=0 \tag{D.1}$$

$$\frac{\partial}{\partial t}\frac{\tilde{p}_e}{p_e} + \frac{c_s}{L_p}\rho_s\frac{\partial}{\partial y}\frac{e\tilde{\Phi}}{T_e} = \Gamma c_s\nabla_\parallel\left(\frac{\tilde{J}_\parallel}{nec_s} - \frac{\tilde{u}_\parallel}{c_s}\right) \quad \leftarrow n_e \text{ continuity} \tag{D.2}$$

$$\begin{aligned}\beta_e\frac{\partial}{\partial t}\frac{\tilde{A}_\parallel}{B\rho_s\beta_e} + \mu_e\frac{\partial}{\partial t}\frac{\tilde{J}_\parallel}{nec_s} &= c_s\nabla_\parallel\left(\frac{\tilde{p}_e}{p_e} - \frac{e\tilde{\Phi}}{T_e}\right)\\ -\frac{c_s}{L_p}\beta_e\rho_s\frac{\partial}{\partial y}\frac{\tilde{A}_\parallel}{\beta_e B\rho_s} - 0.51\mu_e\nu_e\frac{\tilde{J}_\parallel}{nec_s} &\quad \leftarrow \text{Ohm's Law}\end{aligned} \tag{D.3}$$

$$\frac{\partial}{\partial t}\frac{\tilde{u}_\parallel}{c_s} = -c_s\nabla_\parallel\frac{\tilde{p}_e}{p_e} + \frac{c_s}{L_p}\beta_e\rho_s\frac{\partial}{\partial y}\frac{\tilde{A}_\parallel}{\beta_e B\rho_s} + \mu_\parallel\nabla_\parallel^2\frac{\tilde{u}_\parallel}{c_s} \quad \leftarrow \text{total mom. balance} \tag{D.4}$$

where $J_\parallel$ is specified from Ampère's law by $J_\parallel = -\frac{1}{\mu_0}\nabla_\perp^2 A_\parallel$, and the ideal gas law, $p_k = n_k T_k = n_e T_e = n_e T$, is used to relate the pressure and density. Γ is the ratio of specific heats, 5/3 in a neutral gas, and is often taken as 1 in drift wave derivations. In the above, we have separated the equilibrium from the perturbation quantities, with the latter denoted by a tilde overbar. We have also applied $n_e = n_i$. The slab coordinate system is the same as that used in the discussion around Figures 3-1 and 4-1c: $\hat{\mathbf{x}}$ points in the radial direction (across flux surfaces, and down the density gradient), $\mathbf{y}$ points across field lines in the perpendicular direction, and $\hat{\mathbf{z}}$ points along field lines in the parallel direction.

The curvature terms are neglected in this model. To see how, note that for any vector field, $\mathbf{f}$,

$$\nabla\cdot\mathbf{f} = \nabla_\perp\cdot\mathbf{f}_\perp + B\nabla_\parallel\frac{f_\parallel}{B}. \tag{D.5}$$

In Eqs. D.1-D.4, the contribution from $B\nabla_\parallel\frac{f_\parallel}{B}$ is excluded. Including this term allows

for interchange modes, as described in Section 3.3 in Chapter 3; these effects are also treated in detail beginning in Chapters 10 and 11 in [65]. In the discussion below, however, the focus is on drift waves, and this additional complexity is not considered.

Equations D.1, D.2, D.3, and D.4 specify a four-field model in $\{\tilde{A}_\parallel, \tilde{\Phi}, \tilde{p}_e, \tilde{u}_\parallel\}$.

These equations may be nondimensionalized to aid in their solution. For consistency with the literature, we select the nondimensionalization employed by Scott [65], with the following scalings

$$
\begin{aligned}
&\bar{t} = \frac{t}{\tau},\ \tau \equiv \frac{L_\perp}{c_s} \quad \leftarrow \text{time},\\
&\bar{z} = z k_\parallel,\ k_\parallel = \frac{2\pi}{L_\parallel} \quad \leftarrow \text{coordinate along field lines},\\
&\bar{y} = \frac{y}{\rho_s},\ \rho_s \equiv \frac{c_s}{\Omega_i} \quad \leftarrow \perp\text{-coord. in diamag. drift direc.},\\
&\bar{x} = \frac{x}{L_\perp},\ L_\perp = \bar{\omega}_p L_p, L_p \equiv \left| \frac{1}{p_e}\frac{\partial p_e}{\partial x} \right|^{-1} \quad \leftarrow \perp\text{-coord. along pres. gradient direc.}
\end{aligned}
\tag{D.6}
$$

where the variables with overbar superscripts have been normalized as indicated. The factor,

$$
\bar{\omega}_p \equiv \frac{L_\perp}{L_p} \tag{D.7}
$$

allows the perpendicular length scale to be selected independently of the pressure gradient length scale. Here, it is set to $\bar{\omega_p} = 1$.

The differential operators then become

$$
\begin{aligned}
&\frac{\partial}{\partial \bar{t}} \leftarrow \tau \frac{\partial}{\partial t}\\
&\frac{\partial}{\partial \bar{y}} \leftarrow \rho_s \frac{\partial}{\partial y}\\
&\bar{\nabla}_\parallel \leftarrow \frac{1}{k_\parallel}\nabla_\parallel\\
&\bar{\nabla}_\perp \leftarrow \rho_s \nabla_\perp
\end{aligned}
\tag{D.8}
$$

Fourier transforming in the spatial coordinates, and Laplace transforming in the complex frequency, s, for plane waves of the form, $e^{i\mathbf{k}\cdot\mathbf{r}-st}$, these operators become

$$\begin{aligned}
&\frac{\partial}{\partial \bar{t}} = \tau \frac{\partial}{\partial t} \rightarrow -\tau s = -\tau(\gamma + i\omega) = -\bar{s} = -(\bar{\gamma} + i\bar{\omega}) \\
&\frac{\partial}{\partial \bar{y}} = \rho_s \frac{\partial}{\partial y} \rightarrow ik_\perp \rho_s = i\bar{k}_\perp \\
&\bar{\nabla}_\parallel = \frac{1}{k_\parallel}\nabla_\parallel \rightarrow \frac{ik_\parallel}{k_\parallel} = i\bar{k}_\parallel = i \\
&\bar{\nabla}_\perp = \rho_s \nabla_\perp \rightarrow ik_\perp \rho_s = i\bar{k}_\perp
\end{aligned} \tag{D.9}$$

where $\bar{\gamma} = \gamma\tau$ is the normalized damping rate.

A subtlety in this scheme of nondimensionalization is that the different spatial coordinates are each normalized to a different length scale. This necessitates additional nondimensional scale factors for each of the flux variables, accounting for the ratio of length scales. This, together with the normalizations motivated by Equations D.1, D.2, D.3, and D.4, results in the following scaled versions of the evolved quantities:

$$\hat{\bar{\phi}} \equiv \frac{e\tilde{\Phi}}{T_e} \tag{D.10}$$

$$\bar{\tilde{p}}_e \equiv \frac{\tilde{p}_e}{p_e} \tag{D.11}$$

$$\hat{\bar{A}}_\parallel \equiv \frac{\tilde{A}_\parallel}{\bar{\beta} B \rho_s} k_\parallel L_\perp \tag{D.12}$$

$$\bar{\tilde{u}}_\parallel \equiv \frac{\tilde{u}_\parallel}{c_s} k_\parallel L_\perp \tag{D.13}$$

$$\hat{\bar{J}} \equiv \frac{\tilde{J}_\parallel}{n_e e c_s} k_\parallel L_\perp, \tag{D.14}$$

noting that $k_\parallel L_\perp = \frac{2\pi L_\perp}{L_\parallel}$. These definitions arise naturally in the normalization of Equations D.1, D.2, D.3, and D.4, which is accomplished by multiplying each equation by a factor of $\tau = \frac{L_\perp}{c_s}$, and each $\nabla_\parallel$ operator by a unit factor of $\frac{k_\parallel}{k_\parallel}$. Then Eq. D.1

becomes

$$\rightarrow \boxed{\frac{\partial}{\partial \bar{t}} \bar{\nabla}_{\perp}^{2} \hat{\bar{\phi}} = \frac{\partial \bar{\omega}}{\partial t} = \bar{\nabla}_{\parallel} \bar{J}} \tag{D.15}$$

after transforming the differential operators and solving for $\hat{\bar{\phi}}$ in terms of $\hat{\bar{J}}$. $\bar{\omega} = \mathbf{b} \cdot (\nabla \times \mathbf{u})$ is the parallel component of the vorticity; here, only the electrostatic $\mathbf{E} \times \mathbf{B}$ velocity is considered in the evaluation of $\bar{\omega}$.

Similarly, the continuity equation, D.2, is nondimensionalized as

$$\rightarrow \boxed{\frac{\partial}{\partial \bar{t}} \hat{\bar{p}}_{e} + \bar{\omega}_{p} \frac{\partial}{\partial \bar{y}} \hat{\bar{\phi}} = \Gamma \bar{\nabla}_{\parallel} \left(\hat{\bar{J}} - \bar{\bar{u}}_{\parallel} \right)} \tag{D.16}$$

Ohm's law is nondimensionalized as

$$\rightarrow \boxed{\bar{\beta} \frac{\partial}{\partial \bar{t}} \hat{\bar{A}}_{\parallel} + \bar{\mu} \frac{\partial}{\partial \bar{t}} \hat{\bar{J}} = \bar{\nabla}_{\parallel} \left(\hat{\bar{p}}_{e} - \hat{\bar{\phi}} \right) - \bar{\beta} \bar{\omega}_{p} \frac{\partial}{\partial \bar{y}} \hat{\bar{A}}_{\parallel} - 0.51 \bar{\mu} \bar{\nu} \hat{\bar{J}}} \tag{D.17}$$

where

$$\bar{\beta} \equiv \frac{\beta_{e}}{\left(k_{\parallel} L_{\perp} \right)^{2}} \tag{D.18}$$

$$\bar{\mu} \equiv \frac{\mu_{e}}{\left(k_{\parallel} L_{\perp} \right)^{2}} \tag{D.19}$$

$$\bar{\nu} \equiv \nu_{e} \tau = \nu_{e} \frac{L_{\perp}}{c_{s}} \tag{D.20}$$

and $\beta_{e} = \mu_{0} p / B^{2} \approx$ is the dynamical beta.

Finally, the momentum balance equation is normalized as

$$\rightarrow \boxed{\bar{\epsilon} \frac{\partial}{\partial \bar{t}} \bar{\bar{u}}_{\parallel} = -\bar{\nabla}_{\parallel} \hat{\bar{p}}_{e} + \bar{\omega}_{p} \bar{\beta} \frac{\partial}{\partial \bar{y}} \hat{\bar{A}}_{\parallel} + \bar{\mu}_{\parallel} \bar{\nabla}_{\parallel}^{2} \bar{\bar{u}}_{\parallel}} \tag{D.21}$$

where

$$\bar{\epsilon} \equiv \left(\frac{1}{k_{\parallel} L_{\perp}} \right)^{2} \tag{D.22}$$

$$\bar{\mu}_{\parallel} \equiv \frac{\mu_{\parallel}\tau}{L_{\perp}^2} \tag{D.23}$$

with $\mu_{\parallel}$ the normalized parallel viscosity.

Ampère's law may also be used to relate $\hat{\bar{A}}_{\parallel}$ to $\hat{\bar{J}}$:

$$\boxed{\hat{\bar{J}} = -\bar{\nabla}_{\perp}^2 \hat{\bar{A}}_{\parallel}} \tag{D.24}$$

Eqs. D.15, D.16, D.17, and D.21 are in a suitable form for numerical solution with `BOUT++`.

Next, these equations are Fourier transformed in space and Laplace transformed in time, per the normalized transform variables above:

$$\bar{s}\bar{k}_{\perp}^2 \hat{\bar{\phi}} = ik_{\parallel}\hat{\bar{J}} \tag{D.25}$$

$$-\bar{s}\hat{\bar{p}}_e + i\bar{\omega}_p \bar{k_{\perp}}\hat{\bar{\phi}} = \Gamma i\bar{k}_{\parallel}\left(\hat{\bar{J}} - \bar{\bar{u}}_{\parallel}\right) \tag{D.26}$$

$$-\bar{s}\left(\bar{\beta}\hat{\bar{A}}_{\parallel} + \bar{\mu}\hat{\bar{J}}\right) = i\bar{k}_{\parallel}\left(\hat{\bar{p}}_e - \hat{\bar{\phi}}\right) - i\bar{\omega}_p\bar{\beta}\bar{k}_{\perp}\hat{\bar{A}}_{\parallel} - 0.51\bar{\mu}\bar{\nu}\hat{\bar{J}} \tag{D.27}$$

$$-\bar{\epsilon}\bar{s}\bar{\bar{u}}_{\parallel} = -i\bar{k}_{\parallel}\hat{\bar{p}}_e + i\bar{\omega}_p\bar{\beta}\bar{k}_{\perp}\hat{\bar{A}}_{\parallel} - \bar{\mu}_{\parallel}\bar{k}_{\parallel}^2\bar{\bar{u}}_{\parallel} \tag{D.28}$$

with Ampère's law,

$$\hat{\bar{J}} = \bar{k}_{\perp}^2\hat{\bar{A}}_{\parallel}. \tag{D.29}$$

D.2 Analytical Solution Using Simplified, Transformed Slab Model

The fourth-order system described above has four roots for the complex frequency, $\bar{s} = \bar{\gamma} + i\bar{\omega}$. However, this level of detail is not always necessary. Specifically, if the mode parallel phase velocity is much larger than the sound speed, $v_\parallel = \omega/k_\parallel \gg c_s$, then sound waves may be neglected, as the mode travels faster than the sound wave disturbance may be propagated. In the case under study, with a deuterium plasma at $T_e \approx 50$ eV, $B_0 \approx 3$ T, $\omega_{qcm} \sim 2\pi\times$ (100 kHz), $q_{95} \approx 3$, and $k_\parallel \sim \frac{2\pi}{2L_c} = \frac{2\pi}{2\pi R q_{95}} \approx 0.35$ m^{-1}, $v_\parallel \approx 2000$ km/s $\gg c_s \approx 50$ km/s, the approximation is valid. This is tantamount to neglecting the terms proportional to the parallel gradient of the parallel velocity fluctuation, $\bar{\nabla}_\parallel \bar{\tilde{u}}_\parallel, \bar{k}_\parallel \bar{\tilde{u}}_\parallel \to 0$. The order of the system is thereby reduced from four to three.

$\hat{\tilde{\phi}}$ and $\hat{\tilde{p}}_e$ may be eliminated from Eq. D.28 using Eq.'s D.25 and D.26:

$$\Rightarrow \boxed{\left(\frac{\bar{\beta}}{\bar{k}_\perp^2} + \bar{\mu}\right)\bar{s}^3 - \left(i\frac{\bar{\omega}_p\bar{\beta}}{\bar{k}_\perp} + 0.51\bar{\mu}\bar{\nu}\right)\bar{s}^2 + \bar{k}_\parallel^2\left(\frac{1}{\bar{k}_\perp^2} + \Gamma\right)\bar{s} - \frac{i\bar{\omega}_p\bar{k}_\parallel^2}{\bar{k}_\perp} = 0} \quad \text{(D.30)}$$

having made use of Ampère's law, D.24.

The following parameters correspond to Alcator C-Mod Discharge 1120814028 at 1.1964 s at the location of the Mirror Langmuir Probe tip. These parameters were selected for ready comparison with the analysis in [32]. The parameters are evaluated

from MLP and EFIT reconstruction data.

$$
\begin{aligned}
|\mathbf{B}| &\approx 2.25\,\mathrm{T} \\
n_e &\approx 1.46 \times 10^{20}\,\mathrm{m}^{-3} \\
T_e &\approx 48.6\,\mathrm{eV} \\
p_e &\approx 1.15\,\mathrm{kPa} \\
L_p = L_\perp &\approx 3.96\,\mathrm{mm} \\
k_\perp &\approx 150.00\,\mathrm{m}^{-1} \\
L_c &\approx 9.07\,\mathrm{m} \\
k_\parallel &\approx \frac{\pi}{L_c} \approx 0.35\,\mathrm{m}^{-1}\,\mathrm{m}
\end{aligned}
\tag{D.31}
$$

$$
\begin{aligned}
\Omega_i &\equiv \frac{eB}{M_i} \approx \frac{\pi}{L_c} \approx 2\pi \cdot 17.1\,\mathrm{MHz} \\
\omega_{pi} &\equiv \sqrt{\frac{n_i e^2}{\epsilon_0 M_i}} \approx 2\pi \cdot 1789.7\,\mathrm{MHz} \\
c_s &\equiv \sqrt{\frac{T_e}{M_i}} \approx 48.3\,\frac{\mathrm{km}}{\mathrm{s}} \\
v_A &\equiv \frac{c}{\sqrt{1 + \frac{\omega_{pi}^2}{\Omega_i^2}}} \approx 2872\,\frac{\mathrm{km}}{\mathrm{s}} \\
\beta_e &\equiv \frac{c_s^2}{v_A^2} \approx 2.83 \times 10^{-4} \\
\rho_s &\equiv \frac{c_s}{\Omega_i} \approx 0.448\,\mathrm{mm}
\end{aligned}
\tag{D.32}
$$

$$
\begin{aligned}
\bar{\omega}_p &\equiv \frac{L_\perp}{L_p} = 1 \\
\bar{\epsilon} &\equiv \frac{1}{\left(k_\parallel L_\perp\right)^2} \approx 5.32 \times 10^5 \\
\bar{\beta}_e &\equiv \beta_e \bar{\epsilon} \approx 150 \\
\bar{\mu} &\equiv \mu_e \bar{\epsilon} \approx 145 \\
\bar{\nu} &\equiv \frac{L_\perp / c_s}{\tau_{ei}} \approx 1.11 \\
\bar{k}_\perp &\equiv k_\perp \rho_s \approx 0.067 \\
\bar{k}_\parallel &\equiv \frac{k_\parallel}{k_\parallel} \approx 1
\end{aligned}
\tag{D.33}
$$

Using the shorthand notation,

$$
C_3 \bar{s}^3 + C_2 \bar{s}^2 + C_1 \bar{s} + C_0 = 0, \tag{D.34}
$$

for Eq. D.30,

$$
\begin{aligned}
C_3 &\equiv \frac{\bar{\beta}_e}{\bar{k}_\perp^2} \approx 3.34 \times 10^4 \gg \bar{\mu} \sim 150 \\
C_2 &\equiv -\left(i \frac{\bar{\omega}_p \bar{\beta}_e}{\bar{k}_\perp} + 0.51 \bar{\mu} \bar{\nu} \right) \approx -\left(i 2.24 + 0.082 \right) \times 10^3 \\
C_1 &\equiv \bar{k}_\parallel^2 \left(\frac{1}{\bar{k}_\perp^2} + \Gamma \right) \approx 223 \sim \frac{1}{\bar{k}_\perp^2} \\
C_0 &\equiv -i \frac{\bar{\omega}_p \bar{k}_\parallel^2}{\bar{k}_\perp} \approx -i 14.9
\end{aligned}
\tag{D.35}
$$

where we see that the electron inertia is ignorable, $(\mu \to 0)$, as is the ratio of specific heats, Γ, though these terms are retained in the precise calculations for the roots.

While the roots of this dispersion relation may be calculated exactly, it is nonetheless informative to find approximations for these values. This facilitated by splitting Eq. D.34 into its real and imaginary parts, and setting each component separately to zero). Noting that $\Im\{C_3\} = \Im\{C_1\} = \Re\{C_0\} = 0$, and letting the subscripts, r and i, correspond to real and imaginary values, Eq. D.34 becomes

$$C_{3,r}\left(s_r^3 - 3s_r s_i^2\right) + C_{2,r}\left(s_r^2 - s_i^2\right) - 2C_{2,i}s_r s_i + C_{1,r}s_r + \\ i\left[C_{3,r}\left(3s_r^2 s_i - s_i^3\right) + 2C_{2,r}s_r s_i + C_{2,i}\left(s_r^2 - s_i^2\right) + C_{1,r}s_i + C_{0,i}\right] = 0 \tag{D.36}$$

Under the assumption that the real frequency[1], $\omega = s_i$, is much larger than the damping or growth rate, $s_i \gg s_r$, the imaginary part of Eq. D.36 simplifies to

$$-C_{3,r}s_i^3 - C_{2,i}s_i^2 + C_{1,r}s_i + C_{0,i} = 0, \tag{D.37}$$

decoupling the solution of s_i from s_r. It may appear that we have traded one third-order polynomial for another. However, closer inspection of the coefficients reveals that

$$\frac{C_{2,i}}{C_{3,r}} = \frac{-\bar{\omega}_p\bar{\beta}_e/\bar{k_\perp}}{\bar{\beta}_e/\bar{k}_\perp^2} = -\bar{\omega}_p\bar{k}_\perp \tag{D.38}$$

and

$$\frac{C_{0,i}}{C_{1,r}} = -\frac{\bar{\omega}_p\bar{k}_\parallel^2/\bar{k}_\perp}{\bar{k}_\parallel^2\left(\frac{1}{\bar{k_\perp}+\Gamma}\right)} = -\frac{\bar{\omega}_p/\bar{k}_\perp}{\frac{1}{\bar{k_\perp}+\Gamma}} \approx -\bar{\omega}_p\bar{k}_\perp = \frac{C_{2,i}}{C_{3,r}}, \tag{D.39}$$

allowing the factorization,

$$\left(-s_i^2 C_{3,r} + C_{1,r}\right)\left(s_i + \frac{C_{0,i}}{C_{1,r}}\right) = 0 \tag{D.40}$$

of Eq. D.37. The roots of this approximate dispersion relation are identified immediately as

$$\boxed{s_i \approx -\frac{C_{0,i}}{C_{1,r}}, \pm\sqrt{\frac{C_{1,r}}{C_{3,r}}}}. \tag{D.41}$$

The real part of Eq. D.36 may then be eliminated using s_r as a free parameter, still

[1]Note that the real frequency corresponds to the imaginary component of s, $\omega = \Im\{s\}$, the damping rate to $\Re\{s\}$, and the growth rate to $-\Re\{s\}$

assuming $s_r \ll s_i$ and so neglecting terms higher order in s_r:

$$\begin{aligned}
0 &= C_{3,r}\left(s_r^3 - 3s_r s_i^2\right) + C_{2,r}s_r^2 - C_{2,r}s_i^2 - 2C_{2,i}s_r s_i + C_{1,r}s_r \\
&\approx -3C_{3,r}s_i^2 s_r - C_{2,r}s_i^2 - 2C_{2,i}s_i s_r + C_{1,r}s_r \\
&= s_r\left(-3C_{3,r}s_i^2 - 2C_{2,i}s_i + C_{1,r}\right) - C_{2,r}s_i^2 \\
\Rightarrow &\boxed{s_r \approx \frac{C_{2,r}s_i^2}{C_{1,r} - 3C_{3,r}s_i^2 - 2C_{2,i}s_i} = \frac{C_{2,r}}{C_{3,r}}\frac{1}{\frac{C_{1,r}}{C_{3,r}s_i^2} - 3 - 2\frac{C_{2,i}}{C_{3,r}s_i}}}.
\end{aligned} \tag{D.42}$$

Using the parameters in Eq. D.35, these approximate roots of the dispersion relation are calculated as

$$\bar{s} \approx 10^{-2} \times [-0.483 + i6.67, 0.067 - i8.17, 0.676 - i8.17] \tag{D.43}$$

or, multiplying by $1/\tau$ to recover the values in dimensional units,

$$s = 2\pi \cdot [-9.38 + i129.4, 1.304 - i158.5, 13.12 + i158.5]\,\text{kHz}. \tag{D.44}$$

This may be compared with the exact solution for the roots,

$$\bar{s} = 10^{-2} \times [0.560 + i8.35, -0.383 + i6.51, 0.067 - i8.16] \tag{D.45}$$

or, in dimensional units,

$$s = 2\pi \cdot [-7.432 + i126.3, 1.304 - i158.4, 10.87 + i162.0]\,\text{kHz}, \tag{D.46}$$

showing the approximations to be accurate.

The physical origin behind the analytical forms of the approximate roots may now be interpreted. The real frequency of the first root,

$$\boxed{\omega_* = \Im\{s_1\} = -\frac{C_{0,i}}{C_{1,r}}\frac{1}{\tau} = \bar{\omega}_p \bar{k}_\perp \frac{1}{\tau} = \frac{L_\perp}{L_p}k_\perp \rho_s \frac{c_s}{L_\perp} = k_\perp \frac{c_s \rho_s}{L_p} = k_\perp v_*}, \tag{D.47}$$

corresponds precisely to the ideal drift wave examined in Section 3.2.2. The real part

of this eigenvalue, corresponding to the negative inverse of the growth rate, is

$$-\bar{\gamma}_* = \Re\{s\} = \frac{1}{-3\frac{C_{3,r}}{C_{2,r}} - \frac{2}{s_i} + \frac{C_{1,r}}{C_{2,r}s_i^2}} = \frac{C_{2,r}}{C_{3,r}}\frac{1}{-3 + 2\frac{C_{2,r}}{C_{2,i}} + \frac{C_{1,r}C_{3,r}}{C_{2,i}^2}} \approx \frac{C_{2,r}}{C_{3,r}}\frac{1}{\frac{C_{1,r}C_{3,r}}{C_{2,i}^2} - 3} \tag{D.48}$$

after recalling that $s_{i,1} = -C_{0,i}/C_{1,r} \approx -C_{2,i}/C_{3,r}$, and noting that $C_{2,r}/C_{2,i} \sim 0.04 \ll 1$. Substituting expressions from Eq. D.35, and dividing by $\tau = L_\perp/c_s$ to obtain a rate in physical units,

$$\boxed{\gamma_* = -\frac{\Re\{s\}}{\tau} = \eta_s\omega_{pi}^2\epsilon_0\frac{\omega_*^2 k_\perp^2}{\Omega_i^2 k_\parallel^2}\left(\frac{1}{1-\frac{\omega_*^2}{\omega_A^2}}\right) = \frac{\eta_s k_\perp^2}{\mu_0}\frac{\omega_*^2}{\omega_A^2}\left(\frac{1}{1-\frac{\omega_*^2}{\omega_A^2}}\right)}, \tag{D.49}$$

where $\omega_A^2 \equiv k_\parallel^2 v_A^2$ corresponds to the ideal Alfvén continuum frequency, $\eta_\parallel = \eta_s$ is the Spitzer resistivity, which is the parallel resistivity in the Braginskiĭ model, and noting that $\eta_s\omega_{pi}^2\epsilon_0 = 0.51\mu_e/\tau_{ei}$. This corresponds to Eqs. 5.47 and 5.49 in [65, p. 5.12, 5.14] when the terms proportional to Γ are neglected, except that in Eq. D.49, there is an additional multiplicative factor, $\left(1-\frac{\omega_*^2}{\omega_A^2}\right)^{-1}$. Normally, it is expected that $\omega_A \gg \omega_*$; however, in the present case, $\omega_*/\omega_A \approx 0.82$, and so this additional factor is appreciably different from unity.

The remaining two roots have real frequencies,

$$\Im\{s_A\} = \pm\sqrt{\frac{C_{1,r}}{C_{3,r}}}, \tag{D.50}$$

which, after using the expressions in Eq. D.35 and dividing by τ to obtain physical units, can be rewritten as

$$\boxed{\omega_A^2 = \Im\{s_A\}^2 = k_\parallel^2 v_A^2}, \tag{D.51}$$

which is immediately identified as the ideal Alfvén wave dispersion relation. The *damping* rate for these modes is obtained from Eq. D.42:

$$\boxed{\gamma_A = \Re\{s_A\} = \eta_s \omega_{pi}^2 \epsilon_0 \frac{\omega_*^2 k_\perp^2}{2\Omega_i^2 k_\parallel^2} \frac{\omega_A^2}{\omega_*^2} \left(\frac{1}{1 \mp \frac{\omega_*}{\omega_A}} \right) = \frac{\eta_s k_\perp^2}{2\mu_0} \left(\frac{1}{1 \mp \frac{\omega_*}{\omega_A}} \right)}, \tag{D.52}$$

where the selection of the negative root in the damping rate corresponds to the positive root in the Alfvén wave dispersion relation in Eq. D.51.

These damping rates show that the positive root of the Alfvén wave dispersion relation is more strongly damped than the negative root when ω_* is smaller than but close to ω_A. Indeed, the damping rate of this root exhibits a singularity at $\omega_A = \omega_*$. Here, with $\omega_*/\omega_A \approx 0.82$, $\gamma_{A,-}/\omega_{A,-} \approx 6.7\%$. The negative root, by contrast, has a weaker damping rate, with $\gamma_{A,+}/\omega_{A,+} \approx 0.82\%$. As such, both the drift and Alfvén waves have a preferred direction, though the damping rates of both Alfvén waves in this system are still modest.

As noted in Section 3.4.1, the *damping* rate of the two Alfvén waves is half the *growth* rate of the drift wave when the multiplicative factors, $(1 - \omega_*^2/\omega_A^2)^{-1}$ and $(1 - \omega_*/\omega_A)^{-1}$, are ignored, but $\omega_A \sim \omega_*$, though these circumstances are contradictory.

D.3 Slab Geometry

The simplest drift wave model treats the slab geometry, which involves a spatially flat magnetic field (i.e. one with no curvature, $\mathbf{b} \cdot \nabla \mathbf{b} = 0$). This has been the starting point for the drift wave model described in Sections D.1 and D.2. When there is no shear, it is convenient to apply a Cartesian coordinate system, where traditionally, the x axis labels the flux surface, the y axis is the direction in which the wave propagates and is perpendicular to both the field lines and the pressure gradient, and the z axis is the field-aligned direction. The metric tensor for this coordinate system is simply the identity matrix.

It is especially convenient to align one axis with the equilibrium field direction. This is because Alfvén dynamics tend to rapidly smooth out perturbations along field

lines, with the consequence that there are a large number of eigenmodes that change slowly along field lines, but rapidly across them. This gives rise to elongated structures which resemble the fluting motif seen on classical-style architectural columns, hence the name, "flute modes" [65, 98, 70]. It can be advantageous to exploit this property in numerical simulation, since lower grid resolution is needed along the field line direction than across.

However, once shear is introduced, the field changes orientation across flux surfaces. Without a more general curvilinear coordinate system, the slab model loses its field-aligned coordinate, and the a finer discretized spatial grid is needed to achieve adequate resolution. The solution is to transform the coordinates to a new field aligned system [65, 98]. The penalty for the more efficient allocation of grid points is a more complicated geometrical apparatus which makes calculating derivatives and other operations more difficult, and also requires additional care in the application of boundary conditions.

The following sections derive the coordinate system used for the slab geometry along the transformation suggested by Scott [65, Chap. 8], but satisfying the criterion for a Clebsch coordinate system, $\mathbf{B} = \nabla z \times \nabla x$, which enables the use of a number of built-in methods in `BOUT++` [98];

D.3.1 Coordinate System Transformation

Assume a sheared equilibrium magnetic field of the form,

$$\mathbf{B} = B_0(\hat{z} + \hat{y}\sigma_\theta \frac{x}{L_s}) \tag{D.53}$$

written in a flat Cartesian coordinate system with unit basis vectors, $\hat{x}$ and $\hat{y}$ and $\hat{z}$. Here, L_s represents the shear length scale, and is equal to the distance covered in the $\hat{x}$ direction when the field rotates 45° due to shear. σ_θ is the sign of the "poloidal" field component. Note that the field strength, $\|\mathbf{B}\|$, is a function of x, so that there is a well centered at $x = 0$.

Before proceeding, let us introduce normalizations

$$\begin{aligned}\bar{x} &= \frac{x}{\rho_s} \\ \bar{y} &= \frac{y}{\rho_s} \\ \bar{z} &= k_\parallel z = \frac{2\pi z}{L_\parallel} \\ \bar{\mathbf{B}} &= \frac{\mathbf{B}}{B_0} = (\hat{z} + \hat{y}\sigma_\theta \frac{x}{L_s})\end{aligned} \tag{D.54}$$

where the perpendicular directions are normalized to the drift dispersion scale, $\rho_s = c_s/\Omega_{ci}$, while the parallel direction is normalized against the parallel wave number, which is taken to be the minimal possible value, $k_\parallel = 2\pi/L_\parallel$, where $L_\parallel$ is the parallel length scale. Note that x is normalized differently than in Eq. D.6.

Next, introduce a dimensionless shear parameter,

$$\begin{aligned}s &\equiv \frac{L_\parallel}{L_s} \\ \bar{s} &\equiv \frac{k_\parallel L_\parallel}{L_s/\rho_s} = s k_\parallel \rho_s\end{aligned} \tag{D.55}$$

where normalization of this dimensionless parameter is necessitated by the differing perpendicular and parallel length scales. Then we may write the normalized field as

$$\bar{\mathbf{B}} = \hat{z} + \hat{y}\frac{\bar{s}\bar{x}}{2\pi} \tag{D.56}$$

noting that $1/(L_s/\rho_s) = \bar{s}/(2\pi)$.

A simple transformation from the flat Cartesian coordinates, $\{x, y, z\}$, to the field-aligned Clebsch coordinates, $\{\psi, \xi, \zeta\}$, is given by[2]

[2]note that in the BOUT++ literature, x, y, z refers to the field-aligned and generally non-orthogonal coordinate system, while ψ, θ, ζ refers to an orthogonal toroidal coordinate system per the usual convention. Because, in this slab case, the orthogonal coordinate system from which the field-aligned system is derived is the Cartesian coordinate system, it is more natural to express the orthogonal system using x, y, z, and so Greek letters are used for the field-aligned system.

$$\begin{aligned}\psi &= \bar{B}_0\bar{x} = \bar{x} \\ \xi &= z \\ \zeta &= -\bar{y} + \sigma_\theta \frac{\bar{s}\bar{x}\bar{z}}{2\pi}\end{aligned} \tag{D.57}$$

since $\bar{B}_0 = B_0/B_0 = 1$.

This gives rise to contravariant basis vectors,

$$\begin{aligned}\mathbf{e}^\psi &= \bar{\nabla}\psi = \left(\frac{\partial}{\partial\bar{x}}\hat{x} + \frac{\partial}{\partial\bar{y}}\hat{y} + \frac{\partial}{\partial\bar{z}}\hat{z}\right)\psi = \bar{B}_0\hat{x} = \hat{x} \\ \mathbf{e}^\xi &= \bar{\nabla}\xi = \left(\frac{\partial}{\partial\bar{x}}\hat{x} + \frac{\partial}{\partial\bar{y}}\hat{y} + \frac{\partial}{\partial\bar{z}}\hat{z}\right)\xi = \hat{z} \\ \mathbf{e}^\zeta &= \bar{\nabla}\zeta = \left(\frac{\partial}{\partial\bar{x}}\hat{x} + \frac{\partial}{\partial\bar{y}}\hat{y} + \frac{\partial}{\partial\bar{z}}\hat{z}\right)\zeta = -\hat{y} + \sigma_\theta\frac{\bar{s}}{2\pi}(\hat{x}\bar{z} + \hat{z}\bar{x})\end{aligned} \tag{D.58}$$

where the factor of $\bar{B}_0 = 1$ is retained for clarity. To check that this is, indeed, a Clebsch coordinate system, calculate the field directly from

$$\begin{aligned}\bar{\mathbf{B}} &= \mathbf{e}^\zeta \times \mathbf{e}^\psi = \left[-\hat{y} + \sigma_\theta\frac{\bar{s}}{2\pi}\left(\hat{x}\bar{z} + \hat{z}\bar{x}\right)\right] \times (\bar{B}_0\hat{x}) = \hat{z}\bar{B}_0 + \hat{y}\bar{B}_0\sigma_\theta\frac{\bar{s}\bar{x}}{2\pi} \\ &= \bar{B}_0\left(\hat{z} + \sigma_\theta\hat{y}\frac{\bar{x}}{\bar{L}_s}\right) = \hat{z} + \sigma_\theta\hat{y}\frac{\bar{x}}{\bar{L}_s},\end{aligned} \tag{D.59}$$

which is the original normalized magnetic field. Note that this is also $\mathbf{B} = \mathbf{e}_\xi/\mathcal{J}$, where $\mathcal{J} = 1/\sqrt{\det(g^{ij})} = 1/\sqrt{\bar{B}_0^2} = 1/|\bar{B}_0| = 1$ is the Jacobian. Direct calculation gives the same result:

$$\begin{aligned}\bar{B}^\psi &= \bar{\mathbf{B}}\cdot\mathbf{e}^\psi = \bar{B}_0(\hat{z} + \hat{y}\sigma_\theta\bar{s}\bar{x}/(2\pi))\cdot\hat{x}\bar{B}_0 = 0 \\ \bar{B}^\xi &= \bar{\mathbf{B}}\cdot\mathbf{e}^\xi\bar{B}_0(\hat{z} + \hat{y}\sigma_\theta\bar{s}\bar{x}/(2\pi))\cdot\hat{z} = \bar{B}_0 = 1 \\ \bar{B}^\zeta &= \bar{\mathbf{B}}\cdot\mathbf{e}^\xi\bar{B}_0(\hat{z} + \hat{y}\sigma_\theta\bar{s}\bar{x}/(2\pi))\cdot(-\hat{y} + \sigma_\theta\frac{\bar{s}}{2\pi}(\hat{x}z + \hat{z}x)) = 0\end{aligned} \tag{D.60}$$

As desired, the magnetic field in this basis has only a single non-zero component,

$\bar{\mathbf{B}} = B^{\xi}\mathbf{e}_{\xi}$.

To calculate the covariant basis vectors, it is convenient to record the normalized Cartesian coordinates as functions of the transformed coordinates,

$$\begin{aligned} \bar{x} &= \frac{\psi}{\bar{B}_0} \\ \bar{y} &= \sigma_\theta \frac{\bar{s}\psi\xi}{2\pi\bar{B}_0} - \zeta \\ \bar{z} &= \xi. \end{aligned} \tag{D.61}$$

The covariant basis vectors are then found to be

$$\begin{aligned} \mathbf{e}_\psi &= \frac{\partial\bar{\mathbf{r}}}{\partial\psi} = \frac{\partial}{\partial\psi}\left[\hat{x}\bar{x} + \hat{y}\bar{y} + \hat{z}\bar{z}\right] = \frac{\partial}{\partial\psi}\left[\hat{x}\frac{\psi}{\bar{B}_0} + \hat{y}\left(\sigma_\theta\frac{\bar{s}\psi\xi}{2\pi} - \zeta\right) + \hat{z}\xi\right] \\ &= \frac{1}{\bar{B}_0}\left[\hat{x} + \hat{y}\sigma_\theta\frac{\bar{s}\xi}{2\pi}\right] = \frac{1}{\bar{B}_0}\left[\hat{x} + \hat{y}\sigma_\theta\frac{\bar{s}\bar{z}}{2\pi}\right] \\ \mathbf{e}_\xi &= \frac{\partial\bar{\mathbf{r}}}{\partial\xi} = \frac{\partial}{\partial\xi}\left[\hat{x}\frac{\psi}{\bar{B}_0} + \hat{y}\left(\sigma_\theta\frac{\bar{s}\psi\xi}{2\pi} - \zeta\right) + \hat{z}\xi\right] = \hat{y}\sigma_\theta\frac{\bar{s}\psi}{\bar{B}_0 2\pi} + \hat{z} = \hat{z} + \hat{y}\sigma_\theta\frac{\bar{s}\bar{x}}{2\pi} \\ \mathbf{e}_\zeta &= \frac{\partial\bar{\mathbf{r}}}{\partial\zeta} = \frac{\partial}{\partial\zeta}\left[\hat{x}\frac{\psi}{\bar{B}_0} + \hat{y}\left(\sigma_\theta\frac{\bar{s}\psi\xi}{2\pi} - \zeta\right) + \hat{z}\xi\right] = -\hat{y} \end{aligned} \tag{D.62}$$

where $\bar{\mathbf{r}}$ is the normalized abstract position vector.

The contravariant components of the metric tensor (the inverse metric [139]) are found from

$$g^{ij} = \mathbf{e}^i \cdot \mathbf{e}^j \tag{D.63}$$

to be

$$
\begin{aligned}
g^{11} &= \mathbf{e}^{\psi} \cdot \mathbf{e}^{\psi} = \bar{B}_0^2 = 1 \\
g^{22} &= \mathbf{e}^{\xi} \cdot \mathbf{e}^{\xi} = 1 \\
g^{33} &= \mathbf{e}^{\zeta} \cdot \mathbf{e}^{\zeta} = 1 + \left(\frac{\bar{s}}{2\pi}\right)^2 \left(\bar{x}^2 + \bar{z}^2\right) \\
g^{12} &= \mathbf{e}^{\psi} \cdot \mathbf{e}^{\xi} = 0 \\
g^{13} &= \mathbf{e}^{\psi} \cdot \mathbf{e}^{\zeta} = \sigma_\theta \frac{\bar{s}\bar{z}\bar{B}_0}{2\pi} \\
g^{23} &= \mathbf{e}^{\xi} \cdot \mathbf{e}^{\zeta} = \sigma_\theta \frac{\bar{s}\bar{x}}{2\pi}
\end{aligned}
\tag{D.64}
$$

with $\bar{\bar{g}}$ symmetric, $g^{ij} = g^{ji}$.

The covariant components of the metric tensor (the "metric" [139]) are

$$
\begin{aligned}
g_{11} &= \mathbf{e}_{\psi} \cdot \mathbf{e}_{\psi} = \frac{1}{\bar{B}_0^2}\left[1 + \left(\frac{\bar{s}\bar{z}}{2\pi}\right)^2\right] \\
g_{22} &= \mathbf{e}_{\xi} \cdot \mathbf{e}_{\xi} = 1 + \left(\frac{\bar{s}\bar{x}}{2\pi}\right)^2 \\
g_{33} &= \mathbf{e}_{\zeta} \cdot \mathbf{e}_{\zeta} = 1 \\
g_{12} &= \mathbf{e}_{\psi} \cdot \mathbf{e}_{\xi} = \left(\frac{\bar{s}}{2\pi}\right)^2 \frac{\bar{x}\bar{z}}{\bar{B}_0} \\
g_{13} &= \mathbf{e}_{\psi} \cdot \mathbf{e}_{\zeta} = -\sigma_\theta \frac{\bar{s}\bar{z}}{2\pi\bar{B}_0} \\
g_{23} &= \mathbf{e}_{\xi} \cdot \mathbf{e}_{\zeta} = -\sigma_\theta \frac{\bar{s}\bar{x}}{2\pi}
\end{aligned}
\tag{D.65}
$$

and symmetry requires $g_{ij} = g_{ji}$.

In the limit where $\bar{s} \to 0$ (*i.e.* $L_s \to \infty$ and the shear vanishes from the magnetic field), the metric and inverse metric both reduce to the identity matrix, after noting that $\bar{B}_0 = 1$.

D.3.2 System of Equations in Field-Aligned Coordinates

Before writing the system of equations employed in the particular `BOUT++` models whose results are described in Section D.4, we introduce a way to cast advection by a

background electric field, $\mathbf{E}_0$. Taking the background electric field to be electrostatic, it is convenient to write the resulting advection using a Poisson bracket, [3]. This notation is common in the BOUT++ formulation of plasma fluid problems. To see its application, examine the $\mathbf{E}\times\mathbf{B}$ advection for an arbitrary scalar field, u:

$$\begin{aligned}
\mathbf{v}_{E,0}\cdot\nabla u &= \frac{\mathbf{E}_0\times\mathbf{B}}{B^2}\cdot\nabla u = \frac{\mathbf{B}}{B^2}\cdot(\nabla u\times\mathbf{E}_0) = \frac{\mathbf{B}}{B^2}\cdot(\nabla u\times\mathbf{E}_0) = \frac{\mathbf{B}}{B^2}\cdot(\nabla\Phi_0\times\nabla u)\\
&= \frac{1}{B^\xi}\mathbf{e}_\xi\cdot\left(\varepsilon_{ijk}\frac{\partial\Phi_0}{\partial r^j}\frac{\partial u}{\partial r^k}\mathbf{e}^i\right)\\
&= \frac{1}{B^\xi}\mathbf{e}_\xi\cdot\left(\varepsilon_{ijk}\frac{\partial\Phi_0}{\partial r^j}\frac{\partial u}{\partial r^k}\mathbf{e}^i\right)\\
&= \frac{1}{B^\xi}\varepsilon_{2jk}\frac{\partial\Phi_0}{\partial r^j}\frac{\partial u}{\partial r^k}\\
&= \frac{1}{B^\xi}\left(\frac{\partial\Phi_0}{\partial\zeta}\frac{\partial u}{\partial\psi}-\frac{\partial\Phi}{\partial\psi}\frac{\partial u}{\partial\zeta}\right)\\
&= -\frac{1}{B^\xi}\frac{\partial\Phi_0}{\partial\psi}\frac{\partial u}{\partial\zeta}
\end{aligned} \tag{D.66}$$

where $\varepsilon_{ijk}=\varepsilon^{ijk}$ is the third-order alternating tensor, and the identity, $\mathbf{A}\times\mathbf{B}\cdot\mathbf{C}=\mathbf{B}\cdot\mathbf{C}\times\mathbf{A}$, has been used. The last equality follows from the fact that Φ_0 is only allowed to depend upon ψ.

The Poisson bracket is written as

$$\{f,g\}=\sum_{i=1}^{N}\left(\frac{\partial f}{\partial q_i}\frac{\partial g}{\partial p_i}-\frac{\partial f}{\partial p_i}\frac{\partial g}{\partial q_i}\right) \tag{D.67}$$

for coordinates, $\mathbf{q}$ and $\mathbf{p}$. Making the substitution, $q_i\leftrightarrow\zeta$ and $p_i\leftrightarrow\psi$,

$$\bar{\mathbf{v}}_E\cdot\bar{\nabla}u=\frac{1}{\bar{B}^\xi}\left\{\bar{\Phi}_0,u\right\}. \tag{D.68}$$

BOUT++ makes available several routines for calculating bracketed quantities within the mesh constraints. However, when the potential profile is simple enough so that its derivative in ψ can be calculated explicitly, doing so may be preferable to avoid

[3] In this case, the potential becomes the stream function[65].

another finite-differencing step.

This issue of the formulation clarified, the normalized set of equations now follows. Quantities wearing a tilde ($\tilde{()}$) are evolved in the simulation, while the overbar ($\bar{()}$) is a reminder that the quantity underneath has been normalized. Ohm's law is written as

$$\boxed{\frac{\mathrm{d}}{\mathrm{d}\bar{t}}\left(\hat{\tilde{J}}+\frac{\hat{\beta}}{\bar{\mu}}\hat{\tilde{A}}_{\parallel}\right)=\frac{\mathrm{d}\tilde{\mathcal{A}}}{\mathrm{d}\bar{t}}=\bar{\nabla}_{\parallel}\left(\hat{\tilde{p}}_e-\hat{\tilde{\phi}}\right)-\bar{\beta}\frac{\partial\hat{\tilde{A}}_{\parallel}}{\partial\bar{y}}-\bar{\eta}\hat{\tilde{J}}-\bar{\mu}_e\left\{\bar{\Phi}_0,\hat{\tilde{J}}\right\}} \leftarrow \text{Ohm's law} \tag{D.69}$$

where

$$\tilde{\mathcal{A}}\equiv\hat{\tilde{J}}+\frac{\bar{\beta}}{\bar{\mu}}\hat{\tilde{A}}_{\parallel} \tag{D.70}$$

is a convenience quantity lumping together the time differentiation of both $J_{\parallel}$ and $A_{\parallel}$. Recall that $\bar{\beta}\equiv\frac{\mu_0 p_e}{B^2}\left(\frac{1}{k_{\parallel}L_{\perp}}\right)^2$ (Eq. D.18) and $\bar{\mu}\equiv\mu_e/\left(k_{\parallel}L_{\perp}\right)^2$ (Eq. D.19).

The electron continuity equation is

$$\boxed{\frac{\mathrm{d}\hat{\tilde{p}}_e}{\mathrm{d}\bar{t}}=-\frac{\partial\hat{\tilde{\phi}}}{\partial\bar{y}}+\bar{\nabla}_{\parallel}\hat{\tilde{J}}-\bar{\nabla}_{\parallel}\tilde{\bar{u}}_{\parallel}-\{\bar{\Phi}_0,\hat{\tilde{p}}_e\}} \leftarrow \text{Elec. cont. eq.} \tag{D.71}$$

The total momentum equation is

$$\boxed{\frac{\mathrm{d}\tilde{\bar{u}}_{\parallel}}{\mathrm{d}\bar{t}}=\left(k_{\parallel}L_{\perp}\right)^2\left(-\bar{\nabla}_{\parallel}\hat{\tilde{p}}_e+\bar{\mu}_{\parallel}\bar{\nabla}_{\parallel}^2\tilde{\bar{u}}_{\parallel}\right)-\{\bar{\Phi}_0,\tilde{\bar{u}}_{\parallel}\}} \leftarrow \text{Total mom. eq.} \tag{D.72}$$

where $\bar{\mu}_{\parallel}=\frac{1}{c_s L_{\perp}}\mu_{\parallel}=\frac{1}{c_s L_{\perp}}0.96eT_e/(M_i\nu_{ii})$ is the normalized parallel viscosity.

Finally, the quasineutrality (or vorticity) equation is

$$\boxed{\frac{\mathrm{d}\hat{\tilde{\bar{\omega}}}}{\mathrm{d}\bar{t}}=\bar{\nabla}_{\parallel}\hat{\tilde{J}}-\{\bar{\Phi}_0,\hat{\tilde{\bar{\omega}}}\}} \leftarrow \text{Quasineutrality (vorticity) eq.} \tag{D.73}$$

The parallel current is evaluated from

$$\hat{\tilde{J}}=\frac{1}{\bar{\mu}_e}\left(\tilde{\mathcal{A}}-\bar{\beta}\hat{\tilde{A}}_{\parallel}\right), \tag{D.74}$$

while the potential is obtained from $\bar{\omega}$ through an inverse perpendicular Laplacian

operation,

$$\hat{\tilde{\phi}} = \bar{\nabla}_{\perp}^{-2}\hat{\tilde{\omega}}. \tag{D.75}$$

The normalized quantities are defined in Eqs. D.10-D.14, with some modifications: the pressure is normalized by the maximum pressure value in the equilibrium profile,

$$\hat{\tilde{p}}_e = \frac{\tilde{p}_e}{\max\{p_{e,0}\}}. \tag{D.76}$$

The vorticity, not defined in Eqs. D.10-D.14, is normalized through

$$\hat{\tilde{\omega}} = \bar{\omega}\tau. \tag{D.77}$$

where the hat ($\hat{}$, circumflex) is used here to indicate normalization, since the bar already distinguishes $\bar{\omega}$ from ω.

The system of equations presented here have been linearized; extension to the non-linear system can be readily achieved using the `BOUT++` framework, but is nonetheless a complex endeavor and is left to future work.

D.3.3 Boundary Conditions

Since we are ultimately motivated to study a toroidal geometry, it is appropriate to apply periodic boundary conditions in the two dimensions within the flux surface, identifying the $\mathbf{e}^y$ direction with the poloidal direction, $\mathbf{e}^\theta$, and $\mathbf{e}^z$ with the toroidal direction, $\mathbf{e}^\phi$. If the spatial periods are L_y and $L_z = L_\parallel$, then the periodic boundary conditions are expressed as

$$\begin{aligned} u(x, y + L_y, z) &= u(x, y, z) \\ u\left(x, y, z + L_\parallel\right) &= u(x, y, z). \end{aligned} \tag{D.78}$$

The boundary conditions in $\mathbf{e}^x$ direction cannot be periodic since the shear is a secular function of x [65, p. 8.4]. Dirichlet conditions are used, such that the perturbations are zeroed out at the boundaries,

$$u(0, y, z) = u(L_x, y, z) = 0, \tag{D.79}$$

where L_x is the size of the domain in the x dimension.

First, let us re-express these conditions in the normalized Cartesian coordinate system, $\{\bar{x}, \bar{y}, \bar{z}\} = \{x/\rho_s, y/\rho_s, k_\parallel z = 2\pi z/L_\parallel\}$:

$$\begin{aligned} &u(0, \bar{y}, \bar{z}) = u(\bar{L}_x, \bar{y}, \bar{z}) = 0 \\ &u(\bar{x}, \bar{y} + \bar{L}_y, \bar{z}) = u(\bar{x}, \bar{y}, \bar{z}) \\ &u(\bar{x}, \bar{y}, \bar{z} + \bar{L}_\parallel) = u(\bar{x}, \bar{y}, \bar{z} + 2\pi) = u(\bar{x}, \bar{y}, \bar{z}) \end{aligned} \tag{D.80}$$

where $\bar{L}_x \equiv L_x/\rho_s$, $\bar{L}_y = L_y/\rho_s$, and $\bar{L}_\parallel = 2\pi L_\parallel/L_\parallel = 2\pi$.

Next, let us transform the boundary conditions to the field-aligned, normalized coordinate system $\{\psi, \xi, \zeta\}$. Making use of Eq. D.57, we find that

$$\begin{aligned} &u\left(0, \xi, \zeta\right) = u\left(\frac{\bar{L}_x}{\bar{B}_0}, \xi, \zeta\right) = u(\bar{L}_x, \xi, \zeta) = 0 \\ &u\left(\psi, \xi, \zeta + \bar{L}_y\right) = u(\psi, \xi, \zeta) \\ &u\left(\psi, \xi + \bar{L}_\parallel, \zeta + \sigma_\theta \frac{\bar{s}\psi \bar{L}_\parallel}{2\pi \bar{B}_0}\right) = u\left(\psi, \xi + 2\pi, \zeta + \sigma_\theta \bar{s}\psi\right) = u(\psi, \xi, \zeta). \end{aligned} \tag{D.81}$$

The form of the boundary conditions on $\hat{x}$ and $\hat{y}$ are preserved precisely in the transformation as boundary conditions for ψ and ζ. However, the boundary condition on $\hat{z}$ does not appear exclusively as a constraint on the boundary values in ξ. Instead, due to the magnetic shear, there is an additional shift in ζ,

$$\Delta\zeta = \sigma_\theta \frac{\bar{s}\psi \bar{L}_\parallel}{2\pi \bar{B}_0} = \sigma_\theta \bar{s}\psi \tag{D.82}$$

($\bar{L}_\parallel = 2\pi$ and $\bar{B}_0 = 1$). As a matter of practicality, it is convenient to express this shift in terms of unnormalized spatial values, which are more readily available as input to a simulation:

$$\Delta\zeta = \sigma_\theta \bar{s}\bar{\psi} = \sigma_\theta \frac{2\pi L_\parallel / L_\parallel}{L_s/\rho_s}\bar{B}_0\bar{x} = \sigma_\theta \frac{2\pi\rho_s}{L_s}\frac{x}{\rho_s} = \sigma_\theta 2\pi\frac{x}{L_s} = \sigma_\theta s k_\parallel x, \tag{D.83}$$

recalling that $s \equiv L_\parallel/L_s$, and $\bar{s} = sk_\parallel\rho_s$.

D.3.4 Differential Operators

The field-aligning transformation results in modifications to the differential operators from their Cartesian versions. These modifications are well-known and defined by the metric tensor components, and are described in the BOUT++ literature (e.g. [140, 98]). However, we repeat several here for completeness. Of fundamental interest to the drift-wave model employed here (Bruce Scott's "DALF3" model [65, Chap. 8]) are the parallel gradient and perpendicular Laplacian operations. The first of these is found in a straight forward fashion:

$$\begin{aligned}\bar{\nabla}_\parallel u \equiv \frac{\bar{\mathbf{B}}}{|\bar{\mathbf{B}}|}\cdot\bar{\nabla}u = \frac{\mathbf{e}_\xi}{|\mathbf{e}_\xi|}\cdot\left(\mathbf{e}^\psi\frac{\partial}{\partial\psi} + \mathbf{e}^\xi\frac{\partial}{\partial\xi} + \mathbf{e}^\zeta\frac{\partial}{\partial\zeta}\right)u = \frac{1}{|\mathbf{e}_\xi|}\frac{\partial}{\partial\xi}u \\ = \frac{1}{|\mathcal{J}\mathbf{B}|}\frac{\partial}{\partial\xi}u = \frac{1}{\left[1+\left(\frac{\bar{s}\bar{\psi}}{2\pi\bar{B}_0}\right)^2\right]^{1/2}}\frac{\partial}{\partial\xi}u\end{aligned} \tag{D.84}$$

where u is an arbitrary scalar field.

In fact, in the present circumstance, it is the inverse of the perpendicular Laplacian operation that is of interest. This is because the perpendicular Laplacian appears in the evolution equation for the electrostatic potential operating on $\bar{\Phi}$ before it is evolved (*i.e.* the equation specifies the evolution of the vorticity, $\bar{\omega} \approx \nabla_\perp^2\bar{\Phi}$, when it is the electrostatic potential,$\bar{\Phi}$, which appears everywhere else in the model). BOUT++ provides a fast solver for the two-dimensional partial differential equation problem presented by finding the inverse perpendicular Laplacian, using a Fourier expansion in the ζ dimension and finite differencing in the ψ direction.

D.3.5 Summary

In the above, we transformed the Cartesian coordinate system from the slab model in two steps, first normalizing the spatial and field quantities, and then aligning the coordinate system with the field direction. This was done to exploit the property of many plasma fluid models that quantities vary more slowly along field lines than across them, so that computational resources may be used more efficiently if fewer grid nodes are placed along field lines. The penalty for this was a more unwieldy apparatus for handling spatial coordinates and derivatives.

D.4 Early Results

D.4.1 Setup of Simulations

The following results pertain to the case with a flat temperature profile, $T_e = T_i = 50$ eV, an exponential pressure profile with maximum value of 1.5 kPa and a pressure gradient length scale, $L_p = |\nabla p_{e,0}/p_{e,0}|^{-1} = 2$ mm. The domain sizes, in SI Cartesian coordinates, are $L_x = 0.0196$ m, $L_y = 0.126$ m, and $L_z = 8.48$ m. These sizes correspond to half a parallel wavelength (*i.e.* approximately a connection length) long in ξ, three perpendicular wavelengths high in ζ (making $k_\perp = 1.5$ cm^{-1}), and two pressure gradient length scales deep in ψ.

The grid resolution is $N_\psi = 132$, $N_\zeta = 64$, and $N_\xi = 129$. This includes two "guard cells" – grid points used at the boundaries of the domain in, ξ and ψ to facilitate the calculation of differentials on the boundaries of separate parallel subdomains. Moreover, in `BOUT++`, the ζ direction treated through Fourier decomposition, and the number of grid points in this dimension must satisfy $2^n + 1$, with n an integer, in order to make use of fast Fourier transform algorithms. In these simulations, $n = 7$ is selected, making $N_\zeta = 129$.

Periodic boundary conditions are maintained in $\bar{\zeta}$ and $\bar{\xi}$ in the manner described above.

The domain and grid sizes are selected in order to verify the correct physical

behavior of the drift wave model without overtaxing the limited processing capacity afforded in the PSFC computing facility. Larger domain sizes and finer grid resolution is envisaged for "production" simulations, to be carried out on computing facilities elsewhere.

Numerical integration in time is carried out using the `SUNDIALS` solver package, which applies implicit time-integration methods using iterative, preconditioned Krylov subspace methods to solve linear systems that arise in the implicit time stepping. It should be mentioned that `BOUT++` makes available a number of other time-integration solvers, both explicit and implicit and with a high degree of customization. The timestep used in the simulations below is 200 ns.

Computation was performed on the MIT PSFC parallel AMD Opteron/Infiniband cluster, `Loki`; each computation made use of a minimum of 16 processors on two nodes. The domain was split in two in ψ, with half of the processors going to the left side and the other half to the right.

D.4.2 Discussion of Initial Results

The results of initial simulations in the `BOUT++` are shown below. Only the electrostatic case is investigated here, with $\tilde{A}_{\|} \to 0$, so that the model only evolves three quantities, $\left\{\tilde{p}_e, \tilde{\Phi}, \tilde{u}_{\|}\right\}$. Moreover, the equilibrium background field is ignored (*i.e.* the simulation is carried out in the plasma frame, and $\mathbf{E} \times \mathbf{B}$ shear is not included in the model, a major shortcoming).

Figure D-1 shows several x, y cross sections (with spatial quantities transformed back to physical units) for a slab case roughly approximating the temperature and magnetic shear at the outer midplane under plasma conditions in which a QCM might appear. The initial periodic perturbation spreads radially, as expected from the presence of the perpendicular Laplacian appearing in the quasineutrality equation, until it bounces off of the boundaries. Meanwhile, the overall propagation conforms with drifting motion with the electron diamagnetic drift velocity. This is shown clearly in Figure D-2, which illustrates the evolution of a single slice of the domain across the Cartesian slab coordinate, y, holding x and z fixed in the middle of the simulation

space. The black dashed line corresponds to a point propagating in y at the speed and in the direction of electron diamagnetic drift, $\omega = k_\perp v_*$ (here, $\omega \approx 2\pi 200$ kHz); this tracks well with the motion of the peaks and troughs of the disturbance.

The mode is also seen to grow in these two figures. Even though there is magnetic shear, it is too slight to rip apart the disturbance, and so the mode grows linearly through the mechanism introduced by resistivity and parallel currents, as discussed in Section 3.2.2. Similarly, parallel viscosity is also too small to damp the mode.

Indeed, the shear must be increased far beyond the level seen at the outer midplane before its effect is observed. This point is made in Figure D-3, which shows the results of artificially inflating the shear parameter to $s = L_\parallel / L_s = 10^4$, three orders of magnitude larger than the experimental value at the outer midplane. Here, the initial disturbance does appear to shear apart as the simulation proceeds; the effect is small for smaller orders of s, while the mode is efficiently de-phased and broken up for s of larger order.

The simulations speak to the idea that the effect of magnetic shear is much larger at the X-point, rather than the outer midplane, where the simulation parameters apply. A much larger and more complex simulation domains (and computing power) is needed to resolve this effect. Meanwhile, in the local environment of the outer midplane, it is shear in the $\mathbf{E}\times\mathbf{B}$ and diamagnetic flows, v_E and v_*, that is expected to be more important; indeed, measurements with the mirror Langmuir probe [32] appear to show the QCM localized to the layer where the quantity, $v_E + v_*$, is stationary in the flux coordinate, (in the relevant figures in [32], the flux label is the minor radius, r, relative to the LCFS at the outer midplane).

Clearly, a great deal of work remains to examine the antenna-plasma response by this approach. The antenna current and vacuum regions must be incorporated into the model, and inductive effects retained. Moreover, we have seen that shear in $\mathbf{E} \times \mathbf{B}$ flow is a critical feature of the model that must be included, and that an X-point (or two X-points to preserve periodic boundary conditions, at the expense of not capturing the equilibria used in the initial Shoelace experiments) must be included if the effect of magnetic shear is to be appropriately captured in the model. All of this

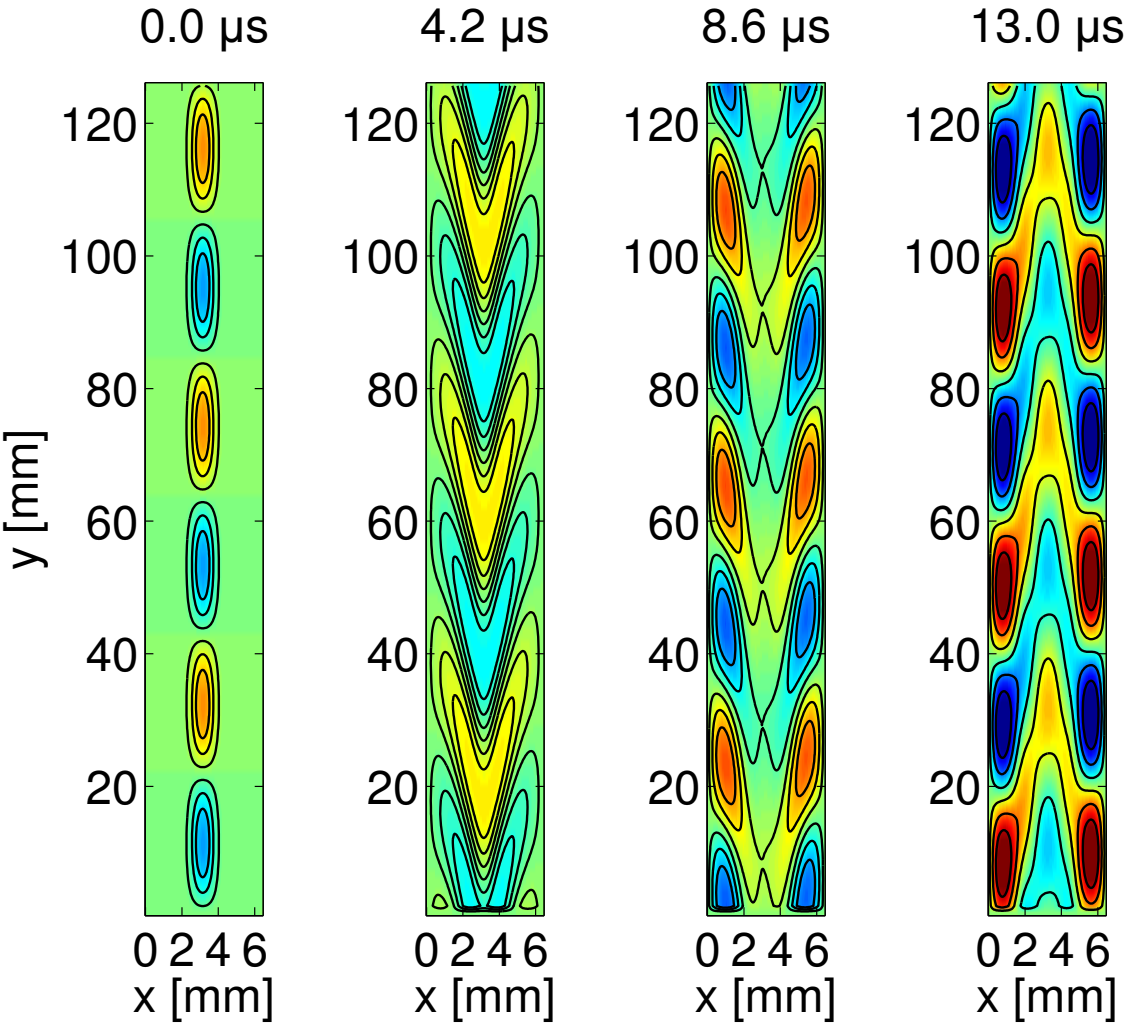

Figure D-1: Four time frames from the three-field electrostatic model, $\{p_e, \Phi, u_\parallel\}$, with $s = 10$, $T_e = 50$ eV, $L_p = 2$ mm, and a timestep, $\Delta t = 200$ ns. The color axis here encodes the normalized pressure perturbation in the range, $-0.015 \leq \tilde{p}_e/p_{e,0} \leq 0.015$.

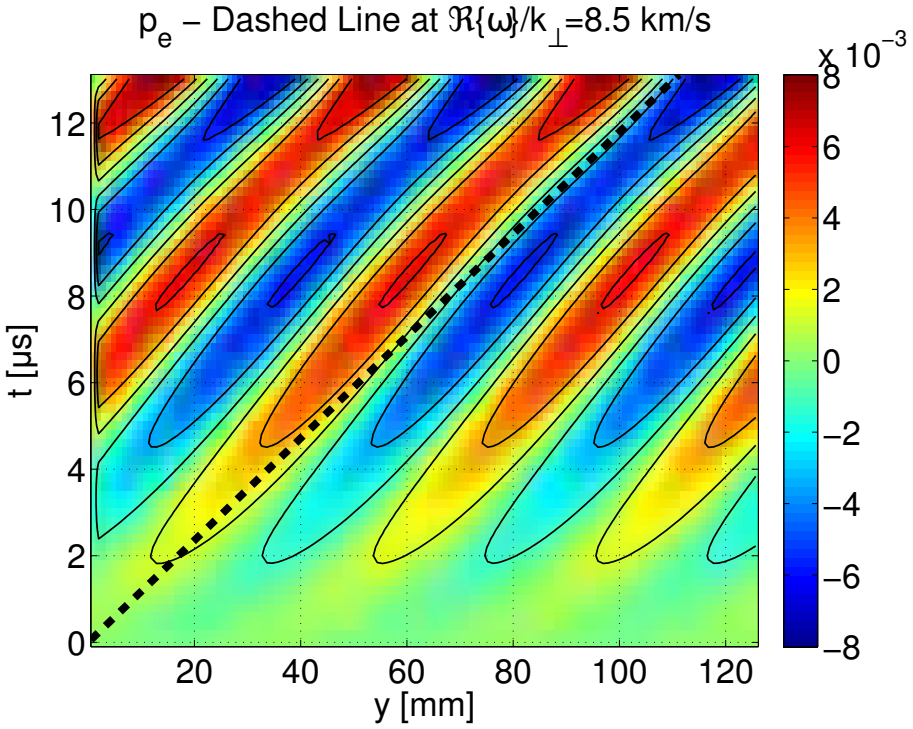

Figure D-2: Plot showing evolution of line slice across $\bar{y}$, holding $\bar{x}$ and $\bar{z}$ fixed in the middle of the domain, for the disturbance pictured in Figure D-1, illustrating propagation and growth of initial perturbation. Dashed line shows phase velocity expected by pure electrostatic resistively-unstable drift wave.

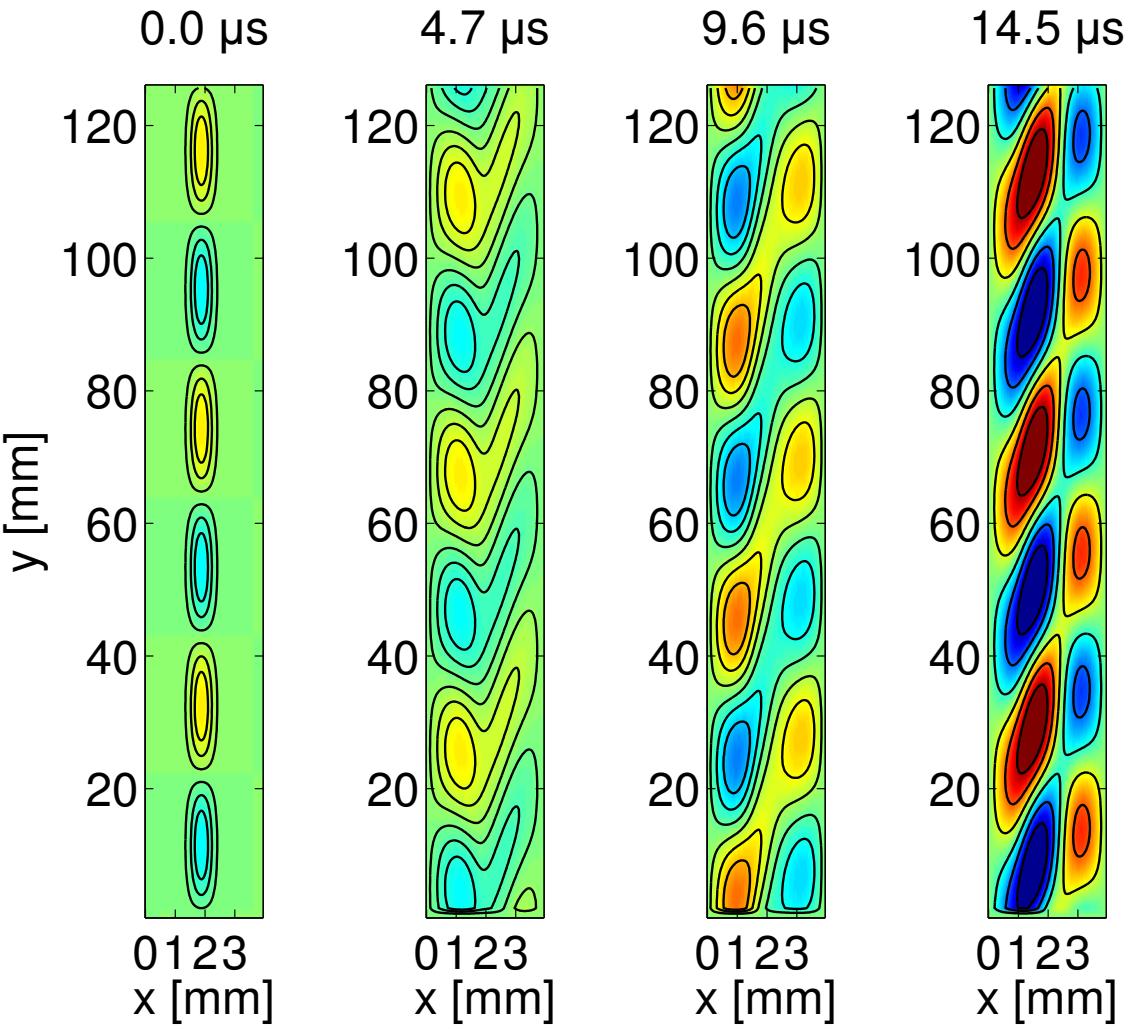

Figure D-3: Same problem as in Figure D-1, but now, with shear parameter, $s = L_\parallel/L_s = 10^4$, where $L_\parallel = 13$ m and $L_s = 0.0013$ m$\approx L_x/3$.

work is still limited to the slab model with no curvature, where curvature must be added if the drift wave and interchange dynamics are to compete and interact with one another. This initial work only demonstrates the utility of BOUT++ in solving numerically the plasma fluid models appropriate to the Shoelace antenna experiments, as well as the challenges associated with this endeavor.

Appendix E

Timebase Error Analysis and Calibration

E.1 Timebase Error Analysis

If the timebases of fluctuation signals, as well as the antenna waveform, are not aligned, errors are produced in the analysis of these signals. These errors can result in falsely identifying resonances in the frequency response, or interfere with the characterization of actual resonances. The following discussion demonstrates this for two kinds of timebase discrepancies: an offset in the start (trigger) time, and a difference between the expected and actual sampling times.

To begin, write a signal, $y(t)$, using the phaser formalism,

$$y(t) = \Re\{\tilde{Y}e^{j\omega t}\}. \tag{E.1}$$

Next, examine a discrete timebase used to sample $y(t)$,

$$t_n = n\tau_s = \frac{n}{f_s}, \tag{E.2}$$

where τ_s is the sampling time and f_s is the sampling frequency. Assume there is an error in the sampling frequency, such that the actual rate, f_s, departs from the

nominal rate, f_s^*, by a constant amount, δf

$$f_s = f_s^* - \delta f. \tag{E.3}$$

Also, define a small temporal offset error, t_0, so that, when the nominal (incorrect) timebase registers as 0, the actual time is t_0.

Then the discrete timebase may be rewritten as

$$t_n = \frac{n}{f_s} = \frac{n^* - \Delta n}{f_s^* - \delta f} \sim \frac{n^* - \Delta n}{f_s^*}(1+\delta) = (t_n^* - t_0)(1+\delta) \sim t_n^*(1+\delta) - t_0 \tag{E.4}$$

when $\delta \equiv \delta_f / f_s \ll 1$, with $t_0 = \Delta n / f_s^*$. The actual continuous time is expressed in terms of the nominal continuous time, t^*, and error parameters as $t = t^*(1+\delta) - t_0$.

The phaser representation of $y(t)$ can also be recast in terms of the nominal timebase and error parameters as

$$y(t) = \Re\left\{\tilde{Y} e^{j\omega[t^*(1+\delta)-t_0]}\right\} = \Re\left\{\tilde{Y}_{eff} e^{j\omega t^*}\right\}, \tag{E.5}$$

where

$$\tilde{Y}_{eff} \equiv \tilde{Y} e^{j\delta\omega t^*} e^{-j\omega t_0} \tag{E.6}$$

is the effective phaser that would appear if the incorrect, nominal timebase, t^*, is used in calculating Y from y (*i.e.* y_n is associated with the time, t_n^*, instead of t_n).

The effect of errors in the trigger time and sampling rate is that the phaser for the sampled signal, and so also the transfer function, H_{eff}, calculated using the incorrect timebase is multiplied by the complex exponential, $e^{j\delta\omega t^*} e^{-j\omega t_0}$. The amplitude is unaffected, but the phase has both an absolute offset and an offset linearly growing in time.

If $\tilde{Y}$ can be represented by a single simple pole (neglecting the complex conjugate pair due to the largeness of ω_0),

$$\tilde{Y} = \frac{a}{\gamma + j(\omega - \omega_0)}, \tag{E.7}$$

which may also be written as

$$\tilde{Y} = \frac{a}{2\gamma}\left(1 + e^{j\theta}\right), \tag{E.8}$$

where

$$\theta \equiv -2\angle\{\gamma + j(\omega - \omega_0)\}, \tag{E.9}$$

and a may be complex. Then

$$\begin{aligned}
\tilde{Y}_{eff} &= \frac{a}{\gamma + j(\omega - \omega_0)} e^{-j\omega(t_0 - \delta t^*)} \\
&= \frac{a}{2\gamma}\left(1 + e^{j\theta}\right) e^{-j\omega(t_0 - \delta t^*)} \\
&= \left[-\frac{a}{2\gamma} + \frac{a}{2\gamma}\left(1 + e^{\theta_a}\right)\right] + \left[-\frac{a}{2\gamma} + \frac{a}{2\gamma}\left(1 + e^{\theta_b}\right)\right]
\end{aligned} \tag{E.10}$$

where

$$\begin{aligned}
\theta_a &\equiv -\omega(t_0 - \delta t^*) \\
\theta_b &\equiv \theta + \theta_a = -2\angle\{\gamma + j(\omega - \omega_0)\} - \omega(t_0 - \delta t^*).
\end{aligned} \tag{E.11}$$

We may neglect the effect of the timebase error if[1] $|\theta_a| = |\omega(t_0 - \delta t^*)| \ll \pi \,\forall\, \omega$. If this is not the case, then the effect is equivalent to changing $\tilde{Y}_{eff}$ such that it appears to be comprised of the sum of two shifted, non-ideal, pole-like terms, with equivalent parameters,

[1] In general, the experiment is designed to vary ω sufficiently so that θ fills the range, $-\pi \lesssim \theta \lesssim \pi$, in order to reveal the pole.

$$\theta_a \equiv -\omega(t_0 - \delta t^*) = -2\angle\{\gamma_a + j(\omega - \omega_a)\}$$
$$\theta_b \equiv -2\angle\{\gamma + j(\omega - \omega_0)\} - \omega(t_0 - \delta t^*) = -2\tan^{-1}\left(\frac{\omega - \omega_0}{\gamma}\right) - \omega(t_0 - \delta t^*)$$
$$= -2\angle\{\gamma_b + j(\omega - \omega_b)\}. \tag{E.12}$$

Strictly speaking, these poles could not be realized unless the equivalent parameters, γ_i and ω_i, were dependent on the frequency. Nonetheless, the locus of points in the complex plane would still trace a circular pattern. This locus would circulate in the counter-clockwise sense with increasing frequency, which would erroneously indicate a negative damping rate (corresponding to a fictitious growing mode), when $(t_0 - \delta t^*) < 0$, (*i.e.* $t_0 < 0$ and/or $\delta > 0$).

If $|\delta\omega t^*| \gtrsim \pi$, then the drift between the actual and nominal sampling rates is appreciable in the θ_a term. Because t^* increments over the course of the shot, this error term tends to cause $\tilde{Y}_{eff}$ to rotate over the course of the shot, from one frequency scan to the next.

Figure E-1 illustrates this behavior when there is only an error in the sampling time. Here, synthetic data is run through a model pole. The data for the input and output functions are resampled on different timebases with the indicated values of δ, but the timebases are aligned at $t = 0$ (*i.e.* $t_0 = 0$). A single chirping frequency scan from 80 to 120 kHz over $t^*_{max} = 0.05$ s is used as input, while the output pole is assumed to have a resonant frequency of $f_0 = 100$ kHz, with a damping rate, $\gamma/\omega_0 = 5\%$. For $\delta\omega_0 t^*_{max} \gtrsim \pi$, the effective transfer function appears to rotate in the direction expected for a negative growth rate.

If $\omega(t_0 - \delta t^*) \lesssim 1/\gamma$, then the phase distortion competes with the phase angle of the actual pole transfer function near resonance in θ_b. This provides the scale for $t_0 < 0$ over which the effective pole appears to rotate in the wrong direction.

Figure E-2 shows this situation. The setup is the same as in Figure E-1, but now, $\delta = 0$, while t_0 is scanned from 0 to $-1/\gamma$. When $t_0 \sim -1/\gamma$, the effective transfer

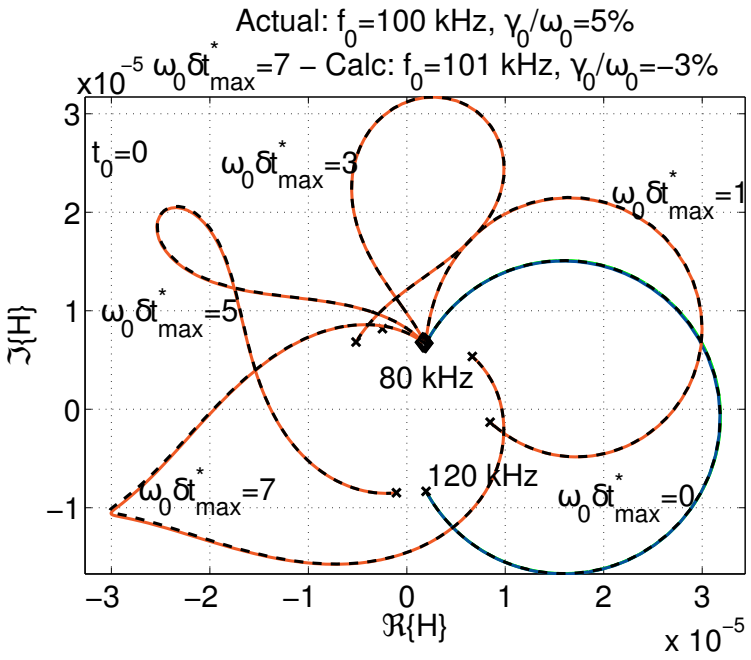

Figure E-1: Effect of sampling frequency offset on effective transfer function for $\delta\omega_0 t^*_{max} = 0$, 1, 3, 5, and 7. The lower endpoint of the frequency scan is indicated by a diamond, while the upper endpoint is indicated by an $\times$. At $\delta\omega_0 t^*_{max} = 5$ and 7, fitting a simple pole to the effective transfer function yields negative damping rates on the order of the true damping rate.

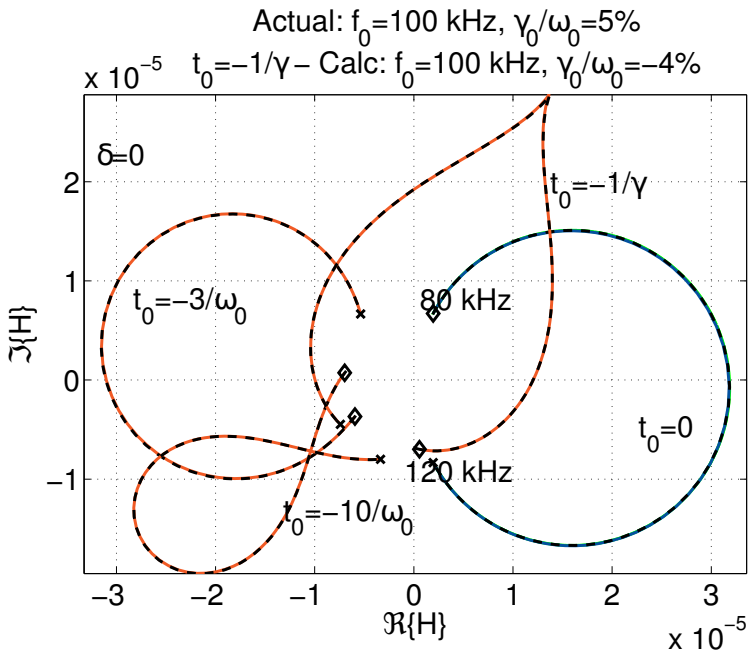

Figure E-2: Effect of timebase offset on effective transfer function for $t_0 = 0$, $-1/\omega_0$, $-10/\omega_0$, and $-1/\gamma$. The lower endpoint of the frequency scan is indicated by a diamond, while the upper endpoint is indicated by an $\times$. At $t_0 = -1/\gamma$, the effective transfer function seems to rotate in the opposite sense as a damped pole response.

function appears to be described by a distorted pole with a negative damping rate.

E.2 Timebase Calibration

The system employed to align and synchronize timebases of fluctuation diagnostics on Alcator C-Mod is described in [136]. The approach is to broadcast an optical signal throughout the C-Mod experimental cell on which the global time is encoded. This signal is then transduced to an analog voltage and digitized on one channel in every set of one or more digitizers which share a clock. The encoded global time is then compared with the timebase of the digitizer set, and a linear fit retrieves the trigger offset and sampling frequency error. This approach corrects timebase errors in an average sense. While it does not address skipped samples, variations between channels, and other ills, it provides sub-microsecond alignment of the timebases, which is adequate for the 100 kHz signals of interest over the $\sim 1-4$ s data collection times.

Unfortunately, the optical signal transducer was not operational on the PCI diag-

nostic for a large span of discharges, including all of those presented here for studying the Shoelace antenna. This meant that the PCI timebase error could not be characterized on those particular discharges. Calculating relative phase differences between PCI chords cancels the timebase phase error, leaving wave number estimates largely immune to the timebase errors. But without accounting for the error, it would not be possible to accurately characterize resonances using the PCI frequency response. This is because the transfer function uses the antenna current waveform, digitized on a separate digitizer with a separate, misaligned clock.

However, the trigger offset and sampling frequency errors are, in fact, fairly constant, usually around a $\sim$20 μs offset for the trigger time, and 6-7 fs for the sampling time. This is shown in Figure E-3, which plots histograms of the trigger and sampling time errors for the 196 discharges for which timebase error information was available prior to the end of the 2012 experimental campaign. The mean trigger offset error in this range was a 20.1 μs delay from the nominal trigger time, -0.3 s, while the mean sampling time error was 6.25 fs, added on to the nominal sampling time of 200 ns.

In a set of 21 tests conducted after the end of the Shoelace experimental campaign, the mean trigger offset error for the PCI digitizers was 17.3 μs$\pm$0.11 μs, while the mean sampling time error was 6.37 ± 0.016 fs, where the number after the $\pm$ symbol is the standard deviation.

The timebase error had been characterized over a much wider range of shots for the Shoelace antenna. Figure E-4 shows histograms of the timebase errors for each of the three Mirnov coil (fast magnetics) digitizers from 2507 discharges over 100 run days. For these digitizers, the nominal trigger time was -0.05 s, with a nominal sampling time of 400 ns and no skipped samples. Figure E-5 plots the average timebase error parameters over each of these 100 run days over the duration of the data collection period. The data show that, while there is systemic variation in the timebase error parameters which is larger than the variation over a single run day, this variability is still much smaller (by a factor on the order of 10) than the magnitude of the error. As such, the trigger and timebase errors can be removed by calibration for each digitizer clock, resulting in a trigger time accurate to the $\sim$ 1 μs level, and to better than

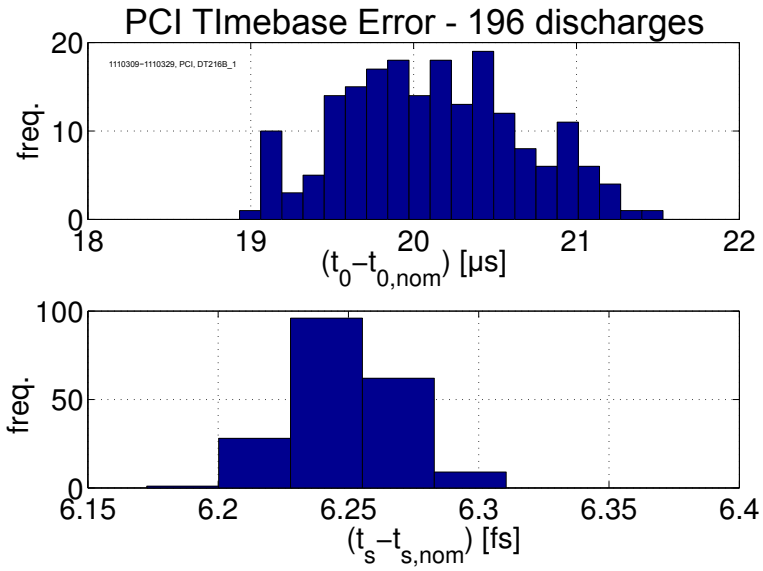

Figure E-3: Histograms of (top) trigger offset error, $t_{0,error}$ = (actual time data begins to store)−(number of skipped samples)*(actual sampling time)−(nominal trigger time), where the nominal trigger time is -0.3 s and 3.5×10^6 samples are skipped, and (bottom) error in sampling time relative to actual sampling time, $t_{s,actual} - t_{s,nominal}$ ($t_s = 1/f_s$, $t_{s,nom}$ = 200 ns) as characterized by database alignment method, where $t_s = 1/f_s$. The data are from the 196 discharges during which timebase error data was available prior to the end of the 2012 experimental campaign.

1 fs accuracy for the sampling time. These levels are of adequate accuracy to align the timebases of different fluctuation diagnostics for the analysis of signals around 100 kHz.

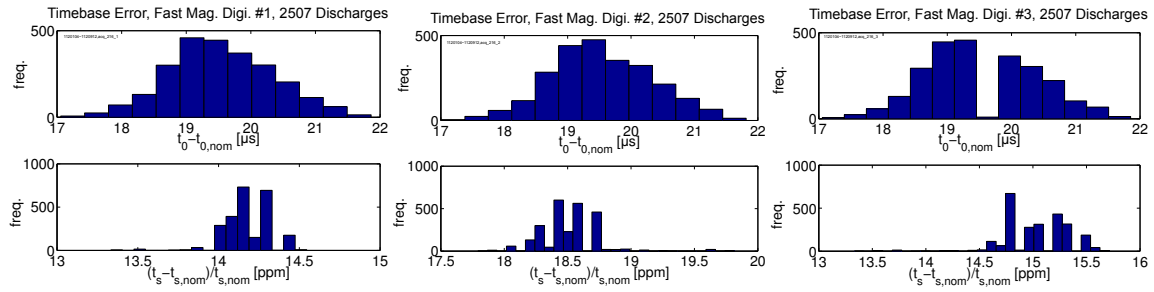

(a) (b) (c)

Figure E-4: Histograms of timebase errors, as in Figure E-3, but for each of the three Mirnov coil (fast magnetics) digitizers. The sampling time error is reported as the fractional error of the nominal start time in parts per million; with the 400 ns nominal sampling time, a 15 ppm error corresponds to a 6 fs absolute error. Similar trigger offset and sampling time errors appear as for PCI, with a similar spread in the error. The data are gathered from 2507 shots over 100 run days between 1120104 and 1120912.

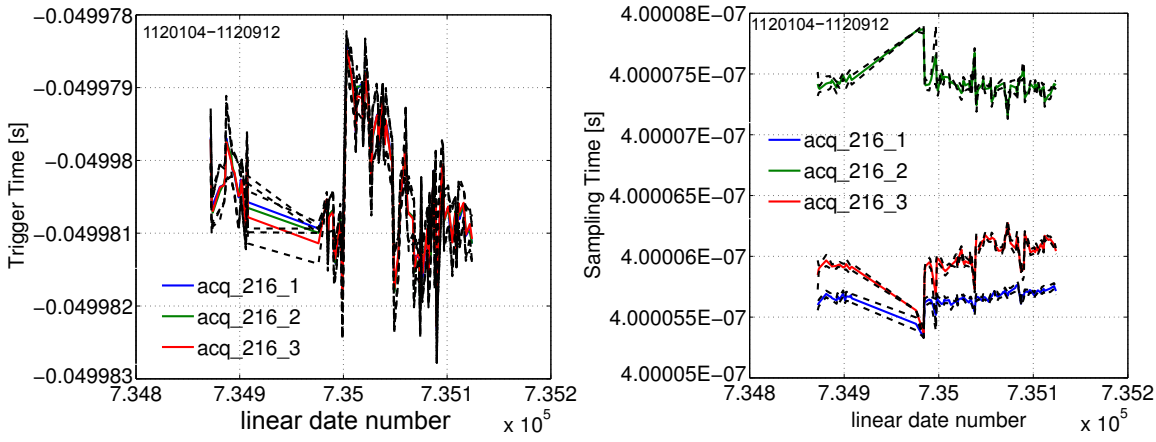

(a) (b)

Figure E-5: Plots of (a) trigger and (b) sampling time errors in each of the three Mirnov coil (fast magnetics) digitizers gathered from the same data set as shown in E-4 (2507 shots over 100 run days between 1120104 and 1120912). Each data point on the solid lines is the average error over the entire run day, while the dashed lines represent the standard deviation from this mean determined from all of the data on the available run day. The systematic shift in the timebase errors with time is larger than the random variation over a run day, but is still small relative to the mean error.

Appendix F

Are the Peaks in the Transfer Function Genuine?

The analysis below addresses the question of whether the peaks observed in the transfer function spectrum are genuine, or an artifact of performing the signal processing operation in the presence of a strong background mode.

Figure 5-14a illustrates that the calculated resonant frequency of the pole in the driven response closely tracks the frequency of the intrinsic QCM (as determined from the time-evolving peak in the PCI spectrogram). While this result is not unreasonable, it underscores the need for caution in assessing whether the signal processing techniques employed in calculating the transfer function do, in fact, isolate the coherent response driven by the antenna from the spectral peak in the background. One way to test this is to apply the signal processing operations to a fictitious data set where the current waveform (the "input") does not correspond to the actual experiment. This is accomplished below in two ways: (1) by time-shifting the true current waveform so that it is advanced by 50 ms, and (2) by substituting the current waveform from a different discharge. The tests are applied to both the transfer function and the magnitude squared coherence calculations.

Figure F-1 shows the magnitude squared coherence, evaluated at the antenna frequency, between a PCI signal and the antenna current. The blue line shows the result when the genuine, measured antenna current waveform is used, while the red

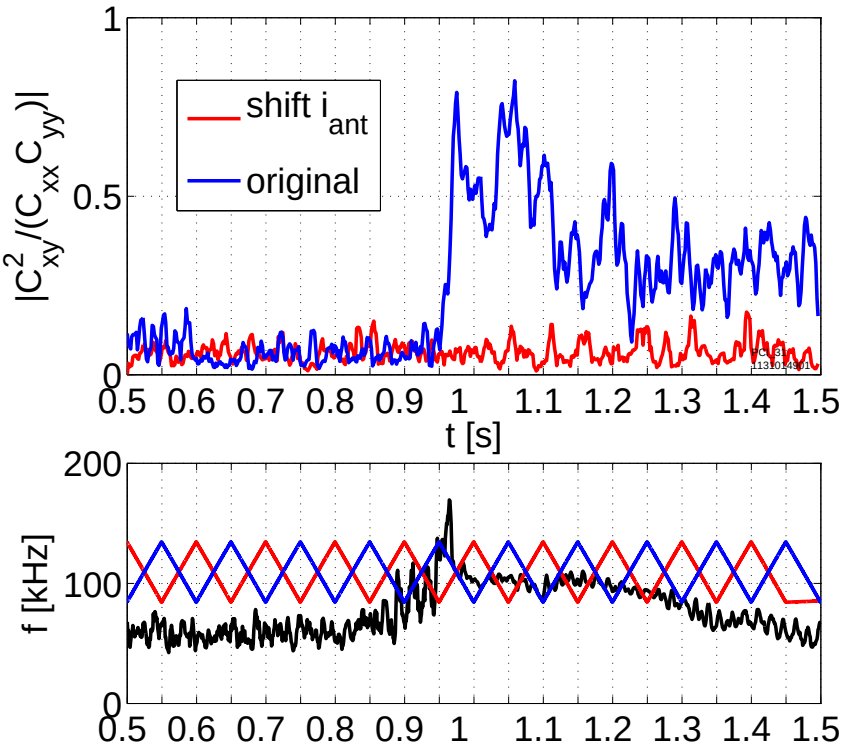

Figure F-1: Comparison of magnitude squared coherence at the antenna frequency between antenna current and PCI signal computed using actual data (blue line), and computed after artificially advancing the current waveform by 50 ms while leaving the PCI fluctuation signal unchanged (red line). The genuine coherence is high during the EDA H-Mode, while the artificially-misaligned current waveform results in small coherence. The subplot shows the antenna current waveform frequency in the genuine and artificially time-shifted cases, together with the peak in the PCI spectrum (black line).

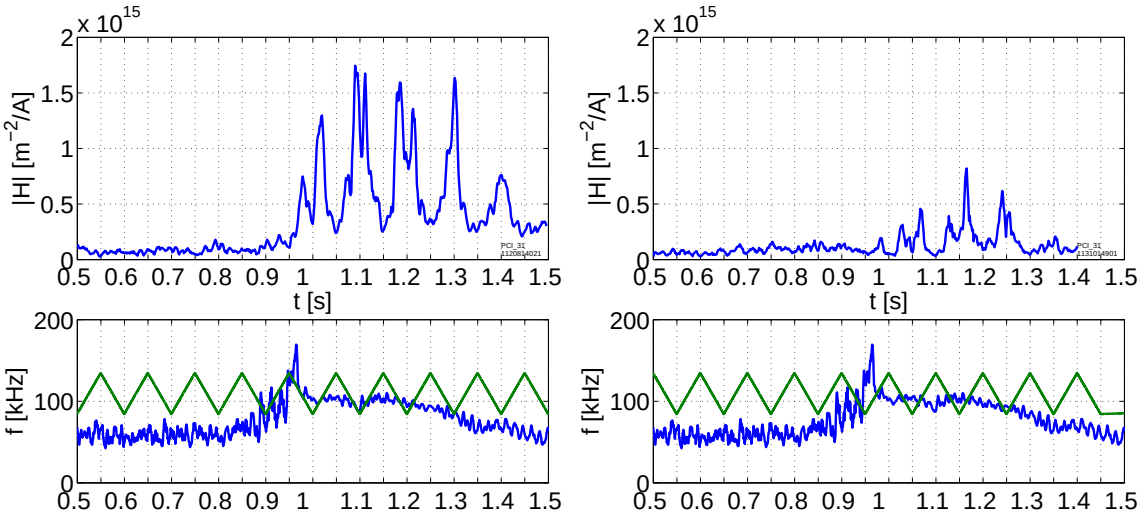

Figure F-2: Transfer function magnitude shown as time series data, calculated using (a) the genuine current waveform data, and (b) the current waveform which has been artificially advanced by 50 ms. The antenna frequency and peak frequency of the PCI spectrogram are also shown.

line shows the result of performing the computation after taking the same current waveform, but advancing it artificially by 50 ms, thereby inverting the direction of the frequency scan. The coherence in the artificial case is near the noise floor.

Figure F-2 applies the same test to the transfer function calculation, again evaluated at the antenna frequency. The artificial case does, in fact, produce erroneous peaks in the magnitude of the transfer function when the modified current waveform's frequency crosses through that of the intrinsic QCM, but they are smaller than the peaks in the genuine case by a factor $\gtrsim 3$.

Replacing the antenna current with a measured current waveform from an entirely different discharge, but retaining the same PCI fluctuation data, we arrive at a similar result, as shown in Figure F-3. Artificial peaks in the magnitude of the transfer function still appear when the (unrelated) current trace crosses the peak in the PCI spectrum, but they are again smaller than the genuine peaks seen in Figure F-2a by a factor $\gtrsim 3$.

It is also prudent to examine whether changing the number of samples used in the time bins in which the spectra are evaluated affects the results. This is done in

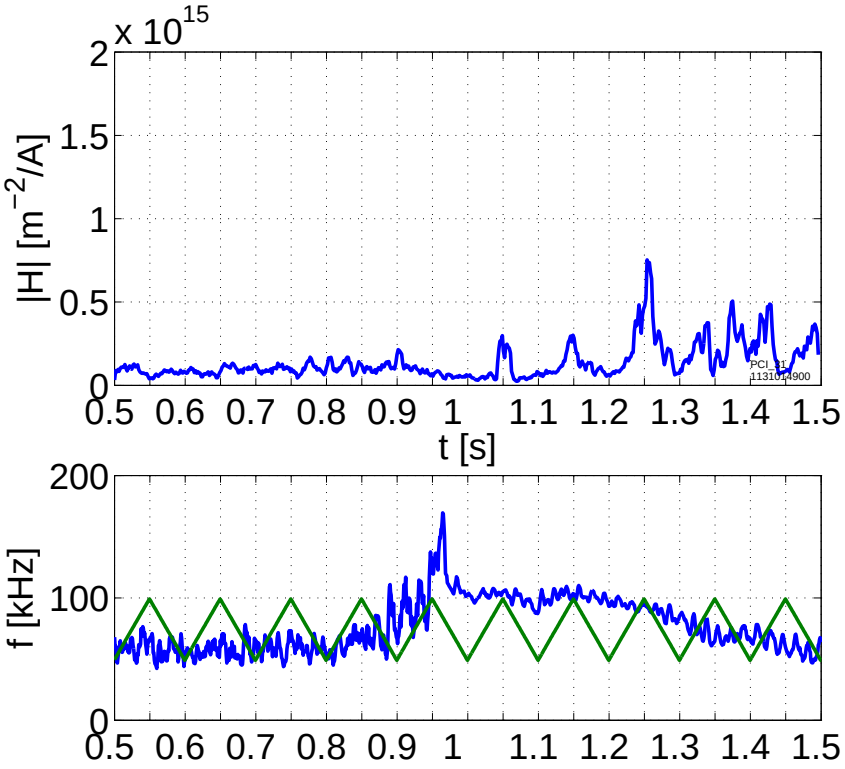

Figure F-3: Transfer function magnitude shown as a time series. Here, the transfer function has been recalculated using the same PCI fluctuation signal as from the previous analysis, but now combined with the antenna current waveform from a different discharge, altogether. Peaks still appear in the magnitude of the transfer function, even though the current data does not correspond to this shot, but they are again smaller than the genuine peaks in Figure F-2a.

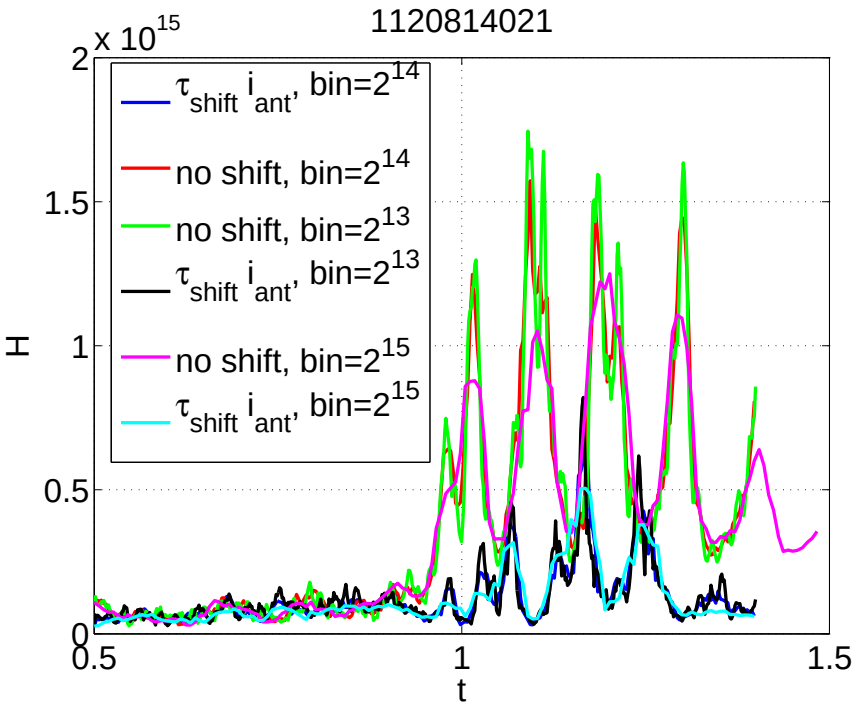

Figure F-4: Examining the effect of increasing the number of samples in the time bins used to estimate the transfer function. The calculation is performed using the same PCI fluctuation signal, and both the genuine and shifted-by-50-ms current waveforms. The number of points used in the bin size of the signal processing operation is scanned from 2^{13} points (3.3 ms) to 2^{14} points (6.6 ms) to 2^{15} points (13 ms). The scan does not change the qualitative results.

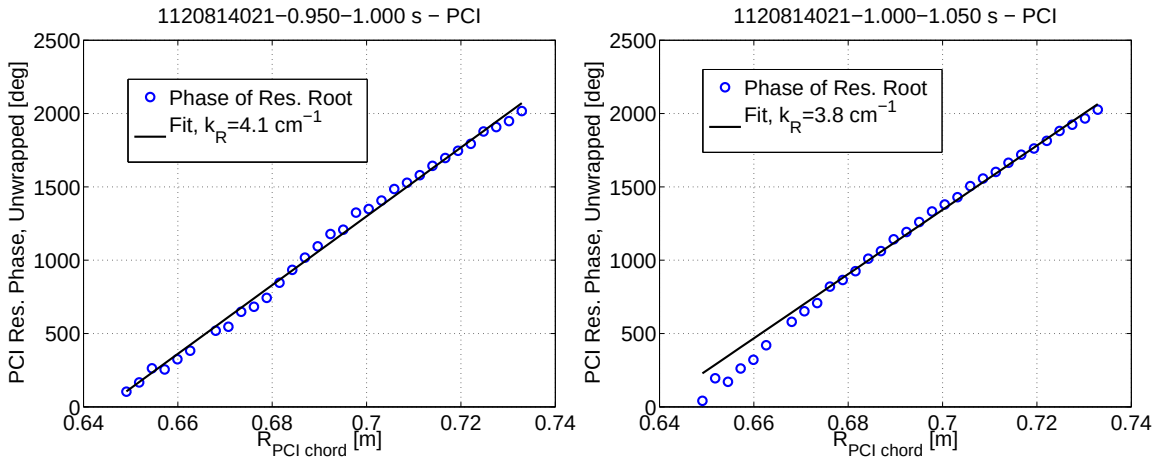

Figure F-5: Plot of unwrapped phase angle from residues of simple poles fit to the transfer function of a number of PCI chords using *genuine* data from the same discharge analyzed throughout this section. (a) corresponds to the time range from 0.95 to 1.0 ms (downward frequency sweep), while (b) uses the time range from 1.0 to 1.05 ms (upward frequency sweep). The estimated value of $k_R \approx 4$ cm^{-1} (measured at the lower intersection between the PCI chords and the LCFS) is the correct value to reproduce the antenna-imposed $k_\perp \approx 1.5$ cm^{-1} (at the outer midplane).

Figure F-4, which shows the transfer function using both the genuine data (blue line), and the current waveform artificially advanced by 50 ms. The transfer function is computed using three different bin sizes: 2^{13} samples (the standard size used in most of the analyses), 2^{14} samples, and 2^{15} samples. The scan in bin size does not change the results observed earlier in Figure F-2 – the effect of increasing the bin size is only to smooth the transfer function time series.

A simple pole may be fit to either set of peaks – genuine or artificial – using the procedure described in Section 5.5 according to Eq. 5.2. If the phase angles from the residues of these poles are used to fit a major radial wave number, k_R, the poles from the genuine data show a stationary (in time) value which is consistent with the perpendicular wave number, $k_\perp = 1.5$ cm^{-1}, imposed by the antenna winding, as seen in Figure F-5. Figure F-6 shows the result of unwrapping the phases from the fictitious poles found using the artificially-modified current waveform. There is still a phase progression that could be incorrectly interpreted as a major radial wave number, having the right order of magnitude, though missing the antenna wave

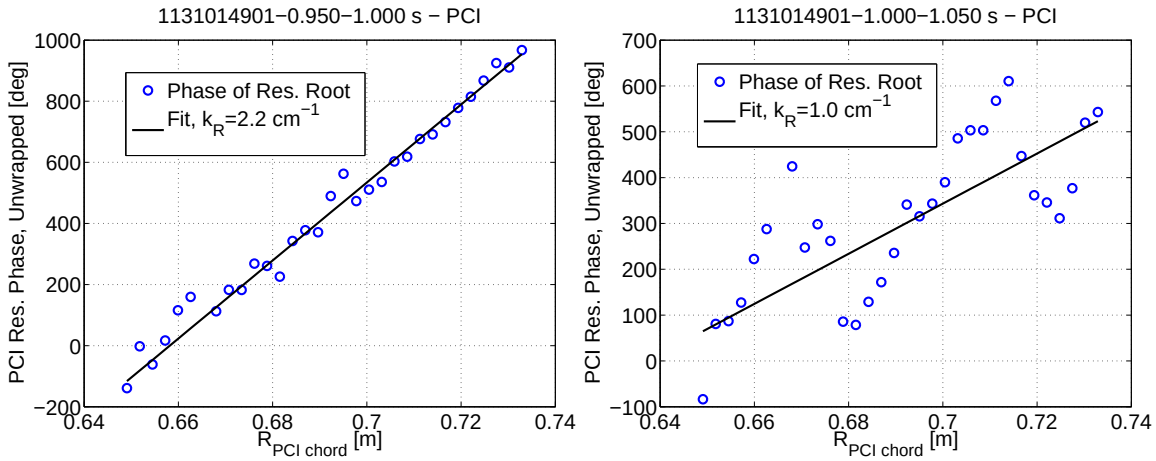

(a) (b)

Figure F-6: Plot of unwrapped phase angle from residues of simple poles fit to the transfer function using the same fluctuation data from the same set of PCI chords as in Figure F-5, but now, using the modified antenna current waveform that has been artificially shifted forward by 50 ms. (a) corresponds to the time range from 0.95 to 1.0 ms (now an upward frequency sweep), while (b) uses the time range from 1.0 to 1.05 ms (now a downward frequency sweep). The measured values of k_R have the same order of magnitude and direction as those found using the genuine data, but they are not consistent from one scan to the next, nor do they reproduce the antenna $k_\perp$.

number by a factor of two or more. But the phase progression of these artificially-generated residues is not stationary, and depends strongly upon whether the direction of the frequency sweep is increasing or decreasing, clearly indicating the poles as false positives. It should be remembered that the timebases of the modified current waveform and genuine fluctuation data cannot be aligned, and that this can have an effect on the transfer function (see Appendix E). However, the effects from timebase misalignment should not matter for the wave number calculation, since it is the *relative* phase difference between PCI chords that matters, and all chords suffer from the same potential timebase error and phase offset.

A better indication, still, of the significance of the observed peaks in the transfer function is found in the fact that resonances are still observed in reverse-field discharges for which there was no prominent QCM. A spectrogram of one such discharge is shown in Figure 5-10, while the peaks in the transfer function for this discharge are analyzed in Figures 5-11 and 5-13.

Appendix G

Images of Hardware

This appendix attempts to document the construction of several of the Shoelace antenna components.

Figure G-1: Sequence of winding the Shoelace antenna. The wire was first bent into shape on a separate, flat, full-size winding fixture mock-up, then unwound from this fixture and transferred to the real antenna. (Photo Credits: B. LaBombard, T. Golfinopoulos)

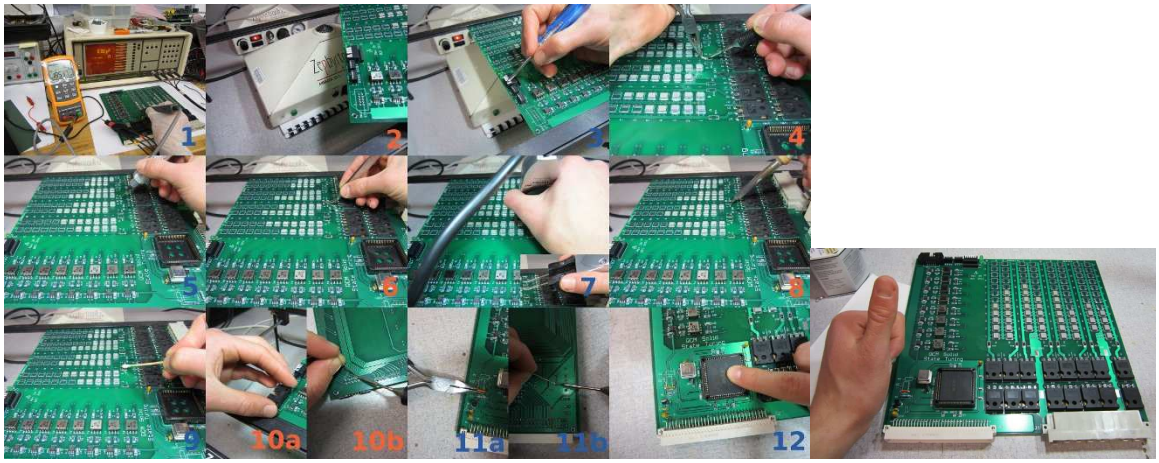

(a) (b)

Figure G-2: (a) Sequence of final assembly steps for capacitor boards: measuring capacitance of each capacitor board channel, in-board and disconnected from transistors, and then soldering in "zero-ohm resistor" shorts to connect channel to transistors. (b) Finished board.

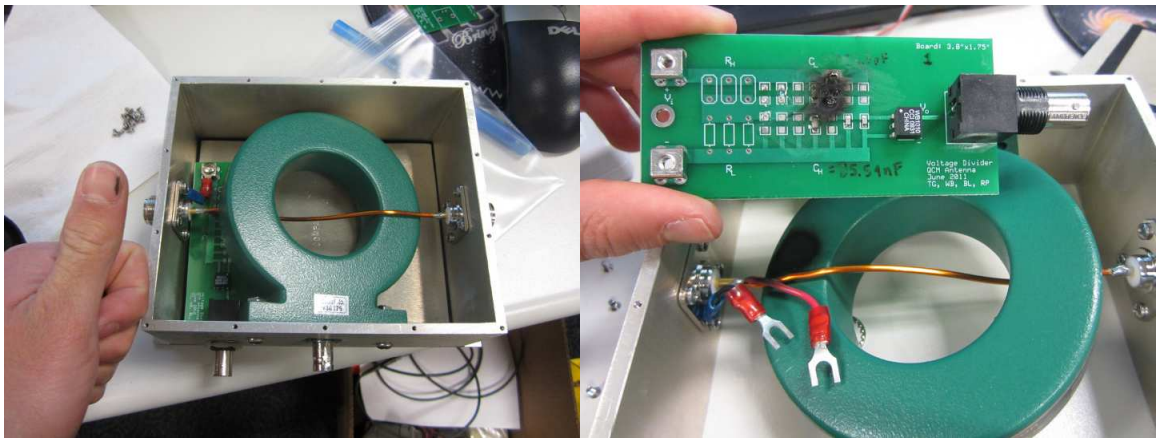

(a) (b)

Figure G-3: (a) Completed voltage and current probe box; (b) box with an early iteration of a capacitive voltage divider board which developed a fault resulting in the destruction of capacitors.

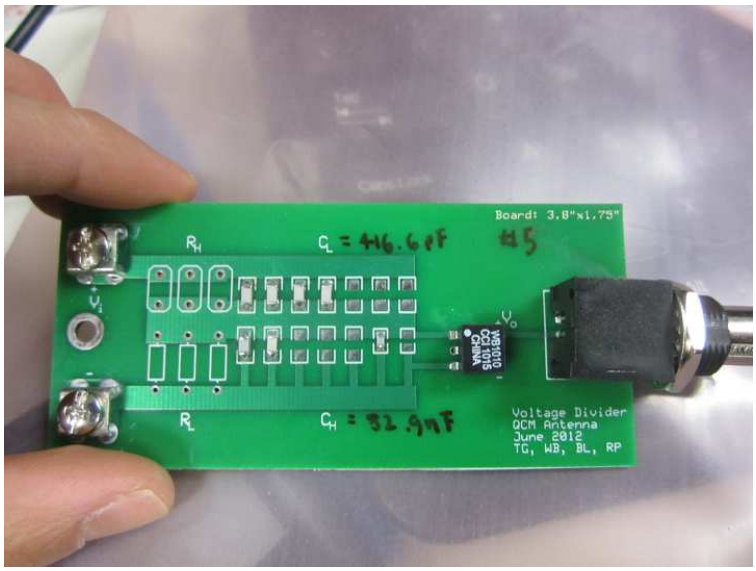

Figure G-4: Repaired capacitive voltage divider board; the number of capacitor components on the high-voltage leg was increased. This board survived the Shoelace experimental campaign.

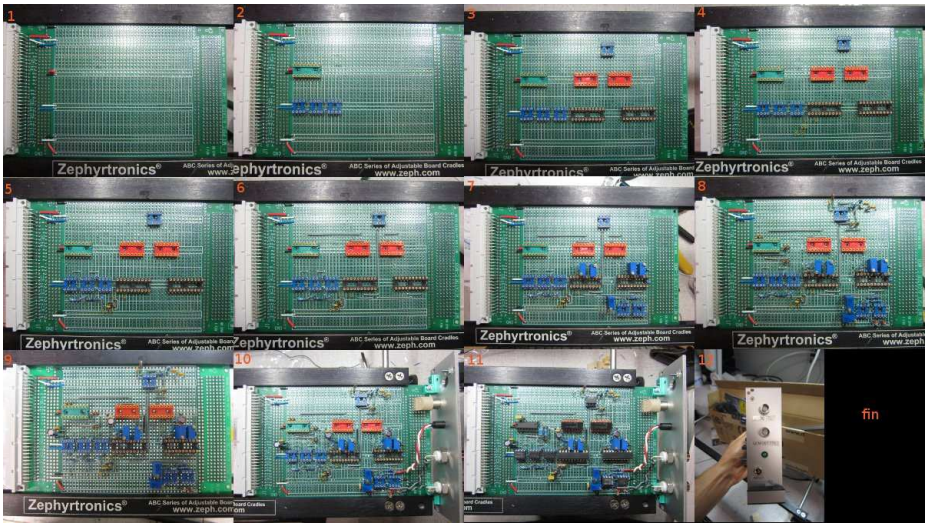

Figure G-5: Sequence of fabrication steps for the phase-locked loop board.

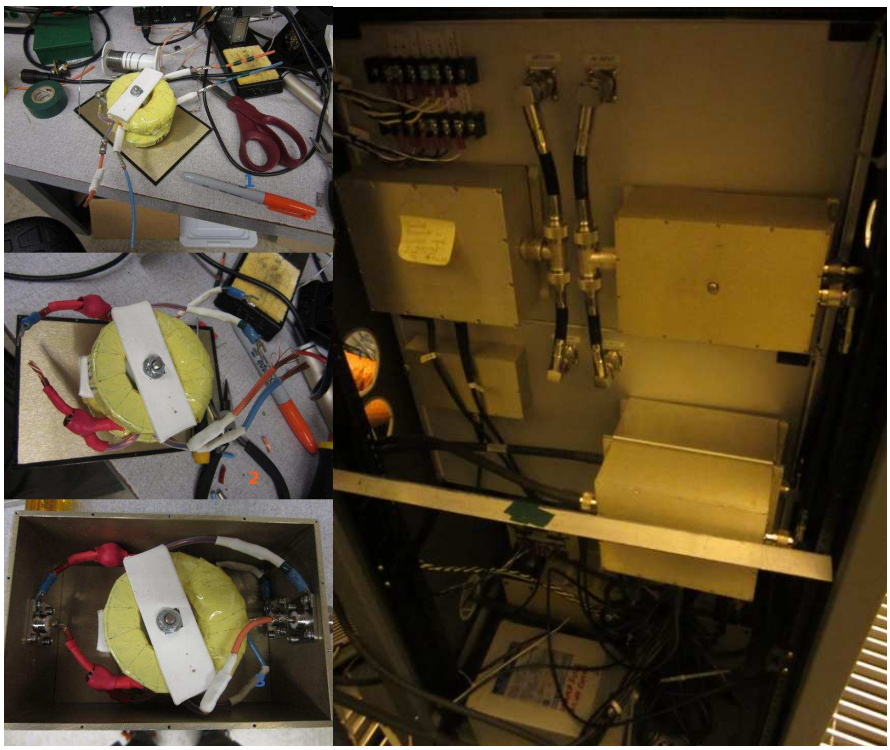

(a) (b)

Figure G-6: (a) Construction of transformer combiner from two cores; these are placed inside a COMPAC RF shielded box. (b) Photograph of transformer/combiner and I/V probes mounted on the rear panels of the matching network.

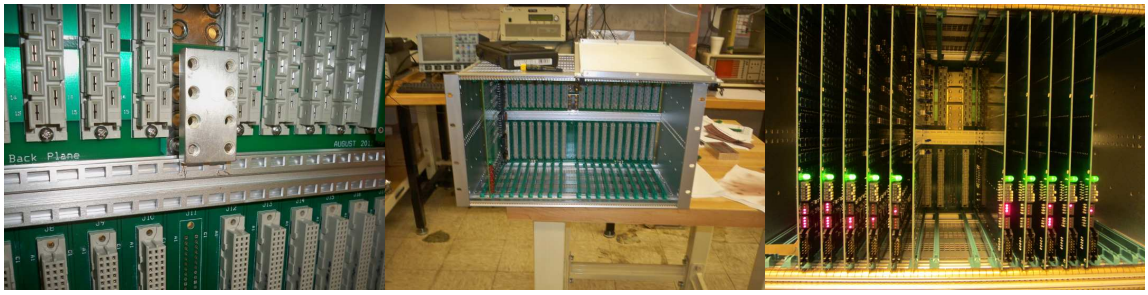

(a) (b) (c)

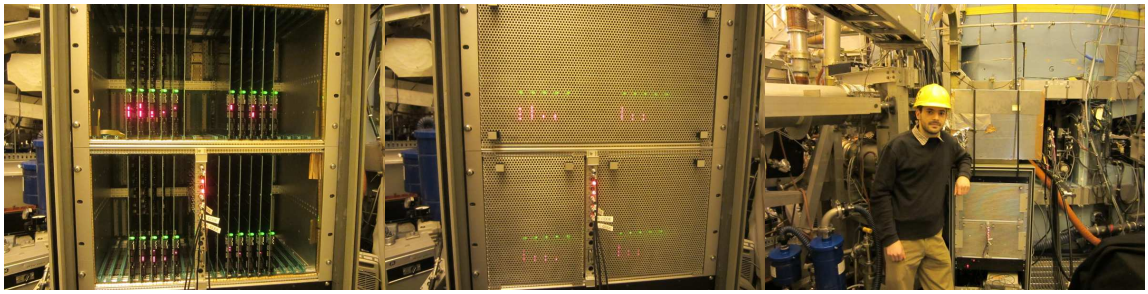

(d) (e) (f)

Figure G-7: (a) Backplane of matching network; the silver-plated copper nut plate is being affixed. (b) One of the two matching network modules, with one board fitted on the left-hand side. (c) One of two matching network subracks with all capacitor boards in place. LEDs indicate state of each board. (d) Both matching network subracks with all boards in place. (e) RF shield covers placed over boards, with Master Control Board outputs connected. (f) Finished matching network rack with covers in place and shielded test load on top of rack. Person (the author) for scale.

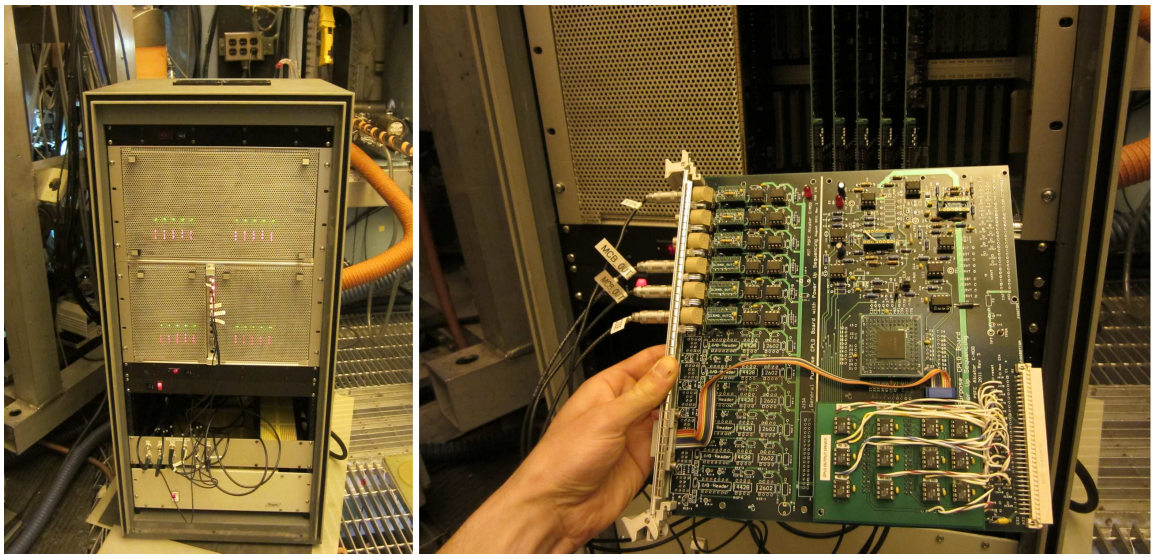

Figure G-8: Photograph showing assembled, integrated matching network in rack, together with the Master Control Board.

Appendix H

Exploring the Damping Rate Measurement

Let us examine whether the strong gradients in the edge region, which give a spatial dependence to the parameters in the parameters affecting the driven mode's dispersion relation, alter the meaning of the measured damping rate.

A "toy" model exploring this effect might give a linear dependence to the real and imaginary parts of the mode frequency through

$$\omega_r = \omega_r(x) = \omega_0 + \frac{\Delta\omega}{\Delta x}x \tag{H.1}$$

and

$$\gamma = \gamma(x) = \gamma_0 + \frac{\Delta\gamma}{\Delta x}\left|x\right|. \tag{H.2}$$

Let $\nu \equiv \gamma_0 + j(\omega - \omega_0)$, $a \equiv \frac{j\frac{\Delta\omega}{\Delta x} - \frac{\Delta\gamma}{\Delta x}}{\nu}$, and $b = \frac{j\frac{\Delta\omega}{\Delta x} + \frac{\Delta\gamma}{\Delta x}}{\nu}$, and moreover, assume that $|aL| \ll 1$ and $|bL| \ll 1$, where L is the radial scale of the mode. In this case, the deviation from the complex frequency at the $x = 0$ mode layer is assumed to be slight.

The transfer function of a nonlocal diagnostic like PCI effectively integrates over a range of flux surfaces, x. If this integration is over an effective length, $-L$ to L, then the effective transfer function has terms like

$$A' \int_{-L}^{L} \frac{1}{\nu + \frac{\Delta\gamma}{\Delta x}|x| + j\frac{\Delta\omega}{\Delta x}x} = \frac{A'}{\nu}\left(\frac{1}{b}\ln(1+bL) - \frac{1}{a}\ln(1-aL)\right)$$
$$\sim \frac{2A'L}{\nu}\left(1 - \frac{\frac{\Delta\gamma}{\Delta x}L}{2\nu}\right) \sim \frac{2A'L}{\nu\left(1+\frac{\frac{\Delta\gamma}{\Delta x}L}{2\nu}\right)} \sim \frac{2A'L}{j(\omega-\omega_0) + \left(\gamma_0 + \frac{\Delta\gamma}{\Delta x}\frac{L}{2}\right)} \tag{H.3}$$

where the units of A' are proportional to $1/x$. The approximations result from expanding the natural logarithm around $aL = bL = 0$. This means that the effective damping rate measured by a line-integrating diagnostic is $\gamma_0 + \frac{1}{2}\frac{\Delta\gamma}{\Delta x}L$. Since the damping rate is expected to be larger than γ_0 off the resonant layer, $x = 0$, $\Delta\gamma/\Delta x > 0$, and so the effective damping rate is larger than that at the resonant layer, γ_0. This result is reasonable, indicating that the effective damping rate averages over the spatially-varying quantity, and implies that accounting for the change in the mode dispersion relation continuously over the flux surfaces spanned by the driven mode, given a measurement which integrates the phase across this entire region, is unlikely to artificially deflate the measured damping rate from some true, larger value.

Another potential complication in the measurement of the damping rate is that the driven mode dispersion relation is only satisfied in a very narrow layer, such that as the frequency is scanned, so, too, is the flux surface which is excited by the antenna. Then scanning the frequency would also entail scanning the flux surface. This means that the mapping, and also the phase, between the antenna and a diagnostic would vary with frequency. In this case, it is possible that scanning the drive frequency may result in a phase variation that looks like a resonance, but is actually an artifact of traversing spatially across a range of flux surfaces, sampling with a radially-narrow layer in which the driven mode dispersion relation is satisfied.

We can explore this effect by examining how the field-aligned, field-line-label coordinate, ζ, of a diagnostic changes with the flux surface on which the mapping operation is carried out. The change in the driven mode phase registered on a diagnostic can then be estimated by scaling the shift, $\Delta\zeta$, resulting from transitioning across flux surfaces by the toroidal mode number, $n \sim 35$. This is done in Figure H-1

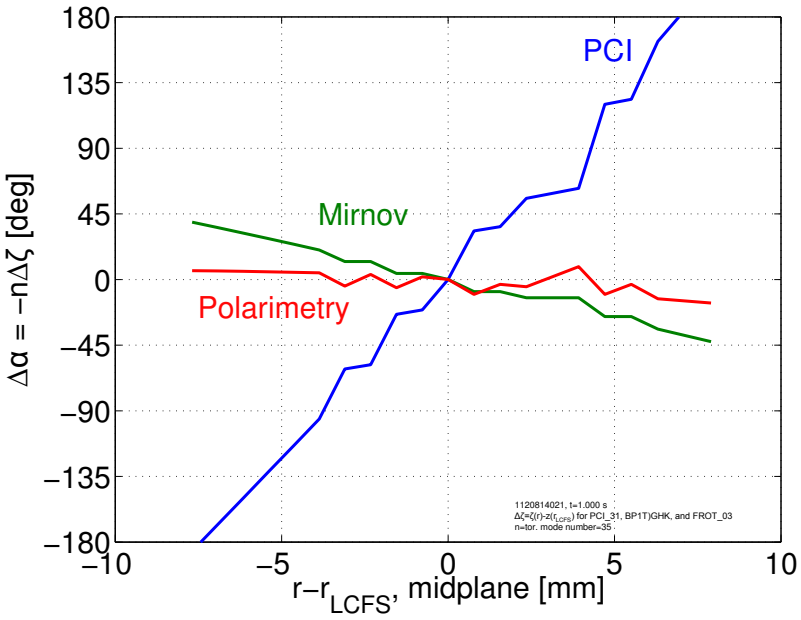

Figure H-1: Estimate for the change in measured mode phase with flux label (here, distance from the LCFS at the midplane) for a particular outer PCI chord, a Mirnov coil, and a polarimetry chord, as measured by considering the change in the field-aligned ζ coordinate multiplied by the mode number.

for an outer PCI chord (96° away toroidally from the Shoelace antenna), a Mirnov coil (15.6° away toroidally from the antenna), and a polarimetry chord (-84° away toroidally from the antenna). The PCI diagnostic is closer than the other two diagnostics to the X-point, and is further from the antenna, and so magnetic shear is more noticeable. However, the mapped perpendicular coordinate of the Mirnov coil and the polarimetry chord are affected only slightly as the flux surface is scanned. Yet all three diagnostics give essentially the same estimate for the damping rate (see Figure 5-12). Even for the PCI diagnostic, the spatial excursion required in order to produce the apparent 180° rotation of a resonance, $\sim$ 6 mm, is also wider than the 3 mm mode layer width measured for the QCM [32]. As such, it is unlikely that the damping rate measurement is an artifact of a change in mapping accompanying a frequency scan.

Appendix I

Additional Spectral Analysis

I.1 Additional Power Spectra

Here, power spectra from a wider selection of time bins are presented, extending the analysis of Section 5.7.2. The locations of the diagnostics are the same as in that analysis, and are shown in Figure 5-16.

I.2 Comparing Spectral Peaks Across Multiple Diagnostics

Figure I-8 compares the peak frequency for all PCI chords with that of the unmapped polarimeter chord and an unmapped Mirnov coil (the upper coil in Figure 5-4); the diagnostics have essentially the same peak, except during the latter part of the discharge, for which the Mirnov peak is higher. This may be reasonable since the unmapped Mirnov coil samples a flux bundle separated by many perpendicular wavelengths from the view of the polarimetry and PCI chords (see Figure 4-18).

Figure I-9 shows again the fact that the sawtooth crash cycle does not synchronize with the frequency modulation of the QCM. The plasma current comes closer to doing so, but its amplitude modulation still does not align precisely with the movement of the QCM peak.

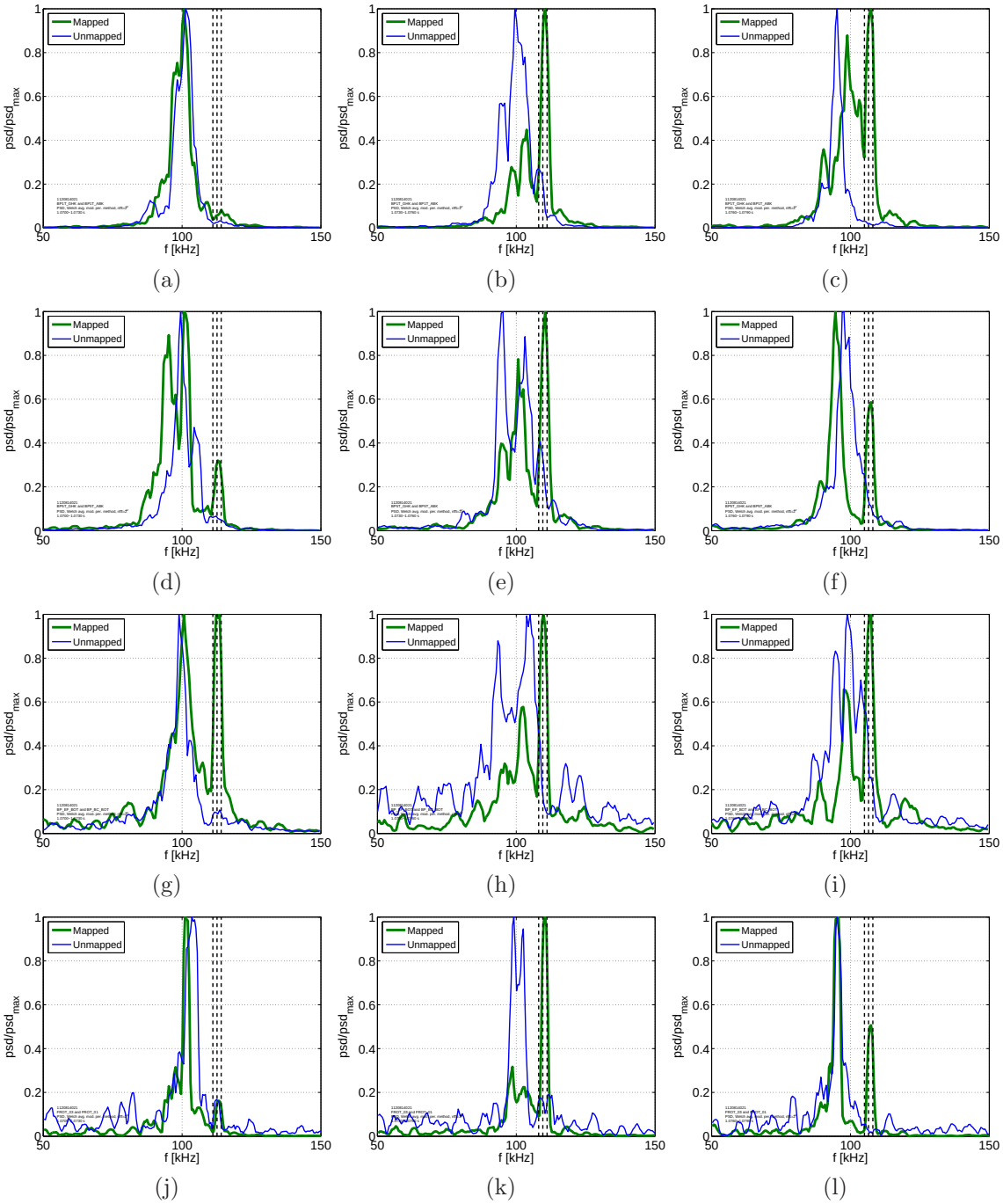

Figure I-1: Comparison of power spectra, normalized to the maximum spectral power for each signal, of pairs of diagnostics, with one mapped (thick green line) and one unmapped (thin blue line) diagnostic in each pair. The frames from the top row, (a)-(c), correspond to the Mirnov coils represented by the large blue circles in Figure 5-16, (d)-(f) to the green diamonds, and (g)-(i) to the orange squares. The bottom row, (j)-(l), shows spectra from two polarimeter chords, the red X's in Figure 5-16. The start times for each column are 1.070 (a,d,g,j), 1.073 (b,e,h,k), and 1.076 s (c,f,i,l), and the width of each bin is 3 ms.

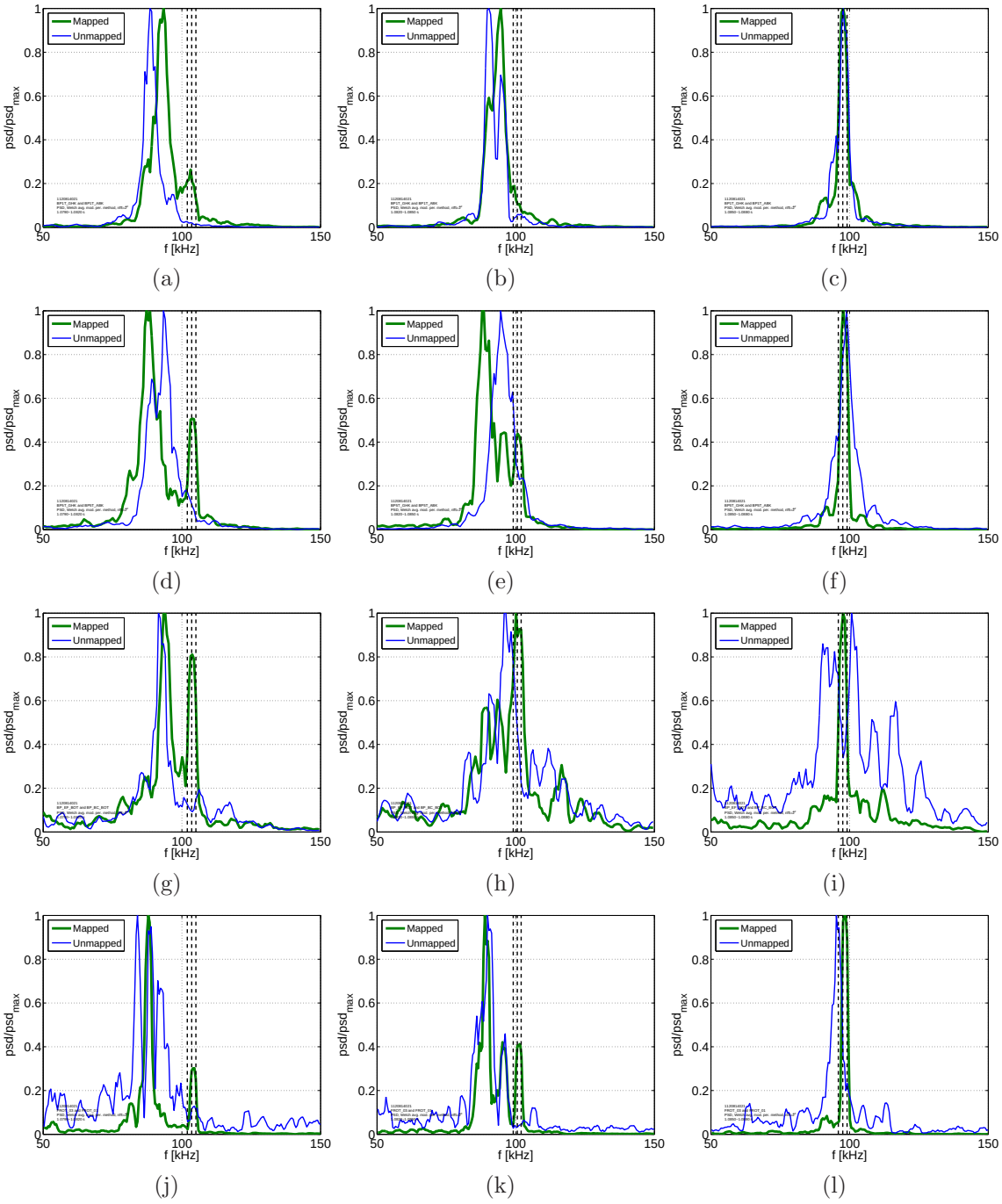

Figure I-2: The start times for each column are 1.079 (a,d,g,j), 1.082 (b,e,h,k), and 1.085 s (c,f,i,l), and the width of each bin is 3 ms.

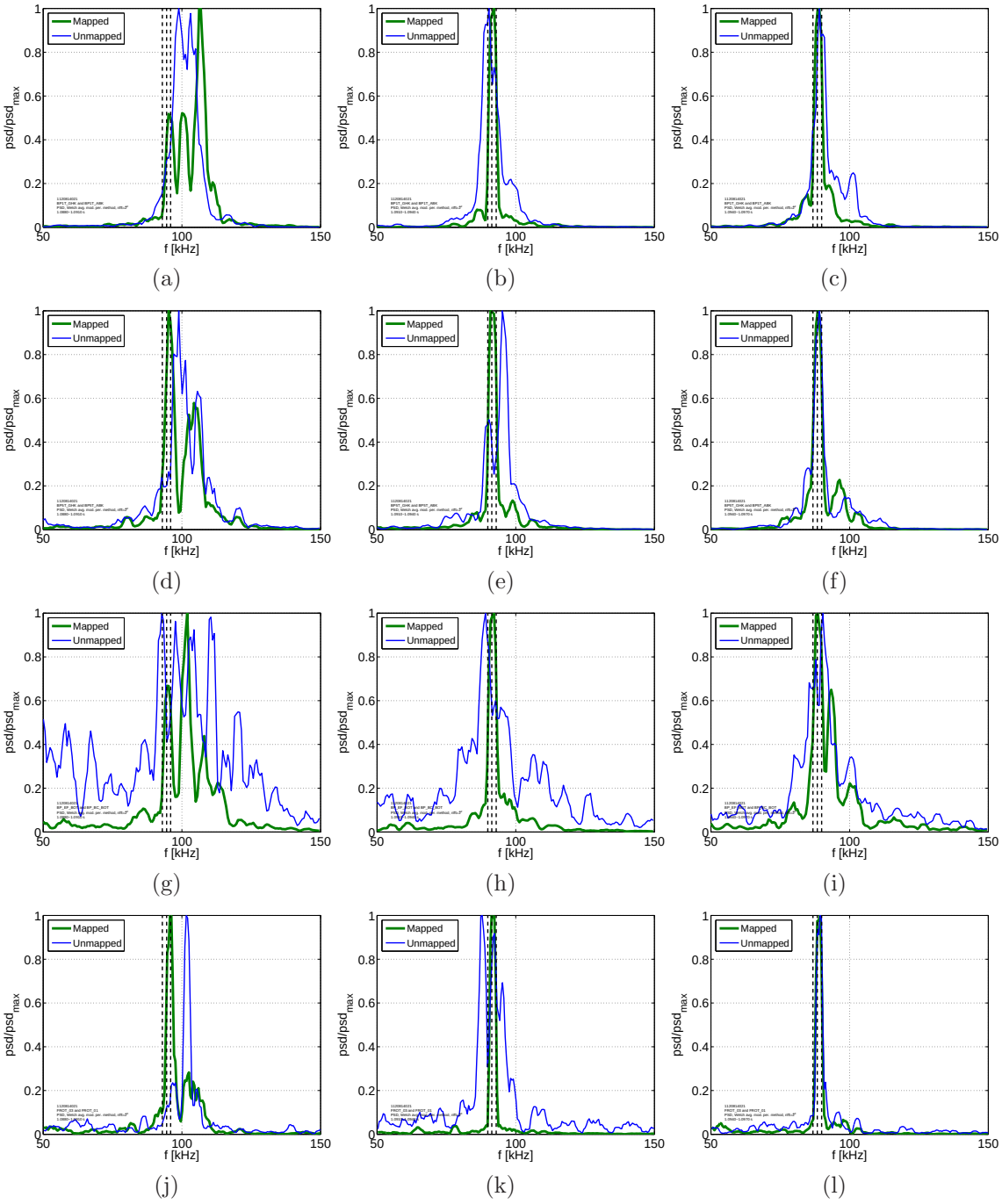

Figure I-3: The start times for each column are 1.088 (a,d,g,j), 1.091 (b,e,h,k), and 1.094 s (c,f,i,l), and the width of each bin is 3 ms. This figure reprises Figure 5-18.

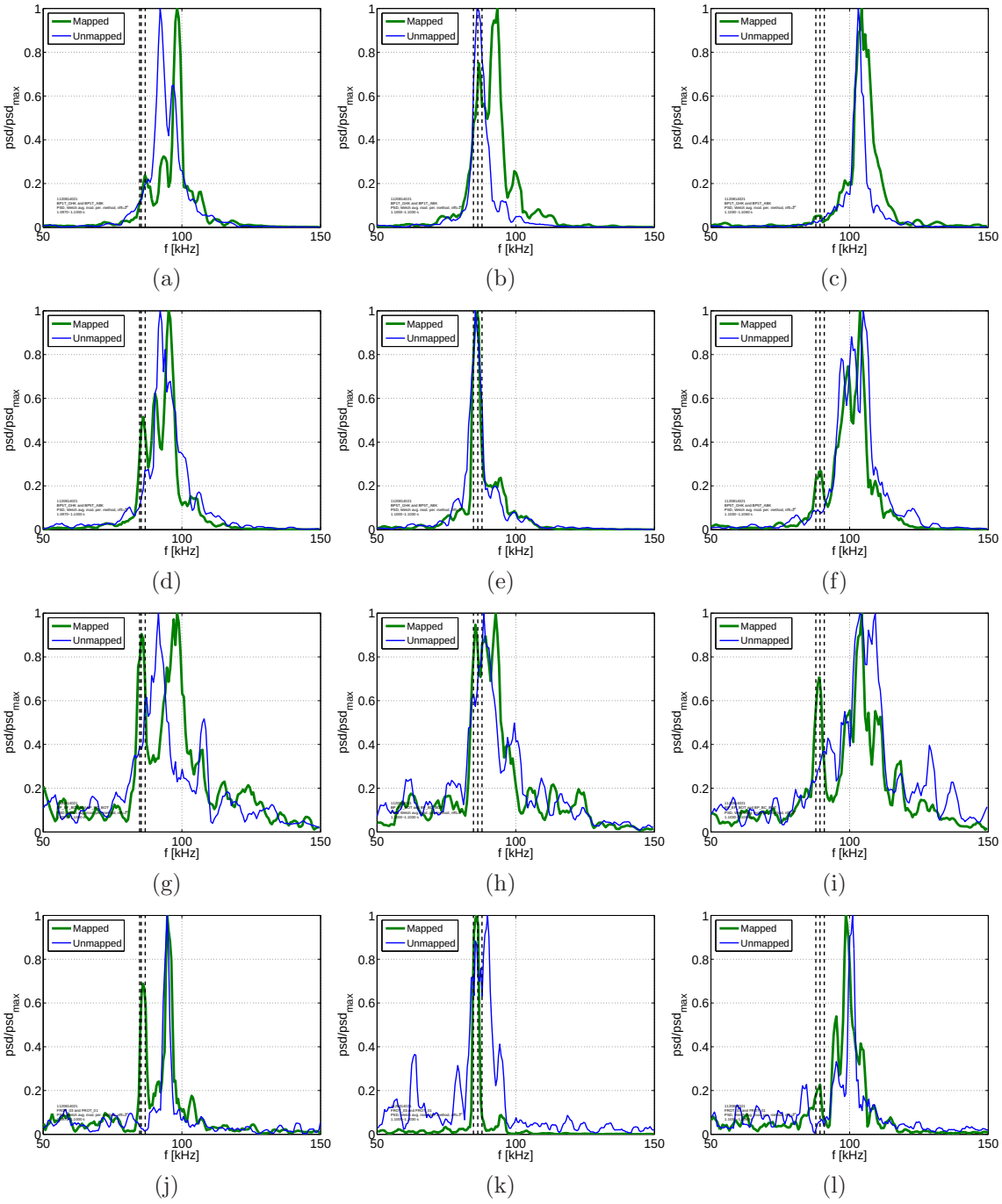

Figure I-4: The start times for each column are 1.097 (a,d,g,j), 1.100 (b,e,h,k), and 1.103 s (c,f,i,l), and the width of each bin is 3 ms. This figure reprises Figure 5-19

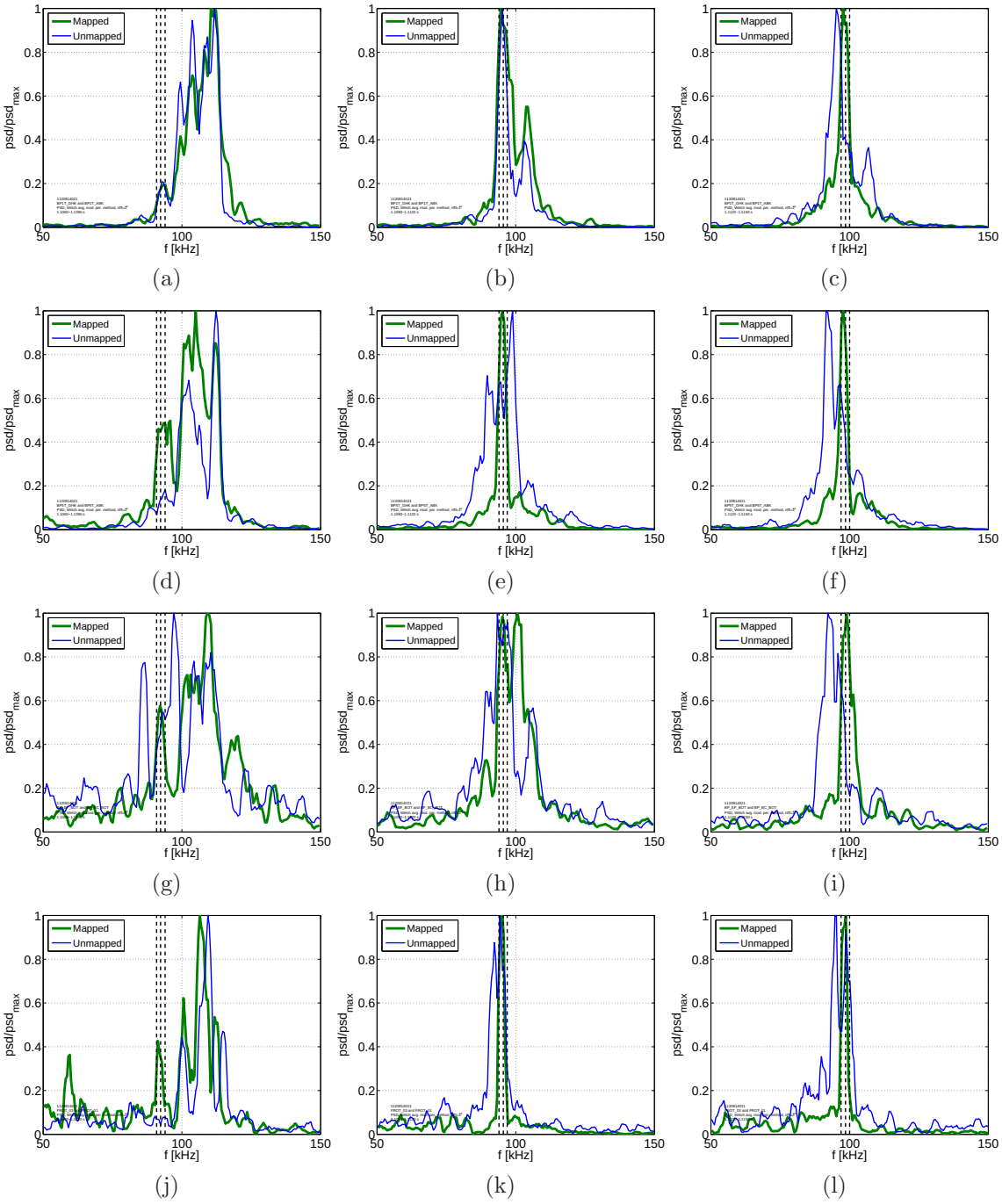

Figure I-5: The start times for each column are 1.106 (a,d,g,j), 1.109 (b,e,h,k), and 1.112 s (c,f,i,l), and the width of each bin is 3 ms.

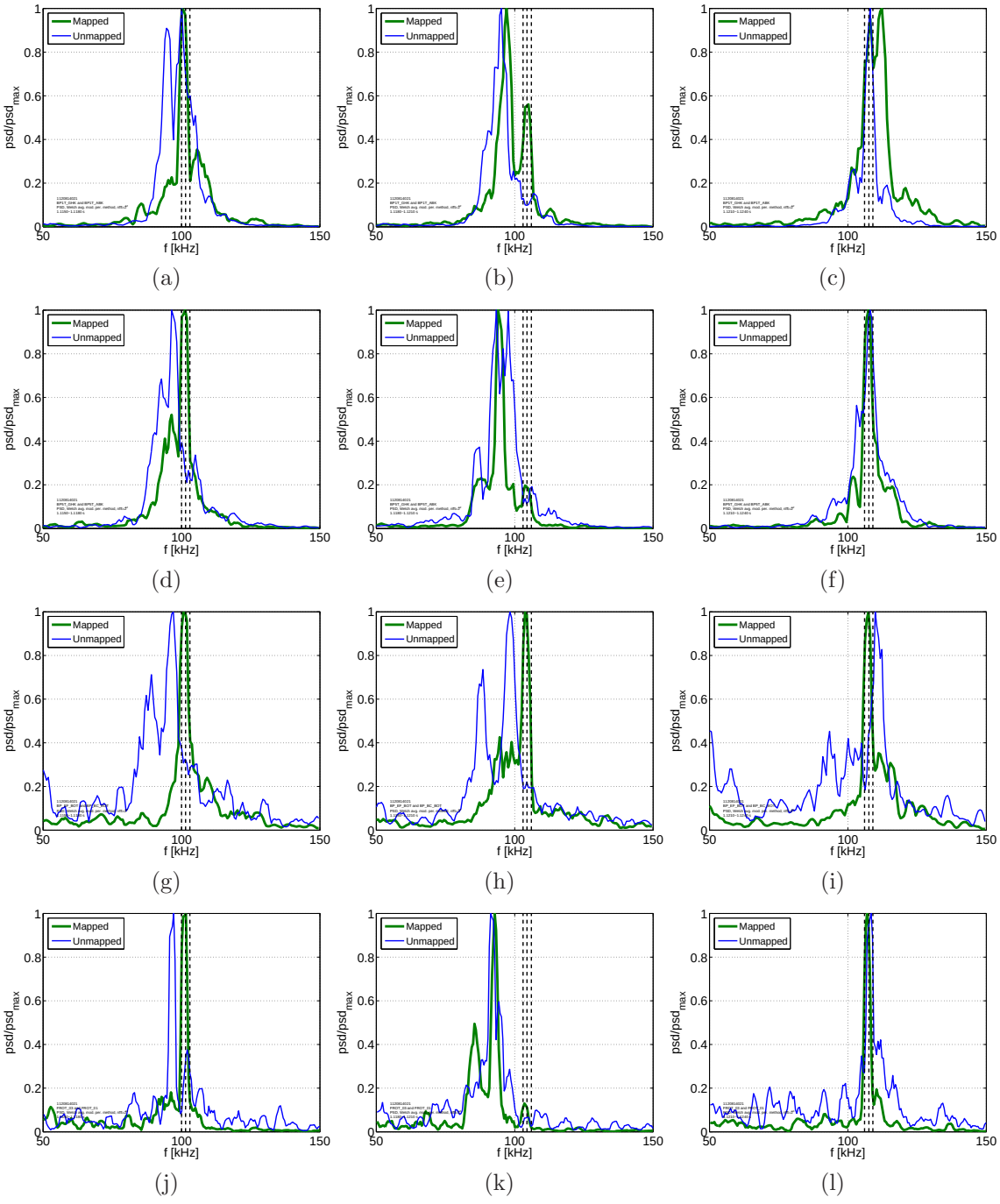

Figure I-6: The start times for each column are 1.115 (a,d,g,j), 1.118 (b,e,h,k), and 1.121 s (c,f,i,l), and the width of each bin is 3 ms.

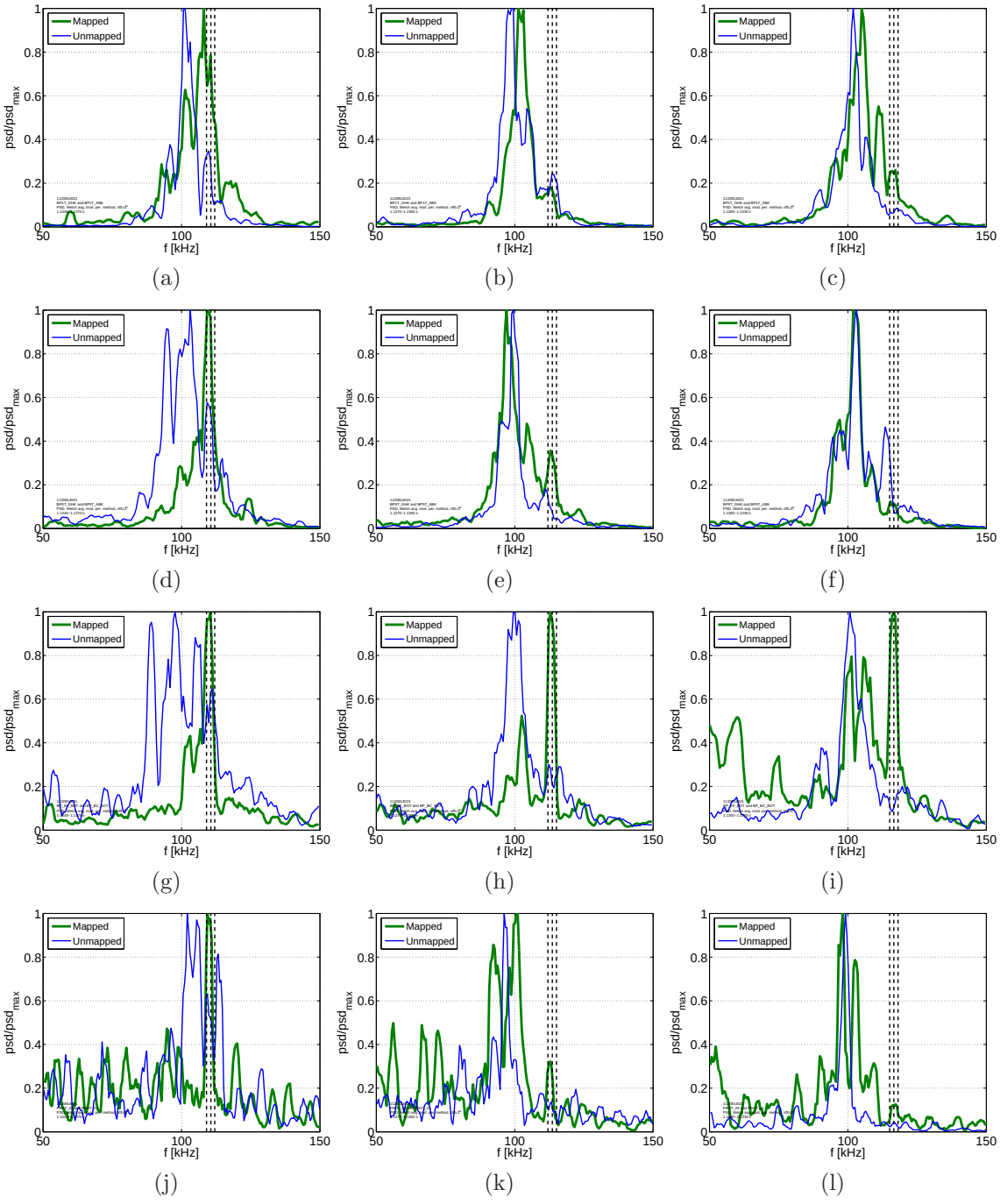

Figure I-7: The start times for each column are 1.124 (a,d,g,j), 1.127 (b,e,h,k), and 1.130 s (c,f,i,l), and the width of each bin is 3 ms.

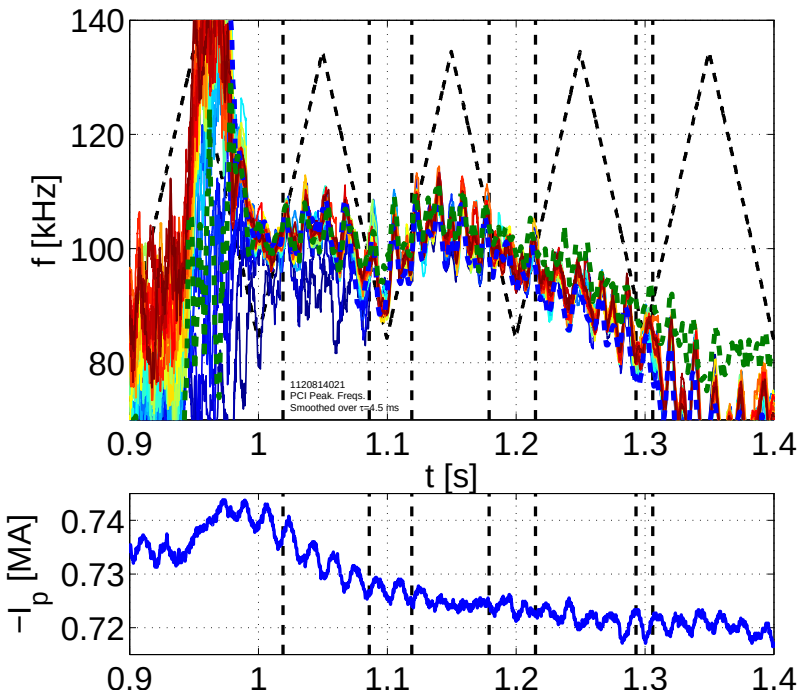

Figure I-8: Spectral peak in all PCI chords, as well as one (unmapped) polarimetry chord (thick dashed blue line) and one (unmapped) Mirnov coil (thick green dashed line). The peak in the polarimetry chord follows that on the majority of the PCI chords, while the Mirnov coil's peak frequency departs from those of the other diagnostics shortly after 1.3 s.

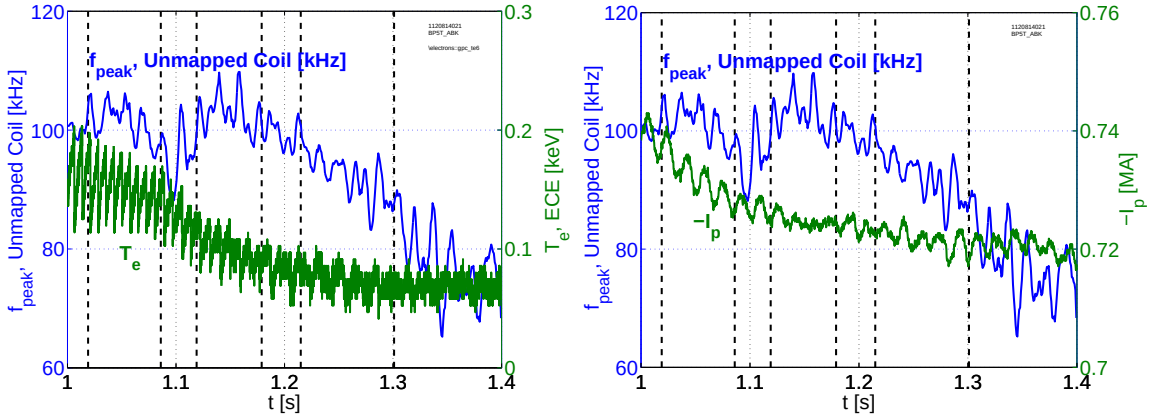

Figure I-9: Peak spectral frequency of the top (unmapped) Mirnov coil referred to in Figure 5-21, plotted together with (a) the electron temperature from an ECE chord and (b) the plasma current. The vertical black dashed lines again indicate crossings between the intrinsic QCM and antenna frequencies. Note that the ECE diagnostic, which provided the temperature measurement, faced calibration difficulties from a low and rapidly varying field.

I.3 Examining Cross Coherence Between Pairs of Diagnostics

Figure I-10 shows the magnitude squared coherence between a pair coils which map to the Shoelace antenna, but not to each other. Their locations are marked by the blue circle and green diamond nearest the Shoelace antenna in Figure 5-16. The signals between the coils are not strongly correlated except at the antenna frequency, and only when the antenna is on. Data from two discharges are shown; in both, amplitude modulation was applied to the antenna current. The phase-lock system was also operating for these discharges, and locked to the QCM for a portion of both.

Figure 5-20a shows the magnitude squared coherence for the same pair of Mirnov coils which both map to the antenna, while Figure 5-20b shows the same analysis for a pair of coils in which one coil maps to the antenna, and one does not (the location of this pair is indicated by the green diamonds in Figure 5-16). The discharge is the same as that from the previous section, and examined in Sections 5.7.2 and 5.7.3.

Interestingly, in both datasets, the cross coherence between the pair of mapped coils vanishes later in the discharge, well after the initial onset of the QCM. Weak cross coherence prior to the onset of H-mode exists for frequencies at and above 110 kHz; the strongest cross coherence appears just after the onset of H-mode, but prior to the development of a robust QCM, during which time the edge is most quiescent.

The color scales in these figures are the same as in the other magnitude squared coherence plots (for example, Figure 5-17).

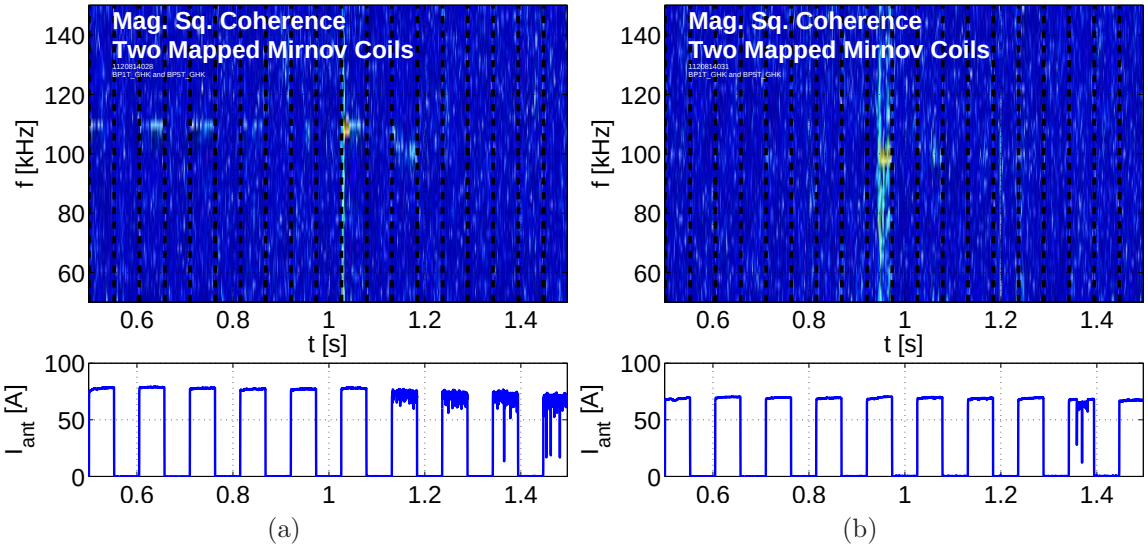

Figure I-10: Magnitude squared coherence between two coils which map to the Shoelace antenna (but not to each other); their locations are marked by the blue circle and green diamond nearest the Shoelace antenna in Figure 5-16. (a) and (b) correspond to two different discharges for which the antenna was operated in phase lock mode. The discharge in (a) is the same as that shown in Figure 5-15; the Shoelace antenna current locks to the QCM around 1.28 s. In (b), showing a different discharge, the antenna locks only from 1.36-1.38 s, and otherwise follows its fixed frequency program at 100 kHz. In both shots, the antenna current is amplitude modulated at 9.5 Hz, with the rising and falling edges indicated by dashed, vertical black lines.

Bibliography

[1] Jefferson W. Tester, Elisabeth M. Drake, Michael J. Driscoll, Michael W. Golay, and William A. Peters. *Sustainable Energy: Choosing Among Options*. The MIT Press, 2012. ISBN 0262017474.

[2] Peter Bien, Edmund Keeley, Karen Van Dyck, and Peter Constantine. *A Century of Greek Poetry 1900-2000: Bilingual Edition*. Cosmos Pub Co Inc, 2004. ISBN 1932455000.

[3] Nazim Hikmet, Randy Blasing, Mutlu Konuk Blasing, and Mutlu Konuk. *Poems of Nazim Hikmet, Revised and Expanded Edition*. Persea, 2002. ISBN 0892552743. URL www.perseabooks.com.

[4] Zachary Weinersmith. Early Fusion Skeptics. "Saturday Morning Breakfast Cereal" (Online), May 1, 2010. URL http://www.smbc-comics.com/index.php?id=1868.

[5] R. M. McDermott, B. Lipschultz, J. W. Hughes, P. J. Catto, A. E. Hubbard, I. H. Hutchinson, R. S. Granetz, M. Greenwald, B. LaBombard, K. Marr, M. L. Reinke, J. E. Rice, D. Whyte, and Alcator C-Mod Team. Edge radial electric field structure and its connections to H-mode confinement in Alcator C-Mod plasmas. *Phys. Plasmas*, 16(5):056103, 2009. doi:http://dx.doi.org/10.1063/1.3080721.

[6] D.G. Whyte, A.E. Hubbard, J.W. Hughes, B. Lipschultz, J.E. Rice, E.S. Marmar, M. Greenwald, I. Cziegler, A. Dominguez, T. Golfinopoulos, N. Howard, L. Lin, R.M. McDermott, M. Porkolab, M.L. Reinke, J. Terry, N. Tsujii, S. Wolfe, S. Wukitch, Y. Lin, and the Alcator C-Mod Team. I-mode: an H-mode energy confinement regime with L-mode particle transport in Alcator C-Mod. *Nucl. Fusion*, 50(10):105005, 2010. doi:10.1088/0029-5515/50/10/105005.

[7] Jeffrey Freidberg. *Plasma Physics and Fusion Energy*. Cambridge University Press, New York, 2007. ISBN 0521733170.

[8] J.D. Lawson. Some Criteria for a Power Producing Thermonuclear Reactor. *Proc. Phys. Soc. B*, 70(1):6, 1957. doi:10.1088/0370-1301/70/1/303.

[9] F. Wagner, G. Becker, K. Behringer, D. Campbell, A. Eberhagen, W. Engelhardt, G. Fussmann, O. Gehre, J. Gernhardt, G. v. Gierke, G. Haas, M. Huang,

F. Karger, M. Keilhacker, O. Klüber, M. Kornherr, K. Lackner, G. Lisitano, G. G. Lister, H. M. Mayer, D. Meisel, E. R. Müller, H. Murmann, H. Niedermeyer, W. Poschenrieder, H. Rapp, H. Röhr, F. Schneider, G. Siller, E. Speth, A. Stäbler, K. H. Steuer, G. Venus, O. Vollmer, and Z. Yü. Regime of Improved Confinement and High Beta in Neutral-Beam-Heated Divertor Discharges of the ASDEX Tokamak. *Phys. Rev. Lett.*, 49:1408–1412, Nov 1982. doi:10.1103/PhysRevLett.49.1408.

[10] Lajos Szanto. Tantalus and his punishment. Digital image. URL clipart.com.

[11] N Oyama, P Gohil, L D Horton, A E Hubbard, J W Hughes, Y Kamada, K Kamiya, A W Leonard, A Loarte, R Maingi, G Saibene, R Sartori, J K Stober, W Suttrop, H Urano, W P West, and the ITPA Pedestal Topical Group. Pedestal conditions for small ELM regimes in tokamaks. *Plasma Phys. Control. Fusion*, 48(5A):A171, 2006. doi:10.1088/0741-3335/48/5A/S16.

[12] E.J. Doyle (Chair Transport Physics), W.A. Houlberg (Chair Confinement Database, Modelling), Y. Kamada (Chair Pedestal, Edge), V. Mukhovatov (co Chair Transport Physics), T.H. Osborne (co Chair Pedestal, Edge), A. Polevoi (co Chair Confinement Database, Modelling), G. Bateman, J.W. Connor, J.G. Cordey (retired), T. Fujita, X. Garbet, T.S. Hahm, L.D. Horton, A.E. Hubbard, F. Imbeaux, F. Jenko, J.E. Kinsey, Y. Kishimoto, J. Li, T.C. Luce, Y. Martin, M. Ossipenko, V. Parail, A. Peeters, T.L. Rhodes, J.E. Rice, C.M. Roach, V. Rozhansky, F. Ryter, G. Saibene, R. Sartori, A.C.C. Sips, J.A. Snipes, M. Sugihara, E.J. Synakowski, H. Takenaga, T. Takizuka, K. Thomsen, M.R. Wade, H.R. Wilson, ITPA Transport Physics Topical Group, ITPA Confinement Database, Modelling Topical Group, ITPA Pedestal, and Edge Topical Group. Chapter 2: Plasma confinement and transport. *Nucl. Fusion*, 47(6): S18, 2007. doi:10.1088/0029-5515/47/6/S02.

[13] ITER Physics Expert Group on Confinement and Transport, ITER Physics Expert Group on Confinement, Modelling and Database, and ITER Physics Basis Editors. Chapter 2: Plasma confinement and transport. *Nuclear Fusion*, 39(12):2175, 1999. doi:http://dx.doi.org/10.1088/0029-5515/39/12/302.

[14] Culham Centre for Fusion Research. Online. URL differ.nl/sites/default/files/images/news/MAST-ELM_web_2.jpg. Accessed March 2014; see also http://www.ccfe.ac.uk/news_detail.aspx?id=164.

[15] T. Uckan, B. Richards, A.J. Wootton, Roger D. Bengtson, R. Bravenec, B.A. Carreras, G.X. Li, P. Hurwitz, P.E. Phillips, W.L. Rowan, H.Y.W. Tsui, J.R. Uglum, Y. Wen, and D. Winslow. Feedback control and stabilization experiments on the Texas Experimental Tokamak (TEXT). *Journal of Nuclear Materials*, 220–222:663–667, 1995. ISSN 0022-3115. doi:http://dx.doi.org/10.1016/0022-3115(94)00561-3.

[16] Kan Zhai, Yi-Zhi Wen, Chang-Xuan Yu, Wan-Dong Liu, Shu-De Wan, Ge Zhuang, Wen Yu, and Zhi-Zhan Xu. Observations of a quasi-coherent fluctuation mode in the KT-5C tokamak during ∼90 degrees phase shift feedback. *Nuclear Fusion*, 37(12):1709, 1997. doi:10.1088/0029-5515/37/12/I04.

[17] Zhai Kan, Wen Yi-zhi, Yu Chang-xuan, Liu Wan-dong, Wang Chao, Zhuang Ge, and Xu Zhi-zhan. Feedback control of edge turbulence in a tokamak. *Phys. Rev. E*, 55:3431–3438, Mar 1997. doi:10.1103/PhysRevE.55.3431.

[18] R. J. Taylor, M. L. Brown, B. D. Fried, H. Grote, J. R. Liberati, G. J. Morales, P. Pribyl, D. Darrow, and M. Ono. *H*-mode behavior induced by cross-field currents in a tokamak. *Phys. Rev. Lett.*, 63:2365–2368, Nov 1989. doi:10.1103/PhysRevLett.63.2365.

[19] R.R. Weynants and R.J. Taylor. Dynamics of H-mode-like edge transitions brought about by external polarization. *Nuclear Fusion*, 30(5):945, 1990. doi:10.1088/0029-5515/30/5/015.

[20] T. E. Evans, R. A. Moyer, P. R. Thomas, J. G. Watkins, T. H. Osborne, J. A. Boedo, E. J. Doyle, M. E. Fenstermacher, K. H. Finken, R. J. Groebner, M. Groth, J. H. Harris, R. J. La Haye, C. J. Lasnier, S. Masuzaki, N. Ohyabu, D. G. Pretty, T. L. Rhodes, H. Reimerdes, D. L. Rudakov, M. J. Schaffer, G. Wang, and L. Zeng. Suppression of Large Edge-Localized Modes in High-Confinement DIII-D Plasmas with a Stochastic Magnetic Boundary. *Phys. Rev. Lett.*, 92:235003, Jun 2004. doi:10.1103/PhysRevLett.92.235003.

[21] I. H. Hutchinson, R. Boivin, F. Bombarda, P. Bonoli, S. Fairfax, C. Fiore, J. Goetz, S. Golovato, R. Granetz, M. Greenwald, S. Horne, A. Hubbard, J. Irby, B. LaBombard, B. Lipschultz, E. Marmar, G. McCracken, M. Porkolab, J. Rice, J. Snipes, Y. Takase, J. Terry, S. Wolfe, C. Christensen, D. Garnier, M. Graf, T. Hsu, T. Luke, M. May, A. Niemczewski, G. Tinios, J. Schachter, and J. Urbahn. First results from Alcator-C-MOD. *Phys. Plasmas*, 1(5):1511–1518, 1994. doi:http://dx.doi.org/10.1063/1.870701.

[22] M. Greenwald et al. *Phys. Plasmas*, 2014. (to be submitted).

[23] Bruce D. Scott. Drift wave versus interchange turbulence in tokamak geometry: Linear versus nonlinear mode structure. *Phys. Plasmas*, 12(6):062314, 2005. doi:10.1063/1.1917866.

[24] Annamaria Mosetto, D. Halpern Federico, Sébastien Jolliet, and Paolo Ricci. Low-frequency linear-mode regimes in the tokamak scrape-off layer. *Phys. Plasmas*, 19:112103 1–15, 2012.

[25] Y. Takase, R. Boivin, F. Bombarda, P.T. Bonoli, C. Fiore, D. Garnier, J. Goetz, S. Golovato, R. Granetz, M. Greenwald, S.F. Horne, A. Hubbard, I.H. Hutchinson, J. Irby, B. LaBombard, B. Lipschultz, E. Marmar, M. May, A. Mazurenko,

G. McCracken, P. O'Shea, M. Porkolab, J. Reardon, J. Rice, C. Rost, J. Schacter, J.A. Snipes, P. Stek, J. Terry, R. Watterson, B. Welch, and S. Wolfe. High power density H-modes in Alcator C-Mod. *Proceedings, 16th International Conference on Fusion Energy, Montreal 1996*, 1:475–485, 1997.

[26] A. E. Hubbard, R. L. Boivin, R. S. Granetz, M. Greenwald, J. W. Hughes, I. H. Hutchinson, J. Irby, B. LaBombard, Y. Lin, E. S. Marmar, A. Mazurenko, D. Mossessian, E. Nelson-Melby, M. Porkolab, J. A. Snipes, J. Terry, S. Wolfe, S. Wukitch, B. A. Carreras, V. Klein, and T. Sunn Pedersen. Pedestal profiles and fluctuations in C-Mod enhanced D-alpha H-modes. *Phys. Plasmas*, 8(5), 2001.

[27] F Ryter, W Suttrop, B Brsehaber, M Kaufmann, V Mertens, H Murmann, A G Peeters, J Stober, J Schweinzer, H Zohm, and ASDEX Upgrade Team. H-mode power threshold and transition in ASDEX Upgrade. *Plasma Phys. Control. Fusion*, 40(5):725, 1998. doi:10.1088/0741-3335/40/5/032.

[28] K H Burrell, M E Austin, D P Brennan, J C DeBoo, E J Doyle, P Gohil, C M Greenfield, R J Groebner, L L Lao, T C Luce, M A Makowski, G R McKee, R A Moyer, T H Osborne, M Porkolab, T L Rhodes, J C Rost, M J Schaffer, B W Stallard, E J Strait, M R Wade, G Wang, J G Watkins, W P West, and L Zeng. Quiescent H–mode plasmas in the DIII-D tokamak. *Plasma Phys. Control. Fusion*, 44(5A):A253, 2002. doi:10.1088/0741-3335/44/5A/325.

[29] K. Kamiya, H. Kimura, H. Ogawa, H. Kawashima, K. Tsuzuki, M. Sato, Y. Miura, and JFT-2M Group. Observation of High Recycling Steady H-mode edge and compatibility with improved core confinement mode on JFT-2M. *Nuclear Fusion*, 43(10):1214, 2003. doi:10.1088/0029-5515/43/10/024.

[30] K Kamiya, M Bakhtiari, S Kasai, H Kawashima, Y Kusama, Y Miura, H Ogawa, N Oyama, M Sato, K Shinohara, K Tsuzuki, K Uehara, and JFT-2M Group. High recycling steady H-mode regime in the JFT-2M tokamak. *Plasma Phys. Control. Fusion*, 46(5A):A157, 2004. doi:10.1088/0741-3335/46/5A/017.

[31] E. Belonohy, G. Pokol, K. McCormick, G. Papp, S. Zoletnik, and W7-AS Team. A Systematic Study of the Quasi-Coherent Mode in the High Density H-Mode Regime of Wendelstein 7-AS. *AIP Conference Proceedings*, 993(1):39–42, 2008. doi:http://dx.doi.org/10.1063/1.2909159.

[32] B. LaBombard, T. Golfinopoulos, J. L. Terry, D. Brunner, E. Davis, M. Greenwald, J. W. Hughes, and Alcator C-Mod Team. New insights on boundary plasma turbulence and the quasi-coherent mode in Alcator C-Mod using a Mirror Langmuir Probe. *Phys. Plasmas*, 21(5):056108, 2014. doi:http://dx.doi.org/10.1063/1.4873918.

[33] J.A. Snipes, B. LaBombard, M. Greenwald, I.H. Hutchinson, J. Irby, Y. Lin, A. Mazurenko, and M. Porkolab. The quasi-coherent signature of enhanced D_α H-mode in Alcator C-Mod. *Plasma Phys. Control. Fusion*, 43:L23–L30, 2001.

[34] Yijun Lin. *Experimental Application and Numerical Study of Reflectometry in the Alcator C-Mod Tokamak*. PhD thesis, Massachusetts Institute of Technology, 2001. URL http://hdl.handle.net/1721.1/8649. PSFC Report RR-01-5.

[35] A. Mazurenko, M. Porkolab, D. Mossessian, J.A. Snipes, X.Q. Xu, and W.M. Nevins. Experimental and Theoretical Studies of Quasicoherent Fluctuations in Enhanced D_α Plasmas in the Alcator C-Mod Tokamak. *Phys. Rev. Lett.*, 89 (22):225004, 1–4, 2002.

[36] D. A. Mossessian, P. Snyder, A. Hubbard, J. W. Hughes, M. Greenwald, B. LaBombard, J. A. Snipes, S. Wolfe, and H. Wilson. High-confinement-mode edge stability of Alcator C-mod plasmas. *Phys. Plasmas*, 10(5):1720–1726, 2003. doi:http://dx.doi.org/10.1063/1.1561618.

[37] Matthew Brian Sampsell. *Beam Emission Spectroscopy on the Alcator C-Mod Tokamak*. PhD thesis, University of Texas at Austin, 2004. URL library.utexas.edu/etd/d/2004/sampselld77810/sampselld77810.pdf.

[38] J.L. Terry, N.P. Basse, I. Cziegler, M. Greenwald, O. Grulke, B. LaBombard, S.J. Zweben, E.M. Edlund, J.W. Hughes, L. Lin, Y. Lin, M. Porkolab, M. Sampsell, B. Veto, and S.J. Wukitch. Transport phenomena in the edge of Alcator C-Mod plasmas. *Nucl. Fusion*, 45:1321–1327, Oct 2005.

[39] J.W. Hughes, P.B. Snyder, J.R. Walk, E.M. Davis, A. Diallo, B. LaBombard, S.G. Baek, R.M. Churchill, M. Greenwald, R.J. Groebner, A.E. Hubbard, B. Lipschultz, E.S. Marmar, T. Osborne, M.L. Reinke, J.E. Rice, C. Theiler, J. Terry, A.E. White, D.G. Whyte, S. Wolfe, and X.Q. Xu. Pedestal structure and stability in H-mode and I-mode: a comparative study on Alcator C-Mod. *Nuclear Fusion*, 53(4):043016, 2013. doi:10.1088/0029-5515/53/4/043016.

[40] A.E. White, P. Phillips, D.G. Whyte, A.E. Hubbard, C. Sung, J.W. Hughes, A. Dominguez, J. Terry, and I. Cziegler. Electron temperature fluctuations associated with the weakly coherent mode in the edge of I-mode plasmas. *Nucl. Fusion*, 51(11):113005, November 2011. ISSN 0029-5515. URL http://hdl.handle.net/1721.1/81467.

[41] Arturo Dominguez. *Study of density fluctuations and particle transport at the edge of I-mode plasmas*. PhD thesis, Massachusetts Institute of Technology, September 2012. URL http://hdl.handle.net/1721.1/79261.

[42] G.S. Xu, L.M. Shao, S.C. Liu, H.Q. Wang, B.N. Wan, H.Y. Guo, P.H. Diamond, G.R. Tynan, M. Xu, S.J. Zweben, V. Naulin, A.H. Nielsen, J. Juul Rasmussen, N. Fedorczak, P. Manz, K. Miki, N. Yan, R. Chen, B. Cao, L. Chen, L. Wang, W. Zhang, and X.Z. Gong. Study of the L–I–H transition with a new dual gas puff imaging system in the EAST superconducting tokamak. *Nuclear Fusion*, 54(1):013007, 2014. doi:10.1088/0029-5515/54/1/013007.

[43] K. Kamiya, N. Oyama, T. Ido, M. Bakhtiari, and JFT-2M Group. Characterization of coherent magnetic fluctuations in JFT-2M high recycling steady high-confinement mode plasmas. *Physics of Plasmas*, 13(3):032507, 2006. doi:http://dx.doi.org/10.1063/1.2169779.

[44] R. Maingi, A.E. Hubbard, H. Meyer, J.W. Hughes, A. Kirk, R. Maqueda, J.L. Terry, MAST the Alcator C-Mod, and NSTX teams. Comparison of small ELM characteristics and regimes in Alcator C-Mod, MAST and NSTX. *Nuclear Fusion*, 51(6):063036, 2011. doi:10.1088/0029-5515/51/6/063036.

[45] E Wolfrum, M Bernert, J E Boom, A Burckhart, I G J Classen, G D Conway, T Eich, R Fischer, A Gude, A Herrmann, N C Luhmann Jr, M Maraschek, R McDermott, H K Park, T Ptterich, J Vicente, B Wieland, M Willensdorfer, and the ASDEX Upgrade Team. Characterization of edge profiles and fluctuations in discharges with type-II and nitrogen-mitigated edge localized modes in ASDEX Upgrade. *Plasma Phys. Control. Fusion*, 53(8):085026, 2011. doi:10.1088/0741-3335/53/8/085026.

[46] T. Ozeki, M.S. Chu, L.L. Lao, T.S. Taylor, M.S. Chance, S. Kinoshita, K.H. Burrell, and R.D. Stambaugh. Plasma shaping, edge ballooning stability and ELM behaviour in DIII-D. *Nuclear Fusion*, 30(8):1425, 1990. doi:10.1088/0029-5515/30/8/003.

[47] K. H. Burrell, W. P. West, E. J. Doyle, M. E. Austin, T. A. Casper, P. Gohil, C. M. Greenfield, R. J. Groebner, A. W. Hyatt, R. J. Jayakumar, D. H. Kaplan, L. L. Lao, A. W. Leonard, M. A. Makowski, G. R. McKee, T. H. Osborne, P. B. Snyder, W. M. Solomon, D. M. Thomas, T. L. Rhodes, E. J. Strait, M. R. Wade, G. Wang, and L. Zeng. Advances in understanding quiescent H–mode plasmas in DIII-D. *Phys. Plasmas*, 12(5):056121, 2005. doi:http://dx.doi.org/10.1063/1.1894745.

[48] W Suttrop, M Maraschek, G D Conway, H-U Fahrbach, G Haas, L D Horton, T Kurki-Suonio, C J Lasnier, A W Leonard, C F Maggi, H Meister, A Mück, R Neu, I Nunes, Th Ptterich, M Reich, A C C Sips, and the ASDEX Upgrade Team. ELM-free stationary H-mode plasmas in the ASDEX Upgrade tokamak. *Plasma Phys. Control. Fusion*, 45(8):1399, 2003. doi:10.1088/0741-3335/45/8/302.

[49] W. Suttrop, V. Hynönen, T. Kurki-Suonio, P.T. Lang, M. Maraschek, R. Neu, A. Stäbler, G.D. Conway, S. Hacquin, M. Kempenaars, P.J. Lomas, M.F.F. Nave, R.A. Pitts, K.-D. Zastrow, the ASDEX Upgrade team, and contributors to the JET-EFDA workprogramme. Studies of the 'Quiescent H–mode' regime in ASDEX Upgrade and JET. *Nuclear Fusion*, 45(7):721, 2005. doi:10.1088/0029-5515/45/7/021.

[50] N. Oyama, Y. Sakamoto, A. Isayama, M. Takechi, P. Gohil, L.L. Lao, P.B. Snyder, T. Fujita, S. Ide, Y. Kamada, Y. Miura, T. Oikawa, T. Suzuki, H. Takenaga, K. Toi, and the JT-60 Team. Energy loss for grassy ELMs and effects

of plasma rotation on the ELM characteristics in JT-60U. *Nuclear Fusion*, 45 (8):871, 2005. doi:10.1088/0029-5515/45/8/014.

[51] M. Greenwald, R.L. Boivin, F. Bombarda, P.T. Bonoli, C.L. Fiore, D. Garnier, J.A. Goetz, S.N. Golovato, M.A. Graf, R.S. Granetz, S. Horne, A. Hubbard, I.H. Hutchinson, J.H. Irby, B. LaBombard, B. Lipschultz, E.S. Marmar, M.J. May, G.M. McCracken, P. O'Shea, J.E. Rice, J. Schachter, J.A. Snipes, P.C. Stek, Y. Takase, J.L. Terry, Y. Wang, R. Watterson, B. Welch, and S.M. Wolfe. H mode confinement in Alcator C-Mod. *Nuclear Fusion*, 37(6):793, 1997. doi:10.1088/0029-5515/37/6/I07.

[52] M Greenwald, R Boivin, P Bonoli, C Fiore, J Goetz, R Granetz, A Hubbard, I Hutchinson, J Irby, Y Lin, E Marmar, A Mazurenko, D Mossessian, T Sunn Pedersen, J Rice, J Snipes, G Schilling, G Taylor, M Greenwald, R Boivin, P Bonoli, C Fiore, J Goetz, R Granetz, A Hubbard, I Hutchinson, J Irby, Y Lin, E Marmar, A Mazurenko, D Mossessian, T Sunn Pedersen, J Rice, J Snipes, J Terry, S Wolfe, and S Wukitch. Studies of EDA H–mode in Alcator C–Mod. *Plasma Phys. Control. Fusion*, 42(5A):A263, 2000. doi:10.1088/0741-3335/42/5A/331.

[53] Alexander Mazurenko. *Phase Contrast Imaging on the Alcator C-Mod tokamak*. PhD thesis, Massachusetts Institute of Technology, Sep 2001. PSFC Report RR-01-2.

[54] Istvan Cziegler. *Turbulence and transport phenomena in edge and scrape-off-layer plasmas*. PhD thesis, Masschusetts Institute of Technology, June 2011.

[55] K. V. Roberts and J. B. Taylor. Magnetohydrodynamic Equations for Finite Larmor Radius. *Phys. Rev. Lett.*, 8:197–198, Mar 1962.

[56] A.A. Galeev and V.N. Oraevskiĭ. "Universal" Instability of an Inhomogeneous Plasma in a Magnetic Field. *Soviet Physics JETP*, 17(3):615–620, Mar 1963.

[57] S.S. Moiseev and R.Z. Sagdeev. On the Bohm Diffusion Coefficient. *Soviet Physics JETP*, 17(2):515–517, 1963. ISSN 0038-5646.

[58] A.B. Mikhaĭlovskiĭ and L.I. Rudakov. The Stability of a Spatially Inhomogeneous Plasma in a Magnetic Field. *Soviet Physics JETP*, 17(3):621–625, Mar 1963.

[59] Marshall N. Rosenbluth and Albert Simon. Finite larmor radius equations with nonuniform electric fields and velocities. *Physics of Fluids*, 8(7):1300–1322, 1965. doi:10.1063/1.1761402.

[60] B. Coppi, G. Laval, R. Pellat, and M.N. Rosenbluth. Convective modes driven by density gradients. *Nucl. Fusion*, 6(4):261, 1966. doi:10.1088/0029-5515/6/4/002.

[61] Kazuo Kitao. Shear stabilization of density gradient drift instabilities. *Plasma Physics*, 9(5):523, 1967. doi:10.1088/0032-1028/9/5/303.

[62] Nicholas A. Krall. Drift Waves. In Albert Simon and William B. Thompson, editors, *Advances in Plasma Physics*, volume 1, pages 153–199. Interscience Publishers, John Wiley and Sons, 1968.

[63] F.L. Hinton and C.W. Horton. Amplitude limitation of a collisional drift wave instability. *Physics of Fluids*, 14(1):116–123, Jan 1971.

[64] Bruce D. Scott. The mechanism of self-sustainment in collisional drift wave turbulence. *Physics of Fluids B: Plasma Physics*, 4(8):2468–2494, 1992. doi:10.1063/1.860215.

[65] Bruce Scott. *Low Frequency Fluid Drift Turbulence in Magnetised Plasmas*. Max-Planck-Institut für Plasmaphysik Research Report: IPP 5/92, March 2001.

[66] A. Kendl and B. D. Scott. Magnetic shear damping of dissipative drift wave turbulence. *Phys. Rev. Lett.*, 90:035006, Jan 2003. doi:10.1103/PhysRevLett.90.035006.

[67] B. LaBombard, J.W. Hughes, D. Mossessian, M. Greenwald, B. Lipschultz, J.L. Terry, and the Alcator C-Mod Team. Evidence for electromagnetic fluid drift turbulence controlling the edge plasma state in the Alcator C-Mod tokamak. *Nucl. Fusion*, 45(12):1658, 2005. doi:10.1088/0029-5515/45/12/022.

[68] J.L. Terry, J.W. Hughes, M.L. Reinke, J.E. Rice, R.M. Churchill, J. Irby, R.R. Parker, S. Shiraiwa, C. Theiler, G.M. Wallace, and P. Xu. Turbulence suppression and confinement improvements with LH power applied to high density H-modes, Nov. 2013.

[69] S.I. Braginskiĭ. Transport Processes in a Plasma. *Rev. Plasma Phys.*, 1:205, 1965.

[70] Jeffrey P. Freidberg. *Ideal Magnetohydrodynamics*. Plenum Press, New York, 1987. ISBN 1475708386.

[71] J. P. Hans Goedbloed and Stefaan Poedts. *Principles of Magnetohydrodynamics: With Applications to Laboratory and Astrophysical Plasmas*. Cambridge University Press, 2004. ISBN 0521626072.

[72] J. R. Myra, D. A. D'Ippolito, and X. Q. Xu. Drift wave instability near a magnetic separatrix. *Phys. Plasmas*, 9(5):1637–1645, 2002. doi:http://dx.doi.org/10.1063/1.1467929.

[73] J. R. Myra and D. A. D'Ippolito. Edge instability regimes with applications to blob transport and the quasicoherent mode. *Phys. Plasmas*, 12(9):092511, 2005. doi:http://dx.doi.org/10.1063/1.2048847.

[74] B. N. Rogers and J. F. Drake. Diamagnetic stabilization of ideal ballooning modes in the edge pedestal. *Physics of Plasmas (1994-present)*, 6(7):2797–2801, 1999. doi:http://dx.doi.org/10.1063/1.873237.

[75] B. Coppi and T. Zhou. Plasma confinement regimes and collective modes characterizing them. *Phys. Plasmas*, 19(10):102509, 2012. doi:http://dx.doi.org/10.1063/1.4757640.

[76] Thomas H. Stix. *Waves in Plasmas*. American Institute of Physics, 1997. ISBN 0883188597.

[77] E.M. Davis, M. Porkolab, J.W. Hughes, B. LaBombard, P.B. Snyder, and X.Q. Xu. BOUT++ simulations of edge turbulence in Alcator C-Mod's EDA H–mode. *APS DPP Meeting*, Nov. 2013. Poster, PP8.00017.

[78] Christiane Schröder, Thomas Klinger, Dietmar Block, Alexander Piel, Gérard Bonhomme, and Volker Naulin. Mode Selective Control of Drift Wave Turbulence. *Phys. Rev. Lett.*, 86:5711–5714, Jun 2001. doi:10.1103/PhysRevLett.86.5711.

[79] Christian Brandt, Olaf Grulke, and Thomas Klinger. Nonlinear interaction of drift waves with driven plasma currents. *Phys. Plasmas*, 17(3):032304, 2010. doi:http://dx.doi.org/10.1063/1.3328820.

[80] C Brandt, O Grulke, and T Klinger. Comparison of electrostatic and electromagnetic synchronization of drift waves and suppression of drift wave turbulence in a linear device. *Plasma Phys. Control. Fusion*, 52(5):055009, 2010. doi:http://dx.doi.org/10.1088/0741-3335/52/5/055009.

[81] G. G. Borg and R. C. Cross. Guided propagation of Alfvén and ion-ion hybrid waves in a plasma with two ion species. *Plasma Phys. Control. Fusion*, 29(6): 681, 1987. doi:http://dx.doi.org/10.1088/0741-3335/29/6/001.

[82] G. A. Collins, F. Hofmann, B. Joye, R. Keller, A. Lietti, J. B. Lister, and A. Pochelon. The Alfvén wave spectrum as measured on a tokamak. *Physics of Fluids*, 29(7):2260–2272, 1986. doi:http://dx.doi.org/10.1063/1.865563.

[83] G A Collins, A A Howling, J B Lister, and P Marmillod. Central mass and current density measurements in Tokamaks using the discrete Alfven wave spectrum. *Plasma Phys. Control. Fusion*, 29(3):323, 1987. doi:10.1088/0741-3335/29/3/004.

[84] A. Fasoli, D. Borba, G. Bosia, D. J. Campbell, J. A. Dobbing, C. Gormezano, J. Jacquinot, P. Lavanchy, J. B. Lister, P. Marmillod, J.-M. Moret, A. Santagiustina, and S. Sharapov. Direct Measurement of the Damping of Toroidicity-Induced Alfvén Eigenmodes. *Phys. Rev. Lett.*, 75:645–648, Jul 1995. doi:10.1103/PhysRevLett.75.645.

[85] A. Fasoli, J.A. Dobbing, C. Gormezano, J. Jacquinot, J.B. Lister, S.E. Sharapov, and A. Sibley. Alfvén eigenmode excitation by ICRH beat waves. *Nucl. Fusion*, 36(2):258–263, 1996.

[86] A Fasoli, D Borba, C Gormezano, R Heeter, A Jaun, J Jacquinot, W Kerner, Q King, J B Lister, S Sharapov, D Start, and L Villard. Alfvén eigenmode experiments in tokamaks and stellarators. *Plasma Phys. and Control. Fusion*, 39(12B):B287–B301, 1997. doi:10.1088/0741-3335/39/12B/022.

[87] A. Fasoli, D. Testa, S. Sharapov, H.L. Berk, Berk Breizman, A. Gondhalekar, R.F. Heeter, M. Mantsinen, and contributors to the EFDA-JET Workprogramme. MHD Spectroscopy. *Plasma Phys. Control. Fusion*, 44:B159–B172, 2002.

[88] T. Panis, D. Testa, A. Fasoli, A. Klein, H. Carfantan, P. Blanchard, and JET-EFDA Contributors. Optimization of the active MHD spectroscopy system on JET for the excitation of individual intermediate and high-n Alfvén eigenmodes. *Nuclear Fusion*, 50(8):084019, 2010. doi:http://dx.doi.org/10.1088/0029-5515/50/8/084019.

[89] Abraham Bers. *Linear Waves and Instabilities*. Gordon and Breach Science Publishers, 1975.

[90] David Anthony Schmittdiel. Investigation of Alfvén Eigenmodes in Alcator C-Mod Using Active MHD Spectroscopy. Master's project, Massachusetts Institute of Technology, Nuclear Engineering Department, 2003. URL http://hdl.handle.net/1721.1/17044.

[91] J. A. Snipes, N. Basse, C. Boswell, E. Edlund, A. Fasoli, N. N. Gorelenkov, R. S. Granetz, L. Lin, Y. Lin, R. Parker, M. Porkolab, J. Sears, S. Sharapov, V. Tang, and S. Wukitch. Active and fast particle driven Alfvén eigenmodes in Alcator C-Mod. *Phys. Plasmas*, 12(5):056102, 2005. doi:http://dx.doi.org/10.1063/1.1865012.

[92] Jason Sears. *Measurement and Interpretation of Stable and Unstable Alfvén Eigenmodes in the Presence of Fast Ions in Alcator C-Mod*. PhD thesis, MIT, 2010. URL http://hdl.handle.net/1721.1/60179.

[93] J. Sears, R.R. Parker, J.A. Snipes, T. Golfinopoulos, A. Bader, G.J. Kramer, and V. Tang. Measurement and calculation of Alfvén eigenmode damping and excitation over a full toroidal spectrum. *Nuclear Fusion*, 52(8):083003, 2012. doi:10.1088/0029-5515/52/8/083003.

[94] T. Golfinopoulos, S. Wukitch, R.R. Parker, A. Bader, A. Frankel, R. Granetz, Y. Ma, J. Sears, and S. Wolfe. MP #620: Driving Alfvén Eigenmodes with Amplitude-Modulated ICRF Waves. PSFC C-Mod Mini Proposal (Distributed Online), July 2010. URL http://www.psfc.mit.edu/research/alcator/miniproposals/620.pdf.

[95] T. Golfinopoulos, J. Sears, and R.R. Parker. MP #590: Reinforcing Characterization of Driven Alfvén Eigenmodes. PSFC C-Mod Mini Proposal (Distributed Online), Dec 2009. URL http://www.psfc.mit.edu/research/alcator/miniproposals/590.pdf.

[96] Alcator C-Mod Team. Alcator C-Mod Experimental Logbook. Published Online. URL https://www.psfc.mit.edu/research/alcator/logbook.php.

[97] Y. Lin, S. Wukitch, E. Marmar, A. Dominguez, and N. Tsujii. MP #600: Exploring the effect of fast RF power modulation on the quasi-coherent mode. PSFC C-Mod Mini Proposal (Distributed Online), Feb 2010. URL http://www.psfc.mit.edu/research/alcator/miniproposals/600.pdf.

[98] B.D. Dudson, M.V. Umansky, X.Q. Xu, P.B. Snyder, and H.R. Wilson. BOUT++: A framework for parallel plasma fluid simulations. *Computer Physics Comm.*, 180:1467–1480, 2009.

[99] Iu. A. Tserkovnikov. Stability of plasma in a strong magnetic field. *Soviet Physics JETP*, 5:58, 1957.

[100] Ferdinand Cap. *Handbook on Plasma Instabilities: v. 1.* Academic Press Inc, 1976. ISBN 0121591018.

[101] Wendell Jr. Horton. *Statistical Physics and Chaos in Fusion Plasmas*, chapter Statistical Description of Drift Wave Turbulence. Nonequilibrium Problems in the Physical Sciences and Biology. Wiley-Interscience, 1984. ISBN 0471883107.

[102] T.T. Ribeiro and Bruce Scott. Gyrofluid turbulence studies of the effect of the poloidal position of an axisymmetric debye sheath. *Plasma Phys. Control. Fusion*, 50(5):055007, 2008. doi:10.1088/0741-3335/50/5/055007.

[103] Paolo Ricci and B. N. Rogers. Plasma turbulence in the scrape-off layer of tokamak devices. *Phys. Plasmas*, 20(1):010702, 2013. doi:10.1063/1.4789551.

[104] Paul M. Bellan. *Fundamentals of Plasma Physics*. Cambridge University Press, 2008. ISBN 0521528003.

[105] R. D. Hazeltine and J. D. Meiss. *Plasma Confinement*. Dover Publications, 2003. ISBN 0486432424.

[106] Akira Hasegawa and Chanchal Uberoi. *The Alfvén Wave*. DOE Critical review Series–Advances in Fusion Science and Engineering. Technical Information Center U.S. Department of Energy, 1982. ISBN 0870791257.

[107] S Poedts, W Kerner, J P Goedbloed, B Keegan, G T A Huysmans, and E Schwarz. Damping of global Alfvén waves in tokamaks due to resonant absorption. *Plasma Phys. Control. Fusion*, 34(8):1397, 1992. doi:10.1088/0741-3335/34/8/003.

[108] King-Lap Wong. A review of Alfvén eigenmode observations in toroidal plasmas. *Plasma Phys. Control. Fusion*, 41(1):R1, 1999. doi:10.1088/0741-3335/41/1/001.

[109] H. H. Kuehl. Resonance cones for frequencies below the ion cyclotron frequency. *Physics of Fluids (1958-1988)*, 17(8), 1974.

[110] R.K. Fisher and R.W. Gould. Resonance Cones in the Field Pattern of a Radio Frequency Probe in a Warm Anisotropic Plasma. *Phys. of Fluids*, 14(4):857–867, Apr. 1971.

[111] Ronald R. Parker and R.J. Briggs. Warm Plasma Effects on Resonance Cone Structure. *MIT Res. Lab. Electronics Quarterly Prog. Report*, 104, 1972.

[112] P. M. Bellan and M. Porkolab. Propagation and mode conversion of lower-hybrid waves generated by a finite source. *Physics of Fluids (1958-1988)*, 17 (8), 1974.

[113] M. Ono. Cold, electrostatic, ion-cyclotron waves and ion-ion hybrid resonances. *Phys. Rev. Lett.*, 42:1267–1270, May 1979. doi:10.1103/PhysRevLett.42.1267.

[114] Donald E. Knuth. Structured programming with go to statements. *Computing Surveys*, 6:261–301, 1974.

[115] Theodore Golfinopoulos, Brian LaBombard, William Burke, Ronald R. Parker, William Parkin, and Paul Woskov. Wide-frequency range, dynamic matching network and power system for fusion plasma antenna. *Rev. Sci. Instrum.*, 85, 2014. doi:http://dx.doi.org/10.1063/1.4871550.

[116] T. Golfinopoulos, B. LaBombard, R. Parker, W. Burke, E.M. Davis, R. Granetz, M. Greenwald, J.W. Hughes, E. Marmar, M. Porkolab, J. Terry, S.M. Wolfe, P.P. Woskov, S.J. Wukitch, X. Xu, and Alcator C-Mod Team. MP #719: Shoelace Antenna Operation in EDA H-Mode. PSFC C-Mod Mini Proposal (Distributed Online), May 2012. URL `http://www.psfc.mit.edu/research/alcator/miniproposals/719.pdf`.

[117] Plansee. Report 530 DE 05.04 (3000) RWF: Molybdenum: Material Properties and Applications. Technical report, Plansee, 2004.

[118] A N James, D Brunner, B Labombard, C Lau, B Lipschultz, D Miller, M L Reinke, J L Terry, C Theiler, G M Wallace, D G Whyte, S Wukitch, and V Soukhanovskii. Imaging of molybdenum erosion and thermography at visible wavelengths in Alcator C-Mod ICRH and LHCD discharges. *Plasma Physics and Controlled Fusion*, 55(12):125010, 2013. doi:10.1088/0741-3335/55/12/125010.

[119] P. Smith. *Electronic Applications of the Smith Chart*. Krieger Pub Co, 1969. ISBN 0898745527.

[120] STMicroelectronics. Datasheet, STW13NK100Z N-channel 1000V - 0.56 Ω, 13A - TO-247 Zener - Protected SuperMESH ™PowerMOSFET. Technical report, ST, 2006.

[121] Coilcraft. Document 606-2: Miniature SMT Transformers (S5499-DL Datasheet). Technical report, Coilcraft, Inc., 2009. URL http://www.coilcraft.com.

[122] Pearson Electronics Incorporated. Pearson Current Monitor Model 101 Datasheet, Doc. 101.SPX_990506. Technical report, 1999. URL www.pearsonelectronics.com.

[123] Theodore Golfinopoulos. Verilog Code for Control of Dynamically-Switched Capacitor Boards. GitHub, Sep 2013. URL https://github.com/golfit/QcmCapBoardMain.

[124] Theodore Golfinopoulos. Verilog Code for Master Control Board. GitHub, Sep 2013. URL https://github.com/golfit/QcmMasterController.

[125] Agilent. Application Note 200 (Electronic Counter Series): Fundamentals of Electronic Counters (Doc. 5965-7660E). Technical report, Hewlett Packard/Agilent, 1997.

[126] Joe Reminder, Alex D. Sulik, and Tomasz J. Mokrzan. Model AG1010 LF Amplifier/Generator Operation Manual, Rev. B. Technical report, T&C Power Conversion, 2009. URL http://www.TCPowerConversion.com.

[127] J.H. Neher and M.H. McGrath. The calculation of the temperature rise and load capability of cable systems. *AIEE Trans. Power. App. Syst.*, 76:752–772, 1957.

[128] Theodore Golfinopoulos. Verilog Code for Phase Delay Board. GitHub, Sep 2013. URL https://github.com/golfit/QcmPhaseDelayBoard.

[129] T. Golfinopoulos, B. LaBombard, R. R. Parker, W. Burke, E. Davis, R. Granetz, M. Greenwald, J. Irby, R. Leccacorvi, E. Marmar, W. Parkin, M. Porkolab, J. Terry, R. Vieira, S. Wolfe, and Alcator C-Mod team team. External excitation of a short-wavelength fluctuation in the Alcator C-Mod edge plasma and its relationship to the quasi-coherent mode. *Phys. Plasmas*, 21(5):056111, 2014. doi:http://dx.doi.org/10.1063/1.4873595.

[130] B. LaBombard, T. Golfinopoulos, R. Parker, W. Burke, R. Granetz, M. Greenwald, E. Marmar, M. Porkolab, S. Wolfe, P. Woskov, S. Wukitch, I. Cziegler, J.L. Terry, and S. Zweben. PSFC C-Mod Mini Proposal (Distributed Online), May 2012. URL http://www.psfc.mit.edu/research/alcator/miniproposals/706.pdf.

[131] W. F. Bergerson, P. Xu, J.H. Irby, D.L. Brower, W.X. Ding, and E. Marmar. Far-infrared polarimetry diagnostic for measurement of internal magnetic field dynamics and fluctuations in the C-MOD Tokamak. *Rev. Sci. Instrum.*, 83 (10E316), 2012. doi:http://dx.doi.org/10.1063/1.4731757.

[132] B. LaBombard and L. Lyons. Mirror Langmuir probe: A technique for real-time measurement of magnetized plasma conditions using a single Langmuir electrode. *Review of Scientific Instruments*, 78(7):073501–073501–9, 2007. ISSN 0034-6748. doi:10.1063/1.2754392.

[133] J.L. Terry, R. Maqueda, C.S. Pitcher, S.J. Zweben, B. LaBombard, E.S. Marmar, A.Yu. Pigarov, and G. Wurden. Visible imaging of turbulence in the SOL of the Alcator C-Mod tokamak . *J. of Nucl. Mater.*, 290–293(0):757–762, 2001. ISSN 0022-3115. doi:http://dx.doi.org/10.1016/S0022-3115(00)00453-0. 14th Int. Conf. on Plasma-Surface Interactions in Controlled Fusion Devices .

[134] Ian H. Hutchinson. *Principles of Plasma Diagnostics*. Cambridge University Press, New York, 2nd edition, 2005. ISBN 052167574X.

[135] D-tAcq Solutions Ltd. 16 Channel Simultaneous High Speed Digitizer ACQ216CPCI (Datasheet). Technical report, May 2007. URL http://www.d-tacq.com/pdfs/d-tacq-acq216cpci-ds.pdf. Doc. 1501 2000-000 Rev 1.7.

[136] Josh Stillerman, William Burke, and Brian LaBombard. An optical timing verification system for Alcator C-Mod. *Fusion Engineering and Design*, 85(3-4):367–369, July 2010. ISSN 0920-3796. doi:http://dx.doi.org/10.1016/j.fusengdes.2010.02.003.

[137] Alan V. Oppenheim and Ronald W. Schafer. *Discrete-Time Signal Processing*. Prentice Hall Signal Processing, 3rd edition, 2009. ISBN 0131988425.

[138] Hung Cheng. *Advanced Analytic Methods in Applied Mathematics, Science, and Engineering*. LuBan Press, 2007. ISBN 0975862510.

[139] Sean Carroll. *Spacetime and Geometry: An Introduction to General Relativity*. Addison-Wesley, 2003. ISBN 0805387323.

[140] Benjamin Dudson. *BOUT++ Users Manual*. University of York, July 2010. URL https://github.com/bendudson/BOUT/tree/master/manual.